Cryogenic Ion Vibrational Spectroscopy of Gas-Phase Clusters:

Structure, Anharmonicity and Fluxionality

Dissertation zur Erlangung des Grades
eines Doktors der Naturwissenschaften (Dr. rer. nat.)
am Fachbereich Physik
der Freien Universität Berlin

von

Matias Ruben Fagiani

2017

The work reported in this thesis was performed from February 2012 to December 2016, at the Fritz Haber Institute of the Max Planck Society in Berlin and at the Wilhelm-Ostwald-Institut für Physikalische und Theoretische Chemie of the Universität Leipzig, under the supervision of Prof. Dr. Knut R. Asmis.

Erstgutachter, Betreuer: Prof. Dr. Knut R. Asmis
Universität Leipzig

Zweitgutachter: Prof. Dr. Gerard J. M. Meijer,
Fritz Haber Institute
Freie Universität Berlin
Radboud Universiteit Nijmegen

Date of defence: 31.03.2017

Selbständigkeitserklärung

Hiermit erkläre ich dass ich die vorliegende Dissertation selbstständig verfasst und keine anderen als die angegebenen Hilfsmittel genutzt habe. Alle wörtlich oder inhaltlich übernommenen Stellen habe ich als solche gekennzeichnet.

Ich versichere außerdem, dass ich die vorliegende Dissertation nur in diesem und keinem anderen Promotionsverfahren eingereicht habe und dass diesem Promotionsverfahren keine endgültig gescheiterten Promotionsverfahren vorausgegangen sind.

Berlin, 27.01.2017 _____

Abstract

Gas-phase clusters are aggregates of a countable number of particles, which exhibit size-dependent physical and chemical properties that typically lie in the non-scalable size regime. These properties can be systematically characterized at a molecular level with respect to composition, size and charge state. This allows studying how macroscopic properties of condensed matter, *e.g.* phase transitions or metallic behavior, emerge from the atomic or molecular properties as a function of cluster size. Furthermore, smaller clusters are also amenable to high-level quantum chemical calculations, making them ideal model systems for understanding phenomena in more complex heterogeneous matter. The main advantage here is that clusters can be studied with a very high degree of selectivity and sensitivity, under well-defined conditions and in the absence of perturbing interaction with an environment. The studies presented in this theses focus on the structure characterization of ionic clusters using cryogenic ion vibrational spectroscopy. This technique combines cryogenic ion trapping with mass spectrometric schemes and infrared photodissociation (IRPD) spectroscopy. It makes use of an ion-trap triple mass spectrometer in combination with various light sources that grant access to a wide range of the infrared spectrum (210–4000 cm^{-1}). Structures are typically assigned by comparing experimental IRPD spectra with computed vibrational spectra.

The structures of aluminum oxide clusters and their interaction with water are studied in the framework of the collaborative research center CRC1109 "Understanding of Metal Oxide / Water Systems at the Molecular Scale: Structural Evolution, Interfaces, and Dissolution". This project aims at gaining a molecular level understanding of the mechanisms involved in oxide formation and dissolution. Section 4.1 and 4.2 present results of IRPD spectroscopy experiments on small mono- and dialuminum oxide anions and on the anionic cluster series $(Al_2O_3)_nAlO_2^-$ with $n = 0$ to 6. These studies discuss the effects of the distribution of the excess charge on the cluster structure, analyze how structural properties evolve with size and how these relate to those of nanoparticles and crystal surfaces. The dissociative adsorption of water by Al-oxide clusters is investigated in Section 4.3.2.

Boron exhibits a rich variety of polymorphs with the B_{12} icosahedron as a common building block. This three dimensional (3D) structure is retained in the halogenated closo-dodecaborate dianions ($B_{12}X_{12}{}^{2-}$). On the other hand, small pure boron clusters are essentially planar. The study presented in Section 5.2 investigates the 3D to 2D structural transition by probing the vibrational spectra of partially deiodinated $B_{12}I_n{}^{2-}$ clusters as a function of decreasing n. The results presented in Section 5.1 show that $B_{13}{}^+$ has a planar structure consisting of two concentric rings. As a result of delocalized aromatic bonding, this structure is particularly stable without being rigid as it permits an almost free rotation of the inner ring.

Protonated water clusters are model systems for understanding protons in aqueous solutions. The interpretation of their vibrational spectra is a challenge for state-of-the-art electronic structure calculations and therefore often prone to controversies. The results presented in Chapter 6 clear existing doubts over the assignment of the protonated water pentamer structure and the vibrational fingerprints of the embedded distorted H_3O^+. This study laid the foundation for a subsequent series of measurements which provided crucial new insights into the proton transfer mechanism in water.

Kurzfassung

Gasphasencluster sind Aggregate mit einer zählbaren Anzahl von Teilchen, deren größenabhängige Eigenschaften typischerweise im nicht-skalierbaren Regime liegen. Deren Eigenschaften lassen sich auf molekularer Ebene hinsichtlich Zusammensetzung, Größe und Ladungszustand systematisch charakterisieren. Dies ermöglicht zu erforschen, wie sich Eigenschaften kondensierter Materie, wie beispielsweise Phasenübergänge oder metallisches Verhalten, aus den Eigenschaften der Bestandteile mit zunehmender Größe entwickeln. Ferner können kleinere Cluster mit hochwertigen quantenchemischen Methoden modelliert werden, was sie zu idealen Modellsystemen für heterogene Materialien macht. Cluster können nicht nur größenselektiv und mit hoher Empfindlichkeit, sondern auch unter wohldefinierten Bedingungen und in Abwesenheit des störenden Einflusses einer Umgebung erforscht werden. Das Ziel der vorliegenden Dissertation ist die Strukturcharakterisierung ionischer Cluster mittels der Schwingungsspektroskopie kryogener Ionen. Hierzu wurden moderne massenspektrometrische Methoden mit der Infrarot-Photodissoziation(IRPD)-Spektroskopie (IRPD) kombiniert. Mit Hilfe unterschiedlicher Strahlungsquellen konnte ein möglichst breiter Spektralbereich (210 bis 4000 cm^{-1}) abgedeckt werden. Die Strukturbestimmung erfolgte typischerweise durch den Vergleich gemessener IRPD-Spektren mit simulierten IR-Spektren.

Die Untersuchungen zur Struktur von Aluminiumoxidclustern sowie deren Wechselwirkung mit Wasser wurden im Rahmen des Sonderforschungsbereichs SFB-1109 “Understanding of Metal Oxide / Water Systems at the Molecular Scale” durchgeführt. Ziel des SFBs ist, die Mechanismen der Oxidbildung und -auflösung auf molekularer Ebene aufzuklären. In den Abschnitten 4.1 und 4.2 werden die Resultate der IRPD-Spektroskopie an kleinen Mono- und Dialuminiumoxidanionen sowie an anionischen Clustern der Serie $(Al_2O_3)_nAlO_2^-$ mit $n = 0$ bis 6 beschrieben. In diesen Studien wurde untersucht, welche Auswirkung die Ladungsverteilung auf die Clusterstruktur hat, wie sich Eigenschaften mit der Clustergröße entwickeln und inwieweit diese sich mit denen entsprechender Nanopartikel und Kristalloberflächen vergleichen lassen. Die dissoziative Wasseradsorption an Aluminiumoxidclustern wurde in Abschnitt 4.3.2) erforscht.

Bor weist einen umfangreichen Polymorphismus auf, wobei als Grundbaustein häufig ein B_{12}-Ikosaeder auftritt. Diese dreidimensionale Struktur liegt auch im halogenierten Closo-Dodekaborat $B_{12}X_{12}^{2-}$ Dianion vor. Andererseits weisen kleine Borcluster planare Strukturen auf. Die in Abschnitt 5.2 beschriebenen Messungen dienen der Untersuchung des Übergangs von einer drei- zu einer zweidimensionalen Struktur am Beispiel des deiodierten $B_{12}I_n^-$. In Abschnitt 5.1 wird gezeigt, dass das kationische B_{13}^+ eine, aus zwei konzentrischen Ringen bestehende, planare Struktur aufweist, die sich durch eine fast freie Rotation des inneren Rings auszeichnet. Aufgrund der aromatischen Bindungsverhältnisse ist dieses System somit besonders stabil, ohne starr zu sein.

Protonierte Wassercluster dienen als Modellsystem für Protonen in wässriger Lösung. Die Modellierung der IR-Spektren dieser Cluster bringt selbst die besten quantenchemischen Methoden an ihre Grenzen, was zu erheblichen Kontroversen geführt hat. Die in Kapitel 6 dargelegten Ergebnisse erlauben eine vollständige Zuordnung der IR-Banden der verzerrten H_3O^+-Gruppe, beseitigen Zweifel an der Struktur des protonierten Wasserpentamers und ebneten einer Reihe von weiteren Messungen den Weg, die neue Einsichten in den Mechanismus des Protonentransfers in Wasser ermöglichten.

Contents

1 Introduction

Many technological advancements rely on the development of materials with new, improved, or even tailor-made properties. Metal oxides based materials were developed as early as 200 BC, when magnetic Fe_3O_4 containing rocks were used in China in compass-like instruments for religious purposes. In the modern age, a more detailed understanding of the magnetic properties of iron oxides has allowed for new applications, such as the use of superparamagnetic iron oxide nanoparticles as a contrast agent to improve the sensitivity in nuclear magnetic resonance imaging [1].

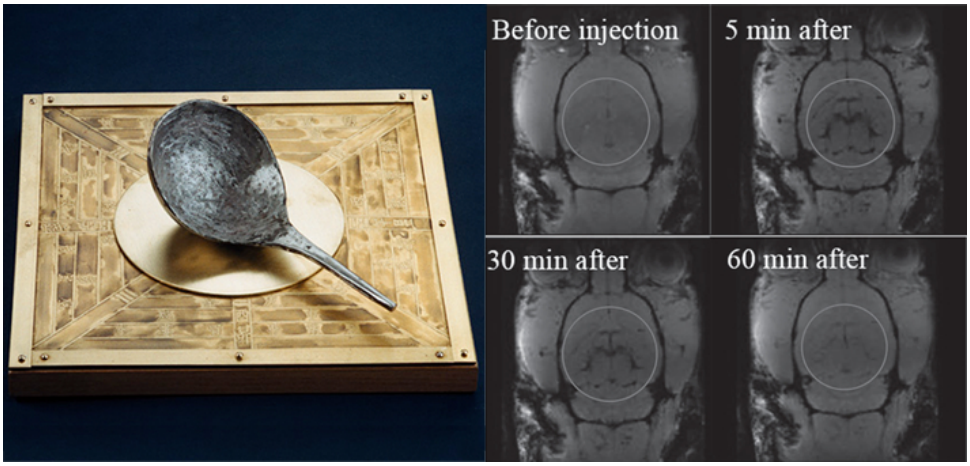

Figure 1.1: (left) Spoon shaped compass made of lodestone or magnetite ore, referred to as "South-pointer" during the Han Dynasty. Picture taken from the Virtual Museum of Ancient Inventions (Smith College History of Science). **(right)** Rat brain nuclear magnetic resonance contrast images pre and post injection with DMSA functionalized iron oxide 4 nm particles (seen as black contrast in the area inside the circle). Picture taken from Ref. [2].

However, despite intense research in material science, it often proves difficult to describe the structure and functionality of these materials at the molecular level. Such a level of insight is especially important to understand the basic physical and chemical processes occurring at material interfaces. For example, the desired chemistry on a solid catalyst can, in principle, be fully controlled by the particular structure and composition of specific surface sites, called active sites, even though their number on the surface is small. Therefore, for a proper description of the catalyst behavior, the surface has to be described at the molecular level and requires highly sensitive techniques. The complexity of the problem is increased by surface

non-crystallinity and restructuring as well as the need to account for interactions with the environment, including gases or solvents containing solutes in the form of neutral particles and ions. In the field of surface science, one approach to this problem is to characterize model systems, typically single crystal surfaces prepared under ultra-high vacuum (UHV) conditions which are then exposed to controlled amounts of gases. However, surface reconstruction that follows the interaction with reacting gases often hinders a precise structural characterization. In addition, extrapolating the information gained in such model systems to real conditions remains difficult as the kinetics and thermodynamics can substantially differ. For example, α-alumina surfaces are considered a good model system for non-crystalline transition alumina or aluminum oxyhydroxides [3, 4]. These materials were extensively studied over the last decades as these are relevant in areas as ceramic processing [5], environmental geochemistry [6] and corrosion science [7], among others. The reactivity and structure of these surfaces are known to change in contact with water [8], but even the interaction of a few water molecules with well-defined alumina surfaces is difficult to describe at a molecular level. Only recently, IR-experiments provided spectroscopic evidence that supports the theoretically predicted water dissociation pathway on the thermodynamically stable α-$Al_2O_3(0001)$ and $(1\bar{1}02)$ surfaces terminations [9, 10].

Characterizing isolated clusters in the gas phase removes the complexity introduced by the perturbing interaction with an environment. Clusters are generally defined as an aggregate of a countable number (up to few thousands) of particles (*i.e.* atoms or molecules). Bigger clusters include a range of complexes that can also be referred to as nanoparticles, which are defined with respect to their diameter ($10^{-9} - 10^{-7}$ m) and typically exhibit mass and stoichiometry distributions. In the work presented in this thesis, the term clusters is used to refer to aggregates of up to few tens of atoms. In particular, my research has focused on the study of ionic clusters which allows for the application of highly selective mass spectrometric techniques. The high degree of control of the particle trajectories enables mass selection, cryogenic ion trapping and ion-messenger complex formation (see Chapter 3). The study of gas-phase ions can therefore achieve high sensitivity and selectivity allowing for a systematic characterization of their chemical and physical properties with respect to composition, charge state, size and structure at the molecular level [11, 12]. However, clusters are not simply a bridge between atoms or molecules and the corresponding bulk material. Their properties evolve in a non-scalable regime such that they cannot be extrapolated from the properties of larger nanoparticles or a single atom [13]. The addition or subtraction of a single atom can in fact change the cluster properties substantially. For example, smaller cationic boron clusters, $B_n{}^+$, exhibit planar, quasi-planar or cylindrical geometries with a 2D to 3D transition at $n = 16$ [14]. Electronic structure calculations on the anionic analogs predict a planar structure for $B_{38}{}^-$ and $B_{40}{}^-$, while $B_{39}{}^-$ is calculated and experimentally proven to have a 3D structure [15, 16]. That the evolution of size-dependent properties can be studied atom-by-atom in gas-phase clusters under well-defined conditions with the use of mass-spectrometric and laser spectroscopic techniques is probably the single most important advantage of the studies

presented in this thesis.

Changes in material properties with particle size and temperature, as well as those due to interaction with other materials and gases, or due to aging, are the manifestation of electronic and geometric variations. It is no surprise then that one of the main goals in the cluster science community is dedicated to the characterization of structural properties. Many of the experimental techniques used to study materials in the condensed phase cannot be directly applied to the study of isolated gas-phase clusters, because of the absence of order (crystallinity) and the lower achievable number density. For instance, a 1 cm long probe of 10^7 particles/cm^3 with an absorption cross section of 10^{-20} cm^2 attenuates a transmitted light beam by 10^{-13} of its initial intensity, which is impossible to detect directly. Other techniques, so-called action techniques, were therefore developed to measure the absorption of photons indirectly by monitoring the response or action induced in the molecule or ion by the photon absorption, *i.e.* a change in quantum state, charge state or mass. In the work presented in this thesis, infrared (IR) photodissociation spectroscopy[17, 18] (see Section 2.2.1) was used to study the structure and properties of mass-selected cluster ions in the gas phase. Interpreting and assigning the measured vibrational fingerprint is not trivial and typically requires the use of electronic structure calculations. Experimentally, the coexistence of multiple isomers, anharmonic effects and high ion internal energy increase the complexity of the measured vibrational spectrum and lead to spectral congestion. These undesired effects become more pronounced with increasing temperature. Thus, performing experiments on internally cold clusters simplifies the interpretation of the measured vibrational spectra substantially. Over the last thirty years, cryogenic ion vibrational spectroscopy, a combination of cryogenic ion trapping, mass spectrometric schemes and infrared photodissociation spectroscopy has evolved as one of the most powerful and broadly applicable tools for the structural characterization of gaseous ions [12, 19, 20].

The interpretation of the spectral features and ultimately the assignment of the geometric structure of the cluster under study typically require the use of high level electronic structure calculations. On the other hand, the prediction of the cluster structure only based on theory can be deceptive, as it remains difficult to calculate sufficiently accurate potential energy surfaces (PES) as well as to identify the global minimum of a complex PES. Theoretical predictions of metal oxide clusters, in particular those containing transition metal atoms with open d-shells, often result in a flurry of possible constitutional and electronic isomers of similar energy. The highly fluxional and strongly anharmonic character of hydrogen-bonded clusters is also challenging to predict and interpret with standard theoretical methods. As clusters containing up to a few tens of atoms are amenable to high level calculations, the comparison of computed spectra with experimental ones allows for testing and benchmarking of these methods. The evaluation of the accuracy of different computational methods applied to small model systems in the form of gas-phase clusters also serves to gauge their applicability to more complex systems. The next sections provide an overview of the cluster studies performed as part of the present thesis.

1.1 Structure and hydration behavior of Al-oxide cluster ions

Metal oxides, like silicon dioxide, iron oxides and aluminum oxide, are the most abundant materials in the Earth's crust. Oxide nanomaterials [21] are characterized by structural variability and diverse properties, *i.e.* hardness, electrical and thermal resistivity, redox activity and chemical reactivity. Their technical applications include nanosensors [22], coatings, photocatalysts and advanced energy systems [23, 24], fuel cells [25] and heterogeneous catalysts [26]. Others, such as photo-voltaic transparent conductive oxides (TCOs), metal oxide thin film transistors (TFTs) and microelectronics (SOI – silicon on insulator) rely on the availability of metal oxide materials with tailored properties for their improvement. The durability of these metal-oxide-based devices also depends on their stability, in particular their resistance to degradation processes. Water plays a central role in both synthesis and corrosion ability. Oxide synthesis is typically performed in aqueous solutions, on one hand, and water, both as a liquid or a gas, is also the most common reactant leading to corrosion and dissolution of these metal oxide materials.

The controlled synthesis of tailor-made oxides with desired properties and durability requires a molecular level understanding of the mechanisms involved in oxide formation and dissolution as well as how molecular level properties evolve into those of macroscopic materials with size. To understand the multi-scale nature of metal-oxide/water chemistry, phenomena that occur at length scales ranging from individual molecules, through clusters and nanoparticles, to extended crystalline and amorphous bulk materials need to be characterized. To tackle this ambitious multidisciplinary task, the DFG-funded Collaborative Research Center CRC-1109 "Understanding of Metal Oxide / Water Systems at the Molecular Scale: Structural Evolution, Interfaces, and Dissolution" was initiated in Berlin in 2014. The studies on aluminum oxides and their interaction with water, presented in Chapter 4, are part of the subproject D01 "Microhydrated metal oxide clusters in the gas phase: structure, stability and reactivity". The project aims to characterize structural motifs and their evolution with cluster size and answer the following questions: To what extent is dissociative absorption observed? How does the absorption mechanism depend on the oxidation state, geometric structure, degree of microhydration and the presence of acidic or basic sites? How does the formation of the hydration shell evolve with the number of water molecules? How do defect sites (removal of oxygen atom) change these observations? Structural investigation is performed by measuring the infrared photodissociation spectra of mass-selected and cryogenically-cooled metal (Al, Fe and Si) oxide cluster ions as well as their complexes with a few water molecules in the gas phase. The project is performed in close-collaboration with the quantum chemistry group of Prof. Joachim Sauer (Humboldt University Berlin), who utilizes global optimization schemes and state-of-the-art quantum mechanical methods to explore complex potential energy surfaces in order to find global and local minimum energy structures and compute their vibrational spectra. The comparison of the experimental and theoretical vibrational spectra typically allows for unambiguous structural assignment [11]. Such experiments also constitute the ideal

arena to test computational models and evaluate their applicability to more complex systems.

Aluminum exhibits only a single stable isotope (^{27}Al) and is characterized by a simple electron configuration ([Ne]3s^{2}3p^1). Therefore, initial experiments were performed on Al-oxide clusters. The results of the IRPD study on small mono- and di-aluminum oxide anions are presented in Section 4.1. The structures of the species studied are characterized, revealing the presence of a common four-membered ring motif in all the dialuminum oxide anions. Comparison of the experimental data with various computational methods shows that in order to account for the delicate balance between localization and delocalization of the unpaired electron, density functionals with a large amount of Fock exchange such as BHLYP need to be used. This study was published in The Journal of Chemical Physics [27].

Section 4.2 presents the structural characterization of the anionic cluster series $(Al_2O_3)_nAlO_2^-$ with $n = 0$ to 6. The stoichiometry was chosen such that it (i) converges to that of bulk alumina for large n and (ii) avoids the radical nature of $(Al_2O_3)^-$, similar to the approach taken in the previous study on $(Al_2O_3)_nAlO^+$ [28]. Cluster structures are assigned and discussed in terms of size-dependent coordination numbers and bond lengths. Results are compared with those already known for cationic and larger neutral clusters as well as thin film and bulk phase data. With the exception of $(Al_2O_3)_3AlO_2^-$, all structures assigned contain edge-sharing and corner-sharing four-membered rings as a common structural motif.

The structural characterization of the complexes formed by the fully oxidized electronic closed-shell $Al_3O_4^+$ with up to four D_2O molecules is presented in Section 4.3. The clusters are obtained by sequential adsorption of single water molecules onto $Al_3O_4^+$ in the reaction channel of a laser vaporization source. To this end a modified source block with two gas channels was designed, constructed and tested as part of this thesis (see Section 3.2.2). We find that water undergoes dissociative adsorption in all the cluster series leading to the formation of terminal and bridging OD groups. The structural assignment allows identification of the vibrational signature of water adsorption, which is in turn used to define characteristic spectral absorption regions containing particular vibrational normal modes as a function of the coordination of the oxygen and of the aluminum atoms.

1.2 Boron clusters

Boron and its compounds find application as fiberglasses [29], ceramics [30] and superhard materials [31], as well as semiconductors [32], superconductors [33], liquid crystals [34] and ionic liquids [35]. Such wide range of applications is possible because of the peculiar structures and unusual chemical bonding of boron based materials. Boron is electron deficient which results in a strong tendency to share electrons [36]. It shows a variety of bonding configurations ranging from the expected two-center two-electron bond (2c-2e) up to 7c-2e bonds [37]. These properties of elemental boron lead to a rich variety of polymorphs with polyhedral building blocks, in particular, the B_{12} icosahedron [38]. The existence of boron nanostructures such as nanotubes, two-dimensional sheets and nanospheres have been postulated based on *ab*

initio computations [39]. The properties of these materials are predicted to be similar and sometimes superior to those of the related carbon compounds. For example, a metallic-like density of states is obtained for all tubular boron compounds considered and these may hence be better conductors than carbon nanotubes with potential applications as high-temperature light materials and electronic devices. Experimentally, only single- and multi-wall nanotubes have been reported [40, 41] to date. Recently, the group of Wu synthesized a boron sheet on a silver substrate using chemical vapor deposition with a pure boron source [42].

A renewed interest in boron clusters and nanostructures followed the recent discovery by Prof. L. S. Wang and coworkers of the first all-boron fullerene or borospherene, B_{40}, and of a planar B_{36} cluster with a central hexagonal hole, the extension of which would give rise to a planar boron sheet analogue to graphene and which the authors termed borophene [43, 44]. Small pure boron clusters are found to be essentially planar, and the chemical bonding analyses suggest that this planarity is the consequence of π-bonding in the clusters [45]. Two-dimensional electron delocalization causes aromaticity or anti-aromaticity in boron clusters that is analogous to that in unsatured hydrocarbons. For instance, the $B_{13}{}^{+}$ cluster is found to be particularly stable (magic number). Its minimum energy structure is predicted to be planar, consisting of an inner atomic triangle surrounded by a ten-member ring. The planarity and exceptional stability of $B_{13}{}^{+}$ have been explained in term of σ- and π-aromaticity [46]. As a consequence of the delocalized bonding the barrier towards internal rotation of the three-member ring is predicted to be very small and has been therefore called a "molecular Wankel motor" [47–49]. The results of IRPD experiments and of Born-Oppenheimer molecular dynamics presented in Section 5.1 confirm the predicted structure and provide the first spectroscopic evidence for its exceptional fluxional character. This study was published in *Angewandte Chemie* and selected as a very important article (top 10%).[50, 51]

A well-studied family of boron clusters with icosahedral structures are the halogenated closo-dodecaborates $B_{12}X_{12}{}^{2-}$ (X= F, Cl, Br, I). Although these compounds have been studied since their synthesis in the 1960s [52], they still are of interest in fundamental and applied research [53]. In 2011, Warneke and coworkers studied the reactivity of these systems using mass spectrometry. They found that $B_{12}I_{12}{}^{2-}$ could be completely dehalogenated [54]. A subsequent theoretical investigation found that the planar B_{12} unit could be obtained through loss of iodide ions or iodine atoms from the fully iodinated system [55]. The opening of the icosahedral boron framework was predicted to take place within the clusters containing 5 to 7 iodine atoms. The study of the vibrational spectra of these clusters, presented in Section 5.2, allowed the experimental identification of $B_{12}I_7{}^{-}$ as the largest partially deiodinated cluster that, under the experimental conditions, prefers an open structure. This study was published in the journal *Chemical Physics Letters* and highlighted as editor's choice [56].

The studies on boron clusters were performed in close-collaboration with the computational chemistry group of Prof. Thomas Heine (Universität Leipzig).

1.3 Protonated water clusters

Water appears as very ordinary and ubiquitous and consequently its properties may be believed to be fully understood: it is transparent, odorless, tasteless, the second most common molecule in the Universe after hydrogen, the most abundant molecule on the earth's surface, and there are a hundred times as many water molecules in our body than the sum of all the other molecules put together. However, in reality its properties are characterized by a flurry of anomalies. For example, under ambient conditions water exhibits a density maximum at 4 °C and the liquid phase is denser than the solid phase. More precisely, the thermal expansion coefficient, α_P, is negative below 4 °C [57]. Other thermodynamic response functions such a specific heat, C_P, and compressibility, κ_T, also manifest anomalies [58, 59].

The water molecule, H_2O, has highly polar covalent bonds between the partially positively charged hydrogen atoms and the more electronegative oxygen atom. This leads to strong and directional electrostatic interactions called hydrogen bond. The hydrogen bond is defined by IUPAC as "an attractive interaction between a hydrogen atom from a molecule or a molecular fragment X–H in which X is more electronegative than H, and an atom or a group of atoms in the same or a different molecule, in which there is evidence of bond formation" [60]. This strong intermolecular interaction and their directional character are at the base of the complexity of the properties of water. The hydrogen bond between water molecules is directed from the center of a water molecule, called donor, in the O–H directions towards the oxygen of a second water called acceptor. Each water molecule can form as many as four hydrogen bonds, two as donor and two as acceptor, ultimately forming a tetrahedral network in the liquid. This network is generally described as dynamic, involving the rupture and formation of hydrogen bonds on time scales on the order of the $10^{-11} - 10^{-14}$ seconds [61].

The ubiquity of water and its unusual properties make it arguably one of the most important materials. As a consequence, it is also the most interdisciplinary studied material. Water participates in the formation of aerosol particles and cloud condensation in the atmosphere [62, 63]; it determines the structure and dynamics of proteins and DNA [64]; processes at water interfaces are of fundamental importance to understand basic questions in geochemistry, electrochemistry, environmental sciences but also in technological applications [65]; in solution chemistry it acts as a medium but often also participates in elementary chemical processes [66]; its chemistry is also of fundamental importance for the study of the universe [67].

The experiments presented in Chapter 6 aim to shed new light on another fundamental process in liquid water: proton transfer. Proton mobility in water (3.6×10^{-3} cm^2 V^{-1} s^{-1} at room temperature) is anomalously high relative to other ions, approximately 5 times that of K^+, and cannot be explained by hydrodynamic diffusion [68]. The generally accepted explanation, typically referred to as the Grotthuss mechanism, encompasses sequential hops of a charge defect along a hydrogen-bonded network of water molecules involving, at each step, intermolecular proton transfer between oxygen atoms along a strong ionic hydrogen bond [69–71]. The process, also termed "structural diffusion", is initiated by a lowering of the

energy barrier caused by thermal rearrangements of the hydrogen bond network distant from the excess charge. Different models have been proposed for the exact mechanism [72, 73]. At the center of the debate are two limiting structures, the Eigen [74] and the Zundel [75] cations, and their relative importance. The first consists of a charge-delocalized symmetrically solvated hydronium ion, $H_9O_4^+$, and the second of a more charge-localized proton equally shared between two water molecules, $H_5O_2^+$. Identifying the nature of the proton at the molecular scale in solution from the experimental vibrational spectrum is challenging given the extremely diffuse nature of the associated absorption features linked to the dynamic hydrogen bond network [76, 77].

Cold protonated water clusters, $H^+(H_2O)_n$, in the gas phase have, over the years, provided crucial experimental data for understanding the origin of the vibrational spectrum of the proton in solution [78–82]. Transient interconverting species from bulk water can be isolated, stabilized and characterized in the gas phase. For example, the study on the protonated water hexamer allowed the isolation of the spectral signal of coexisting Eigen-type and Zundel-type isomers [83]. However, the interpretation of the vibrational spectra of protonated water clusters is far from trivial due to static and dynamic anharmonic effects, and represents a true challenge for state-of-the-art theoretical models.

Ongoing controversies regarding the assignment of the vibrational spectrum of the protonated water pentamer have motivated the study presented in Chapter 6. Y.T. Lee and coworkers originally assigned the IRPD spectrum of $H^+(H_2O)_5$ to an Eigen-type structure [84]. This assignment was confirmed by follow-up studies, which investigated broader IR regions, the effect of messenger-tagging and deuteration. However, not all spectral features were readily assignable to fundamental transitions, suggesting that anharmonic effects may play an important role [79, 82]. More recently, this original assignment was questioned based on results from AIMD simulations that suggested the presence of two isomers, both different from the originally assigned one [85]. The study described in Chapter 6 shows that the original assignment to the Eigen isomer was correct. The presence of multiple isomers is excluded by exploiting the reduced anharmonicity of the perdeutereted complex and by using, among other techniques, an isomer-specific detection technique. A simple kinetic treatment shows that the conclusions derived from the AIMD simulations were flawed due to the neglect of nuclear quantum effects. This work was published in the journal *Physical Chemistry Chemical Physics* [86]. An important result of this study is the elucidation of the assignment of the O–H stretches of the embedded distorted H_3O^+. This provided a central piece of information for understanding the proton transfer mechanism and culminated in a collaborative effort, which involved the spectroscopy group of Prof. Mark A. Johnson and the theoretical chemistry groups of Prof. Ken Jordan and of Prof. Anne McCoy, in which cluster spectroscopy was exploited to obtain spectroscopic snapshots of the proton transfer mechanism in water. This work was published in *Science* [87].

2 Infrared Spectroscopy

Infrared (IR) spectroscopy is a well-established technique to investigate the structure of molecules. IR radiation probes the forces between the atoms in a molecule from which information on their spatial arrangement can be obtained. It typically provides a unique spectral pattern that allows unambiguous identification, quantification and often structural characterization of the investigated species. IR spectroscopic techniques are used in the experiments presented in this work to study the vibrations of mass-selected ionic clusters in the gas phase. In this chapter the theoretical concepts of molecular vibrations are explored, followed by an introduction to gas-phase IR spectroscopy, with particular focus on Infrared Multiphoton Dissociation (IRMPD) and Infrared Vibrational Predissociation (IRVPD) spectroscopy. Finally, the standard method of obtaining structural information using computational methods is discussed.

2.1 Molecular vibrations

A vibration is defined as a periodic motion of a rigid or elastic body forced from its equilibrium state that results from the response of the forces that tend to restore it. A molecular vibration is thus the oscillation of atoms about their equilibrium positions in a molecule. The bonding interactions between atoms are liable for the unique vibrational response typical of each molecule. Experimental investigation, together with theoretical description of the interactions playing a role in the specific system, generally allows for the extraction of structural information. Quantum mechanics is the tool of choice for describing molecular vibrations. It involves solving the time-independent Schrödinger equation,

$$\hat{H}\psi(\mathbf{r},\mathbf{R}) = E\psi(\mathbf{r},\mathbf{R}),$$

with the Hamilton operator, $\hat{H}$, acting on the wave function of the system, ψ, and yields the energy of the system multiplied by ψ. ψ depends on the coordinates of electrons and nuclei $\mathbf{r}$ and $\mathbf{R}$ respectively, and E the eigenvalue of the Hamiltonian. Given that the mass of a proton is roughly three orders of magnitude larger than the mass of an electron, nuclei can typically be considered stationary during the time scale of electron motion. This is known as the Born-Oppenheimer approximation and under such conditions the wave functions and the Hamiltonian can be separated in an electronic (ψ_{el} and $\hat{H}_{el}$) and a nuclear part (ψ_n and $\hat{H}_n$).

The electronic Schrödinger equation,

$$\hat{H}_{el}\psi_{el}(\mathbf{r},\mathbf{R}) = E(\mathbf{R})\psi_{el}(\mathbf{r},\mathbf{R}),$$

yields the electronic energy as a function of the nuclear coordinates, *i.e.* the so called potential energy surface (PES). The force constants of the interatomic bonds determine the properties of the PES.

A useful approximation to treat molecular vibrations is to describe them as harmonic oscillators. A polyatomic molecule consisting of N atoms has $3N-6$ ($3N-5$ for linear molecules) vibrational degrees of freedom. Molecular vibrations are typically described in the context of normal modes, as they simplify the mathematical treatment. Each normal mode represents a single harmonic oscillator with displacement along a single coordinate, the mass-weighted normal coordinate q_i, and a characteristic frequency ω_i. All the atoms in the molecule oscillate in phase with frequency ω_i but with different amplitudes. The Hamiltonian is then of the form:

$$\hat{H} = \sum_{i}^{3N-6}\left(-\frac{\hbar^2}{2}\frac{\partial^2}{\partial q_i^2} + \frac{1}{2}k_i q_i^2\right),$$

for which the eigenvalues are given by:

$$E_i = (n_i + \frac{1}{2})\hbar\omega_i \qquad \text{where} \qquad \omega_i = \sqrt{k_i} \qquad \text{and} \qquad i = 1, 2, ..., 3N-6, \tag{2.1}$$

with k_i the eigenvalue of the mass-weighted Cartesian force constants matrix and n_i the energy level of the i-th normal mode (see Fig. 2.1 for an example of diatomic harmonic PES). Equation (2.1) shows that with zero quanta of vibrational energy ($n_i = 0$) the energy of the oscillator is non-zero. This energy, equal to $\frac{1}{2}\hbar\omega_i$ for each vibrational mode, is referred as zero point energy (ZPE) and is a direct consequence of the Heisenberg uncertainty principle. Chapter 6 provides an example for the importance of considering the ZPE to describe the energetic ordering of the isomers of the protonated water pentamer.

Inspection of Fig. 2.1 shows that the harmonic oscillator approximation fails to accurately describe the behavior of a real molecule when it is in a high vibrationally exited state. Under this approximation the more the molecule deviates from equilibrium, the stronger is the restorative force it experiences. In fact, equation (2.1) predicts an infinite number of equally spaced energy levels. On the other hand, as more vibrational energy levels of a real molecule are populated, the energy gap between them reduces and once the molecule has enough internal energy, it will eventually dissociate. A simple potential that includes these anharmonic effects is the Morse potential [88]:

$$V(x) = D_e\Big(1 - e^{-a(x-x_e)}\Big)^2 \qquad \text{with} \qquad a = \sqrt{\frac{k_e}{2D_e}},$$

where D_e is the depth of the potential well at the equilibrium inter-nuclear separation x_e, x

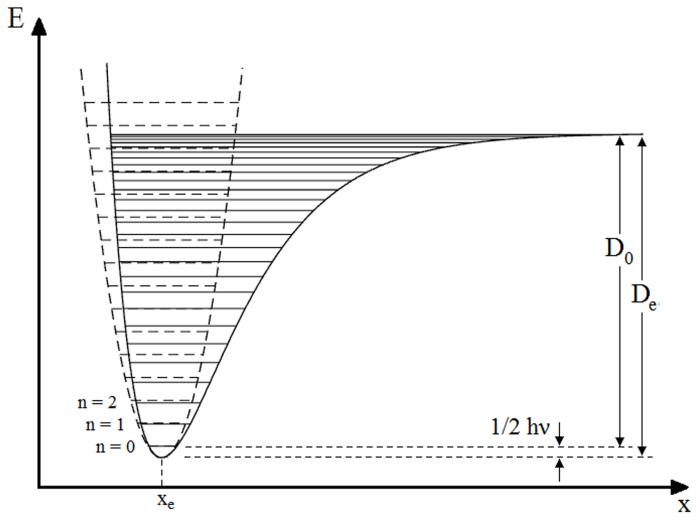

Figure 2.1: PES of a diatomic molecule described by the Morse (solid line) and by the harmonic potential (dashed line).

is the instantaneous inter-nuclear separation and k_e is the force constant at the equilibrium inter-nuclear separation. The eigenvalues of a quantum Morse oscillator are given by:

$$E_{vib} = \hbar\omega\left(n + \frac{1}{2}\right) - \frac{\hbar\omega^2}{4D_e}\left(n + \frac{1}{2}\right)^2,$$

which yields successive energy levels that are no longer equally spaced but the spacing between neighboring levels decreases with increasing energy. Fig. 2.1 provides a comparison of a Morse and a harmonic potential. Anharmonicities also lift the orthogonality of the vibrational wave functions. Off-diagonal matrix elements are present in the Hamiltonian, leading to the non-zero IR intensities of overtones and combination bands. The coupling of vibrational modes allows the energy to flow throughout the molecule via internal vibrational energy redistribution (IVR) [89]. IVR plays a fundamental role in the photodissociation experiments presented in this thesis (see Section 2.2.1).

2.2 Gas Phase Infrared Spectroscopy

The standard technique to record vibrational spectra of molecules is IR absorption spectroscopy [90]. It consists of measuring the frequency-dependent absorption of IR light by a sample. The light transmission through a sample at frequency ν according to the Lambert-Beer law is

$$\frac{I(\nu)}{I_0(\nu)} = e^{-\sigma(\nu)\cdot n\cdot l}. \tag{2.2}$$

$I(\nu)$ and $I_0(\nu)$ are the intensities of the transmitted and incident light, respectively, $\sigma(\nu)$ the absorption cross section, n the particle number density and l the path length of the light through the sample.

The sensitivity of this technique is limited in the gas phase by the IR absorption cross section ($\sim 10^{-20}$ cm^2) of gas-phase molecules. This requires values of n to be greater than $\sim 10^{10}$ molecules/cm^3 to acquire an absorption spectrum. The sensitivity can be enhanced by elongating the optical beam path. In cavity ring-down spectroscopy (CRDS), for example, the absorption cell is placed inside an optical cavity. In this way, the laser beam passes through the sample cell several thousand times. The effective path lengths are then of the order of kilometers reducing the constrains on the number density to $\gtrsim 10^8$ molecules/cm^3 [91, 92].

In the present work, the vibrational spectra of charged particles are investigated. The maximum achievable ion densities are on the order of $10^6 - 10^7$ ions/cm^3, close to the space-charge limit (10^8 ions/cm^3) [93]. Alternative approaches are therefore typically necessary to measure IR spectra of gas-phase ions. IR *action spectroscopy* is a method that relies on detecting the response of the system to photon absorption rather than direct detection of the absorption of light. Action techniques typically involve detecting fluorescence, ionization, change in quantum state or fragmentation. Infrared photodissociation (IRPD) spectroscopy is the most common action spectroscopy method used and is employed in the work presented in this thesis.

2.2.1 Infrared Photodissociation Spectroscopy

This technique uses mass spectrometric techniques to monitor the photodissociation yield as a function of the laser frequency. The ions of interest ($AB^{+/-}$) are irradiated with an intense IR laser pulse. When the frequency of the incident light is in resonance with that of an IR-active vibrational transition, one or multiple photons are absorbed. When their internal energy exceeds the dissociation threshold they can undergo fragmentation:

$$AB^{+/-} \xrightarrow{n \cdot h\nu} \left(AB^{+/-}\right)^* \rightarrow A^{+/-} + B.$$

The ratio of the population prior, N_0, and after, $N(\nu)$, interaction with the light can be described in a similar fashion to Lambert-Beer's law (Equation (2.2)):

$$\frac{N(\nu)}{N_0} \propto e^{-\sigma(\nu) \cdot F(\nu)},$$

where $F(\nu)$ is the photon fluence and $\sigma(\nu)$ the absorption cross section [90]. This technique relies on a very large number of photons, and thus requires intense light sources, in analogy to the high number densities required in direct absorption techniques.

Infrared Multiple Photon Dissociation

The dissociation threshold, D_0, of a molecule or a strongly bound cluster is typically larger than the IR photon energy. Hence, multiple IR photons need to be absorbed to induce dissociation. Below a certain photon fluence, the absorption process can be assumed to be sequential and non-coherent. It can be divided in three overlapping regions: the resonant region, the quasi-continuum and the true-continuum region [94, 95]. In the first region, resonant absorption of multiple photons excites discrete vibrational transitions in a sequential manner. As the vibrational quantum number increases, the anharmonicity of the potential manifests itself in the change of the energy spacing between consecutive vibrational levels. The (fixed) laser frequency will eventually run out of resonance with the vibrational transition. This phenomenon is referred to as the "anharmonic bottleneck". It is, to some extent, compensated by the bandwidth of the laser and the presence of rotational levels that broaden the transition.

The density of rovibrational states increases rapidly with the internal energy of the system, E_i, roughly with E_i^N, with N the number of vibrational degrees of freedom [96]. Therefore, even small molecules quickly reach the quasi-continuum absorption region upon excitation. Another anharmonic effect, namely IVR, starts playing an important role as E_i, and hence the coupling between vibrational modes, increases. IVR facilitates photon absorption by quickly depopulating the upper resonant vibrational level, thus avoiding the "anharmonic bottleneck". At the same time it leads to spectral broadening by reducing the lifetime of vibrational levels. For highly excited polyatomic molecules, typical IVR rates are on the order of $10^{11} - 10^{12}$ s^{-1}. Considering Heisenberg's uncertainty principle, $\Delta E \Delta t \geq \frac{\hbar}{2}$, a Δt on the order of 10^{-12} s corresponds to a width of the resonance of $\Delta E \approx 3$ cm^{-1}.

The true continuum region is accessed when E_i exceeds the dissociation limit and a dissociative channel opens up. IVR rates increase such that the internal energy is statistically distributed over all vibrational degrees of freedom [97]. Hence, the dissociation takes place typically through the breaking of the weakest bond in the system. However, when sufficient energy is pumped in the system, several dissociation channels can be accessed.

As discussed above, shifting of fundamental vibrational modes and band broadening leads to spectral congestion which are common effects in IRMPD spectra making them typically more difficult to assign than IRPD spectra. Another effect that might occur is the so called IRMPD transparency [12, 98]. The term refers to IR-active modes which are not observed in IRMPD spectra. This phenomenon can arise from different mechanism: unavoidable "anharmonic bottlenecks" in smaller species with high dissociation energies, change of transition dipole moment upon heating and non-statistical mode-specific fragmentation [98–101].

Infrared Vibrational Predissociation

A useful method to circumvent the need of multiple photon excitation is the *messenger* technique [17, 18]. Instead of the bare ion as in the case of IRMPD, IRVPD investigates a weakly bound ion-ligand complex. Rare gas atoms or an inert molecule like He and H_2 are

typically used as messenger ligands. The dissociation threshold of the complex ($AB^{+/-} \cdot M$) is substantially lower than that of the ion ($AB^{+/-}$) and often the absorption of a single photon is sufficient to induce fragmentation:

$$AB^{+/-} \cdot M \xrightarrow{h\nu} \left(AB^{+/-}\right)^* \cdot M \xrightarrow{IVR} AB^{+/-} + M.$$

The cluster is excited by resonant photoabsorption and the energy is quickly redistributed among all vibrational modes. IVR, which typically proceeds on a nanosecond time scale or faster, leads to the dissociation of the weak ion-messenger bond. The vibrational spectrum is obtained by monitoring the ion yield as a function of the photon energy. Ideally, the vibrational modes of the cluster $AB^{+/-}$ remain unperturbed upon complex formation and the experimental IRPD spectrum can be directly compared to computed linear absorption spectra.

The dominant attractive force between nonpolar messenger atom/molecule and an ion is due to the charge-induced dipole interaction. Typically, binding energies below 1600 cm^{-1}allow for the measurement of IR photodissociation spectra in the linear regime over most of the IR spectral range. Another advantage of this technique is that narrower linewidths ($<$ few cm^{-1}), often limited by the laser bandwidth, are obtained compared to IRMPD spectra. IVR occurs relatively slowly ($\sim 10^{-9} - 10^{-10}$ s) upon absorption of a single IR photon because of the weak coupling of the excited mode to the low energy ion-messenger modes reducing the contribution from lifetime broadening ($\sim 10^{-2} - 10^{-3}$ cm^{-1}). This technique is also referred to as infrared vibrational predissociation (IRVPD) spectroscopy [102].

Ideally, the geometry and electronic structure of the cluster ion is not significantly perturbed by the presence of the ligand and thus the vibrational spectrum of the ion-messenger reflects that of the bare ion [103]. A helium atom often represents an ideal messenger, but He-complexes are typically difficult to form. More polarizable ligands such as argon and krypton bind more strongly, but also exert a stronger perturbation on the structure of the ion. This can lead to marked shifts of vibrational frequencies but also to changes in the energetic order of isomers [104, 105]. A systematic study of the effect of different messengers was performed by Mizuse and Fuji on protonated water clusters [80, 106]. Among other results, they found that the Zundel isomer of the protonated water hexamer is preferentially stabilized by addition of an argon atom.

In the work presented in this thesis He and D_2 (or H_2) are mostly used as messengers. D_2 complexes are readily formed with many ions, in particular also with molecular anions, but one has to pay attention that D_2 does not (dissociatively) chemisorb and forms covalently bound products.

2.3 Structural Assignment

Molecular vibrations and consequently the vibrational spectrum of a molecule depend on molecular structure. If the vibrational spectrum is rotationally resolved, rotational constants and hence structural properties can, in principle, be directly extracted from the observed spectral features. However, the spectral bandwidth in IRPD experiments on molecular ions with more than a few atoms is typically too large (> 1 cm^{-1}) to resolve rotational features. In these cases, the molecular structure is characterized by comparison of the experimental spectrum to simulated spectra obtained from electronic structure calculations on a trial and error basis.

To this end, the geometries of different configurational isomers are optimized by minimizing their energy using electronic structure calculations. Vibrational frequencies and intensities are commonly determined within the harmonic approximation. In problematic cases, the application of more sophisticated quantum chemical methods is needed. This is particularly true for clusters containing stronger hydrogen bonds, where anharmonic effects cannot be neglected (see Chapter 6). In all cases, the comparison with the experimental spectra is useful to test and benchmark theoretical predictions.

The internal temperature of the ions under study plays an important role in the identification of their structure. In fact, higher internal energies lead to broadening of the spectral features arising from the population of excited rovibrational levels eventually leading to fluxional structures characterized by large amplitude motion. A gentle thermalization to cryogenic temperatures, as is the case when using buffer gas filled cryogenic ion traps, can considerably ease the assignment, because it generally allows the system to assume a global minimum energy structure. In some cases, multiple isomers are populated, even at low temperatures, complicating the assignment of the spectra and hence the structure characterization. A spectroscopic approach to isolate the spectral signatures of individual isomers when multiple isomers are present is illustrated in Section 3.4.1.

The vibrational spectrum obtained from quantum chemical calculations corresponds, within certain approximations, to the linear IR absorption cross section. Hence, IRVPD spectra of cold ions are often in quantitative agreement with computed IR spectra and allow for an unambiguous structural assignment. If more than a single photon is required to induce photodissociation the experimental and calculated spectra is typically in poorer agreement. In particular, the relative intensities of IRMPD bands may differ substantially from those in the linear absorption spectrum [107]. This effect is generally more pronounced in the lower frequency range of the spectrum, where more photons are required to overcome the dissociation limit. A representative example is provided in Fig. 2.2 that depicts a comparison of the IRVPD, the IRMPD and the calculated harmonic spectra of the $[Fe_3O_2(OH)_4]^+$ cation. However, previous experiments have shown that, particularly in the case of large systems with high density of vibrational states, IRMPD spectra often show a reasonable agreement with the calculated linear absorption cross section [12, 107].

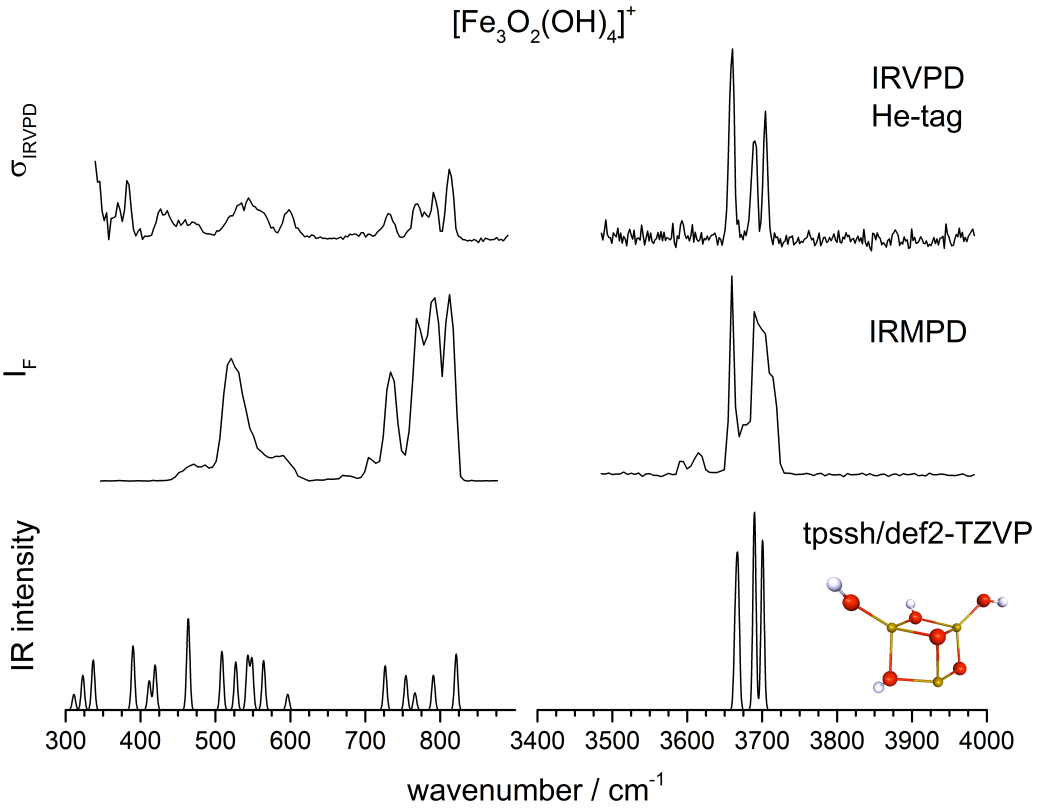

Figure 2.2: Comparison of the IRVPD spectrum of He-tagged $[Fe_3O_2(OH)_4]^+$, the IRMPD spectrum of bare $[Fe_3O_2(OH)_4]^+$ and with the computed (TPSSH/def2-TZVP) harmonic spectrum of bare $[Fe_3O_2(OH)_4]^+$. The vibrational frequencies above 3000 cm^{-1}, from which the computed spectrum is derived, are scaled by 0.97 to account for anharmonic effects as well as systematic errors.

3 Experimental Setup

All experiments reported in this thesis were conducted using either one of two ion-trap triple mass spectrometers. The two setups differ in the minimum ion trap temperature achievable and were hence termed the 10 K and the 6 K setup (see Fig. 3.1). In this chapter the common general operating principles of the two instruments are first described, mainly focusing on the 10 K spectrometer. More detailed descriptions of the design and operational conditions of the two setups are given in Ref. [12, 108–111]. A description of three different type of ion sources used, *i.e.* theElectrospray Ionization (ESI), the laser vaporization and magnetron sputter source, is given in Section 3.2. This is followed by an introduction to the basic concepts of ion trajectory manipulation with radio frequency (RF) devices (Section 3.3). Ion detection schemes and modes of operation of the setup are discussed in Section 3.4, followed by the description of the IR laser sources used in the experiments.

3.1 Operating principles

Fig. 3.1 shows a schematic overview of the ion optics of the two mass spetrometers. Ions are produced, or transferred from analytes in solution, in the gas phase using various ionization techniques. These include electrospray ionization, laser vaporization and magnetron sputtering (see Section 3.2). Gaseous ions of a particular charge are transferred into the high vacuum chamber passing one or more differentially pumped vacuum stages separated by skimmers. They are then focused with an Einzel lens into a RF linear ion guide. The 10 K setup features

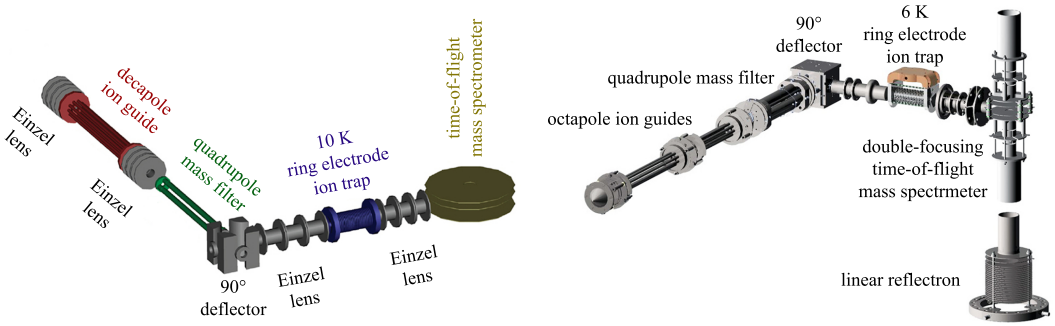

Figure 3.1: Schematic 3D views of the 10 K (left) and 6 K (right) cryogenic ion trap mass spectrometers used in this thesis. Figures adapted from Ref. [110] and [111].

a decapole ion guide, filled with a buffer gas, generally helium, to reduce the distribution of kinetic energies and collimate the molecular ion beam. After a second Einzel lens, parent ions are mass-selected by a quadrupole mass filter (4-2000 amu), deflected into 90° using an electrostatic quadrupole deflector and refocused by an Einzel lens into a RF linear ion trap. The ring-electrode trap (RET) is mounted on a close-cycle helium cryostat and the temperature is controlled over a range from 10 K to 350 K. The RET plays a central role in all mass spectrometric and spectroscopic experiments. In fact, it can be viewed as a pulsed source for mass-selected, thermalized and messenger-tagged ions. Here all mass-selected ions are accumulated and thermalized by means of thousands of collisions with the buffer gas atoms or molecules continuously supplied to the ion trap. The gentle thermalization down to cryogenic temperatures generally ensures that the ions adopt their global minimum energy structure and low internal energies, significantly simplifying the IRPD spectra and their assignment. Messenger tagging, when required, is performed inside the ion trap at sufficiently low temperatures via three-body collisions [109, 112]. All ions are then extracted and focused both temporally and spatially into the center of the extraction region of an orthogonally-mounted double focusing reflectron time-of-flight (TOF) photofragmentation mass spectrometer (only explicitly shown for the 6 K instrument in Fig. 3.1). Here the ions are irradiated with a counter-propagating (or a perpendicular) IR laser pulse (see Section 3.5). All parent and photofragment ions are accelerated by the application of two properly timed high voltage pulses and finally their TOF mass spectrum is determined using a microchannel plate (MCP) detector. IRPD spectra are obtained by recording the TOF mass spectra as a function of the irradiation wavelength.

The construction of the 6 K setup is based on the same principles, but with minor modifications that enhance performance. (i) The source chamber is mounted on a translation stage, which allows the optimization of the distance between the end of the ion source region and the entrance skimmer to the ion guides. (ii) Two octapole ion guides with individual buffer gas supplies are used instead of the decapole ion-guide of the 10 K setup for more flexibility in the room temperature ion thermalization stage. (iii) The mass range of the commercial quadrupole mass filter extends to 4000 amu compared to 2000 amu in the 10 K instrument. (iv) The RET consists of twelve instead of six variable DC voltage stages, which allows for greater flexibility in the ion trapping, storing and extraction settings and leads to higher ion signal intensities. (v) A lower minimum RET temperature (6 K vs. 10 K) is achieved by the use of an improved cryo-shield together with a more powerful close-cycle cryostat.

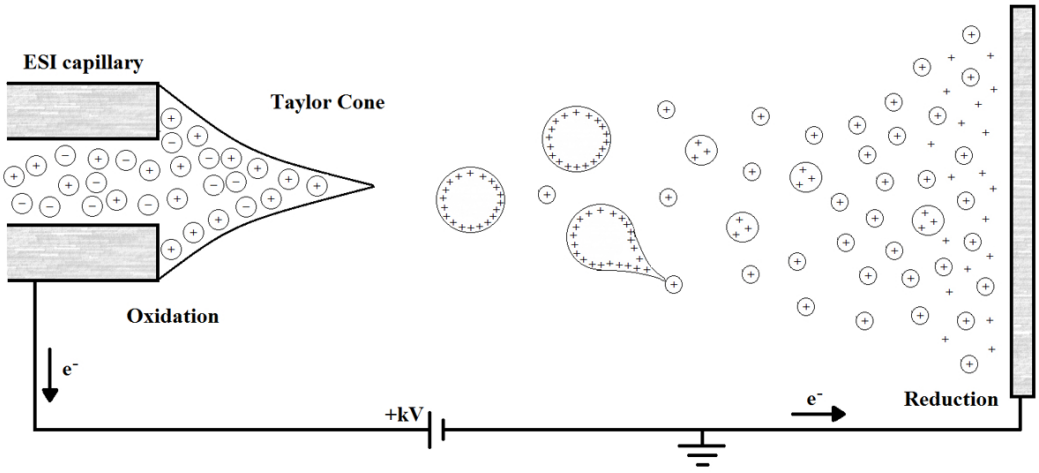

Figure 3.2: Schematics of an ESI source operated in positive ion mode.

3.2 Ion Sources

3.2.1 Electrospray Ionization and Ion Spray Sources

Electrospray Ionization (ESI) is a widely used technique for transferring atoms or molecules from a solution fragment- and solvent-free into the gas phase. It was first developed by Malcom Dole in the late 1960's and used by John Fenn some 20 years later to successfully produce gaseous biopolymers such as oligonucleotides and proteins. Work that was awarded the Nobel Prize in Chemistry in 2002 [113, 114]. This soft ionization technique allows for the gas-phase production of weakly bound compounds without fragmentation, and it has revolutionized the field of mass spectrometry [115]. The same source setup is called Ion Spray when used to transfer charged species already present in the solution into the gas phase. Despite its great success, the details of the ion spray process are still not completely understood and remain an active area of research [116–120]. In the following, the basic steps of the ion spray process (see Fig. 3.2) are described.

The analyte solution is passed through a conductive capillary kept at high voltage. In the absence of solvated ions, a reduction-oxidation (redox) reaction leads to the formation of charged species (negative or positive depends on the polarity used) in the solution as it is pulled through the capillary. The electric field at the capillary tip is very high ($E_c \approx 10^6$ V/m) [116] and penetrates the solution causing a polarization of the solvent near the meniscus of the liquid. This induces a deformation of the meniscus leading to the formation of a Taylor cone (see Fig. 3.2). A fine jet is formed at the tip of this cone when the field applied is

sufficiently high, *i.e.* exceeding the critical voltage [121, 122]:

$$E_0 = \sqrt{\frac{2\gamma \cos(49.3°)}{\epsilon_0 r_c}}, \tag{3.1}$$

where γ represents the surface tension of the solvent, ϵ_0 the vacuum permittivity and r_c the capillary radius. An approximate equation to calculate the potential required to onset the electrospray was derived by Smith and coworkers [116, 122, 123]:

$$V_{on} \approx \left(\frac{r_c \gamma \cos\theta}{2\epsilon_0}\right)^{1/2} \ln\left(\frac{4d}{r_c}\right) \approx 2 \times 10^5 (\gamma r_c)^{1/2} \ln\left(\frac{4d}{r_c}\right), \tag{3.2}$$

With the half angle of the Taylor cone $\theta = 49.3°$ and $\epsilon_0 = 8.8 \times 10^{-12}$ J^{-1} C^2. The onset of spray formation of a water solution thus requires a voltage of about 4 kV for a given capillary radius of 0.1 mm and a distance from the tip to the counter electrode of 4 cm. Table 3.1 reports the estimated V_{on} voltages needed for different solvents.

Table 3.1: Estimated onset voltages for ESI of solvents with different surface tension γ, calculated using Equation (3.2) and considering a capillary tip of 0.1 mm radius and 4 cm distance from the tip to the counter electrode. Table adapted from Ref. [116].

	CH_3OH	CH_3CN	$(CH_3)_2SO$	H_2O
γ (N/m)	0.0226	0.030	0.043	0.073
V_{on} (Volt)	2200	2500	3000	4000

Under such conditions, the repulsion between the charges destabilizes the jet and triggers the formation of small charged droplets with a radius of about 1 μm. The droplets shrink due to solvent evaporation to a smaller diameter D, while drifting towards the oppositely charged electrode. Consequently, the electric field normal to the surface of the droplets increases, ultimately exceeding their surface tension (Rayleigh limit, $q = \sqrt{8\pi\epsilon_0\gamma D^3}$). This causes the fission of the droplets, also called coulomb fission, which generates a number of smaller droplets. The newly formed droplets undergo the same mechanism until very small (nano-scale) droplets are generated. Several different mechanisms, including the ion evaporation model (IEM), charged residue model (CRM) and chain ejection model (CEM) have been proposed for explaining the last steps that lead to the formation of gas phase ions from the small droplets [116, 118].

ESI sources used in this thesis work

A modified commercial Z-spray ESI source (*Waters*) and a home-built linear nanospray (nESI) source were used for the experiments presented in this thesis work. Schematic drawings of

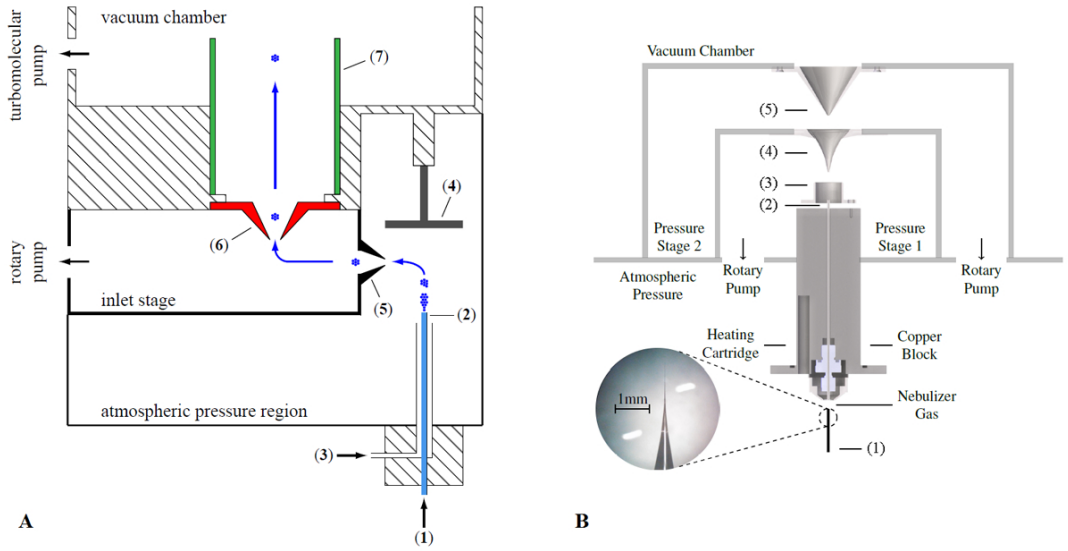

Figure 3.3: A Schematic of the Z-spray ESI source taken from Ref. [110]: (1) sample solution, (2) stainless steel capillary, (3) nebulizer gas (N_2), (4) grounded counter electrode, (5) skimmer 1, (6) skimmer 2, (7) cylindrical lens. **B** Schematic of nESI source taken from Ref. [111] and a picture of the glass needle through a microscope [124]: (1) metal-coated borosilicate needle, (2) stainless steel capillary, (3) cylindrical lens, (4) skimmer 1, (5) skimmer 2.

these sources are shown in Fig. 3.3. Further details, including typical operation conditions, can be found elsewhere [110, 111].

The operational principles of the ESI and the nESI sources are similar. The main difference lies in the size of the capillary diameter, which is $\sim 1-2$ μm in the nESI setup compared to the ~ 100 μm in the Z-spray source. The Z-spray source produces bigger droplets and thus requires large distances between the spray tip and the sampling orifice. The result is that only a small fraction of the ions is sampled by the orifice and thus most of the analyte is wasted. The smaller diameter of the tip in the nESI setup improves the efficiency of the gas-phase ion generation and also requires substantially smaller amounts of analyte solution. The higher efficiency also allows for the reduction of the concentration of the analyte solution, typically, by one order of magnitude. The two sources also differ in the way ions are transferred into the high vacuum chamber. The Z-spray source is equipped with a Z-shaped source block which prevents neutral particles from passing the inlet region. Similar ion distributions can be obtained with the two sources (see Fig. 3.4). However, the nESI source performs better in forming non-covalently bound clusters, in particular microhydrated species, because of the more gentle ionization conditions and the more direct transition into the high vacuum region via a transfer capillary.

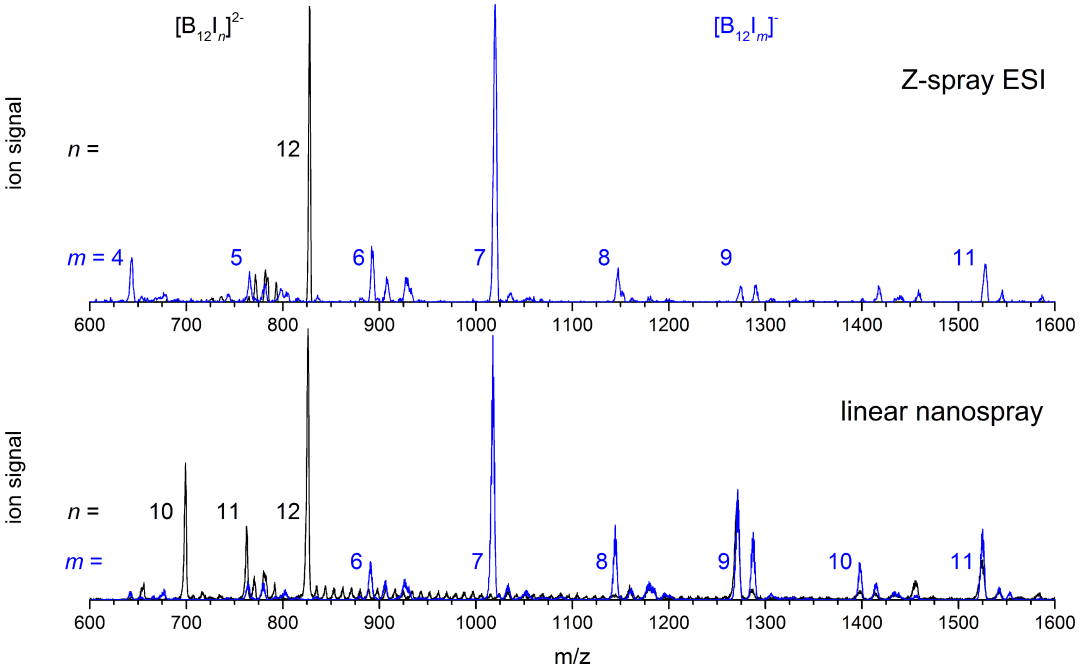

Figure 3.4: Quadrupole mass spectra showing the cluster distribution produced with the Z-spray source on the 10 K setup (top), and with the nESI source on the 6 K setup (bottom). Settings were optimized for $[B_{12}I_{12}]^{2-}$ (black traces) and for $[B_{12}\ I_7]^-$ (blue traces). A 0.48 mmol/L solution of $[B_{12}I_{12}]^{2-}[C_6H_5CH_2N(CH_3)_3{}^+]_2$ in 2:1 CH_3CN was used with the Z-spray, while for the nanospray the solution was diluted 1:1 in H_2O and CH_3CN.

3.2.2 Laser Vaporization Sources

Laser vaporization is a standard technique for the production of metal containing neutral and ionic clusters [125]. It was first developed in 1981, independently by the groups of R. Smalley at Rice University and V. Bondybey and H. English at the Bell Laboratories [126–128]. A schematic of the original design of the Smalley source is shown in Fig. 3.5. The principle of operation is simple although subtle design features have a substantial influence on the number, size, temperature, composition, state and charge of the clusters produced. A tightly focused laser pulse vaporizes a small portion of a metallic sample. The laser pulse promotes the formation of a dense metal plasma which is then cooled in a confinement channel by collisions with an inert gas. The clusters form in the channel and are stabilized *via* three body collisions. At the end of the channel the gas expands freely, ideally forming a supersonic beam.

The critical parameters that determine the source performance are: type of expansion gas; valve backing pressure; temporal pulse lengths and relative timing of the gas and of the laser pulses; laser pulse energy, wavelength and focusing conditions; sample holder and confinement channel design. Laser vaporization sources that use metals in different forms and

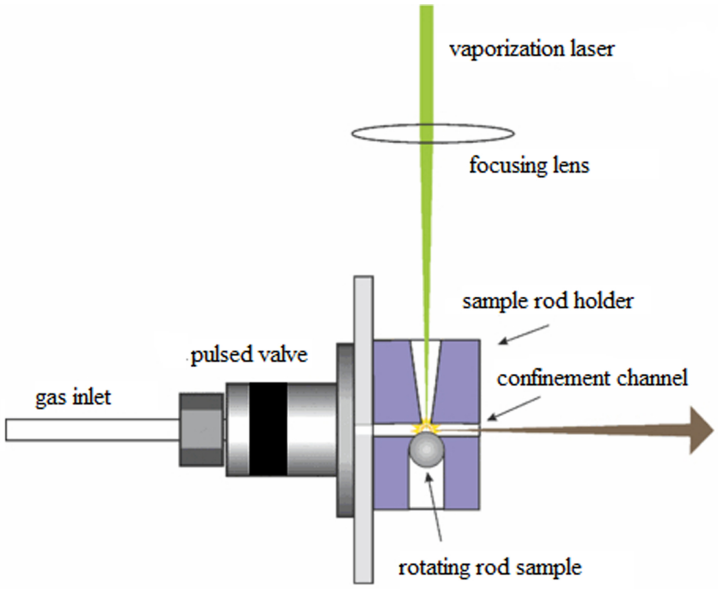

Figure 3.5: Schematic illustration of a laser vaporization source. Adapted from Ref. [125].

shapes have been reported over the years, including disks [129], rods [130, 131], wires [132] and liquid samples [133]. The performance and especially the stability of the ablation process depend on the rate with which the "fresh" metal surface is sampled. Soft metals, *e.g.* tin, require higher sampling rates to avoid deep scars of the sample. The use of a pulsed laser with high peak power ($\gtrsim 10^5$ W) is a prerequisite for efficient metal vaporization [125]. Lasers with pulse lengths on the order of 0.1–1 ms vaporize more material than nanosecond lasers. However, when using long pulses the dominant process is the ejection of large liquid droplets into the gas stream which then inhibit the efficient formation of a saturated metal atom vapor [127]. Nanosecond lasers are most commonly used today. In this case, vaporization occurs during the first picoseconds of the laser pulse. The plasma formed above the metal surface starts absorbing photons for the remaining time of the laser pulse, is superheated and hinders further vaporization from the metal surface. The optimal laser pulse energy when employing nanosecond lasers ranges from 1 to 30 mJ. It depends on the other source parameters and determines the cluster size distribution [125, 134]. Since collisional cooling is necessary to promote cluster growth, the choice of expansion gas and the design of the source block are crucial. The choice of expansion gas for a particular experiment is complicated by excitacion and relaxation processes in which the gas can partecipate in the plasma [125]. Helium or argon are often used but molecular gases and gas mixtures can also prove beneficial [125]. A pre-expansion zone and/or optimal length of the confining channel leads to improved thermalization [135–137].

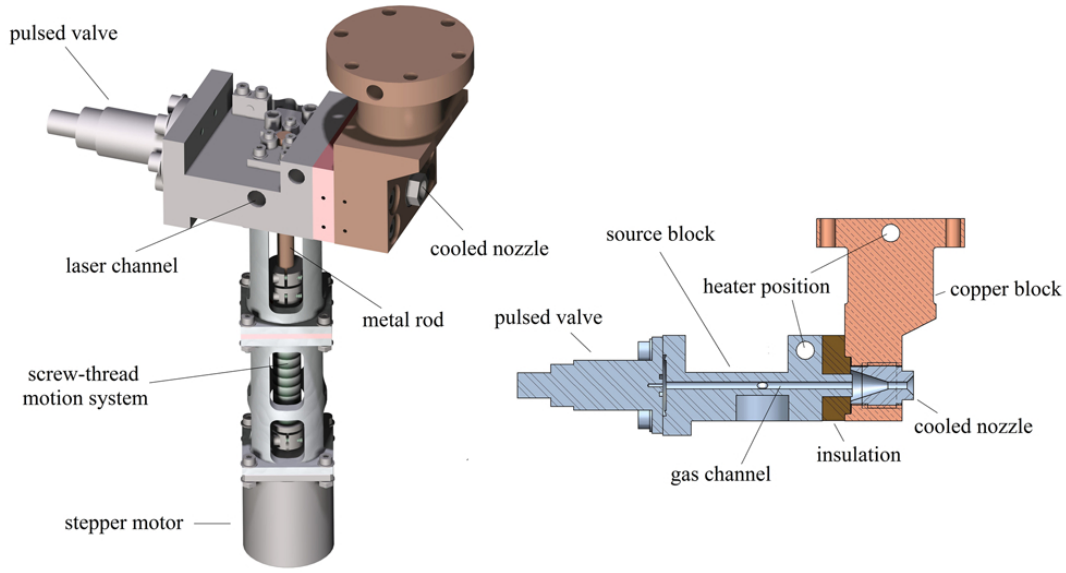

Figure 3.6: Schematic illustration of a laser vaporization source. Adapted from Ref. [125].

The laser vaporization source used in this thesis work

A schematic view of the laser vaporization source used in this thesis work is shown in Fig. 3.6. The target rod is moved vertically in a translational rotation by a screw-thread motion system attached directly below the source block and powered by a stepper motor. A solenoid valve (Parker, Series 99) injects the gas pulse in a 2.5 mm diameter gas channel, positioned orthogonal to the sample rod and the laser channel. The gas channel extends 30 mm past the intersection region with the rod to ensure thermalization of the metal vapor saturated gas pulse and clustering. The channel ends with a cooled nozzle mounted on a close-cycle helium cryostat (20-350 K). The second harmonic (532 nm) of a 50 Hz Q-switched Nd:YAG laser is used for vaporization of the metal target. The laser power is attenuated with a commercial beam attenuator equipped with Brewster type polarizers. The laser beam is then focused onto the target with a lens ($f = 40$ cm) mounted on a translation stage for fine adjustment. The opening of the gas valve is synchronized with the firing of the laser pulse and the temporal delay between the two is adjusted with microsecond precision to optimize the ion signal. Typically, the opening of the valve is triggered 100 to 600 μs before the Q-switch of the laser. Further details on the design and operation of the source are described in the thesis of T. Wende [110].

In the course of this thesis work the source block was modified and improved with regard to long term stability. Prior to these modifications, the ion signal would drop and become unstable, due to deposition of the vaporized material along the gas channel, after one or at best two days of operation, depending on the vaporized material. This leads to charging

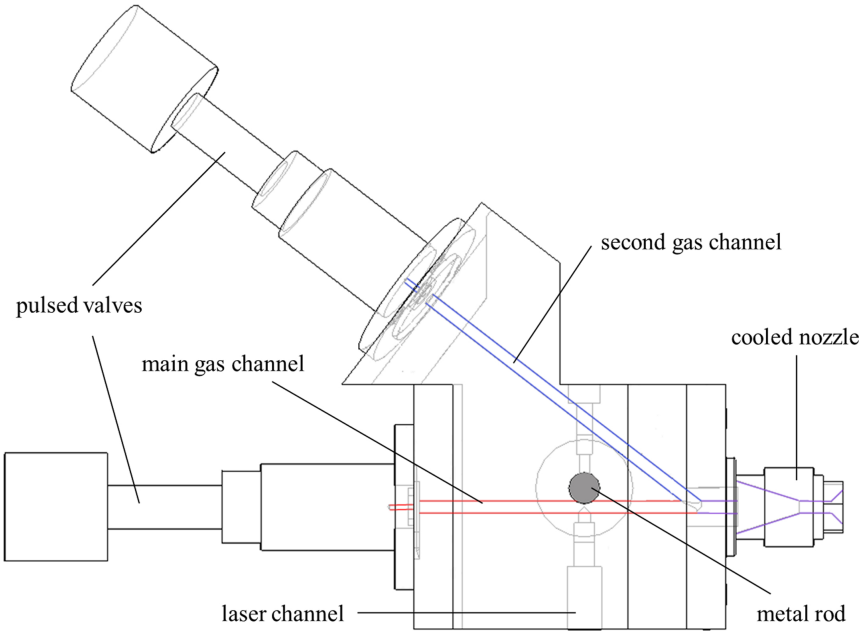

Figure 3.7: Schematic illustration of the dual-gas channel source bock of the laser vaporization source.

effects and eventually to the physical obstruction of the channel. To reduce these charging effects and the frequency with which the source needed to be disassembled and cleaned, a new source block with a gas channel diameter of 5 mm was machined. The new block prolonged the long term stability of the source, did not negatively affect the cooling capabilities of the source and lead to an increase of the ion signal up to 50%, probably due to improved ion transmission.

Another goal was to design a source block that allows preformed metal-containing clusters to react with gases other than helium and without influencing the cluster aggregation process. In particular, the goal was to study the addition of individual water molecules to Al- and Fe-oxide clusters (see Section 4.3). A schematic of this dual gas-channel source-block is shown in Fig. 3.7.

The new source block features a second gas channel that intersects the main one at an angle of 38 degrees and at a distance of 24 mm from the crossing of the latter with the laser channel. This configuration ensures that the vaporization process, and the subsequent clustering along the channel, remains largely unperturbed by the addition of a second gas pulse. Note that the reaction gas is not exposed to the hot plasma generated by the laser pulse, which could lead to the formation of undesirable side products. After the production of the (bare) metal oxide clusters of interest is optimized, the second pulsed valve is activated, requiring little or no changes to the rest of the source parameters. A comparison of quadrupole mass spectra of Fe-oxide cluster cations without and with reaction with water molecules is shown in Fig. 3.8.

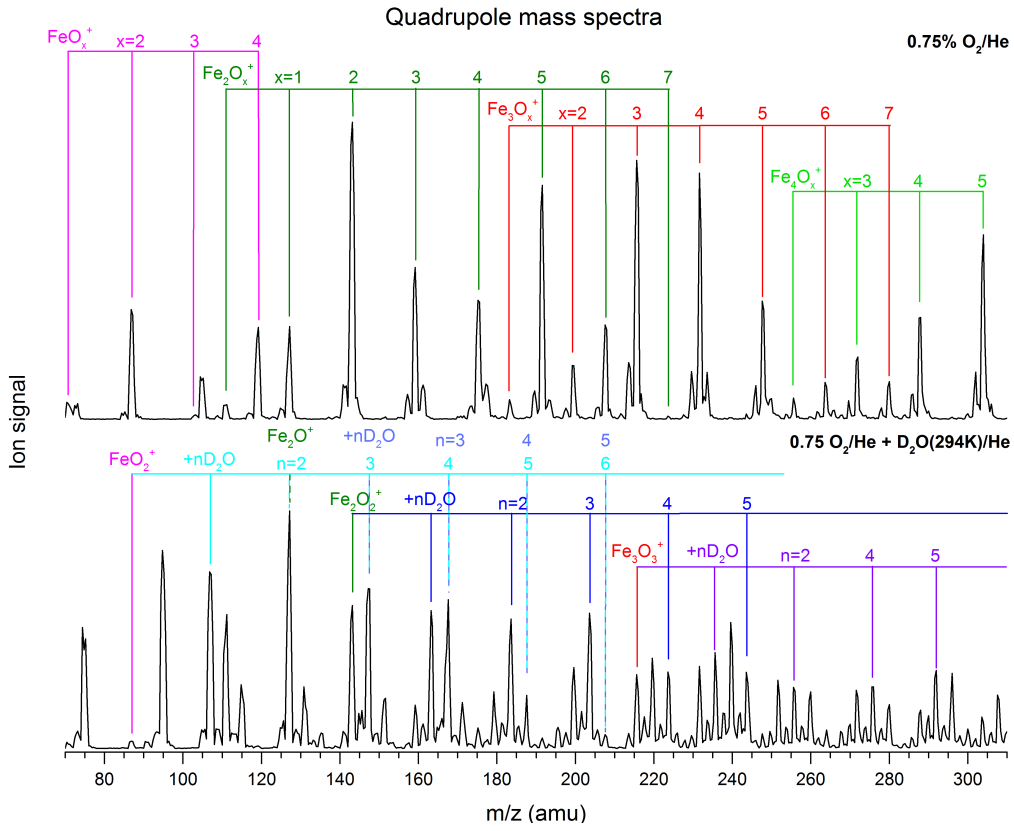

Figure 3.8: Quadrupole mass spectra of Fe-oxide cluster cations and Fe-oxide cluster cation/heavy water complexes produced with the dual gas-channel laser-ablation source. The traces show the respective cluster mass distribution obtained by vaporizing an iron rod and using a 0.75 % mixture of oxygen in helium without (upper trace) and in combination with (lower trace) a second helium gas pulse containing D_2O vapor (see Fig. 3.7 for the arrangement of the gas channels).

The water vapor is introduced by a pulse of helium that flows through a bubbler filled with water kept at room temperature.

The comparison of the two mass spectra in Fig. 3.8 shows that Fe-oxide/water complexes are readily obtained with the dual gas-channel source-block without formation of undesirable side products. Relatively low ($\sim$ 1.5 bar) backing pressures of the He/water vapor pulse provides the best ion signal. The delay between the two gas pulses shows little effect on the ion signal with optimum performance obtained when the water containing pulse is triggered $\sim$ 100 μs after the O_2/He pulse. The distribution of the number of water molecules reacting with a particular cluster can be influenced by changing the amount of water vapor supplied by the valve. This is controlled by varying the voltage applied to the second pulsed valve and monitored with the total pressure measured in the source chamber. Fig. 3.9 shows the normalized ion count depending on the number of D_2O molecules in the cluster for four

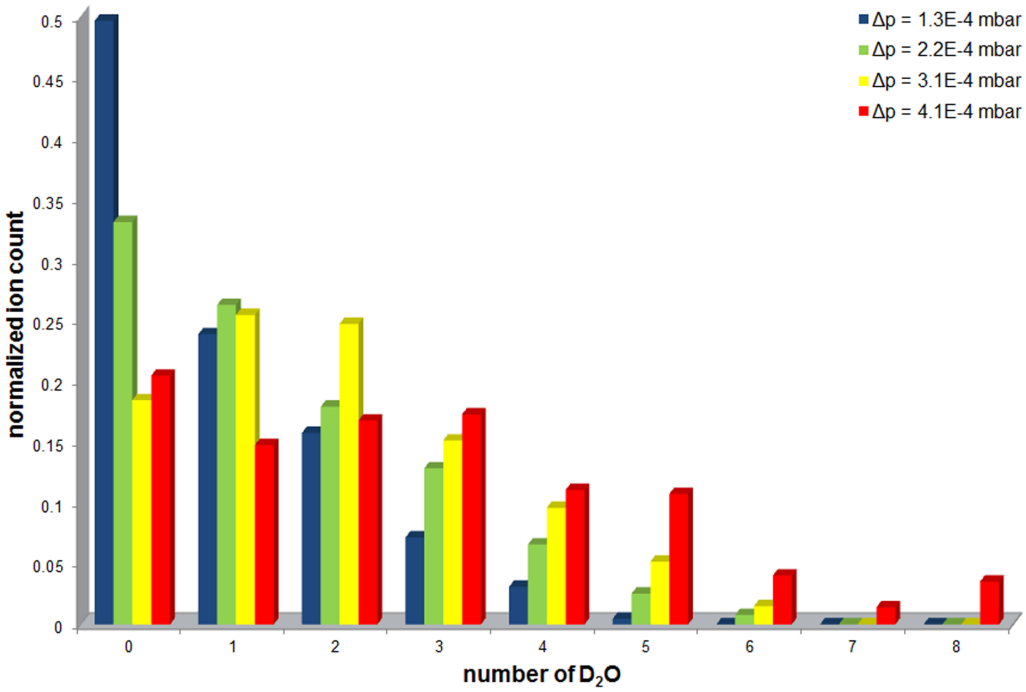

Figure 3.9: Normalized ion count distribution of the cluster series $FeO_2{}^+(D_2O)_n$ for four pressure changes (Δp) of the source chamber induced by the activation of the second valve.

pressures. The reported Δp's refer to the pressure change induced in the source chamber by the activation of the second pulsed valve. The graph shows an optimum in the formation of complexes with one and two water molecules achieved for a Δp of 2.2 and 3.1×10^{-4} mbar, respectively. The ion count of the complexes with the larger amount of D_2O molecules increases with Δp. Complexes with a maximum of eight water molecules can be produced, which is ultimately limited by the pumping speed with which the source chamber is evacuated. In order to produce complexes containing more water molecules, the temperature of the water in the bubbler can be increased to raise the partial pressure of H_2O gas. In contrast, lower water temperatures led to lower ion signals of the water complexes and to shorter water complex mass peak series.

3.2.3 Magnetron Sputtering Source

Magnetron sputtering has become an established technique for the production of gas-phase ions from solid targets [138]. Sputtering is used commercially for the production of a wide range of coatings [139].

The sputtering is initiated by the bombardment of a target by high energy ions generated in a glow discharge plasma [140]. As a consequence, atoms are eroded from the target and

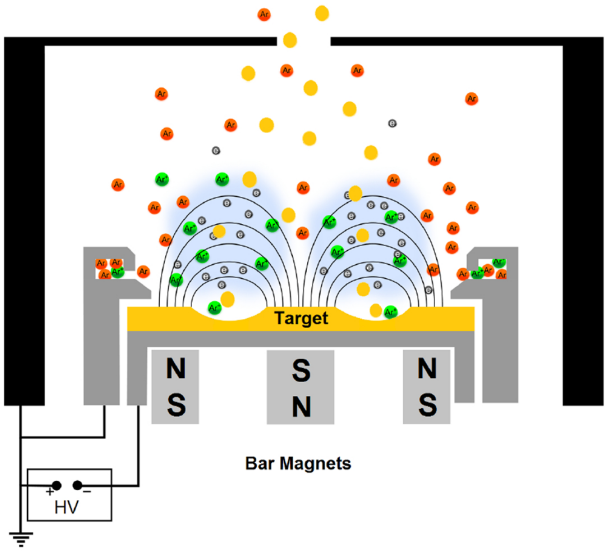

Figure 3.10: Schematic drawing of the magnetron sputter source used in this work from Ref. [142] showing the position of the magnets and the resulting magnetic field (black lines). The blue-shaded areas represent areas of high electron density. Argon atoms, injected by a ring-shaped inlet, are shown in red and Ar ions in green. The black housing represents the aggregation chamber.

secondary electrons are emitted. These electrons play an important role in maintaining the plasma, by ionizing the bombardment gas by collisions with the neutral atoms. In a variation of this technique called magnetron sputtering, a more efficient ionization of the sputter gas by secondary electrons is achieved by confining the secondary electrons in the vicinity of the target and hence increasing their effective path length. To this end, an array of magnets is arranged such that one magnet is positioned on the central axis with one pole facing the target while the peripheral magnets are aligned antiparallel with the opposite pole facing the target's outer edge (see Fig. 3.10). The resulting magnetic field forces the electrons to move in a circular path parallel to the target surface. This increases plasma density near the target, improving the sputter rate. The localized nature of the plasma and thus of the sputter emission of atoms makes this variant less suitable for the production of uniform coatings. The erosion of the cathode is also localized resulting in a poor utilization of the target [141].

The sputter source used for the production of aluminum oxide clusters (see Section 4.1) consists of a Torus 2" sputter head (Kurt J. Lesker). It has a set of interchangeable bar magnets located on the bottom of the water-cooled copper target holder. The gas is injected above the target by a ring-shaped inlet. Argon is used as sputter gas because of its inert nature, the larger mass and lower ionization energy (15.8 eV) compared to helium and neon ensuring more energetic collisions and lowering the electric potential required to ignite a plasma. The head is located in a double-walled home-built aggregation chamber that follows

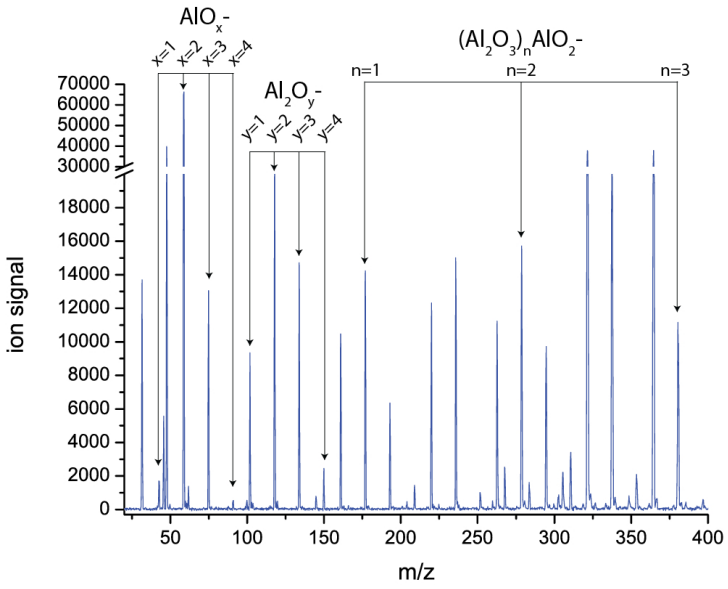

Figure 3.11: Quadrupole mass spectrum of Al-oxide anions produced by reactive sputtering of an aluminum target using the magnetron sputter source. A mixture ($< 10\%$) of oxygen in argon was used as a sputter gas. The aggregation chamber was held at a temperature of about 150 K.

the design proposed by Haberland *et al.* [143]. This design allows optimizing the aggregation volume by varying the axial position of the head. A nitrogen flow cooled in a liquid nitrogen bath is used to regulate the temperature of the housing. The aggregation chamber is filled from the back with a continuous flow of helium gas that promotes collisional cooling and thus clustering. To improve signal stability, mass-flow controllers are used to regulate the partial pressure of each gas independently. In this work the sputter source was used to produce small aluminum oxide anions. They were generated from an aluminum target *via* reactive sputtering using a mixture of oxygen ($< 10\%$) and argon as a sputtering gas. Fig. 3.11 depicts a typical mass spectrum obtained under such conditions.

3.3 Multipole RF devices

After ions are brought into the high vacuum chamber of the experimental setup, their trajectories are manipulated to achieve their guiding, mass-selection and trapping. This is achieved by the use of a variety of ion optics to which DC and AC voltages are applied. The use of fast oscillatory inhomogeneous electric fields in the kilo- and megahertz range make ion trajectory manipulation possible even at higher pressures, where ion-neutral collisions come into play. The first multipole lenses for neutral atoms and polar molecules in atomic

and molecular beams were developed in the 1950s by W. Paul *et al.* [144, 145] followed in 1958 by the construction of the first quadrupole mass filter [146].

Both experimental setups used in this work consist of several linear multipole devices. Ion guides are used in the form of a decapole in the 10 K setup and two octupoles in the 6 K setup. Mass selection is performed with quadrupole mass filters and ring electrode traps are employed to accumulate, thermalize and messenger-tag the ions. In the following, the principles of operation of such devices are summarized. Design and operational details of these devices can be found in the Ph.D. theses of T. Wende and N. Heine [110, 111].

A linear $2n$-multipole, such as a quadrupole ($n = 2$), is composed of $2n$ parallel electrodes symmetrically arranged on a circle (see Fig. 3.13). The potential of amplitude $|\Phi_0|$ is applied to each electrode with adjacent poles having opposite polarity. A stack of ring electrodes, with adjacent electrodes having opposite polarity, also constitutes a linear multipole device. Starting out from Maxwell's equation in vacuum it can be shown that the electric potential generated from a linear multipole device is described by Laplace equation [147]:

$$\nabla^2\Phi = 0. \tag{3.3}$$

A direct consequence of Laplace's equation is that an electric potential cannot exhibit a local minimum, or maximum, in free space. The Earnshaw theorem naturally follows: *a charged particle cannot be held in a stable equilibrium by electrostatic forces alone* [148]. The electric potential can however have a saddle point in three dimensions. The inversion of the saddle point with an appropriate frequency results in a net force on a charged particle towards the saddle point. The directions of the forces at play are analogous to those acting on a ball placed on a rotating saddle surface (see Fig. 3.12). The ball will roll downhill unless the surface rotates with the appropriate frequency, which depends on the mass of the ball (particle) and on the surface (potential) parameters.

The potential applied to the electrodes of a confining multipole has then a DC (U) and an AC (V) component and is described by their sum

$$\Phi_0(t) = U + V\sin(\omega t). \tag{3.4}$$

The potential of a linear multipole with a given geometry is conveniently described in polar coordinates (r, ϕ). Assuming infinite long electrodes, the potential is uniform along the z-coordinate. Imposing the boundary conditions on the potential of a linear multipole $\Psi(r = r_0, \phi) = \Phi_0 cos(n\phi)$, where r_0 is the radius of the circle inscribed by the electrodes of the multipole, and $\Phi(r = 0, \phi) = 0$, one obtains:

$$\Phi(r, \phi) = \Phi_0 \left(\frac{r}{r_0}\right)^n \cos(n\phi). \tag{3.5}$$

The solutions for the case of the quadrupole, $n = 2$, as a function of ωt are shown in Fig.

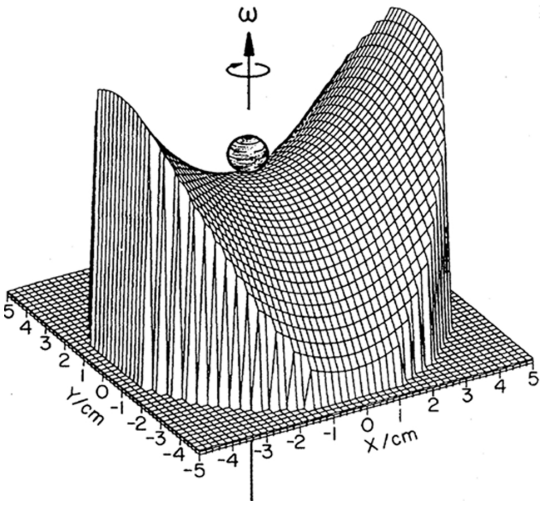

Figure 3.12: A ball on a rotating saddle surface is a mechanical analogue model of a charged particle in a RF confining potential. Figure adapted from Ref. [149]

3.13. They are characterized by the presence of the saddle point along the center axis of the multipole.

Ion trajectories in an electric potential Φ can be calculated by solving the appropriate equation of motion. Assuming sufficiently low ion velocities such that relativistic effects can be ignored, this can be written as

$$m\ddot{\vec{r}} = -q\nabla\Phi(x, y, t), \tag{3.6}$$

where m is the mass of the ion, q its absolute charge, and $\ddot{\vec{r}}$ the second time derivative of its position vector. In contrary to what one may expect, the time-dependent force term does not cancel out in the time average. In a periodic inhomogeneous field, as is the case for multipole fields, a small average force that points towards the lower field (the multipole center) remains, leading to a net focusing force [146]. An analytic solution of the equation of motion (3.6) only exists for a linear quadrupole and assumes the form of the Mathieu equations [146]. It is then possible to determine those parameters, like the RF amplitude and frequency, that lead to stable ion trajectories and transmission of ions through the quadrupole as a function of the geometry. The values of the parameters also depend on the mass-to-charge ratio and initial kinetic energy of the ions.

Despite the lack of an analytical solution for $n > 2$, the trajectory of ions in higher order multipole fields can be treated in the adiabatic approximation as proposed by D. Gerlich [93]. Here, ions experience a time-averaged potential that features a minimum in the center of the multipole. Mathematically this requires decomposing the ion motion into a rapidly oscillating

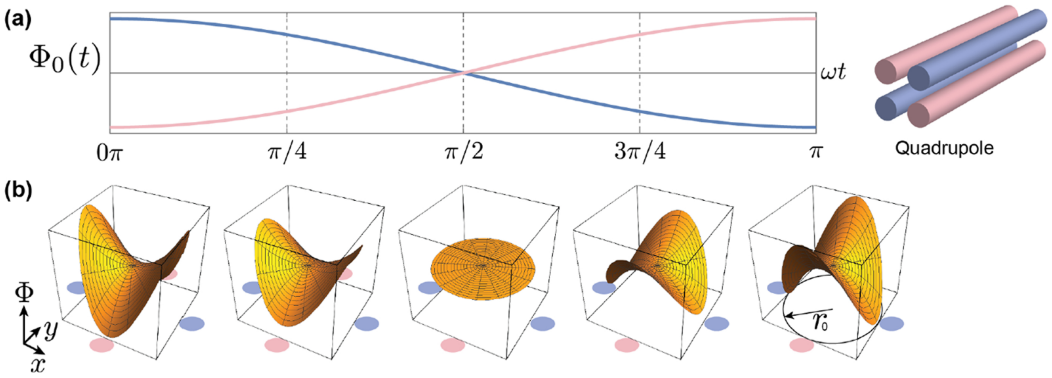

Figure 3.13: (a) Typical time evolution of the RF electric potential $\Phi_0(t)$ and a schematic drawing of a quadrupole (right). The different colors represent electrodes with opposite phases. **(b)** The electric potential calculated according to Equation (3.5) with $n = 2$ for RF phases corresponding to $\omega t = 0\pi, \pi/4, \pi/2, 3\pi/4$, and π. The electrode positions are indicated by the colored circles. Figure adapted from Ref. [150].

term $\vec{R_1}(t)$ and a smooth drift motion $\vec{R_0}(t)$ such that

$$\vec{r}(t) = \vec{R_0}(t) + \vec{R_1}(t). \tag{3.7}$$

A solution of the equation of motion for short times can be found for the micromotion $\vec{R_1}(t)$ after a Taylor expansion of the electric field. The resulting secular equation is averaged over a full oscillation yielding a differential equation involving the secular motion $\vec{R_0}(t)$ [93],

$$m\ddot{\vec{R_0}}(t) = \nabla V^*\left(\vec{R_0}\right), \tag{3.8}$$

with the time-independent mechanical potential, often referred as the effective potential V^*, which is given by

$$V^*\left(\vec{R_0}\right) = \frac{q^2}{4m\omega^2}\left(\nabla\Phi_{AC}\left(\vec{R_0}\right)\right)^2 + q\Phi_{DC}. \tag{3.9}$$

In the case of a linear multipole, for example, the effective potential can be simplified and written as [93]

$$V^*(r) = \frac{n^2q^2V^2}{4m\omega^2r_0^2}\left(\frac{r}{r_0}\right)^{2n-2} + qU\left(\frac{r}{r_0}\right)^n \cos(n\phi). \tag{3.10}$$

Fig. 3.14 compares the radial behavior of the effective potentials calculated for different multipoles. Increasing the order of the multipole results in a larger field-free region at its center and a steeper slope of the repulsive walls approaching $r = r_0$. A wide field-free region is beneficial for collisional cooling since the ions only experience the RF field for a short time at the turning point and RF heating effects are minimized. For this reason the 22-pole ion

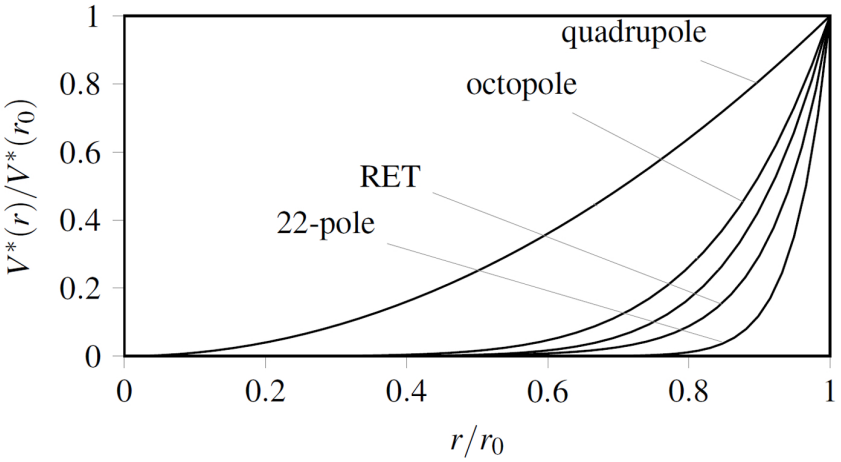

Figure 3.14: Radial dependence of relative effective potential for several linear multipoles and a ring electrode trap (RET).

guide is often the configuration of choice for cryogenic ion traps. On the other hand, precise control of the ion motion along the z-axis is not readily achievable in linear pole traps. In an ion trap with a ring electrode configuration, on the other hand, the axial potential is easily manipulated by superimposing individually adjustable DC voltages on each ring electrode pair. For this reason the ion traps used in the present two instruments are based on the ring electrode configuration, originally proposed by D. Gerlich [151].

As long as the adiabatic approximation holds, *i.e.* as long as the variation of the RF-field over one oscillation period of the micromotion, R_1, is small, the effective potential provides a useful description. Mathematically, this is expressed by the adiabaticity condition [93]

$$\eta = -\frac{2q|\nabla(\nabla\Phi_{AC})|}{m\omega^2} \ll 1. \tag{3.11}$$

In addition, ion velocities need to be slow compared to the frequency of the oscillating field (and small compared to the speed of light such that the magnetic component of the electromagnetic field can be neglected). There is no general way of determining η_{max} for stable operation conditions, because of the lack of an analytical solution to the equation of motion. For the stable confinement of ions in two- or three-dimensional effective potential wells η_{max} occurs at the turning points of the trajectories. Heuristic criteria for stable operation conditions can be determined from computer simulations of ion trajectories in different multipole geometries [93]. These yield

$$\eta\Big(\frac{r}{r_0} = 0.8\Big) \leq 0.3 \qquad \text{and} \tag{3.12}$$

$$V^*\Big(\frac{r}{r_0} = 0.8\Big) \geq E_t, \tag{3.13}$$

where the turning points are expressed in terms of the ratio r/r_0 and E_t is the transverse energy of the ion entering the multipole field. These relations allow estimating the smallest ion mass safely transmitted for a given amplitude of the RF voltage, as well as the minimum RF voltage amplitude required to guide an ion with a given transverse energy. Ion transmission increases in multipole guides with the introduction of buffer gas, because the initial transverse energy of the ions is reduced by collisions with the background gas. Hence, the amplitude of the RF voltage can be reduced, which, in turn, leads to a lowering of the minimum ion mass transmitted.

3.4 Measurements and detection schemes

The experimental setups used in this work were operated in two general modes: the quadrupole (QMS) and the TOF mass spectra (TOF-MS) mode. In the QMS mode transmitted ions are counted using an off-axis detector installed along the trap axis, behind the TOF extraction electrode plates. This detector is either a channeltron electron multiplier (*Burle*, 10 K instrument) or a high energy dynode detector (*SGE*, DM 283, 6 K Instrument). In the latter instrument, an additional channeltron detector (*Extrel*) is mounted directly after the quadrupole mass filter (and before the ion trap) for signal monitoring purposes. The detector signal is preamplified (*Advanced Instrument Research Corporation*, MTS-100) and processed with a *National Instruments* counter/timer card. In the QMS mode the RET is used as an ion guide (RF-only mode) and the TOF extraction plates are grounded. QMS are acquired by scanning the transmitted mass of the quadrupole mass filter and monitoring the ion signal. Ion source conditions and ion optics voltages are typically optimized in the QMS mode for a fixed mass, either manually or using a recently implemented genetic algorithm [124].

The TOF-MS mode requires pulsing the ions out of the ion trap in order to obtain sufficiently high detection efficiency. To this end the quadrupole mass filter is set to the ion mass-to-charge ratio of interest. To ensure radial and axial trapping conditions the RET is filled with a buffer gas, the RF voltage is increased and a first set of DC voltages is superimposed and applied to the ring electrodes such that a potential well is formed along the trap axis. In this way mass-selected ions are trapped, continuously accumulated, thermalized and, at sufficiently low ion-trap temperatures, ion-messenger complexes are formed. After a fixed trapping time, typically every 100 or 200 ms, the DC voltages applied to the RET are quickly switched to a second set DC voltages (extraction voltages), which produce an axial declining voltage ramp for ~ 1 ms. All trapped ions are then focused temporally and spatially at the extraction point of the Wiley-McLaren type TOF mass spectrometer for analysis [152]. When the extraction voltage pulses are applied, the ions separate in the TOF tube depending on their mass-to-charge ratio and are detected as a function of flight time. Ions are detected at

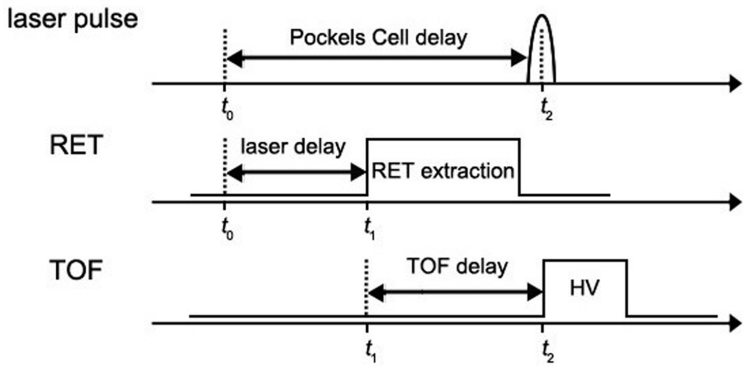

Figure 3.15: Trigger scheme for IRPD experiments.

the end of the field-free TOF tube using a dual stage microchannel plate (MCP) detector. The signal from the MCP detector is amplified by a fast pre-amplifier (*Ortec*, 9305 Fast Preamp) and subsequently acquired using a fast digital oscilloscope (*Acquiris*, DP310). For each mass, integration of the signal over a defined time windows determines the ion yield, I. The TOF-MS mode is used for optimizing trapping conditions and tagging efficiencies by tuning the DC and RF trap voltages, the ion trap temperature and the buffer gas flow. Typically, voltage differences in between adjacent ion optical elements are kept as low as possible to avoid heating effects. Buffer gas mixtures are often used to further optimize the tagging efficiency.

IRPD spectra are measured in the TOF-MS mode. For optimal detection of all ions, parent ions are irradiated with a synchronized IR laser pulse in the TOF mass spectrometer extraction region prior to or simultaneously with the application of the high voltage extraction pulses. The trigger scheme for IRPD experiments is illustrated in Fig. 3.15.

When the frequency of the IR laser pulse is in resonance with a vibrational transition in the irradiated ions, the parent ions absorb one or multiple photons. The vibrational energy is redistributed in the system through IVR and when sufficient energy is absorbed the parent ions undergo dissociation on the time scale of the experiment. Photodissociation leads to a decrease of the parent ion signal, $I_P(\nu)$, and, if ions are formed, an increase of the fragment ions signal, $\sum I_F(\nu)$. Parent and fragment ion intensities are normalized to the total ion signal, $I_P(\nu) + \sum I_F(\nu) = 1$, to account for parent ion signal variations due to ion source instabilities. The photodissociation cross section, $\sigma_{IRPD}(\nu)$, is obtained by normalizing the logarithm of the relative parent ion abundance to the photon fluence, $F(\nu)$ [12, 90]:

$$\sigma_{IRPD}(\nu) = -ln\left[\frac{I_P(\nu)}{I_P(\nu) + I_F(\nu)}\right] \Big/ F(\nu) = -ln\big[I_P(\nu)\big]/F(\nu). \tag{3.14}$$

The photon fluence corresponds to the number of photons passing the cross sectional area of

the interaction volume determined by the overlap of the ion cloud and the laser beam. However, the cross sectional area is difficult to determine due to (i) changes in the laser beam diameter with frequency and, (ii) ion packet dimension not exactly known. Assuming that the diameter of the collimated laser beam is smaller than the diameter of the ion cloud, the (relative) photon fluence is obtained from the measured laser pulse energy $P(\nu)$ as $F(\nu) = P(\nu)/h\nu$.

The normalization procedure described assumes a one photon process, which is generally true when using the messenger-technique. In the case of IRMPD experiments, the logarithm of the relative parent ion abundance is normalized to $P(\nu)$. This normalization approach has been empirically shown to yield spectra very similar to one photon absorbption spectra [153]. A compensation of effects related to the changes in the laser beam diameter or to the changes in the photodissociation efficiency, due to the multiple photon absoprption, may be the reasons behind the obtained improvement of the relative intensities.

Both instruments are equipped with a linear double-focusing reflectron time-of-flight mass spectrometer. Details on the design can be found elsewhere [111]. It consists of a 180° linear reflectron stage and two additional, symmetrically arranged TOF electrodes (see Fig. 3.1). These electrodes allow to pulse the ion packet into the opposite extraction direction, leading to two improvements. First, TOF-MS can be measured with higher mass resolution, due to the increase of the effective flight length and the flight time of the ions. Second, ions can be accelerated into the reflectron stage, refocused in between the TOF-extraction plates and reaccelarted by the application of a second set of HV pulses. The latter acceleration scheme is used for experiments requiring tandem-TOF mass spectrometer capabilities with the possibility of additionally irradiating the ions in-between the two TOF-MS stages. This proves very useful for background-free IRPD experiments on messenger-tagged species and is a prerequisite for performing double resonance isomer-specific experiments, as discussed in the next Section.

3.4.1 Double Resonance Isomer-Specific Spectroscopy – IR^2MS^2 Scheme

IR^2MS^2 is a double-resonance spectroscopy technique that allows for isolation of the vibrational predissociation spectra of structural isomers of mass-selected cluster ions. It is a variant of ion dip spectroscopy [154–156], a term that refers to a family of spectroscopic techniques that employ (i) a probe laser, usually an ultraviolet (UV) or visible (vis) laser pulse whose frequency is fixed in resonance with an electronic transition of the species of interest producing a constant signal, *i.e.* fluorescence, depletion and ionization, and (ii) a frequency scanned laser pulse. When the scanned laser is in resonance with the initial state monitored by the probe laser it induces a population change which manifests itself as a dip in the otherwise constant signal of the probe laser. IR^2MS^2 spectroscopy, first used by the group of Prof. Mark Johnson at Yale University [157], is a particularly attractive version of the method because it does not require the presence of a UV-vis chromophore in the investigated system, but uses two tunable IR lasers in combination with messenger-tagged species and two stages of

mass separation. In order to probe isomer-specifically, an isomer needs to exhibit an isolated vibrational transition at a wavelength that is specific to that isomer. Fig. 3.16 schematically illustrates the experimental implementation of the technique in three steps.

Panel 1 of Fig. 3.16 shows the mass-selected parent ion packet (black area) focused in-between the extraction plates of the tandem TOF mass-spectrometer after extraction from the RET. A first IR laser pulse (scan pulse) is applied. It induces photodissociation producing fragment ions (green), whenever its wavelength is in resonance with a vibrational transition of any of the isomers present. The first set of HV pulses is then applied to the extraction plates, accelerating the ions towards the reflectron stage. Ions separate out in time and space according to their mass-to-charge ratio and are refocused into the extraction region (panel 2). The second IR laser pulse (probe pulse) is tuned to an isomer-specific transition and is timed such that it irradiates the parent ion packet in between the TOF extraction region. It produces an isomer-specific photofragment ion signal (red). Subsequently, a second set of HV pulses is applied to the extraction plates re-accelerating only the parent and isomer-specifically prepared fragment ions towards the MCP detector. Note, the fragment ions generated by the first laser pulse have already passed the extraction region are *not* re-accelerated. The reaccelerated ions again separate in time and space according to their mass-to-charge ratios and a TOF-MS is measured (panel 3). The isomer-specific depletion spectrum is obtained by scanning the wavelength of the scan pulse and manifests itself in the form of dips in the isomer-specifically-prepared fragment ion signal.

In an alternative implementation of this technique, the order of the probe and the scan laser is inverted. The probe pulse, which produces fragment ions isomer-specifically, is fired first and the scan pulse is applied second, after the parent ion pass the extraction region on their way back from the reflectron stage. This implementation requires the acquisition of two TOF-MS: one with and the second without irradiation by the probe pulse. The difference spectrum then contains the isomer-specific IR spectrum. This experimental implementation is required when the probe pulse is generated by the IR free electron laser (see below) *i.e.* typically when the wavelength of the probe pulse lies in the fingerprint or even far-IR spectral region. In this case, the length of the probe pulse is several microseconds and thus requires that the laser beam is aligned counter-propagating to the ion cloud extracted from the trap and prior to acceleration into the tandem TOF mass spectrometer to ensure sufficient temporal overlap.

3.5 Infrared light sources

The application of action spectroscopy techniques (see Section 2.2) requires the use of intense and tunable radiation sources. Widely tunable and intense laser sources in the IR spectral region remain scarce. Since the early 90s optical parametric lasers have become accessible, initially producing light in the < 5 micron region [158]. Only about ten years later further developments of nonlinear crystals allowed extending the wavelength range up to 16 micron [159]. Tunable IR free electron lasers (FELs) are limited in number but remain the only

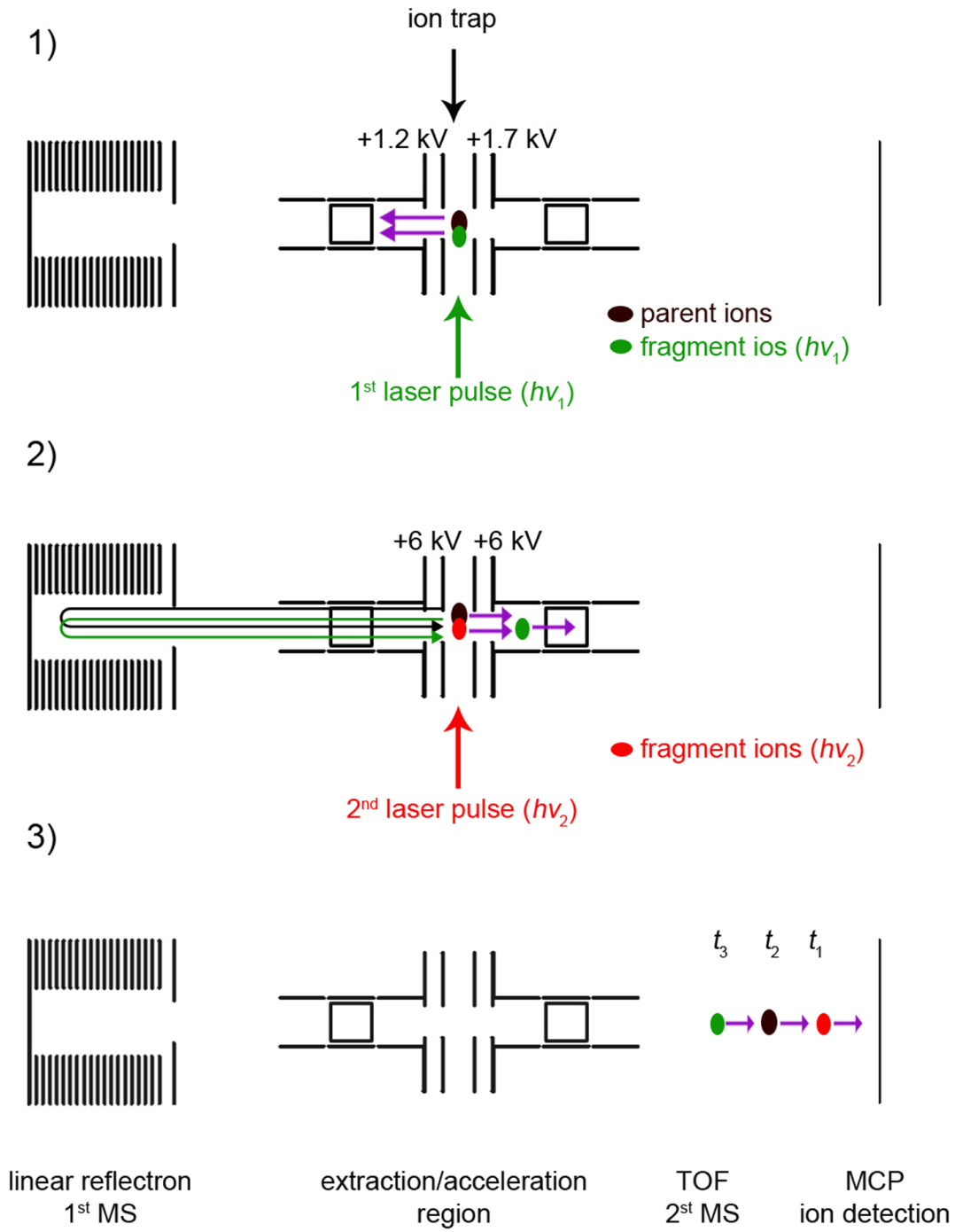

Figure 3.16: Scheme of the experimental implementation of the isomer-selective IR^2MS^2 technique. See text for details. Image adapted from Ref. [111].

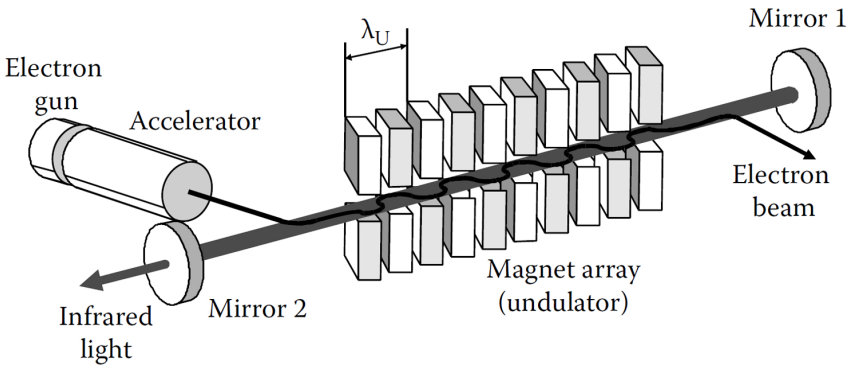

Figure 3.17: Schematic view on a FEL consisting of an electron gun, an accelerator, and an undulator placed in a resonator. Taken from Ref. [90].

source of tunable and intense radiation over a wide IR range. In the work presented in this thesis both type of light sources have been used. In the next section the operating principles of FELs are presented followed by the description of the IR FEL of the Fritz Haber Institute (FHI FEL) and of the parametric oscillator/amplifier (OPO/OPA) system available in our group.

3.5.1 IR FELs operating principle

While conventional laser sources make use of transitions between energy levels in atoms, molecules or crystals, free electrons represent the lasing medium in free electron lasers. The radiation is emitted by relativistic electrons sustaining a wiggling motion in an alternating static magnetic field. A schematic view of an FEL is shown in Fig. 3.17. Electrons are produced in an electron gun, brought to relativistic velocities with an accelerator and injected into an undulator, which is positioned in an optical resonator consisting of two high-reflectivity mirrors. The undulator consists of a periodic structure of dipole magnets generating a static magnetic field that alternates with period λ_U along its length. Due to the Lorentz force, electrons are forced on oscillatory trajectories while travelling through the undulator, stimulating the emission of synchrotron radiation in a cone around the forward direction.

The electron path length over the undulator period λ_U determines the wavelength of the emitted light. The path length depends on the strength of the magnetic field and is elongated with respect to λ_U by a factor $(1 + K^2)$ [160], with

$$K = \frac{eB_0\lambda_U}{\sqrt{8}\pi m_e c}, \tag{3.15}$$

where B_0 is the magnetic field strength, m_e the mass of the electron in the rest frame and c the speed of light. The relativistic nature of electrons with velocity v in the rest frame

manifests itself in a contraction of space by the Lorentz factor γ:

$$\gamma = \frac{1}{\sqrt{1-\beta^2}} \quad \text{with} \quad \beta = \frac{v}{c}. \tag{3.16}$$

The wavelength emitted is further reduced in the laboratory frame by a factor 2γ due to a strong Doppler shift, resulting in the wavelength [160]

$$\lambda_{FEL} = \frac{\lambda_U}{2\gamma^2}\left(1+K^2\right). \tag{3.17}$$

The emitted wavelength is typically controlled by adjusting the strength of the magnetic field B_0 experienced by the electrons. The emitted radiation is monochromatic but initially, due to the large spatial spread of the electrons with respect to λ_{FEL}, also incoherent and thus not very intense. The ponderomotive force, resulting from the interaction of the electromagnetic field of the radiation with the charge of the electrons, leads to microbunching of the electrons at a distance corresponding to one optical wavelength. Consequently, the microbunched electrons emit coherently resulting in a light intensity gain of several orders of magnitude. The strong interaction of the radiation with the electrons is made possible in IR FELs by placing the undulator in a cavity. The cavity length is chosen such that its round-trip time equals a multiple of the time between subsequent electron bunches. As a results, a radiation pulse oscillating back and forth within the cavity is amplified each time it propagates through the undulator in the forward direction. A small fraction of the coherent radiation can exit the resonator through a small hole in one of the cavity mirrors and is guided through an evacuated beam line to a particular experiment.

3.5.2 The FHI FEL

Most of the experiments presented in this Ph.D. thesis were performed with the use of the intense and widely tunable IR radiation produced by the FHI FEL [161] (see Fig. 3.18). A thermionic electron gun generates electrons at a rate of 1 GHz producing micro-pulses with a temporal length on the order of a few picoseconds. Thousands of such pulses, spaced by a nanosecond, form a macro-pulse up to 15 μs long. The electrons are subsequently accelerated by two RF linear accelerators to energies that can be tuned between 15 and 50 MeV. A series of dipole and quadrupole magnets allows manipulating the electron beam and steering it into the undulator. The undulator is 2 m long and contains 50 periods of 40 mm length. At the end of it the beam is steered into a beam dump. The undulator is located between two gold plated mirrors that constitute a 5.4 m long cavity. One side of the cavity is equipped with a motorized in-vacuum mirror exchanger to adjust the outcoupling-hole diameter for different wavelength regions. Five mirrors are available, with hole diameters of 0.75, 1.0, 1.5, 2.5 and 3.5 mm. The out-coupled radiation is guided through a vacuum system to the user stations.

The emitted light has a temporal structure that resembles that of the electron beam. Each

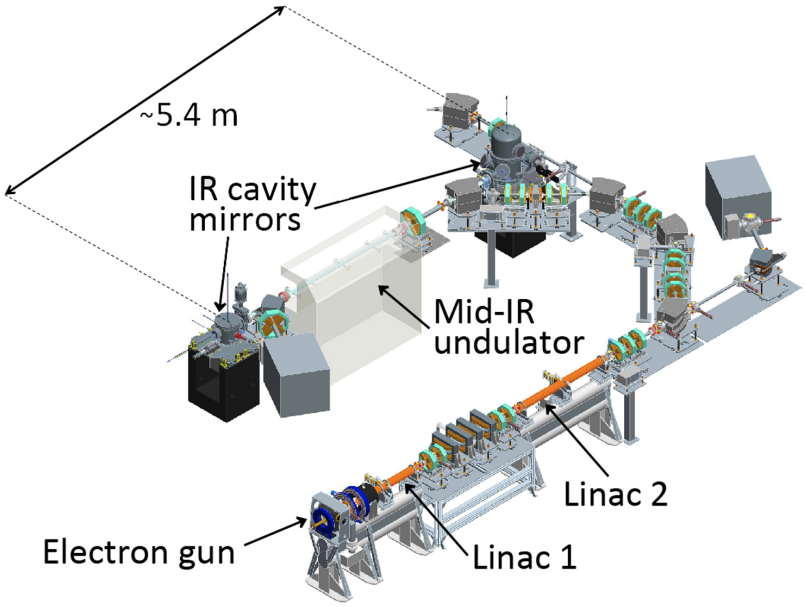

Figure 3.18: Overview of the FHI FEL installation. Figure adapted from Ref. [161].

$\sim$ 10 microsecond long macropulse consists of thousands of 1-5 picosecond long micro-pulses spaced by a nanosecond. The IR spectral range currently extends from 200 to 3000 $cm^{-1}$with a full width half maximum (FWHM) bandwidth between 0.3 and 1% of the central wavelength. The accessible frequency range is limited by the electron energy and wavelength scans are performed by varying the undulator gap from about 17 to 40 mm. Macro-pulses with energies up to 100 mJ can be produced.

3.5.3 Optical parametric laser systems

Two optical parametric devices (*LaserVision*) [158], composed of an oscillator (OPO) and an amplifier (OPA) stage were used in this work. The systems rely on the frequency conversion of a 1064 nm pump beam achieved by means of non-linear optical processes, such as difference frequency mixing (DFM), in non-linear crystals. The OPO stage consists either of one or two KTP (Potassium Titanyl Phosphate, $KTiPO_4$) crystals. For this reason we refer to the systems either as the *single* and *double* (crystal) OPO. The OPA stage in both laser systems composes of four KTA (Potassium Titanyl Arsenate, $KTiOAsO_4$) crystals. This combination of crystals produces tunable mid-IR radiation in the range 2000–4600 cm^{-1}. DFM in an additional $AgGaSe_2$ crystal positioned after the OPA stage extends the accessible wavelength range, producing light from 2300 down to 625 cm^{-1}. The 1064 nm pump pulse for the single OPO system is generated by an unseeded 10 Hz Nd:YAG laser (*Innolas*, Spitlight 600) while a seeded system (*Continuum*, Powerlite DLS 8000) is used to pump the double OPO. The

differences in the pump laser, in particular the produced beam profile, and in the OPO stage, result in different final energies and bandwidths. The characteristic parameters of the two systems along with those of the FHI FEL are summarized in Table 3.2.

Table 3.2: Comparison of the characteristic laser pulse parameters of the FHI FEL and the two OPO/OPA/$AgGaSe_2$ systems available in our group.

	FHI FEL	double OPO	signle OPO
tuning range	200–3000 cm^{-1}	625–4700 cm^{-1}	625–4700 cm^{-1}
pulse energy	< 100 mJ	< 34 mJ	< 12 mJ
pulse duration	$\sim$ 5–10 μs	7 ns	7 ns
repetition rate	5 / 10 Hz	5 / 10 Hz	5 / 10 Hz
spectral bandwidth	0.3–1% FWHM	~ 1.3 $(1.8)^a$ cm^{-1}	~ 3.6 $(5.1)^a$ cm^{-1}
pump energy (1064 nm)		590 mJ	550 mJ

[a] Spectral bandwidth after $AgGaSe_2$ crystal.

A schematic overview of the double OPO system that elucidates the conversion scheme of such parametric systems is shown in Fig. 3.19. The 1064 nm beam of the Nd:YAG laser enters the system and is collimated to the size of the crystal with a telescope. Subsequently, the beam is divided into two perpendicular beams with a beam splitter. Two rotatable half-wave plates are used as beam attenuators to continuously regulate the intensity of each beam. Two KTP crystals placed within a cavity constitute the OPO stage, which is pumped by 532 nm radiation produced by doubling of the 1064 nm pump pulse in a KTP crystal. For each photon entering the OPO crystal, a signal and an idler photon is produced by non-linear optical processes. The energy of the pump photon is equal to the sum of the signal and idler photon energies:

$$\frac{1}{\lambda_{pump}} = \frac{1}{\lambda_{signal}} + \frac{1}{\lambda_{idler}} \quad \text{with} \quad \lambda_{signal} < \lambda_{idler}.$$

The OPA idler wavelength is tunable in the mid-IR region from 2.1 to 5.0 μm while the signal wavelength tunes from 1.4 to 2.1 μm. The idler beam is typically selected with a Brewster port for experiments. The port is removed to extend the spectral range by DFM of the signal and idler beams in a $AgGaSe_2$ crystal. In this conversion stage, light with a wavelength ranging from 5.0 to 16.0 μm is produced. The residual pump pulse of this stage is separated by means of filters (ZnSe, Ge or Si-based), which are choosen depending on the wavelength range required.

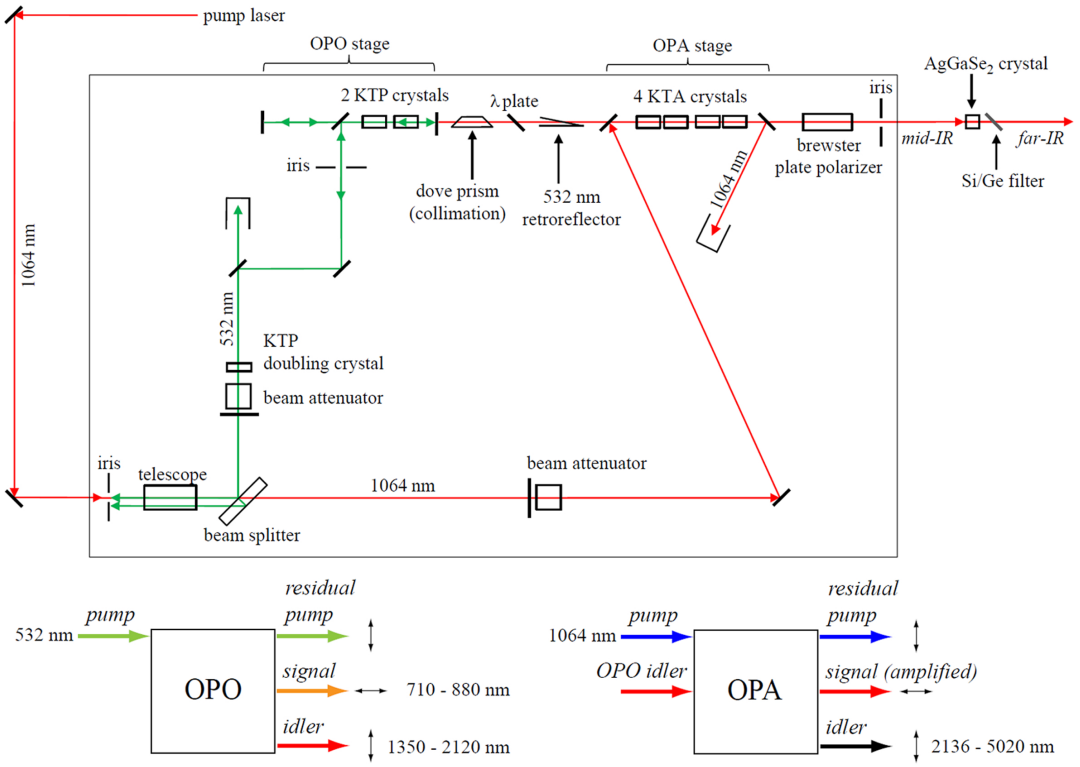

Figure 3.19: Schematic overview of the OPO/OPA/AgGaSe2 system (top). Coloured arrows illustrate the light path. Representation of the frequency conversion process in the OPO and OPA stages (bottom). The horizontal and vertical double arrows indicate the polarization direction of the laser beams produced with respect to the plane of the system. Figure adapted from Ref. [110].

4 Aluminum-Oxides Clusters

In this Chapter cryogenic ion trap vibrational spectroscopy is used in combination with quantum chemical calculations to study the structure of Al-oxide clusters and of the complexes formed with water. Mono- and di-aluminum oxide anions are characterized in Section 4.1. The size dependence of stoichiometric Al_2O_3 materials is investigated at the atomic scale by characterizing the structure of $(Al_2O_3)_{1-6}AlO_2^-$ cluster anions (Section 4.2). Finally, in section 4.3 the reaction products of $Al_3O_4^+$ with up to four D_2O molecules are investigated. Results are then summarized in Section 4.4.

4.1 Gas Phase Structures and Charge Localization in Small Aluminum Oxide Anions: Infrared Photodissociation Spectroscopy and Electronic Structure Calculations*

4.1.1 Introduction

Aluminum oxides are widely used as ceramics, coatings, abrasives, adsorbents as well as components of solid catalysts[162]. For such complex materials it remains difficult to characterize or predict the molecular scale properties and structures with atomic resolution. Gas-phase clusters, in contrast, are amenable to highly sensitive and selective experimental techniques as well as higher level computational methods. Experiments on these model systems thus provide insights into structure-reactivity correlations as well as the transition from molecular to condensed phase properties[11, 163, 164]. Small aluminum oxide cluster cations[165, 166] and anions[167] containing oxygen-centered radicals have raised interest recently as models for understanding water chemisorption and C–H bond activation. There is also an astrochemical interest in the role that small aluminum oxide clusters play in the formation of circumstellar corundum (Al_2O_3) grains[168].

In the present study, we use cryogenic ion trap vibrational spectroscopy of messenger-tagged, mass-selected anions in combination with density functional theory (DFT) to examine the geometric structure of AlO_{1-4}^- and $Al_2O_{3-6}^-$ ions formed by sputtering of elemental aluminum in the presence of oxygen. We are particularly interested in the identification of reactive oxygen species like $O_2^{-\cdot}$ (superoxo), O_2^{2-} (peroxo) and $O^{-\cdot}$ (atomic oxygen radicals).

*Chapter based on the work published in Xiaowei Song, Matias R. Fagiani, Sandy Gewinner, Wieland Schöllkopf, Knut R. Asmis, Florian A. Bischoff, Fabian Berger and Joachim Sauer, *J. Chem. Phys.* **2016**, *144*, 244305

The computed structures of the aluminum oxide clusters containing oxygen-centered radicals sensitively depend on the amount of exact exchange mixed into the exchange-correlation functional. Moreover, anharmonic effects, like Fermi-resonances, prove to be important for explaining the experimental IR spectra.

Previous mass spectrometric investigations on gas-phase aluminum oxide cluster ions have focused on their reactivity towards water[166, 169], carbon monoxide[170], ammonia[171], methane[165, 166] and larger alkanes[167]. The smaller anions show a variety of reactions, but react more selectively than the corresponding cations. The electronically closed-shell AlO_2^- ion readily adsorbs two water molecules forming $Al(OH)_4^-$ in a barrierless reaction[169]. $Al_2O_3^-$ and $Al_2O_4^-$ react with CO under atomic oxygen loss, suggesting the formation of CO_2[170]. In $Al_2O_4^-$ and $Al_2O_6^-$ the atomic oxygen radical is predicted to be the active site for hydrogen atom abstraction from *n*-butane[167]. Mass spectrometry has also been used to determine ionization energies by way of bracketing experiments[172].

Less is known about the vibrational spectroscopy of small aluminum oxide clusters. Matrix isolation IR spectroscopy has been used to study neutral clusters up to AlO_6 and Al_2O_3[173–176]. Aluminum oxide anions up to $Al_7O_5^-$ have been studied using anion photoelectron (APE) spectroscopy[177–181]. The APE spectra of the smaller anions are vibrationally resolved and, combined with electronic structure calculations, they allowed identifying an Al–$(O)_2$–Al rhombus as a common structural motif of small neutral and anionic dinuclear aluminum oxides[178]. Recently, vibrational and rotational molecular constants of AlO^- were determined by means of autodetachment spectroscopy[182]. Detailed structural information on gas-phase clusters can be obtained from infrared photodissociation (IRPD) spectroscopy, but until now IRPD spectra have only been reported for aluminum oxide cations $[(Al_2O_3)_{1-4}(AlO)]^+$[28].

Electronic structure studies on smaller aluminum oxides containing up to two Al atoms have focused mainly on neutral[183–193] and to a lesser extent on anionic[167, 185, 186, 194–196] clusters. For AlO^-, AlO_2^- and AlO_4^- closed shell electronic ground states of $^1\Sigma^+$ ($C_{\infty v}$), $^1\Sigma_g$ ($D_{\infty h}$) and $^1A_1$ (D_{2d}) symmetry, respectively, have been predicted[185, 186, 195]. Di-aluminum oxide anions, $Al_2O_n^-$, contain an uneven number of electrons and, for n = 2–6, are characterized by a rhombic Al–$(O)_2$–Al structural motif[167, 194]. The unpaired electron is found to be localized on one of the two terminal O-atoms in $Al_2O_4^-$ (C_{2v} structure), while in $Al_2O_6^-$ it is delocalized equally over the two terminal η^2-O_2 groups (D_{2h} structure)[167].

4.1.2 Eperimental methods

Infrared photodissociation experiments are conducted on the 10 K ion-trap tandem mass spectrometer described in Chapter 3. Briefly, aluminum oxide anions are generated using the magnetron sputtering source described in Section 3.2.3. Compared to more commonly used laser ablation sources, this source often yields higher ion signals for smaller metal oxides ions ($\lesssim$ 10 atoms). Continuous flows of Ar and O_2 buffer gases are injected in front of the Al-sputtering target. He gas is introduced from the back of the sputtering chamber.

The partial pressures inside the sputtering chamber are controlled individually by mass-flow controllers and allow optimizing the cluster composition and size distribution (see Fig. 3.11 for a typical quadrupole mass spectrum). Typically, the O_2 to Ar flow-ratio is below 10% and the total flow results in a pressure up to 10^{-3} mbar in the source chamber. Clusters nucleate and grow in a cooled aggregation chamber held at temperatures between 100 and 200 K. The distance between the sputter head and the aggregation chamber nozzle (10–25 cm) is optimized for best signal. The cluster beam is collimated using a 4 mm diameter skimmer. Subsequently, negative ions are compressed in phase using a radio-frequency decapole ion-guide filled with He as buffer gas and mass-selected using a quadrupole mass-filter. Mass-selected anions are deflected by 90° and focused into a RF linear ring-electrode ion-trap held at cryogenic temperatures (15-19 K) and continuously filled with D_2 gas. Trapped ions are accumulated and internally cooled by collisions with the D_2 gas. Aluminum oxide anions are messenger-tagged with D_2 via three-body collisions: $Al_{1,2}O_n^- + 2\ D_2 \rightarrow Al_{1,2}O_n^- \cdot D_2 + D_2$. After an ion trap fill time of 199 ms all ions are extracted from the ion trap and focused in the center of the extraction region of a time-of-flight mass spectrometer. There they are irradiated by an intense and wavelength-tunable IR laser pulse. When resonant with a vibrational transition parent ions absorb a photon and eventually lose one or more messenger molecules via intramolecular vibrational predissociation.

The intense and tunable IR pulses are generated by the FHI FEL (see Section 3.5.1 and references therein). The wavelength of the IR radiation is tuned from 8 to 25 μm with a bandwidth of ca. 0.2% root mean square (rms) of the central wavelength and pulse energies of ∼0.5 to 14 mJ. IR spectra are recorded by averaging over 60 TOF mass spectra per wavelength step. The intensities are normalized to the total number of parent and fragment ions, to account for fluctuations in the total ion signal. Typically, distributions of $(D_2)_m$-tagged anions, peaking at m=1 and extending up to m=4, were produced in the ion trap. However, the differences between the action spectra of anions with a single (m=1) and with more than one tag (m>1) were negligible and therefore the ion yields of all tagged anions were summed up for determining the parent ion yield. The IRPD cross section σ is determined as described in Section 3.4.

4.1.3 Computational methods*

For DFT structure prediction, the potential energy surface (PES) is searched first for the global minimum structures with a genetic algorithm[197, 198] using the BP86 functional[199, 200] together with the split-valence polarized basis set SVP[201] (denoted BP86/SVP). The genetic algorithm run is repeated three times for 500 structures, after which convergence is checked. Then, the ten lowest energy structures of the GA run are refined using the B3LYP[202] functional with the TZVPP[201] basis set (Al: 5s5p3d1f, O: 5s3p2d1f). These

*Calculations were performed by Florian A. Bischoff and Fabian Berger in the group Prof. Joachim Sauer at the Institut für Chemie, Humboldt-Universität zu Berlin.

basis sets, denoted "def-2" in the Turbomole library [203], are sufficiently diffuse and, hence, adequate for a study on metal oxide anions. Finally, the structures are reoptimized using BHLYP[204]/TZVPP which includes 50% Fock exchange in the exchange-correlation functional. For the smaller AlO_n^- systems the coupled cluster singles and doubles with perturbative triples method CCSD(T) (see Ref. [205] and references therein) with the aug-cc-pwCVTZ[206] basis set and frozen core orbitals are also applied. Closed-shell anions were computed in the spin-restricted formalism of the respective theories, open-shell species in the spin-unrestricted formalism (DFT) and ROHF/UCCSD(T) formalism (CCSD(T)). The dodo program[207] is used for the genetic algorithm.

Unless explicitly stated otherwise, IR spectra are computed within the double harmonic approximation. Anharmonic corrections to the vibrational energies including Fermi resonances were computed as implemented in Gaussian 09[208]. Simulated harmonic spectra are derived from computed stick spectra and convoluted with a 10 cm^{-1} full width at half maximum Gaussian line shape function to effectively account for rotational band contours and the spectral width of the laser pulse.

Electronic structure calculations are performed using the following program packages: MOLPRO 2012 (Coupled-Cluster)[209], Turbomole (DFT structure optimization and harmonic frequencies)[203], and Gaussian 09 (DFT anharmonicities)[210].

4.1.4 Results and discussion

Experimental results

IRPD spectra of D_2-tagged AlO_{1-4}^- and $Al_2O_{3-6}^-$ anions, measured in the spectral range from 400 to 1200 cm^{-1} and monitoring the D_2 loss channels, are shown in Fig. 4.1. Spectral features are labeled with capital letters from A-H. Experimental band positions are summarized in Tables 4.1 and 4.2.

Monoaluminum oxide anions The IRPD spectrum of D_2-tagged AlO^- exhibits a single band, labeled **A** in Fig. 4.1, with a full width at half maximum (FWHM) of 31 cm^{-1} and a rotational envelope characteristic of a linear rotor. Simulation of the rotational band contour yields a band origin of 957 cm^{-1} and rotational temperature of ∼50 K. This band corresponds to excitation of the Al–O stretching fundamental (ν), in agreement with the value of 953.7 $cm^{-1}$for bare AlO^- in its $^1\Sigma^+$ ground state determined from autodetachment spectroscopy[182]. In the isoelectronic SiO ($^1\Sigma^+$) this band is observed 225 cm^{-1} higher in energy at 1182 cm^{-1}[211].

The experimental IRPD spectrum of D_2-tagged AlO_2^- exhibits a single band at 1134 cm^{-1} (**A**), blue-shifted by 177 cm^{-1} with respect to band **A** in the AlO^- spectrum. This blue shift is comparable to that observed in the IR spectra of SiO_2 (versus SiO) of 198 cm^{-1}, where the band at 1380 cm^{-1} corresponds to the antisymmetric stretch fundamental ν_{AS} of linear silicon dioxide[211]. Hence, band **A** is assigned to the ν_{AS} mode of a linear O–Al–O structure,

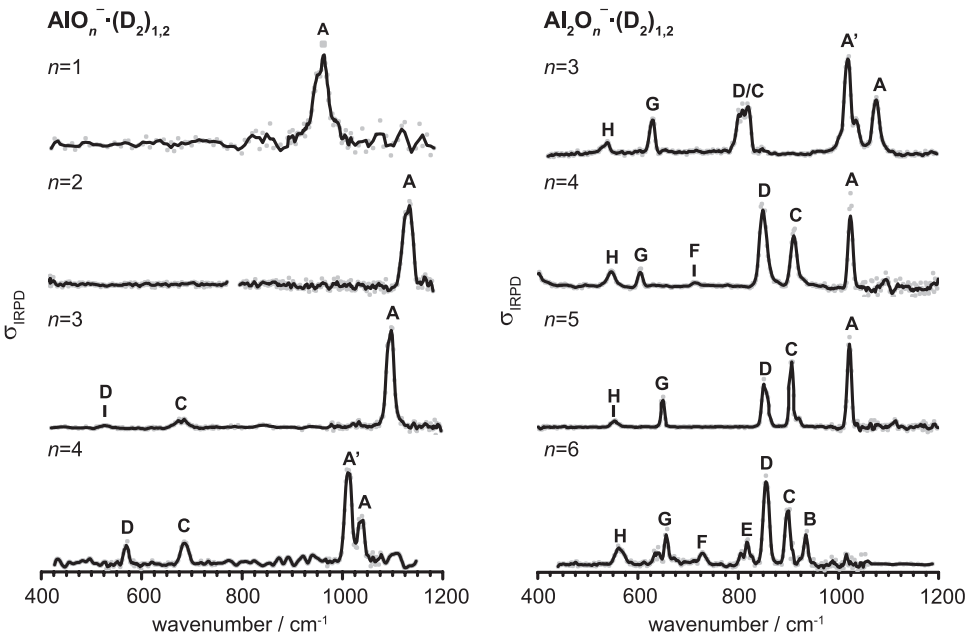

Figure 4.1: IRPD spectra of D_2-tagged AlO_{1-4}^- (left) and $Al_2O_{3-6}^-$ (right) in the spectral range from 400 to 1200 cm^{-1}. The raw data (gray dots) and the three point adjacent-averaged trace (solid line) are plotted. Spectral features are labeled with capital letters. See Tables 4.1 and 4.2 for band positions and assignments.

similar to the ground state structures reported for the analog group III oxides BO_2^- and GaO_2^-[212, 213]. A linear structure was also derived from APE spectra, which reveal the IR-inactive symmetric stretching mode in form of a hot band at 680±60 cm^{-1}[177].

The IRPD spectrum of D_2-tagged AlO_3^- looks similar to the one of AlO_2^- in that it is also dominated by an intense band at high energies (**A**, 1098 cm^{-1}), indicating the presence of terminal metal-oxo bonds. In addition, two weaker bands are observed at lower energies at ∼680 (**C**) and 526 cm^{-1} (**D**). The isoelectronic silicon trioxide exhibits a closed-shell singlet ground state with a planar C_{2v} structure that contains a strained SiO_2 ring[214, 215]. The IR spectrum of SiO_3 is characterized by a dominant peak at high energies (1364 cm^{-1}), 16 cm^{-1} below the corresponding intense absorption in SiO_2 (1380 cm^{-1}), and two weaker absorptions roughly 500 cm^{-1} to the red at 877 and 855 cm^{-1}. This compares favorable with the present IRPD spectrum of AlO_3^-, which is characterized by a red shift of the most intense absorption (versus AlO_2^-) of 36 cm^{-1} and additional considerably weaker features ∼420 cm^{-1} lower in energy, indicating a similar geometric arrangement as in SiO_3. A C_{2v} structure with a peroxo-group as part of a three-membered ring has also been predicted for the ground state of GaO_3^-[216].

Finally, the IRPD spectrum of D_2-tagged AlO_4^- exhibits four bands at 1039 (**A**), 1011 (**A′**), 685 (**C**) and 572 cm^{-1} (**D**). It looks rather similar to that of AlO_3^- suggesting a related structure. The main difference is two bands instead of one band above 1000 cm^{-1}, which are also slightly red-shifted compared to the corresponding band in AlO_3^-. No experimental reference data for either neutral SiO_4 or group III tetraoxide anions is available in the literature. A highly symmetric (D_{2d}) $^1A_1$ ground state has been predicted for AlO_4^-, which is characterized by three IR-active bands in-between 400-1200 cm^{-1} instead of four that are observed in the present IRPD spectrum[195]. An assignment to a kite-like O–Al–O_3 structure, as predicted for GaO_4^-, is unlikely, as the most intense IR transition associated with this structure is expected at lower energies (862 cm^{-1}), a region where no signal is observed in the IRPD spectrum of AlO_4^-[217].

Dialuminum oxide anions The IRPD spectra of $Al_2O_{3-6}^-$ (see Fig. 4.1) show considerably more IR activity compared to those of the mono-aluminum oxide anions, in particular in-between 700 and 950 cm^{-1}. The $Al_2O_{3-6}^-$ spectra share some common features, like strong IR-activity near 850 cm^{-1} (band **C** and **D**) as well as two characteristic bands, labeled **G** and **H**, in-between 500 and 700 cm^{-1}, indicating that they share a common geometric motif. Previous APE spectra for $Al_2O_{2-5}^-$ reported by Desai *et. al.* [178] found that this common motif is a Al–$(O)_2$–Al rhombic ring. Such cyclic structures have also been predicted for $B_2O_4^-$, $Ga_2O_{3-4}^-$ and the Si_2O_3[216, 219–221]. The lower energy absorptions can then likely be assigned to various vibrational modes involving this four-membered ring[222, 223].

The previous APE study also suggested that $Al_2O_{3-5}^-$ exhibit terminal Al-O groups and, indeed, the IRPD spectra of $Al_2O_{3-5}^-$ are characterized by strong absorptions slightly above 1000 cm^{-1}, typical for the presence of such terminal Al-O groups. However, the number

Table 4.1: Experimental and calculated harmonic vibrational frequencies (in cm^{-1}) of $AlO_{1\text{-}4}^-$.

Species	Mode	Band	Expt.	Irrep.	B3LYP	BHLYP[a,b]	CCSD(T)
AlO^-	ν(AlO)	A	957	σ	977	971 (83)	953
AlO_2^-	ν_{AS}(OAlO)	A	1134	σ_u	1131	1159 (160)	1127
	ν_S(OAlO)			σ_g	784	809 (0)	786
AlO_3^-	ν(AlO)	A	1098	a_1	1116	1101 (204)	1094
	$\nu(O_2^{2-})$	B	842	a_1	801	820 (1)	742
	$\nu_{AS}(AlO_2)$	C	685/675	b_1	662	647 (25)	670
	$\nu_S(AlO_2)$	D	526	a_1	586	598 (20)	538
AlO_4^-	$\nu_S(AlO_2^{sym.\ str.})+\nu_{AS}(O_2^{str.})$	A	1039	a_1+b_2			1063[c]
	$\nu_{AS}(AlO_2^{sym.\ str.})$	A′	1011	b_2	1040	1029 (228)	1021
	$\nu_{AS}(AlO_2)$	C	685	e	675	659 (26)	683
	$\nu_{AS}(O_2^{str.})$	D	572	b_2	683	716 (57)	587

[a] Frequencies are scaled by 0.9339 (from Tab. II of Ref. [218]).
[b] IR intensities (in km/mol) are listed in parentheses.
[c] Sum of frequencies: 476 cm^{-1}(a_1,$\nu_S(AlO_2^{sym.\ str.})$) and 587 cm^{-1}(b_2,$\nu_{AS}(O_2^{str.})$).

of IRPD bands observed (*e.g.* two for $Al_2O_3^-$) does not always correlate with the number of terminal Al-O groups expected (*e.g.* one for $Al_2O_3^-$), requiring further explanation (see below). No significant absorption is observed in this region for $Al_2O_6^-$, supporting the predicted O_2–Al–$(O)_2$–Al–O_2 structure, which contains two terminal η^2-O_2 groups but no terminal O-atoms[167].

In more detail, the IRPD spectrum of $Al_2O_3^-\cdot D_2$ is characterized by five absorption features at 1076 (**A**), ∼1019 (**A′**), ∼818/800 (**C**/**D**), 629 (**G**), and 539 cm^{-1} (**H**). Four of these bands (**C**, **D**, **G** and **H**) are also observed in the IRPD spectrum of $Al_2O_4^-\cdot D_2$. While no absorption corresponding to band **A** in the $Al_2O_3^-\cdot D_2$ spectrum is observed, an additional intense feature appears at 913 cm^{-1} (**C**). The IRPD spectrum of $Al_2O_5^-\cdot D_2$ looks very similar to that of $Al_2O_4^-\cdot D_2$ with five bands at 1022 (**A**), ∼907 (**C**), 851 (**D**), 650 (**G**) and 554 cm^{-1} (**H**), but no absorption in the vicinity of the weak feature **F** (715 cm^{-1}) observed for $Al_2O_4^-\cdot D_2$. Note, for $Al_2O_4^-$ and $Al_2O_5^-$ Desai *et. al.* [178]. reported features at low electron binding energies in the APE spectra that they assigned to hot bands involving vibrational modes at 1090 cm^{-1} ($Al_2O_4^-$) and 1170 cm^{-1} ($Al_2O_5^-$). We find no evidence of IR-active modes at such high energies, suggesting that these modes are either not IR-active or these features are of other origin. Finally, the IRPD spectrum of $Al_2O_6^-\cdot D_2$ resembles that of $Al_2O_5^-\cdot D_2$ with respect to the bands **C**, **D**, **G** and **H**. It shows additional features at 937 (**B**), ∼819 (**E**) and 729 cm^{-1} (**F**), and lacks any significant absorption above 950 cm^{-1}.

Computational results

Monoaluminum oxide anions AlO^- and AlO_2^- are electronic closed shell systems and all three computational methods (B3LYP, BHLYP, and CCSD(T)) predict the same electronic and geometric structures. CCSD(T) and B3LYP vibrational frequencies are close to the experimental ones, while the BHLYP frequencies are blue-shifted (see Tab. 4.1). Previous

Table 4.2: Experimental and calculated harmonic vibrational frequencies (in cm^{-1}) of $Al_2O_{3\text{-}6}^-$ including main contributions of local modes and irreducible representations (Irrep.) of the delocalized normal modes.

Cluster	Mode	Band	Expt.	Irrep.	BHLYP[a]
$Al_2O_3^-$	ν(AlO)	A	1076	a_1	1026[b]
	$2\nu_{AS,2}$(ring)	A′	1019		1053[b]
	$\nu_{S,1}$(ring), $\nu_{AS,1}$(ring)	C/D	818/800	a_1/b_1	809/791
	$\nu_{S,2}$(ring)	G	629	a_1	623
	$\nu_{AS,2}$(ring)	H	539	b_1	527
$Al_2O_4^-$	ν(AlO)	A	1024	a_1	1035
	ν(AlO)	C	913	a_1	914
	$\nu_{AS,1}$(ring)	D	850	b_1	843
	$\nu_{S,1}$(ring)	F	715	a_1	699
	$\nu_{S,2}$(ring)	G	606	a_1	600
	$\nu_{AS,2}$(ring)	H	546	b_1	535
$Al_2O_5^-$	$\nu({O_2}^{2-})$	*	1113	a_1	1202
	ν(AlO)	A	1022	a_1	1032
	$\nu_{S,1}$(ring)	C	907/921	a_1	884
	$\nu_{AS,1}$(ring)	D	851	b_1	844
	$\nu_{S,2}$(ring)	G	650	a_1	645
	$\nu_{AS,2}$(ring)	H	554	b_1	542
$Al_2O_6^-$	$\nu({O_2}^{2-})$	*	1016	a_1	1202
	ν(Al–${O_2}^{2-}$)	B	937	a_1	941
	$\nu_{S,1}$(ring)	C	900	a_1	881
	$\nu_{AS,1}$(ring)	D	855	b_1	842
		E	819/807		
	$\nu({O_2}^{2-})$	F	729	a_1	726
	$\nu_{AS,2}$(O–Al–O)			b_2	655
	$\nu_{S,2}$(ring)	G	640	a_1	648
	$\nu_{AS,2}$(ring)	H	560	b_1	558

[a]Frequencies are scaled by 0.9339 (from Tab. II of Ref. [218]).
[b]Anharmonic BHLYP frequencies: 1089 and 1046 cm^{-1}(Fermi resonance).

CCSD(T) calculations on AlO^- predicted a harmonic vibrational frequency of 969 cm^{-1} and an equilibrium bond length of 164 pm[185], whereas our CCSD(T)/aCVTZ calculations yield values of 953 cm^{-1} and 165 pm, respectively. In AlO_2^- the Al–O stretching mode is predicted higher (1127 cm^{-1}) and the bond distance is slightly shorter (164 pm).

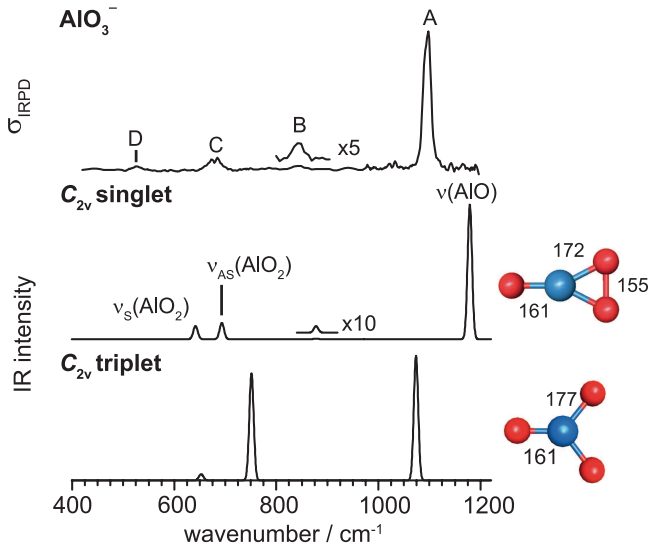

Figure 4.2: IRPD spectrum of D_2-tagged AlO_3^- (top) compared to simulated IR spectra derived from harmonic BHLYP vibrational frequencies and intensities of low energy structures (Al=blue, O=red, bond lengths are in pm). Assignments of the IR-active vibrational modes are indicated (ν: stretch, ν_S/ν_{AS}: symmetric/antisymmetric stretch). See Tab. 4.1 for band positions and assignments.

For AlO_3^-, B3LYP and CCSD(T) calculations yield a closed-shell singlet ground state with a planar O–Al–O_2 structure of C_{2v} symmetry (see Fig. 4.2) containing a peroxo group (155 pm). In contrast, an open shell species with three isolated oxygen atoms as part of a distorted D_{3h} structure (see Fig. 4.2) is predicted at slightly lower energy using BHLYP. Using B3LYP and CCSD(T) this species has significantly higher energies, 39 and 87 kJ/mol, see Fig. 4.3.

The harmonic IR spectra (BHLYP) of both of these structures are compared to the experimental IRPD spectrum in Fig. 4.2. The agreement is much better for the O–Al–O_2 structure (singlet state) than for the Al(-O)$_3$ structure (triplet state). For the O–Al–O_2 structure, the calculations yield three IR-active bands at 1179 cm^{-1}, 693 cm^{-1}, and 642 cm^{-1}. While the BHLYP frequencies are significantly blue-shifted by up to 120 cm^{-1} with respect to the experimentally observed IRPD bands **A**, **C** and **D** (see Tab. 4.1), the relative band positions and intensities agree favorably, supporting an assignment to the closed-shell C_{2v} structure. As in AlO^- and AlO_2^-, the terminal Al–O stretching mode of AlO_3^- is calculated highest in energy (1179 cm^{-1}). The two bands at lower energies then correspond to the antisymmetric and symmetric stretching mode of the Al–O_2 moiety (see Fig. 4.4). The intensity of the peroxide stretching mode at 878 cm^{-1} is found to be small (<1% relative

intensity) by BHLYP. Indeed, we observe a small feature, labeled **B** in Fig. 4.2, at 842 cm^{-1} that could tentatively be attributed to this mode. Note, the CCSD(T) calculations (see Tab. 4.1) predict the peroxide stretching mode at considerably lower energy (742 cm^{-1}).

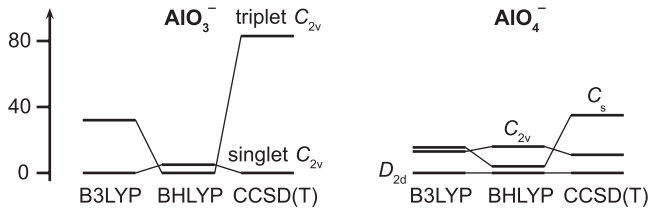

Figure 4.3: Relative energies in kJ/mol of the low-energy isomers of AlO_3^- and AlO_4^- computed with different methods.

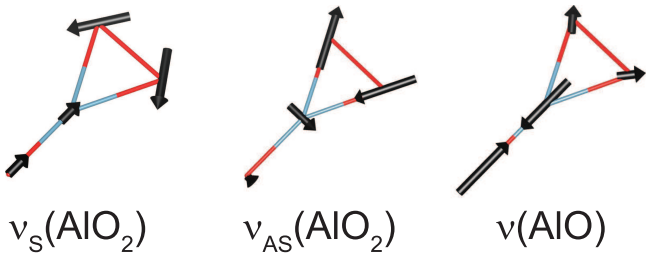

Figure 4.4: Visualization of three normal modes (ν: stretch, ν_S/ν_{AS}: symmetric/antisymmetric stretch) of the closed-shell C_{2v} structure of AlO_3^-.

For AlO_4^-, the genetic algorithm yields three low energy structures shown in Fig. 4.3. Fig. 4.5 (right panel) shows the relative stability of these structures as obtained with different methods. These are a D_{2d} structure containing two η^2-peroxo motifs, a planar C_{2v} structure containing an O_3 moiety (+14 kJ/mol) and a non-planar biradical C_s structure containing a single η^2-superoxo motif (+18 kJ/mol). The C_s structure may be considered as a superoxide radical $O_2^{-\cdot}$ coordinated to an asymmetric, bent AlO_2 radical with the extra electron localized on a single oxygen atom. In previous work[195], the ground state structure was assumed to be a singlet state of D_{2d} symmetry, consistent with the B3LYP, BHLYP and CCSD(T) results of this work.

There are two possible assignments for the experimental spectrum shown in Fig. 4.5: (i) The harmonic BHLYP results for the C_s structure may explain three of the four bands of the experimental IR spectrum. The calculated IR-active bands at 1081, 722, and 524 cm^{-1}which correspond to excitations of the Al–O stretch ν_1 involving the shorter Al–O· bond (161 pm), the Al–O stretch ν_2 of the longer Al–O bond (176 pm), and the symmetric stretch ν_S of the AlO_2 η^2-superoxo motif, respectively, can be assigned to bands **A**, **C**, and **D**, respectively. The fourth observed band **A′** may result from a Fermi resonance, as anharmonic BHLYP calculations of the biradical C_s structure show (see Fig. 4.5). A resonance between the first

overtone $2\nu_S$ and the ν_1 fundamental yields a doublet at 996 and 1068 cm^{-1}(see Fig. 4.5), which could be attributed to bands **A′** and **A**, respectively. However, quantitative agreement for the band positions is not achieved.

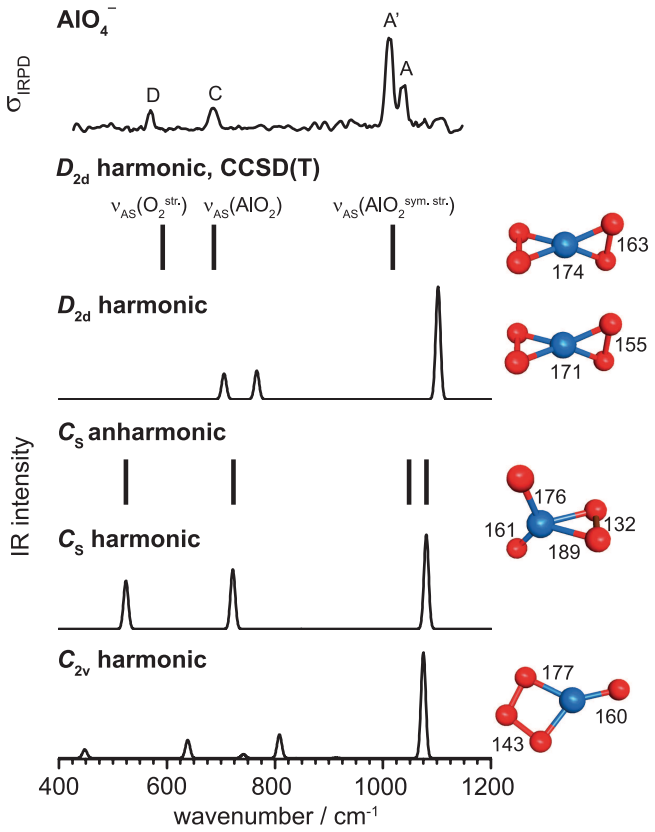

Figure 4.5: IRPD spectrum of D_2-tagged AlO_4^- (top) compared to calculated IR spectra of low-energy structures (bond length are in pm) of AlO_4^-. The harmonic CCSD(T) stick spectrum (no intensities available) is shown beneath the experimental spectrum. All other panels show BHLYP results for different structures. Since intensities are not available the anharmonic BHLYP results for the C_s structure are also shown as stick spectrum. Assignments of the IR-active vibrational modes are indicated (ν_S/ν_{AS}: symmetric/antisymmetric stretch) and summarized together with experimental and calculated band positions in Table 4.1. See text for details.

(ii) The harmonic CCSD(T) results of the D_{2d} structure for the band position are in very good agreement with the experiment. The most intense band **A′** at 1011 $cm^{-1}$is calculated at 1021 $cm^{-1}$and corresponds to $\nu_{AS}(AlO_2{}^{sym.\ str.})$, an antisymmetric combination (b_2) of the two AlO_2 symmetric stretches. The **C** and **D** bands at 685 and 572 cm^{-1}then are $\nu_{AS}(AlO_2)$, the two degenerate AlO_2 antisymmetric stretches (e), and $\nu_{AS}(O_2{}^{str.})$, the antisymmetric combination (b_2) of the two O_2 stretches, respectively, calculated at 683 cm^{-1}(e) and 587 m (b_2). Band **A** cannot be explained by a calculated fundamental transition.

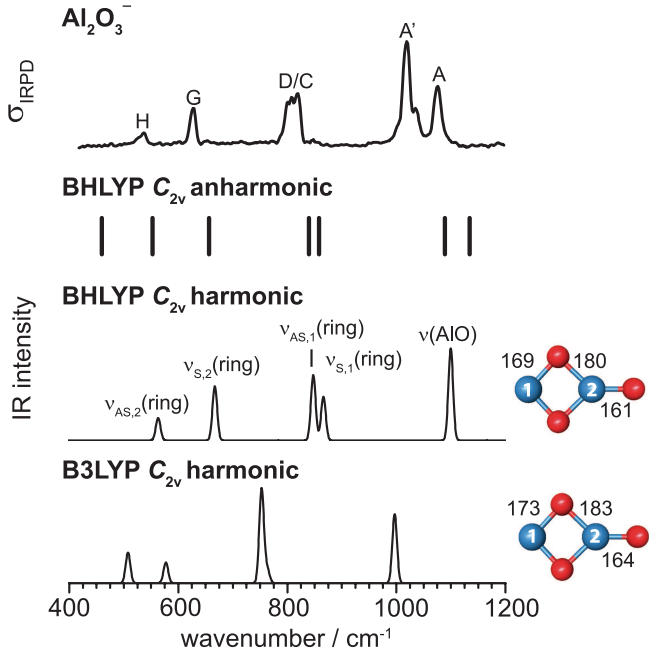

Figure 4.6: IRPD spectrum of D_2-tagged $Al_2O_3^-$ (top) compared to simulated BHLYP anharmonic frequencies and harmonic IR spectrum of the minimum energy structure (bond lengths in pm) of $Al_2O_3^-$. The B3LYP harmonic spectrum is also shown with the minimum structure. Assignments of the IR-active vibrational modes are indicated (ν: stretch, ν_S/ν_{AS}: symmetric/antisymmetric Al–$(O)_2$ stretch, '1', and '2' refer to the doubly and triply coordinated Al-atom, respectively). See Table 4.2 for band positions and assignments.

However, similar to the above discussed anharmonic spectrum of the C_s structure, the $\nu_S(AlO_2^{\text{sym. str.}}) + \nu_{AS}(O_2^{\text{str.}})$ combination band (see Table 4.1) is expected close in energy to the $\nu_{AS}(AlO_2^{\text{sym. str.}})$ fundamental and could borrow intensity from it by way of Fermi coupling. B3LYP and BHLYP also show all these bands; however, the energetic ordering of the modes at 685 and 572 cm^{-1}(Bands **C** and **D**) is exchanged. The too high $\nu_{AS}(O_2^{\text{str.}})$ frequency is also reflected in a too short bond distance in BHLYP of 155 pm, compared to 163 pm in CCSD(T) (see Fig. 4.5). We therefore assign the IRPD spectrum of AlO_4^- to an electronically closed-shell D_{2d} structure, because (i) of the better agreement of the simulated spectrum with experiment and (ii) of its much lower CCSD(T) energy.

Dialuminum oxide anions The BHLYP global minimum-energy structure of $Al_2O_3^-$ is a planar Al–(O_2)–Al ring with an exocyclic oxygen atom radical and overall C_{2v} symmetry, see Fig. 4.6. A noncyclic C_{2v} isomer is found more than 100 kJ/mol higher in energy.

Five of the six features observed in the IRPD spectrum of $Al_2O_3^-$ are reproduced by the harmonic BHLYP calculation (see Fig. 4.6). However, the most intense band $\mathbf{A}'$ at 1019 $cm^{-1}$is missing in the simulated spectrum. Band **A** corresponds to the stretching mode of

the terminal Al–O group (harmonic 1099 cm^{-1}). Bands **C**, **D**, **G**, and **H** correspond to four characteristic modes involving the Al–$(O)_2$–Al ring, respectively. These four ring modes are observed for all dialuminum oxide anions studied here. They are best visualized as symmetric and antisymmetric stretches of the Al–$(O)_2$ moieties involving one or the other Al-atom, labeled as $\nu_{S,1}$ (harmonic 866 cm^{-1}, **C**), $\nu_{AS,1}$ (harmonic 847 cm^{-1}, **D**), $\nu_{S,2}$ (harmonic 668 cm^{-1}, **G**), and $\nu_{AS,2}$ (harmonic 564 cm^{-1}, **H**) in Fig. 4.6, where the index 1 (2) refers to the doubly (triply) coordinated Al-atom in $Al_2O_3^-$. This leaves band **A′** unassigned, whose identity is revealed by the BHLYP anharmonic calculation (see Fig. 4.6). It results from Fermi type coupling involving the overtone $2\nu_{AS,2}$, which borrows intensity from the intense ν(Al–O) stretch fundamental, resulting in anharmonic frequencies calculated at 1046 cm^{-1}(**A′**) and 1089 cm^{-1}(**A**).

The predicted structures of $Al_2O_4^-$ are strongly affected by the different balance of electron delocalization versus localization across the DFT functionals. Both BHLYP and B3LYP functionals predict an Al–$(O)_2$–Al ring with two terminal oxygen atoms and similar structural parameters, see Fig. 4.7. However, B3LYP yields a higher symmetric D_{2h} structure, which corresponds to an energetically high-lying local minimum in BHLYP, while BHLYP localizes the electron on one of the two terminal oxygen atoms, resulting in a more distorted C_{2v} structure. Consequently, the predicted harmonic spectra of these two structures are characteristically different, with the higher symmetry D_{2h} species yielding a much simpler IR spectrum with three instead of seven IR-active bands. For example, the symmetric stretching mode involving the two terminal Al–O bonds is IR-forbidden for the D_{2h} structure, but IR active for the C_{2v} structure (1108 cm^{-1}). Indeed, the symmetry lowering induced by the electron localization with BHLYP results in an IR spectrum that qualitatively agrees with the experimental one (see Fig. 4.7) and allows assigning all six observed bands. Whereas bands **A** and **C** correspond to the terminal Al=O and Al–O stretching modes, respectively, bands **D**, **F**, **G**, and **H** correspond to the four characteristic ring deformation modes $\nu_{S,1}$, $\nu_{AS,1}$, $\nu_{S,2}$, and $\nu_{AS,2}$, respectively. Note the different energetic ordering of the four ring modes for $Al_2O_4^-$ compared to $Al_2O_3^-$ which results from a pronounced coupling between the ν(Al–O) and $\nu_{S,1}$ mode, and red shifts the $\nu_{S,1}$ mode below 800 cm^{-1}in $Al_2O_4^-$. Furthermore, the rise in intensity observed at the edge of the experimental IRPD spectrum around 400 $cm^{-1}$is attributed to the band onset of a ring out-of-plane bending mode.

$Al_2O_5^-$ also contains an Al–$(O)_2$–Al ring with a terminal oxygen atom bound to one Al atom, and a superoxo group on the other Al atom. This removes the coupling between the ν(Al–O) and $\nu_{S,1}$(ring) mode, observed for $n = 4$, and restores the original energetic order of the four ring modes as in $Al_2O_3^-$ (and $Al_2O_6^-$). Similar to $Al_2O_4^-$, the charge delocalization of B3LYP yields a simulated spectrum that disagrees with the experimental one. Two very similar stable structures were found with BHLYP, namely, a peroxide and the superoxide structure. Their energies differ by less than 3 kJ/mol. The computed spectrum of the superoxide structure is in better agreement with the experimental one (see Fig. 4.8), indicating that this is the structure probed in the experiment. In particular, the distance

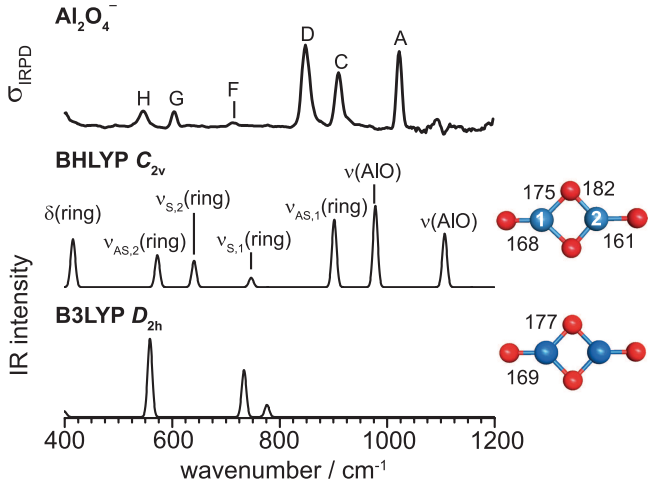

Figure 4.7: IRPD spectrum of D_2-tagged $Al_2O_4^-$ (top) compared to simulated BHLYP harmonic IR spectrum of the C_{2v} minimum-energy structure (bond lengths in pm) of $Al_2O_4^-$. The B3LYP harmonic spectrum of the D_{2h} structure is also shown (see text). See Table 4.2 for band positions and assignments.

between bands **A** and **C**, and the appearance of only the two bands **G** and **H** in the 850–500 cm^{-1}region, is well-reproduced by the calculation for the superoxide structure. The superoxide symmetric stretching mode is predicted at 1288 $cm^{-1}$with very low intensity (< 1% relative intensity). We tentatively attribute it to the weak signal observed around 1113 cm^{-1}in the experimental spectrum, labeled '*' in Fig. 4.8.

The C_{2v} structure shown in Fig. 4.9 represents the global minimum-energy structure of $Al_2O_6^-$ on the BHLYP PES. This structure is derived from that of $Al_2O_5^-$ by replacing the single oxygen atom with a peroxo group. Hence, this structure contains a stretched peroxo (155 pm) and a superoxo (132 pm) group. As for $Al_2O_4^-$, B3LYP yields a charge-delocalized D_{2h} structure, which represents an energetically higher lying minimum on the BHLYP PES.

Comparison of the simulated harmonic spectra with the experimental IRPD spectrum (see Fig. 4.9) supports an assignment to the C_{2v} structure. Bands **B** and **F** correspond to the Al–O_2 and O–O stretching modes involving the peroxo group. Bands **C**, **D**, **G**, and **H** are the four in-plane ring deformation modes $\nu_{S,1}$, $\nu_{AS,1}$, $\nu_{S,2}$, and $\nu_{AS,2}$, respectively. The superoxo stretching mode is calculated at 1287 $cm^{-1}$with little IR activity (< 1% relative intensity). Similar to $Al_2O_5^-$, weaker features are indeed observed to the blue of the more intense IR transitions in the experimental spectrum. Band **E** has no counterpart in the simulated IR spectrum [176].

Discussion

The common features observed in the IR spectra of small aluminum oxide clusters can be grouped in four spectral regions. Superoxo stretching modes are found at highest energies

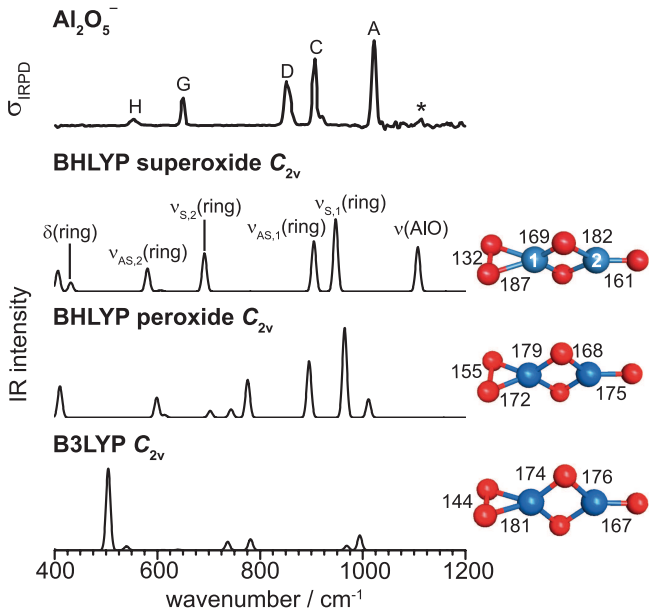

Figure 4.8: IRPD spectrum of D_2-tagged $Al_2O_5^-$ (top) compared to the simulated BHLYP harmonic IR spectrum of the superoxide C_{2v} minimum-energy structure (bond lengths in pm) of $Al_2O_5^-$. The BHLYP harmonic spectrum of the peroxide C_{2v} structure and the B3LYP harmonic spectrum of the C_{2v} structure are also shown (see text). See Table 4.2 for band positions and assignments. '*' denotes the weak absorption for O–O stretching.

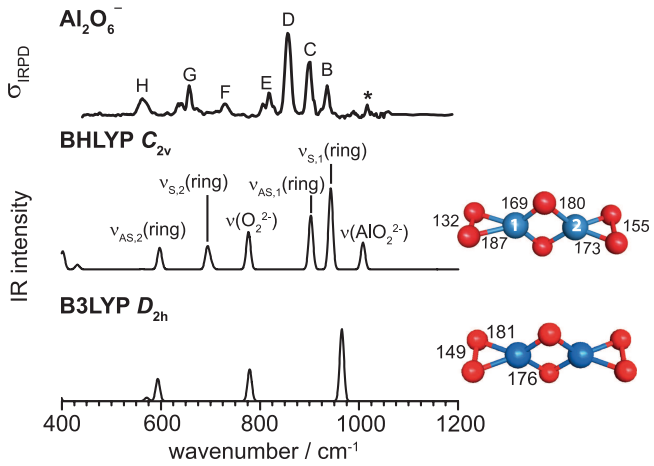

Figure 4.9: Experimental IRPD spectrum of D_2-tagged $Al_2O_6^-$ (top) compared to the simulated BHLYP harmonic IR spectrum of the C_{2v} minimum-energy structure (bond lengths in pm) of $Al_2O_6^-$. The B3LYP harmonic spectrum of the D_{2h} structure is also shown (see text). See Table 4.2 for band positions and assignments. '*' denotes the weak absorption for O–O stretching.

(1120–1010 cm^{-1}), but with very little IR intensity, complicating their identification. Peroxo modes are considerably lower in energy (850–570 cm^{-1}) and are predicted with slightly more IR intensity. Terminal Al–O stretching modes are found in the intermediate energy region (1140–960 cm^{-1}). The vibrational frequencies of superoxo, peroxo, and terminal Al–O groups are summarized in Table 4.3.

Table 4.3: Experimental and calculated harmonic vibrational frequencies (in cm^{-1}) of different oxygen species in $AlO_{1\text{-}4}^-$ and $Al_2O_{3\text{-}6}^-$, including irreducible representations (Irrep.) of the delocalized normal modes.

Species	Cluster	Expt.	Irrep.	BHLYP[a]	Bond Length
Superoxo	$Al_2O_5^-$	1113	a_1	1202	132
	$Al_2O_6^-$	1016	a_1	1202	132
Terminal Al–O	AlO_2^-	1134	σ_u	1159	163
	AlO_3^-	1098	a_1	1101	161
	$Al_2O_3^-$	1076	a_1	1026	161
	$Al_2O_4^-$	1024	a_1	1035	161
	$Al_2O_5^-$	1022	a_1	1032	161
	AlO^-	962	σ	971	164
Peroxo	$Al_2O_6^-$	729	a_1	726	155
	AlO_3^-	842	a_1	820	155
	AlO_4^-	572	b_2	716[b]	155[b]

[a]Frequencies are scaled by 0.9339 (from Tab. II of Ref. [218]).
[b]CCSD(T) values: 587 $cm^{-1}$and 163 pm.

The common structural motif of dialuminum oxide clusters is a four-membered Al–$(O)_2$–Al ring to which additional O-atoms add in an exocyclic manner, similar to other metal oxide clusters, *e.g.* , vanadium oxides [223]. This ring is characterized by four IR active in-plane ring deformation modes between 910 and 530 cm^{-1}. The predicted energetic ordering is typically $\nu_{S,1}(\text{ring}) > \nu_{AS,1}(\text{ring}) > \nu_{S,2}(\text{ring}) > \nu_{AS,2}(\text{ring})$ with wavenumber ranges of 910–710 cm^{-1}($\nu_{S,1}$), 860–800 cm^{-1}($\nu_{AS,1}$), 650–600 ($\nu_{S,2}$), and 560–530 cm^{-1}($\nu_{AS,2}$). Out of plane bending modes are predicted below 400 cm^{-1}.

The electronic and geometric structures of the aluminum oxide clusters $Al_2O_{3\text{-}6}^-$ are governed by localization of the excess charge. In many cases, there is a competition between more symmetric structures with delocalized charge and less symmetric structures with more localized charge. As a consequence of charge localization, the electronic structures of the open-shell clusters $Al_2O_n^-$ are characterized by mixed valence [205]. Hence, the calculated electronic structure is very sensitive towards the amount of exact exchange that is mixed into the density functional. This is well known in the literature [205, 224] and has been observed before, *e.g.* , with the size-induced d-electron localization in polyhedral vanadium oxide anion

cages [225] and the formation of electron holes in solid oxides [226, 227]. The crossover point between DFT functionals with increasing amount of exact exchange for the physically correct description of the electronic structure depends on the observed system. In the present study, standard GGA functionals, and also hybrid functionals with the standard amount of Fock exchange, *e.g.* , 20% for B3LYP, incorrectly predict the electronic structure to be delocalized and the geometric structure to be D_{2h} symmetric (if possible by stoichiometric composition). However, BHLYP (50% exchange) localizes the charge leading to a C_{2v} symmetric distortion. The surplus electron is localized on a terminal O-atom or O_2^- group, as indicated by bond lengths and population analyses and confirmed by the agreement of simulated and experimental spectra.

With the exception of AlO_3^-, the BHLYP functional (50% Fock exchange) provides a qualitatively correct description of all systems studied, although the calculated harmonic wavenumbers show a rather large rms deviation of 85 $cm^{-1}$for the 33 assigned wavenumbers in Tables 4.1 and 4.2. Applying the global scale factor of 0.9339 [218] the rms deviation is reduced to 45 cm^{-1}. If we use our data to derive a global scale factor, we obtain 0.919 with the rms value of 42 cm^{-1}.

4.1.5 Summary

We have studied the structure and vibrational spectra of small aluminum oxide cluster anions. The structures were determined computationally by using a genetic algorithm for finding the global minimum and subsequently confirmed by comparison of the predicted spectra with measured IRPD spectra. The mononuclear species $AlO_{1,2}^-$ are linear, closed shell molecules. AlO_3^- has a planar, triangular structure with a peroxo group, and AlO_4^- is a closed-shell D_{2d} symmetric molecule with two overstretched peroxo groups. The binuclear species $Al_2O_{3\text{-}6}^-$ are all open-shell doublets and oxygen centered radicals. The common motif is a four-membered Al–(O_2)–Al ring, with one or two terminal oxo groups (n = 3, 4), or with oxo/superoxo (n = 5) and peroxo/superoxo groups (n = 6). The electronic structure is characterized by the localization of the unpaired electron on one side of the cluster, lowering its symmetry from D_{2h} to C_{2v} (for n = 4, 6). A correct description requires the use of density functionals with a large amount of Fock exchange such as BHLYP, otherwise the electron will delocalize and the vibrational spectra will not be reproduced.

4.2 Gas Phase Vibrational Spectroscopy of $(Al_2O_3)_{1-6}AlO_2^-$*

4.2.1 Introduction

The thermodynamically most stable alumina polymorph is α-Al_2O_3 (corundum), but the metastable γ-, η-, θ- and δ-Al_2O_3 phases are also quite common [228, 229]. These various

*Chapter based on manuscript in preparation by Xiaowei Song, Matias R. Fagiani, Sandy Gewinner, Wieland Schöllkopf, Knut R. Asmis, Florian A. Bischoff, Fabian Berger and Joachim Sauer

allotropic forms of aluminas have attracted much attention due to their use in various technological applications [230]. They are also a major component of mineral dust aerosols, which influence atmospheric processes like raindrop formation and ice nucleation [231, 232]. The structural variability of aluminas raises the question, how the structure of stoichiometric Al_2O_3 materials depends on their size, when comparing bulk-like aggregates with thin films, nanoparticles and smaller gas phase clusters. Here, we address this question on the atomic scale by studying the vibrational spectra of size-selected aluminum oxide clusters with three to 33 atoms. Inferences on the atomic structure are made from comparison of the experimental spectra with predictions from density functional theory (DFT) calculations on minimum energy structures.

4.2.2 Experimental methods

Infrared photodissociation experiments are conducted with the 10 K setup described in Chapter 3. Aluminum oxide cluster anions, particularly $(Al_2O_3)nAlO_2^-$ with $n < 3$ are generated using a magnetron sputtering source as described in Section 4.1.2 (see also Section 3.2.3). For larger clusters (n=4-6) a pulsed laser vaporization source was used (see Section 3.2.2). The second harmonic output of 50 Hz Nd:YAG laser is focused onto a moving aluminum rod, and the resulting plasma is entrained in a pulse of 0.5% O_2 in He from a General Valve. Clusters are formed during subsequent expansion through a clustering channel. The cluster ion beam passes through a 4 mm skimmer, is then collimated in a decapole ion guide filled with He as buffer gas and mass-selected using a quadrupole mass-filter. Mass-selected ions are accumulated in a linear radio frequency ring-electrode ion-trap held at 16-30 K and continuously filled with D_2 gas as a buffer gas. Trapped ions are internally cooled by collisions with the buffer gas and messenger-tagged with D_2 via three-body collisions: $(Al_2O_3)_nAlO_2^-$ $+2\ D_2 \rightarrow (Al_2O_3)_nAlO_2^- \cdot D_2 + D_2$. , enhancing the formation of weakly bound ion-D_2 complexes [104]. After an ion trap fill time of 199 ms all ions are extracted from the ion trap and focused in the center of the extraction region of a time-of-flight (TOF) mass spectrometer. There they are irradiated by an intense and wavelength-tunable IR laser pulse. When resonant with a vibrational transition parent ions absorb a photon and eventually lose one or more messenger molecules via intramolecular vibrational predissociation. The IR free electron laser FHI FEL (see section 3.5.1 and references therein) is used as a source for intense and tunable IR radiation. The wavelength of the IR radiation is tuned from 8 to 25 μm with a bandwidth of ca. 0.2% root mean square of the central wavelength and pulse energies of $\sim$ 1 to 12 mJ. IR spectra are recorded by averaging over 90 TOF mass spectra per wavelength step. The intensities are normalized to the total number of parent and fragment ions, to account for fluctuations in the total ion signal (see Section 3.4).

4.2.3 Computational methods*

Firstly, the potential energy surface (PES) was searched by a genetic algorithm (GA) using the BP86 functional together with the split-valence polarized basis set SVP (denoted BP86/def2-SVP) to find the global minimum structures. The GA run was repeated 3 times for 500 structures, after which convergence was checked. Then the ten lowest energy structures of the GA were refined using the B3LYP functional with the def2-TZVPP basis set (Al: 5s5p3d1f, O: 5s3p2d1f) in the closed-shell Kohn-Sham formalism. This basis set was diffuse enough to account for the anionic character of the clusters. No qualitative changes in the geometric and electronic structure were found after refinement. The only exception from this protocol was $(Al_2O_3)_4AlO_2^-$, where an educated guess from the corresponding cationic structure $(Al_2O_3)_4AlO^+$ yielded the global minimum while the GA search failed. All optimized structures were checked for imaginary frequencies and for triplet instabilities. The simulated spectra are derived from computed stick spectra and convoluted with a 10 cm^{-1}fwhm Gaussian line shape function to account for rotational band contours and as well as the spectral width of the laser pulse.

4.2.4 Results and discussion

The vibrational spectra of the clusters anions $(Al_2O_3)_n$ AlO_2^- with $n = 0$ to 6, measured by IRPD spectroscopy of the corresponding D_2-tagged species formed by three-body collisions in a cryogenic ion trap held at ≤ 30 K, are shown in the upper part of Fig. 4.10. The $n = 0$ spectrum was reproduced from Ref. [27]. The cluster stoichiometry was chosen such that it converges towards that of bulk alumina for large n, but at the same time compensates for the additional unpaired electron by including a formally fully oxidized and electronically closed-shell AlO_2^- moiety. The charge is required for mass selection of the clusters but in this way a system with an even number of electrons is obtained and effects related to the radical nature of $(Al_2O_3)^-$ anions are avoided, similar to the previous study on $(Al_2O_3)_nAlO^+$ cations [28].

Substantial IR activity above 1000 $cm^{-1}$is only observed in the spectra of the two smallest clusters ($n < 2$). This range is characteristic for stretching modes of terminal Al–O groups [27]. On the other hand, the clusters with $n \geq 2$ reveal characteristic absorptions bands in the spectral range from 1000 cm^{-1}down to ~ 750 cm^{-1}. The spectra of all clusters with $n > 0$ show multiple absorption features below 750 cm^{-1}, but these are typically less intense than the bands observed at higher energies.

Also shown in Fig. 4.10 are vibrational spectra of larger Al_2O_3 aggregates. These include the IR resonance-enhanced multiple photon ionization (IR-REMPI) spectra of neutral $(Al_2O_3)_{28}AlO$ and $(Al_2O_3)_{53}AlO$ as well as a simulated spectrum, derived from the optical constants of amorphous Al_2O_3, for spherical particles in the Rayleigh limit [163, 233–236].

*Calculations were performed by Florian A. Bischoff and Fabian Berger in the group Prof. Joachim Sauer at the Institut für Chemie, Humboldt-Universität zu Berlin.

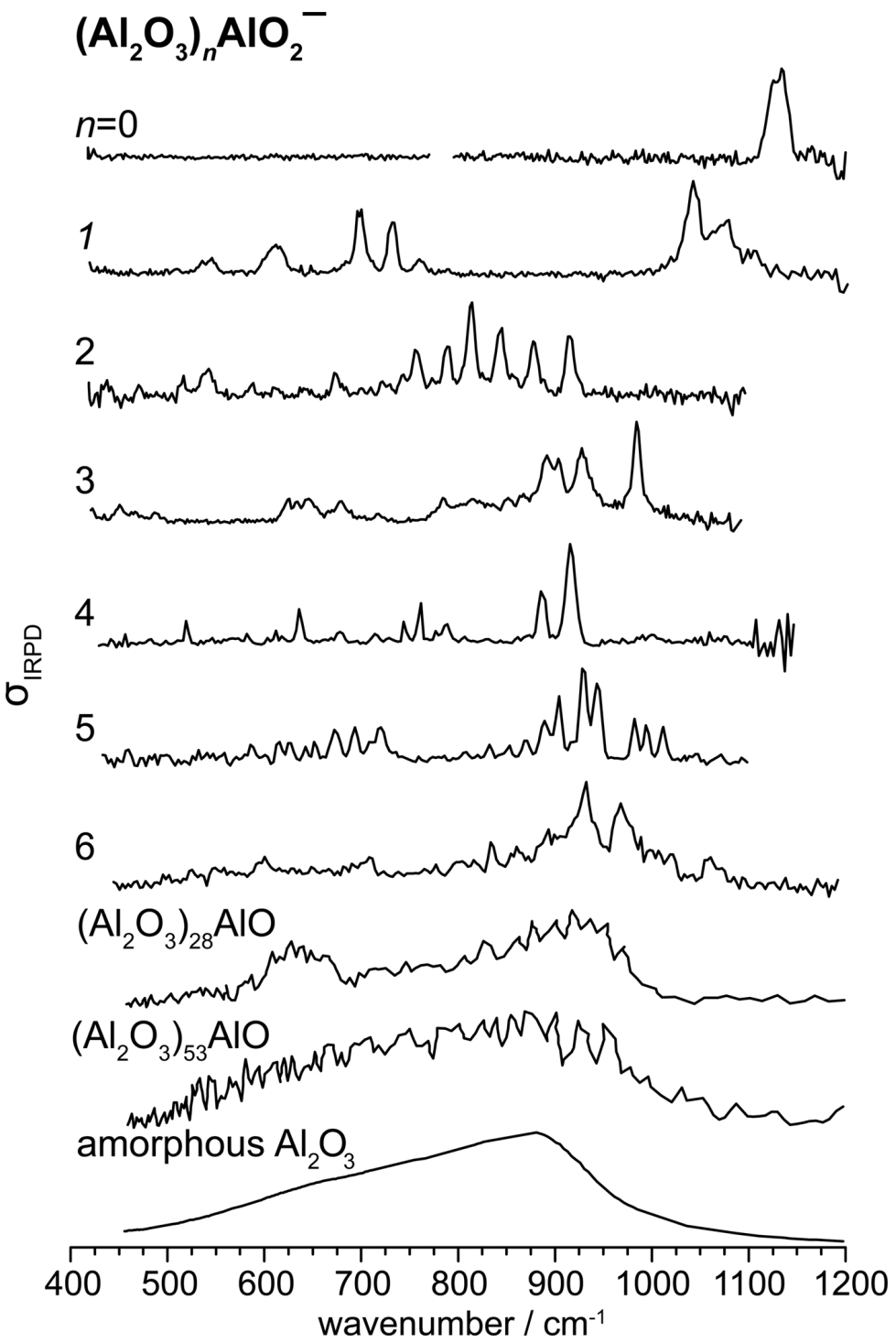

Figure 4.10: Experimental IRPD spectra of D_2-tagged $(Al_2O_3)_{0\text{-}6}AlO_2^-$ anions compared to the IR-REMPI spectra [233] of neutral gas-phase $(Al_2O_3)_{28,53}AlO$ and the IR spectra of amorphous Al_2O_3 particles, derived from the optical constants of bulk aluminum oxide for spherical particles in the Rayleigh limit [234]. The $n = 0$ spectrum is reproduced from Ref. [27]. See Fig. A.1 and Table A.1 for band positions.

The latter two spectra have in common that they show a broad absorption maximum centered around $\sim$ 900 cm^{-1}with a pronounced tail that extends to $\sim$ 500 cm^{-1}. The similarity of these spectra suggests that aluminum oxide particles with more than $\sim$ 100 atoms are amorphous-like [235]. Compared to the IRPD spectra of the smaller $(Al_2O_3)_nAlO_2^-$ clusters probed here, distinct differences but also similarities are apparent, suggesting that the onset for the formation of unordered $Al_2O_3^-$ based structures may lie well below $n = 28$. The IRPD spectra for $n < 3$ have little in common with those of the larger aggregates. However, a trend can indeed be observed in the spectra of the larger clusters probed here. The strongest IR activity for the $n \geq 3$ clusters accumulates around 900 cm^{-1}. Moreover, the IRPD spectra of $n = 5$ and $n = 6$ show an intensity distribution of their (discrete) absorption features in this spectral region, which is not unlike the intensity profile towards the higher energies of the larger amorphous particles. This similarity may be fortituous, given the small size and hence low average coordination numbers and high surface to volume ratio of the $n = 5$, 6 clusters, but may also be taken as the onset of the evolution of structural motifs similar to those in the larger aggregates. On the other hand, the striking simplicity of the $n = 4$ spectrum hints at a higher symmetry structure, and its spectrum in fact looks more like the high resolution electron-energy-loss (HREELS) spectrum of an Al_2O_3/NiAl thin film [234].

Additional structural information on the $(Al_2O_3)_n(AlO_2)^-$ clusters can be gained from a comparison to the IRPD spectra of the analogous cationic clusters, $Al_2O_3(AlO)^+$, which were studied previously up to $n = 4$ using a similar technique (see Fig. A.2) [28]. The IRPD spectra of the anion and the corresponding cation for $n = 2$ are strikingly different, suggesting an $Al_5O_8^-$ structure that differs substantially from the conical-like $Al_5O_7^+$ structure identified previously [28]. In contrast, the IRPD spectra for $n = 3$ are quite similar, indicating comparable structures. For $n = 1$ and $n = 4$, the situation is intermediate, suggesting different structures containing similar motifs.

In Fig. 4.11 global minimum structures of bare $(Al_2O_3)_{1\text{-}6}AlO_2^-$ clusters, obtained by DFT calculations (for computational details see below), are compared with the corresponding experimental IRPD spectra of the D_2-tagged species. The minimum energy structures are also shown and labeled with *n-x*, where *n* refers to the number of Al_2O_3 units in the cluster and *x* is an index indicating the energetic ordering. Up to $n = 4$, we find satisfactory agreement between the experimental IRPD spectrum and the simulated spectrum of the lowest minimum-energy isomer. Moreover, the spectra of the higher energy isomers up to $n = 4$ do not agree with the measured IRPD spectra, supporting an assignment to the structures shown in Fig. 4.11 (see Figs. A.3 to A.6). Structure **1-1** is in agreement with the only previously predicted structure of this clusters series, namely a kite-like geometry of C_{2v} symmetry with two characteristic edge-sharing four-membered rings with two terminal Al–O groups [186]. For $n > 4$, the simulated spectra of the lowest energy structure accounts for most but not all of the observed IRPD bands, suggesting that additional low-energy isomers contribute to the experimental IRPD spectra of the larger clusters (see Figs. 4.11, A.7 and A.8). Note that the increasing number of structural isomers with similar energies with

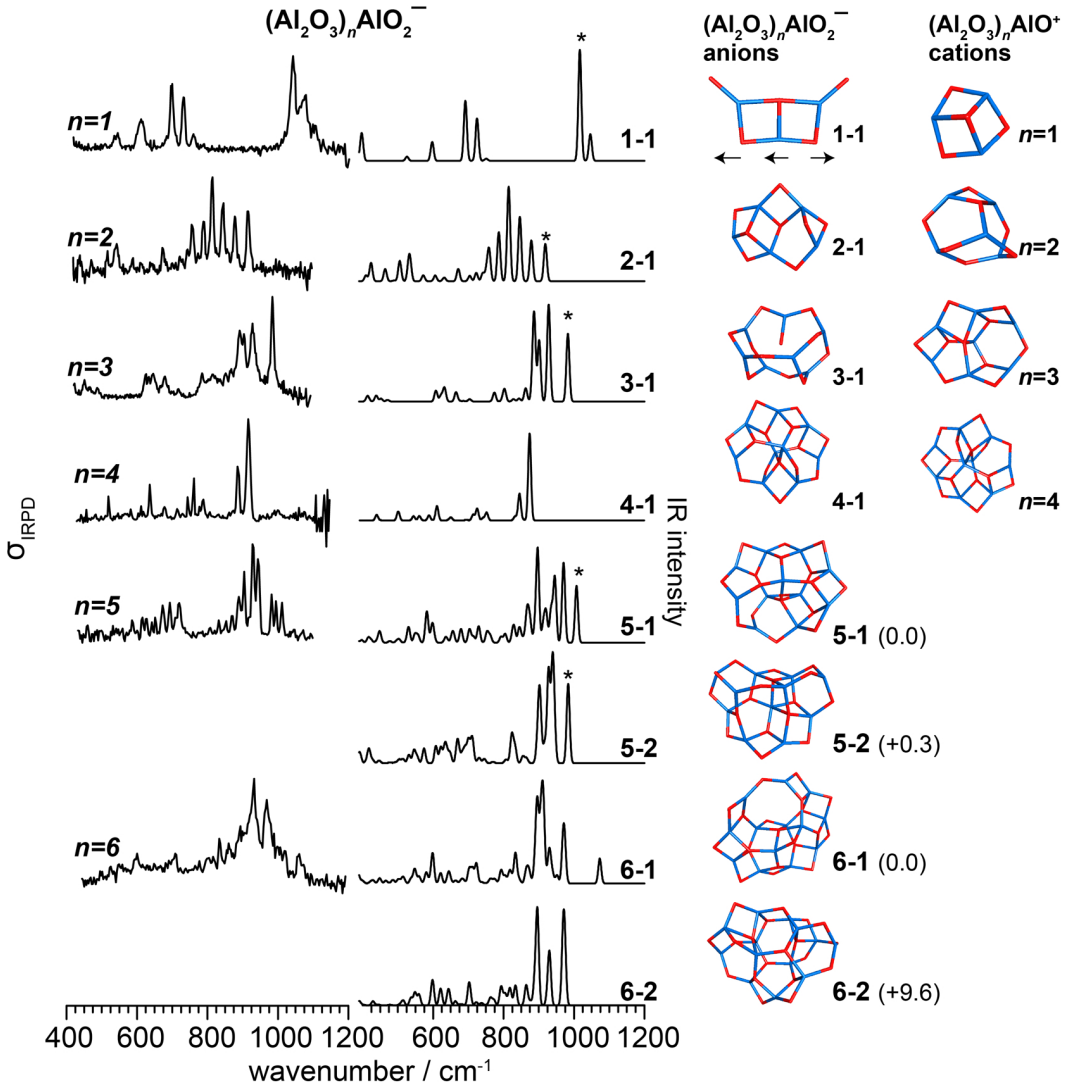

Figure 4.11: Experimental IRPD spectra (1st column) of $(Al_2O_3)_nAlO_2^-{\cdot}D_2$ and harmonic IR spectra (2nd column) of low-energy isomers of $(Al_2O_3)_nAlO_2^-$ for $n = 1$–6 (3rd column). Structures and relative energies (in kJ/mol) are shown and compared with their cationic analogs $(Al_2O_3)_nAlO^+$ for $n = 1$–4 from Ref. [28]. Bands labeled with an asterisk '*' in the calculated spectra are assigned to normal modes localized on the T-shaped AlO_3 motif. See Table 4.5 for band positions.

increasing cluster size complicates the localization of the global minimum structure, making the structure assignment for $n > 4$ of tentative nature.

Table 4.4 shows the average O and Al coordination numbers and the relative coordination number distribution for the O and Al atoms for the low-energy isomers of the $(Al_2O_3)_nAlO_2^-$ clusters. In the following, coordination numbers are indicated as superscripts, e.g. Al^4 refers to a four-fold coordinated Al-atom. The increasing resemblance of the cluster spectra with those of larger aggregates and that of bulk amorphous alumina with increasing cluster size (see Fig. 4.10) implies that also the cluster structures and hence the average coordination numbers and bond lengths should become more and more similar to those of bulk Al_2O_3.

With the exception of structure **3-1**, the average coordination numbers increase with cluster size, from 1.8 (O) and 3.0 (Al) in **1-1** to 2.5 (O) and 3.85 (Al) in **6-1**, approaching the coordination numbers of amorphous Al_2O_3, 2.1–3.0 (O) and 4.1–4.8 (Al) and of the thin film, 3.0 (O) and 3.9 (Al). In the crystalline bulk phases, the coordination numbers are much higher, between 3.33 and 4 for O, and between 5 and 6 for Al.

Table 4.4: O/Al stoichiometric ratio, average O and Al coordination numbers, and O and Al relative coordination number distribution for low-energy isomers of $(Al_2O_3)_nAlO_2^-$ with $n = 1$–6 compared to different solid alumina polymorphs.

Isomer	**O/Al ratio**	**Coordination number**									
		O^{avg}	**Al^{avg}**	**relative distribution**							
				O^1	**O^2**	**O^3**	**O^4**	**Al^3**	**Al^4**	**Al^5**	**Al^6**
1-1	1.67	1.80	3.00	0.40	0.40	0.20	0	1	0	0	0
2-1	1.60	2.25	3.60	0	0.75	0.25	0	0.40	0.60	0	0
3-1	1.57	2.09	3.29	0	0.91	0.90	0	0.71	0.29	0	0
4-1	1.56	2.36	3.67	0	0.64	0.36	0	0.33	0.66	0	0
5-1	1.54	2.41	3.73	0	0.65	0.29	0.06	0.27	0.73	0	0
5-2		2.47	3.82	0	0.65	0.23	0.12	0.27	0.64	0.09	0
6-1	1.54	2.50	3.85	0	0.55	0.40	0.05	0.15	0.85	0	0
6-2		2.50	3.85	0	0.60	0.30	0.10	0.15	0.85	0	0
amorphous alumina	1.53[a]	2.10–3.00	4.10–4.80[b]								
thin film[c]	1.3	3	3.9	0	0	1	0	0.40	0.30	0.30	0
θ-alumina[d]	1.5	3.33	5.00	0	0	0.66	0.33	0	0.50	0	0.50
γ-alumina[e] **(spinell)**	1.5	3.33	5.20	0	0	0.66	0.33	0	0.40	0	0.60
γ-alumina[f] **(krokidis)**	1.5	3.66	5.50	0	0	0.66	0.33	0	0.25	0	0.75
κ-alumina[g]	1.5	3.50	5.50	0	0	0.50	0.50	0	0.25	0	0.75
α-alumina[h]	1.5	4	6	0	0	0	1	0	0	0	1

[a] Ref. [237]. [b] Refs. [235, 238]. [c] Ref. [239]. [d] Ref. [240]. [e] Ref. [241]. [f] Refs. [242, 243]. [g] Ref. [244]. [h] Ref. [245].

A comparison of the cation structures of the $(Al_2O_3)_nAlO^+$ series (see Fig. 4.11) to those

of the corresponding anions $(Al_2O_3)_nAlO_2^-$, which differ formally by an O_2^- unit, shows more similarities than is expected from the comparison of the IRPD spectra (see Fig. A.2). Indeed, all four cluster pairs (n = 1–4) share characteristic structural motifs. For $n = 1$ these are the two edge-sharing four-membered rings containing three three-fold coordinated Al-atoms (Al^3, see Tab. 4.4). The additional O-atom leads to an opening of the third edge-sharing four-membered ring in the cation, which is replaced by two terminal O-atoms (O^1). For $n = 2$, three of the five Al^3 centers in the cation are replaced by Al^4 centers with the additional O-atom adding in a triply-coordinated site. For $n = 3$ and $n = 4$ the extra oxygen-atom adds to the center of the conical structure of the cation, replacing the hollow character by a 3D network structure in the anion. Both of these anion structures are unique and quite different from the other structures. Even though the **3-1** structure only has C_1 symmetry, it is rather regular in that it is only composed of six-membered rings with ten O^2, one O^3, five Al^3 and two Al^4 atoms. The absence of smaller rings leads to unusually low average coordination number of $O^{avg} = 2.1$ and $Al^{avg} = 3.3$ (see Tab. 4.4) in this case. On the other hand, **4-1** exhibits a highly symmetric C_{3v} structure, as the simplicity of the corresponding IRPD spectrum already suggested. As a result of the five O^3- and six Al^4-centers, compared to one and two, respectively, for **3-1**, structure **4-1** also exhibits the narrowest bond distance distribution of 170.5–189.9 pm (see Table A.2). Finally, the low-energy structures **5-1**, **5-2**, **6-1** and **6-2**, which are assigned to the measured IRPD spectra, are considerably more irregular and indeed their spectra appear more amorphous-like. These clusters are the smallest that contain four-fold coordinated O atoms (O^4) and one of them (**5-2**) already contains a five-fold coordinated Al atom (Al^5).

Table 4.5: Experimental and calculated vibrational wavenumbers (in cm^{-1}) and Al^3–O^2 bond lengths (in ppm) of the characteristic T-shaped $Al(–O)_3$ motif in $(Al_2O_3)_nAlO_2^-$ clusters. The corresponding bands are marked with an asterisk in Fig. 4.11.

Isomer	Wavenumber		Bond length	
	exp.	cal.	Al^3–O^2	average
1-1	1042	1024	168.0, 168.0	168.0
5-1	1011	998	168.3, 169.7	169.0
5-2	994	975	168.1, 170.3	169.2
3-1	985	974	169.3, 169.3	169.3
2-1	916	911	170.7, 171.6	171.2

Inspection of the normal modes of the assigned structures reveals that a general categorization of these is difficult, mainly due to their delocalized nature. Only the assignment of the higher energy modes is straightforward. For $n = 1$ the highest energy IRPD band at 1074 cm^{-1}can be assigned to the quasi-degenerate symmetric and antisymmetric stretching modes of the two terminal Al–O oscillators, calculated at 1075 $cm^{-1}$and 1072 cm^{-1}, respectively. Interestingly, the second band at 1042 cm^{-1}, is thus not a terminal Al–O stretch, but due to

an unexpectedly high-lying antisymmetric stretching mode of the O^2–Al^3–O^2 moiety. Similar modes to this one are also present in some of the larger clusters. They are indicated by an asterisk in Fig. 4.11 and their characteristic parameters are summarized in Table 4.5. Note, in the absence of terminal Al–O bonds, *i.e.* for $n > 1$, this mode corresponds to the highest energy IR-active mode, when this structural motif is present, *i.e.* for $n = 2$, 3 and 5, and scales inversely with the average Al^3–O^2 bond length (see Table 4.5).

Table 4.6: Correlation between Al–O bond coordination number and its bond length in pm.

Al coordination	O coordination 2	3	4	γ-Al_2O_3	amorphous Al_2O_3	α-Al_2O_3
3	171.3	178.2				
4	173.5	185.5	193.7	178[a]	180[b], 171-179[c]	
5		180.2	201.6			
6				184-224[a]		186-196[d]

[a] Ref. [246]. [b] Ref. [238]. [c] Liquid Al_2O_3. Ref. [247]. [d] Ref. [248].

The average bond lengths for a given pair of Al/O-atom coordination numbers are summarized in Table 4.6 (see Table A.2 for a more detailed table for each isomer). The trend shows increasing bond lengths with increasing coordination numbers, with the only exception of Al^5O^3. It should be noted that the bond distances show a considerable spread, *e.g.* the bonds of the fairly common Al^4–O^3 coordination vary between 173.4 pm (isomer **5-1**) and 215.3 pm (isomer **2-1**). The literature values for the amorphous Al_2O_3 and γ-Al_2O_3 are in line with the present results. The coordination numbers of Al and O in amorphous Al_2O_3 is primarily Al^4-O^3 (Ref. [247]) and Al^4-$O^{unknown}$ (Ref. [238]), whereas in γ-Al_2O_3 both tetrahedral and octrahedral sites are partially filled [246]. However, in α-Al_2O_3 (corundum) only octahedral sites are filled with coordination Al^6O^4, with reduced bond lengths compared to γ-Al_2O_3 and to the larger clusters in the present work.

In conclusion, the structures assigned to the $(Al_2O_3)_nAlO_2^-$ with n = 1–6, with the exception of that of $n = 3$, all contain edge-sharing and corner-sharing four-membered rings as a common structural motif. The average coordination numbers of O and Al increase with cluster size, except for $n = 3$, and approach those reported for amorphous alumina[249]. With the notable exception of $n = 4$, which has C_{3v} symmetry, the larger clusters exhibit no long-range ordering and even larger clusters are thus expected to approach the properties of amorphous Al_2O_3 particles quickly.

4.3 Dissociative Water Adsorption by $Al_3O_4^+$ in the Gas Phase: A Combined Cryogenic Ion Vibrational Spectroscopy and Density Functional Theory Study*

4.3.1 Introduction

Alumina based materials are used in many technological and environmental applications, *e.g.* as catalysts and catalyst support, coatings, abrasives and nanosensors [5, 162, 250]. In these applications the interaction of the alumina surfaces with water is ubiquitous and its understanding is crucial in predicting the evolution of their properties with time [251, 252]. However, our molecular-level understanding of alumina-water interactions is limited, in particular, because of the multiscale nature of the processes involved as well as difficulties in preparing clean surfaces with a well-defined surface termination. Such limitations can be overcome when studying these surfaces in ultrahigh vacuum. The dissociative adsorption of individual water molecules on alumina surfaces was recently characterized using vibrationally resonant sum frequency generation (VSF) spectroscopy combined with electronic structure theory [9, 10, 253]. These pioneering studies provide valuable new insight into the water/Al_2O_3 interaction, but also revealed some discrepancies between experimental observations and theoretical predictions. Complementary experimental information on the vibrational signature of water adsorption can be obtained from studies on isolated aluminum oxide aggregates in the gas phase. The advantage of investigating mass-selected gas phase clusters lies in the high selectivity and sensitivity achievable experimentally, the absence of any interfering interactions with their environment together with the feasibility of performing higher level computations to test and benchmark theoretical models. Here, we use cryogenic ion vibrational spectroscopy in combination with density functional theory (DFT) computations to investigate the adsorption of up to four water molecules by $Al_3O_4^+$ cations in the gas phase.

While much spectroscopic work has been performed on bare aluminum oxide clusters in the gas phase, see *e.g.* Sections 4.1 and 4.2, Ref. [27, 28, 176, 181, 182] and references therein, previous experimental studies on their interaction with water are scarce. Jarrold and coworkers used anion photoelectron spectroscopy to investigate the reaction of $Al_3O_3^-$ and $Al_5O_4^-$ with water [180, 254, 255]. They found dissociative water adsorption to be energetically favored over physisorption, which was supported by subsequent computational studies of the underlying reaction paths [256–259]. Subsequently, Schwarz and coworkers studied the reactivity of the radical $Al_2O_7^+$ towards water using mass spectrometry [256]. Here, we focus on studying the reaction of $Al_3O_4^+$ with water vapor under multiple collision conditions and near room temperature using vibrational spectroscopy. This particular cluster stoichiometry was chosen to avoid highly reactive radicals by nominally obtaining fully oxidized cluster cations without unpaired electrons. This has been confirmed experimentally, revealing that

*Chapter based on manuscript in preparation by Matias R. Fagiani, Xiaowei Song, Sreekanta Debnath, Sandy Gewinner, Wieland Schöllkopf, Knut R. Asmis, Florian A. Bischoff, Fabian Müller and Joachim Sauer.

$Al_3O_4^+$ has a C_{3v} conical geometric and closed-shell electronic structure [28].

4.3.2 Experimental methods

IRPD experiments are conducted on the 10 K setup described in Chapter 3. A pulsed beam of cationic aluminum-oxide clusters is formed by laser vaporization with the suorce described in Section 3.2.2 using the dual-gas channel source block. Vaporization is induced by focusing (30 cm focal length) the second harmonic output (532 nm) of a pulsed 50 Hz Nd:YAG laser (*Quantel*, Q-smart 100) onto the surface of a moving metal-rod target. The ablated ions are then entrained in a carrier gas pulse of 0.16 % O_2 seeded in helium, and aluminum-oxide clusters $Al_mO_o^+$ are subsequently formed through expansion in a clustering channel ending with a cone-shaped nozzle held at a temperature of 270 K. In order to obtain a stable cluster signal, the turning speed of the rod is set to ~ 3 turns per minute and laser pulse energies of up to 4 mJ are applied. Using a backing pressure of ~ 5.5 bar, $Al_mO_o^+$ clusters are efficiently produced in the mass range from 100 to 500 amu., as displayed in Fig. B.1 (top panel). The time delay between firing of the laser and opening of the pulsed valve is adjusted to optimize the formation of $Al_3O_4^+$ clusters. A flow of helium at 1.5 bar passes through a bubbler containing D_2O at room temperature (294 K). Water vapor pressure mixes with He and the gas mixture is injected with the second pulsed valve in the source block expanding through the separated gas channel. $Al_mO_o^+(D_2O)_n$ complexes with $n \leq 6$–8 are efficiently formed. The beam of ions passes a 4 mm diameter skimmer, is then collimated in a RF buffer-gas-filled decapole ion-guide, and ions of interest are selected according to their mass/charge ratio using a quadrupole mass-filter. The mass-selected beam is focused into a cryogenically-cooled RF ring electrode ion-trap. The trap is continuously filled with He (1% D_2/He) buffer gas at a trap temperature of 13–15 K, which allows for the accumulation and thermalization of the trapped ions. Inside the ion trap, $Al_3O_4^+(D_2O)_n$ ions undergo three-body collisions with the buffer gas, which promote the formation of weakly bound ion–He (ion-D_2) complexes. After an ion trap fill time of 199 ms all ions are extracted from the ion trap and focused in the center of the extraction region of the TOF mass spectrometer, where they are irradiated by an intense and wavelength-tunable IR laser pulse. When resonant with a vibrational transition, the parent ions can absorb a photon, eventually leading to loss of one or more messenger molecules via intramolecular vibrational predissociation. For the larger water complexes ($n > 2$) ion-messenger complex formation is not efficient and the vibrational spectra are measured via IRMPD.

The IR free electron laser at the FHI (see Section 3.5.2) is used as a light source for the wavelength from 3.3 to 5 (IRMPD) and from 8.3 to 23 μm with a bandwidth between 0.3 and 0.6 % root mean square of the central wavelength. Laser light for IRPD experiments in the O–D stretch region, from 3.3 to 4 μm, is produced by an OPO/OPA laser system (double OPO, see Section 3.5.3). The infrared photodissociation cross sections σ_{IRPD} is obtained as described in Section 3.4. The IRMPD vibrational spectrum is obtained by monitoring the

fragment originating from the loss of one D_2O molecule. Each spectrum is averaged over at least 60 measurements.

4.3.3 Computational methods*

Low energy isomers of $Al_3O_4^+$ $(H_2O)_n$ ($n = 0$–4) are generated using a genetic algorithm (GA) and employing the BP86 functional [200, 260] together with a split valence polarized basis set SVP (Al: 4s3p1d, O: 3s2p1d). For each composition 2000 isomers are generated. The ten most stable structures each are then re-optimized with the B3LYP functional [202] and a triple zeta polarized basis set def2-TZVPP (Al: 5s5p3d1f, O: 5s3p2d1f) [201]. There were no significant changes in the structures and relative energies by means of re-optimization.

As a genetic algorithm the hybrid approach of the dodo program [197, 198] is employed. DFT calculations are performed with the TURBOMOLE 7.1 programs [203] assuming always a closed shell electronic structure. Thus, a restricted Hartree-Fock (RHF) reference is invariably used. IR spectra are computed within the double harmonic approximation as implemented in TURBOMOLE. For a better comparison of the computational stick spectra the sharp features are convoluted with a 10 cm^{-1}full width at half maximum Gaussian line shape function.

4.3.4 Results and discussion

The vibrational spectra of $Al_3O_4^+$ with zero up to four adsorbed D_2O molecules, obtained by IRPD spectroscopy for $n < 2$ and IRMPD spectroscopy for $n = 3$–4, are shown in Fig. 4.12 (left). Experimental bands are labeled with capital letters and their positions are summarized in Table B.1. The spectra were measured in the O–D stretching (3000–2000 cm^{-1}) as well as the fingerprint spectral region (1300–400 cm^{-1}). The O–D stretching region contains information on the nature of the adsorbed D_2O molecules. For example, free O–D stretching modes are expected in the region in-between 2800-2650 cm^{-1}, while hydrogen-bonded O–D stretches are red-shifted and found below 2670 cm^{-1}[86, 261–263]. It also allows discerning between physi- and chemisorption. The fingerprint region mainly contains contributions from Al–O stretching modes (ν) as well Al-O-D bending and deformation modes (δ) and allows insight into structural changes of the $Al_3O_4^+$ substrate cluster upon water adsorption.

The IRPD spectrum of $Al_3O_4^+$, taken from Ref. [28], shows IR absorption only below 900 $cm^{-1}$and its most intense feature, labeled E in Figure 4.12, is centered at 871 cm^{-1}. Adsorption of up to four water molecules leads to substantial changes in both spectral regions. In the O–D stretching region, adsorption of the first D_2O molecule is signaled by band A at 2806 cm^{-1}, which lies at higher wavenumbers with respect to both the symmetric (ν_S, 2671 cm^{-1}) and antisymmetric (ν_{AS}, 2788 cm^{-1}) O–D stretches of a free water molecule [264]. Its position (see Table B.1) varies only by 10 cm^{-1}between $n = 1$ and $n = 4$ (2807–2797 cm^{-1}). Upon adsorption of the second D_2O molecule a second free O–D stretching band is observed

*Calculations were performed by Fabian Müller and Florian A. Bischoff in the group Prof. Joachim Sauer at the Institut für Chemie, Humboldt-Universität zu Berlin.

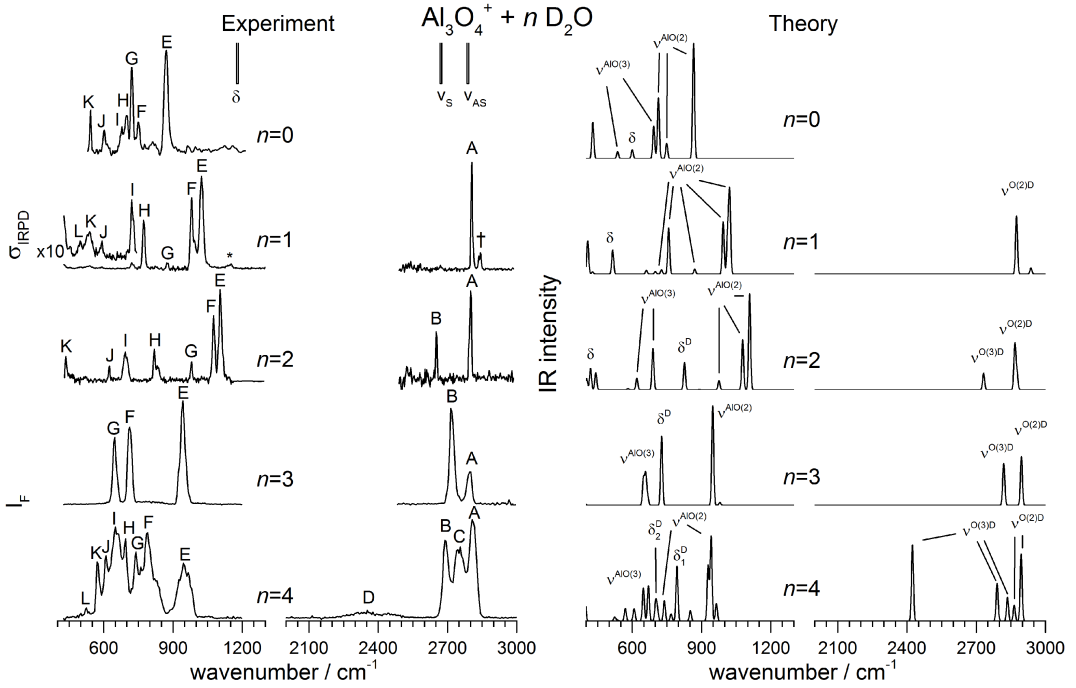

Figure 4.12: Experimental (**left**) and computed (**right**) vibrational spectra of $[Al_3O_4(D_2O)_n]^+$ clusters containing n adsorbed water molecules. (**left**) IRPD (n = 0–2) and IRMPD (n = 3,4) spectra are obtained by monitoring the messenger-tag loss (He loss for $n = 0$, D_2 loss for $n = 1$, 2) and D_2O loss ($n = 3$, 4) channel, respectively. (**right**) Computed vibrational spectra derived from B3LYP/def2-TZVPP harmonic frequencies and intensities of the global minimum energy structures (see Fig. 4.13) and convoluted with a Gaussian line shape function (fwhm width: 10 cm^{-1}) to account for the spectral width of the laser radiation as well as rotational broadening. Numbers in parentheses indicate the coordination number of the respective atoms. See Table B.1 for the band assignments to stretching (ν) and deformation (δ) normal modes. The experimental band positions of the antisymmetric streching (ν_{AS}), symmetric streching (ν_S) and bending mode ((δ) of free D_2O are indicated by the bars. The $n = 0$ spectrum was previously reported [28].

at 2651 cm^{-1}(B), 151 $cm^{-1}$to the red of band A. The separation between band A and B is reduced upon addition of the third and fourth D_2O molecules. For $n = 4$ an intermediate band C is also observed, leading to a quasi-continuous absorption of the free O–D oscillators ranging from 2850 to 2650 cm^{-1}. A hydrogen-bonded O–D stretching mode is only observed for $n = 4$, leading to band D (2352 cm^{-1}), which extends from 2500 down to 2200 cm^{-1}. Band D appears very broad, typical for D-atom delocalization as a result of thermally induced fluctuations in the associated hydrogen bonding network [265].

The changes observed in the fingerprint region are also substantial. Adsorption of up to two D_2O molecules leads to a blue shift of the highest energy absorption band E from 871 cm^{-1}($n = 0$), over 1023 cm^{-1}($n = 1$) to 1104 cm^{-1}($n = 2$). Concomitant, a second intense

band (F) appears at slightly lower energies at 971 $cm^{-1}(n = 1)$ and 1077 $cm^{-1}(n = 2)$. Less intense bands, labeled with G to L, are observed at lower energies. Interestingly, adsorption of the third D_2O reverses the trend described for band E and leads to a simpler IR spectrum, exhibiting similarities to that of $n = 0$, suggesting similar structural motifs. Finally, adsorption of the fourth D_2O molecule leads to a substantial increase of the spectral complexity, resulting in a quasi-continuous absorption involving bands E-L from about 1000 down to 500 cm^{-1}in the fingerprint region.

In order to interpret and assign the measured vibrational spectra we performed DFT calculations to find minimum energy structures and their associated IR spectrum. The sequential water binding energies decrease with n and range from 437 kJ/mol for $n = 1$ to 106 kJ/mol for $n = 4$. For all systems the reaction with D_2O is highly exothermic and up to $n = 4$ dissociative adsorption is energetically favored over molecular adsorption (see Table 4.7). The lowest energy structure containing at least one physisorbed D_2O molecule lies 199 kJ/mol (12 kJ/mol) above the all-chemisorbed species for $n = 1$ ($n = 4$).

Table 4.7: B3LYP/def2-TZVPP sequential binding energies (in kJ/mol) $\Delta(E_{n-1} - E_n)$ for the reaction $[Al_3O_4(D_2O)_{n\text{-}1}]^+ + D_2O \rightarrow [Al_3O_4(D_2O)_n]^+$ and relative energies of the lowest energy structure containing at least one physisorbed D_2O molecule $\Delta(E_{n,physisorbed} - E_n)$. All energies include zero-point-energies. BSSE corrections are neglected.

	$n = 1$	$n = 2$	$n = 3$	$n = 4$	$n = 5$
$\Delta(E_{n-1} - E_n)$	437	271	286	106	82
$\Delta(E_{n,physisorbed} - E_n)$	199	69	139	12	0

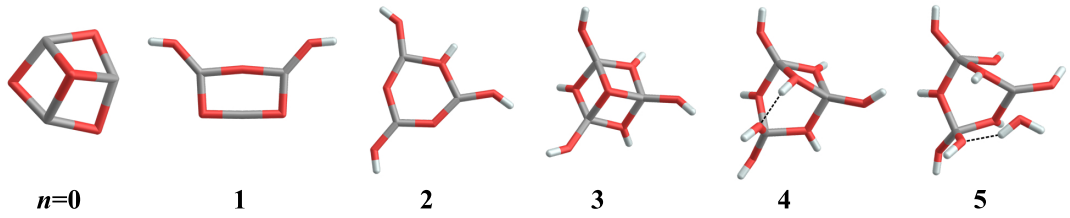

Figure 4.13: B3LYP/def2-TZVPP minimum-energy structures of the $[Al_3O_4(D_2O)_n]^+$ clusters containing n adsorbed water molecules.

The simulated IR spectra, derived from B3LYP/def2-TZVPP frequencies and intensities, of the lowest energy isomers (see Figure 4.13 for minimum energy structures) for each system are shown in Fig. 4.12 (right). In all four cases dissociative water adsorption is found to be energetically favored. For the smaller systems ($n < 2$) the messenger species used in the experiment has a significant effect on the IR spectrum and hence the spectrum of the complex containing the messenger species is shown (see Appendix B for a comparison of all simulated

IR spectra).

The computed spectra of the lowest energy structures for each cluster size are in very good agreement with the experimental data over both spectral regions probed. O–D stretching frequencies are overestimated by about 70 cm^{-1}probably due to the harmonic approximation. Up to $n = 3$ the relative band positions and in most part also the relative intensities are qualitatively reproduced. The remaining discrepancies are mainly attributed to deviations of the experimentally determined dissociation yield from the calculated linear absorption cross section. For $n \leq 2$ (IRPD spectra) this can result in less intense peaks at lower photon energies, which lie close to the dissociation limit of the ion-messenger tag complex (*e.g.* band K in the $n = 1$ spectrum), while for $n > 2$ (IRMPD spectra) the (sequential) absorption of multiple photons is probably the origin of the deviations. Note that for the sake of simplicity, we convoluted all harmonic stick spectra with a Gaussian line shape function of identical width, which is the origin of some of the discrepancies between experimental and predicted IR spectra of the larger clusters.

As shown previously [28] the structure of $Al_3O_4^+$ has C_{3v} symmetry consisting of a triply coordinated O-atom (μ_3-O) capping a six-member ring (-Al-O-)$_3$. The six-membered ring is a structural motif that persists throughout all the systems studied here except for the structure with $n = 1$, where a sheet structure – *i.e.* a distorted or opened six-membered ring – can be found. Bands E to H arise from the Al_2-(μ_2-O) stretching modes (involving doubly coordinated O-atoms). The bands at lower energies are associated with modes that involve the triply coordinated oxygen: two Al_3-(μ_3-O) stretching modes (I, K) and a frame-deformation mode (J).

Dissociative adsorption of the first D_2O molecule leads to the six-membered sheet structure with two exocyclic OD groups bound to individual Al atoms (see Fig. 4.12). The two hydroxyl groups combine to two nearly isoenergetic normal modes, a symmetric (calc. 2874 cm^{-1}) and an antisymmetric (calc. 2876 cm^{-1}) combination, and are assigned to the intense band A (2806 cm^{-1}). The small peak labeled † in Fig. 4.12 then corresponds to excitation of the perturbed D–D stretching mode of the D_2 tag. It is IR-forbidden in a free D_2 molecule (2994 cm^{-1}) [266], but obtains IR-intensity and is substantially red-shifted by 152 cm^{-1}through the strong polarization interaction with the ion. Peaks G to I are assigned to Al_2-(μ_2-O) stretching modes. The highest energy bands E and F arise from the symmetric and antisymmetric stretches involving the two Al–OD moieties. An in-plane mode of Al_3-(μ_3-O) coupled with the Al–O–D bending modes is predicted at lower energies (calc. 515 cm^{-1}) and attributed to peak K at 539 cm^{-1}. For the $n = 1$ system a corresponding anionic structure was studied previously, lacking the two deuterons, but with the same number of electrons. Its structure is very close to the one discussed here, and also the spectrum is very similar. In particular the E and F bands can be assigned to the same stretching vibrations, only slightly red-shifted in the anionic $Al_3O_5^-$ system.

The dissociative adsorption of the second D_2O molecule leads to a minimum energy structure containing the six-member ring with three exocyclic hydroxyl groups, each bound to one of

the three Al atoms and one bridging Al_2-(μ_2-OD) group (see Fig. 1). The hydroxyl stretching modes are calculated at 2878, 2870 and 2868 $cm^{-1}$and contribute to a single band (A), which is red-shifted by 6 $cm^{-1}$with respect to the corresponding band for $n = 1$. On the other hand, the Al_2-(μ_2-OD) stretch is predicted $\sim$ 140 cm^{-1}lower in energy (calc. 2733 cm^{-1}) and is assigned to band B (2651 cm^{-1}). The two IR-active modes highest in energy in the fingerprint region (calc. 1109 and 1079 cm^{-1}) are all Al_2-(μ_2-O) stretching modes and assigned to bands E (1104 cm^{-1}) and F (1077 cm^{-1}). Band G (981 cm^{-1}) most likely arises from the Al–OD stretch modes. The in-plane bend of the bridging Al_2-(μ_2-OD) is calculated at 826 cm^{-1}(δ^{D}) and assigned to band H (819 cm^{-1}), while bands I (694 cm^{-1}) and J (625 cm^{-1}) are assigned to Al_2-(μ2-O) stretches (calc. 689 cm^{-1}, 620 cm^{-1}). Ring deformation modes δ (Al_2-(μ_2-OD) out-of-plane motions) are predicted below 500 cm^{-1}.

The structural motif of the lowest energy structure found for $n = 3$ is similar to the C_{3v} structure of $n = 0$, but now contains only fourfold coordinated Al-atoms, due to the presence of three terminal hydroxyl groups. The remaining three D-atoms form three bridging Al_2-(μ_2-OD) moieties. This high symmetry is reflected in the simple nature of the predicted IR spectrum, which contains five bands. These are assigned, from high to low energy, to the terminal O–D stretches (A), Al_2-(μ_2-OD) stretches (B), Al–OD stretches (E), in-plane bends involving predominantly the bridging Al_2-(μ_2-OD) groups (F) and the Al_3-(μ_3-O) stretches (G).

Finally, the $n = 4$ structure is the first that contains an intramolecular hydrogen bond, which leads to additional features in the O–D stretching region, next to the free hydroxyl and Al_2-(μ_2-OD) stretches, which are attributed to bands A and B, respectively, analogous to the IR spectra of the smaller clusters. The additional features predicted at 2835 $cm^{-1}$and 2424 cm^{-1}, corresponding to bands C (2750 cm^{-1}) and D (2352 cm^{-1}) in the experimental spectrum, stem from those bridging Al_2-(μ_2-OD) and terminal hydroxyl groups, which act as hydrogen bond donor and acceptor, respectively. The heterogeneity of the $n = 4$ structure is also reflected by the many bands in the fingerprint region. The Al_2-(μ_2-O) stretching modes (calc. 965, 942, 929 and 739 cm^{-1}), are assigned to band E (946 cm^{-1}). Bands F (790 cm^{-1}), G (740 cm^{-1}) and H (695 cm^{-1}) stem from the in-plane bending modes of the bridging Al_2-(μ_2-OD) (calc. 852 for hydrogen bonded OD, 794, 768, 709 and 702 cm^{-1}). Further coupled Al_2-(μ_2-O) modes are predicted at lower energies ($\leq$ 670 cm^{-1}) and attributed to the remaining bands I–L.

The unambiguous assignment of the reported vibrational spectra allows identifying characteristic IR absorption regions for O–D stretching, Al–O stretching and Al–O–D bending modes as a function of the Al- and O-atom coordination (see Fig. 4.14). The region of the stretching mode of D_2 in D_2-tagged ionic complexes (2994–2850 cm^{-1}), with the low and high wavenumber limit defined by the present study and a study on free D_2 [266], respectively, is also shown for comparison. The O–D stretching region extends roughly from 2830 cm^{-1}down to 2650 $cm^{-1}$and can be grouped into two non-overlapping regions, depending on whether the O-atom is part of a terminal OD or bridging Al_2-(μ_2-OD) hydroxyl group. The terminal O–D

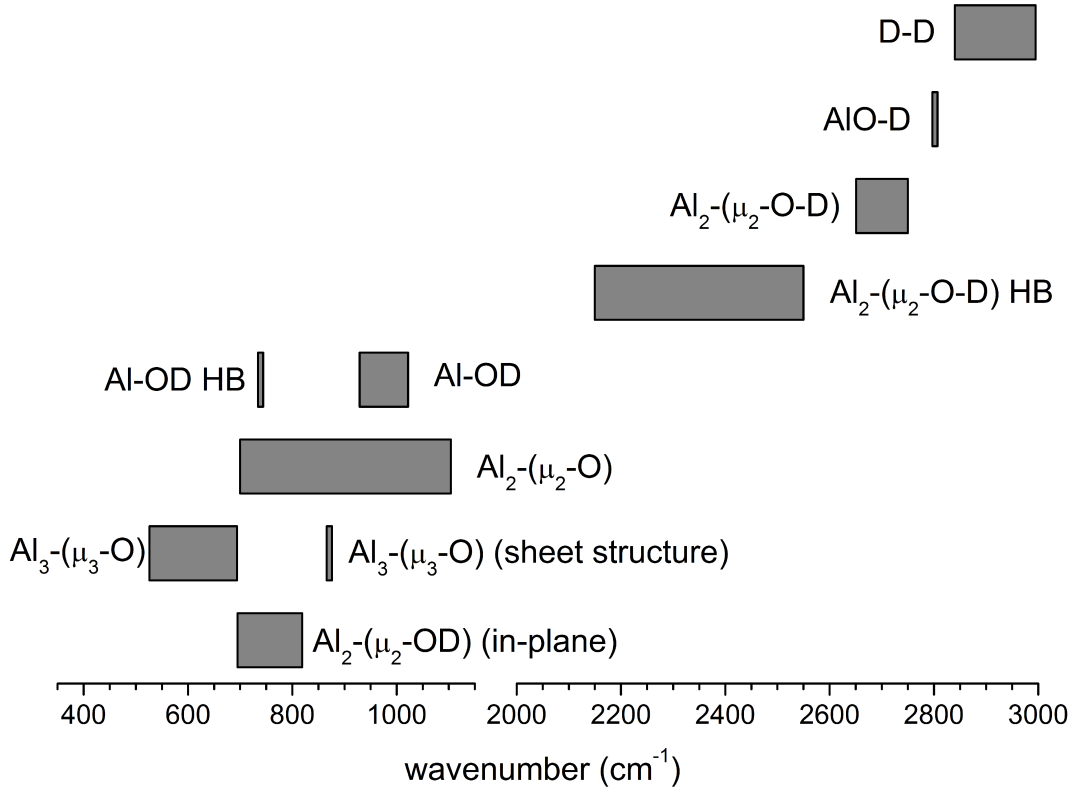

Figure 4.14: Characteristic IR absorption regions, determined from the experimental gas phase vibrational spectra of $[Al_3O_4(D_2O)_{0-4}]^+$ shown in Fig. 4.12, of various O–D and Al–O stretching as well as Al–O–D in-plane bending modes, grouped as a function of Al- and O-atom coordination (see also Table B.3). The spectral region of the stretching mode of D_2 in messenger-tagged ionic complexes, which gains IR activity by polarization, is also shown [266].

stretches are found in the narrow spectral region 2830–2790 cm^{-1}. The bridging Al_2-(μ_2-O-D) stretches lie well separated and lower in energy (2760–2650 cm^{-1}). Hydrogen-bonded O–D stretches are found even further to the red, below 2400 cm^{-1}.

Four characteristic absorption regions are identified in the fingerprint spectral region. Al–OD stretching modes involving terminal hydroxyl groups are found at highest energy (1030–850 cm^{-1}), followed by Al_2-(μ_2-O) stretching modes involving bridging O-atoms (1100–615 cm^{-1}). Al_3-(μ_3-O) stretching modes (700–510 cm^{-1}) absorb at lower energies. Al_2-(μ_2-OD) in-plane bending modes are found in the 855–470 cm^{-1}region.

Fig. 4.15 shows the wavenumbers as a function of the formal oxygen charge of the OD group, and compares it with the data collected by Knözinger [267, 268] for different alumina surfaces. The formal oxygen charge is obtained from the charge of oxygen (-2) and the sum of the electrostatic bond strengths of the adjacent aluminium atoms/ions. The latter is defined

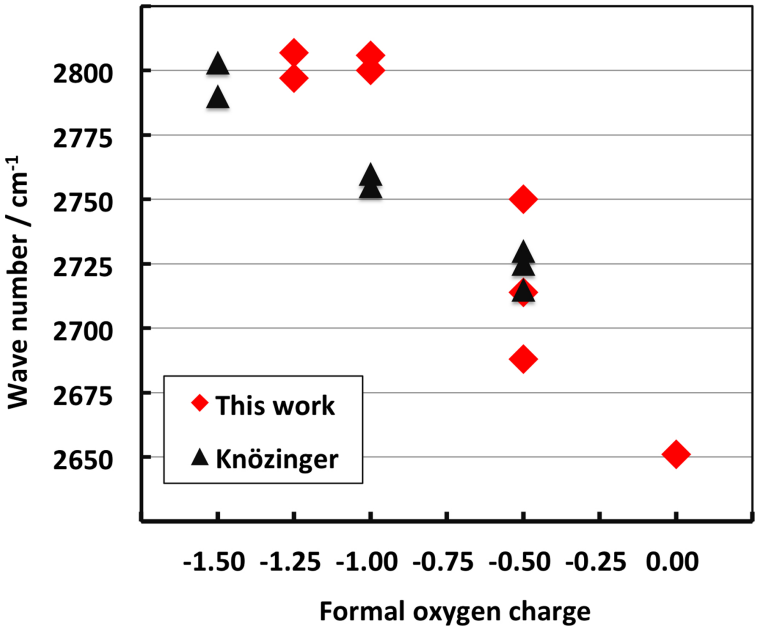

Figure 4.15: Observed wavenumbers for O-D stretching vibrations of $[Al_3O_4(D_2O)_n]^+$ gas phase clusters and different solid aluminas [268] as function of the formal oxygen charge.

as the cation charge divided by its coordination number. For a terminal OH group on a six-coordinated Al^{3+} ion it is $-2+3/6=-1.5$, whereas on a four- and three-coordinated Al^{3+} ion as in the clusters with $n=4$ and $n=3$, respectively, it is $-2+3/4=-1.25$ and $-2+3/3=-1.0$. For the bridging Al_2-(μ_2-OD) group it is $-2+2(+3/3)=0$. Figure 2 shows that the O-D stretching wavenumbers reported for different alumina phases [268], $2803-2715$ cm^{-1}, are within the same range as our results for the gas phase $[Al_3O_4(D_2O)_{1\text{-}4}]^+$ clusters. Moreover, our results for the gas phase model systems support the assignment based on the trend with the formal oxygen charge.

The safe assigment reached for the model systems will provide guidance for understanding O–D stretching vibrations in more complex alumina systems. For example, only three of the five O–D vibrations observed by VSF on an α-Al_2O_3 (0001) surface [9] at 2790 ± 3 $cm^{-1}$and $2764/2729\pm5$ cm^{-1}fall into the range of terminal and bridging O-D groups, respectively, established by our experiments on gas phase model systems and previous experiments for alumina surfaces. The two additional bands observed by VSF [9] at 2910 and 2900 $cm^{-1}$are clearly outside, by about 100 cm^{-1}, the range of O–D wavenumbers established here for surface O–D groups on alumina which calls for additional work on this problem.

The results of the present study can be also used to assist the assignment of O–H stretching modes of different aluminium oxide/water systems. We make use of the empirical frequency-scaling factor of 1.36 determined for all-H and all-D isotopologues of the protonated water pentamer, which is in good agreement to that obtained for isolated O–H *vs.* O–D oscillators

(1.37) [86]. This yields estimated spectral windows for (free) terminal and bridging O–H stretching modes of 3820–3800 and 3740–3600 cm^{-1}, respectively. The OH data between 3800 and 3700 cm^{-1}collected by Knözinger and Ratnasamy [267] for different alumina phases fall into this region. The IR peaks at 3742 and 3704 cm^{-1}reported [269] for α-Al_2O_3 as well as the broad peak at 3730–3720 cm^{-1}in the high resolution electron energy loss spectra (HREELS) of the Al_2O_3 (0001) surface [270] correspond to bridging hydroxyl groups.

In conclusion, the unambiguous assignment for gas phase model systems of O-D (O-H) stretching wavenumbers to terminal (μ_1) and bridging (μ_2) hydroxyl groups on aluminium/oxide water systems sheds new light on controversial assignment issues for solid Al_2O_3 phases. The good agreement between experimental and calculated O–D wavenumbers lends credit to DFT calculations also for more complex systems.

4.4 Summary

The studies presented in Section 4.1 allow the identification of the structures of small mono- and di-aluminum oxide anions. The smaller ions prefer linear structures with formation of superoxo groups as the number of oxygen atoms increases. The di-aluminum ions studied all exhibit a four-member Al-(O_2)-Al ring common structural motif with oxygen atoms adding in an exocyclic fashion similarly to other metal-oxides [223]. The electronic structure is characterized by localization of the excess charge, which in some cases results in a reduction of the cluster symmetry. DFT calculations require the use of functionals with a large amount of Fock exchange such as BHLYP for a correct description of the charge distribution and consequently of the vibrational spectra.

Larger Al-oxides clusters, $(Al_2O_3)_{0–6}AlO_2^-$, whose stoichiometry tends to that of bulk alumina while compensating for the additional unpaired electron, are investigated in Section 4.2. The structural analysis reveals the persistence of a four-member ring, already identified in the di-aluminum ions, as a common structural motif throughout the cluster series with the exception of $n = 3$. The larger clusters exhibit no long-range ordering and O and Al average coordination numbers tending to those reported for amorphous alumina. Even larger clusters are thus expected to approach the properties of amorphous Al_2O_3 particles.

These studies are part of a collaborative effort (CRC-1109) that aims at understanding the multi-scale nature of the metal-oxide/water interactions. The next step was then of adding water molecules in a step-wise fashion to the Al-oxide clusters. $Al_3O_4^+$, an electronic close-shell species, is chosen in order to avoid the high and unselective reactivity typically associated with radical cations. The results reveal that water absorption takes place through a dissociative mechanism for all the four D_2O molecules added. The resulting hydroxides contain terminal and bridging OD groups with characteristic vibrational signatures. DFT calculations predict the fifth water molecule to be molecularly absorbed but experiments were hindered by the simultaneous production of isobaric species. Consequently, with the present experimental setup it is not possible to use the quadrupole mass filter to isolate the system.

This could be alternatively achieved spectroscopically by using double resonance techniques as IR^2MS^2 (see Section 3.4.1).

Al-oxide clusters were so far the focus of the project. These species can be viewed as model systems for Fe-oxide clusters. In fact, Al-oxide favor the same oxidation state (+III) and coordination numbers (4 or 6). On the other hand, the redox activity and the complex electronic structure typical of transition metals make experiments and calculations on Fe-oxide clusters more demanding. Preliminary experimental and theoretical results are reported in Appendix C. Fig. C.2 present results of the addition of up to four water molecules on $Fe_3O_4^+$. The structures of the Fe- and Al-oxide are similar and exhibit the same connectivity. Even though the agreement of experimental and theoretical vibrational spectra in the case of the Fe-oxide is poorer with respect to the analogous Al-oxide, the results indicate again a dissociative absorption process of water at least for the first three molecules. Fig. C.3 and C.4 report the vibrational spectra of $Fe_3O_3^+$ and $Fe_4O_5^+$ and of the complexes obtained adding a single water molecule. Structural characterization of these systems will provide insights on the effect of the Fe oxidation state on water absorption.

5 Boron Clusters

Boron compounds can form a rich variety of polymorphs, with the B_{12} icosahedron being a common building block. On the other hand, small boron clusters assume planar structures. The studies on the pure boron cluster, B_{13}^+, and on the perhalogenated dodecaborates, $B_{12}I_{12}^{2-}$ and $B_{12}I_n^-$ with $n = 7 - 9$, presented in this Chapter encompass both structural arrangements as well as the transition from one to the other.

5.1 Structure and Fluxionality of B_{13}^+ Probed by Infrared Photodissociation Spectroscopy*

5.1.1 Introduction

Boron is electron deficient and therefore has a strong tendency to share electrons. Consequently, pure boron compounds can exhibit pronounced delocalized bonding and aromatic behavior. These unusual electronic properties of elemental boron lead to a rich polymorphism [38]. Bulk boron prefers three-dimensional structures based on deltahedral, mainly icosahedral or octahedral, subunits. Various boron nanostructures including nanosheets, nanotubes, nanoribbons and nanospheres with similar and sometimes superior properties as their carbon-based analogues have been predicted [39]. Experimentally, only the synthesis of single- and multi-wall boron nanotubes has been reported [40, 41]. Larger boron clusters in the gas phase can adopt aromatic fullerene-like structures. The smaller clusters prefer planar, quasi-planar or cylindrical geometries with a charge-state dependent 2D to 3D transition at $n = 16$ for cations and $n = 39$ for anions [14, 16, 37]. Since the first mass spectrometric experiments on boron clusters by Anderson and coworkers, B_{13}^+ has been known to be particularly stable and unreactive [271]. However, its structure remained subject to debate for some time [272]. While the results from theoretical methods have converged and now predict a planar C_{2v} global minimum energy geometry consisting of an inner triangle surrounded by a ten-membered external ring, its spectroscopic verification has remained open [46]. The special stability of this C_{2v} structure has been explained by its σ- and π-aromaticity [45, 46]. As a result of the delocalized bonding it is predicted to exhibit a very small barrier (0.4 kJ/mol) towards the internal rotation of the inner C_3 ring and has hence been termed a "molecular

*Section based on: Matias R. Fagiani, Xiaowei Song, Petko Petkov, Sreekanta Debnath, Sandy Gewinner, Wieland Schöllkopf, Thomas Heine, André Fielicke and Knut R. Asmis, very important paper in *Angew. Chem. Int. Ed.* (Accepted) DOI: 10.1002/anie.201609766

Wankel motor", but this awaits experimental verification [47–49]. Here, we use cryogenic ion vibrational spectroscopy in combination with density functional theory (DFT) computations and Born-Oppenheimer molecular dynamics (BOMD) simulations to characterize the structure and fluxionality of cold, mass-selected B_{13}^+ clusters in the gas phase, providing the first experimental evidence for internal quasi-rotation in B_{13}^+ already at very low temperatures.

In contrast to the wealth of experimental work on pure carbon clusters, spectroscopic studies on pure boron clusters are scarce and have predominantly focused on negative ions. Wang and coworkers have applied anion photoelectron spectroscopy (APS) in their pioneering work on boron anions up to B_{40}^-. With computational support from the Boldyrev group they were able to show that up to $n = 36$ boron cluster anions adopt planar or quasi-planar structures [43, 45]. Recently, they reported the first experimental evidence for a 3D cage structure, a so-called borospherene, for B_{40}^-, the smallest all-boron fullerene [43]. Subsequently, they found evidence that B_{39}^-, another member of the borospherenes, is chiral [16]. In principle, APS accesses the neutral manifold, but it is limited by Franck-Condon considerations to probe structures that are similar to that of the anion ground state. More direct experimental information on the structure of neutral boron clusters has been limited to B_{11}, B_{16} and B_{17}, which have been probed by IR/vacuum-UV two color ionization experiments [273]. These experiments confirmed the (quasi-)planar structures found by APS. The only experimental information on the structure of the cationic boron clusters B_n^+ comes from ion mobility measurements combined with a genetic algorithm search of low energy structures from Kappes, Ahlrichs and coworkers [14]. Their experimental collision cross section for B_{13}^+ is in agreement with that of the predicted global minimum energy C_{2v} structure (isomer **I** in Fig. 5.1). However, an energetically substantially higher lying non-planar isomer (isomer **IV** in Fig. 5.1) exhibits a nearly identical collision cross section, calling for a more definitive, spectroscopic identification. Moreover, the vibrational spectrum of B_{13}^+ does not only allow assigning its structure unambiguously, but it should also contain characteristic signatures of its unusual fluxional behavior.

5.1.2 Experimental and Computational Methods

Experimental methods

Infrared photodissociation (IRPD) experiments are conducted on the 6 K ion-trap triple mass spectrometer described in Chapter 3. A pulsed beam of cationic boron clusters is formed by laser vaporization using a Smalley-type rotating rod source (see Section 3.2.2 and references therein). Vaporization is induced by focusing (30 cm focal length) the second harmonic output (532 nm) of a pulsed 50 Hz Nd:YAG laser (Soliton, Nano LG 100-50) onto the surface of a moving ^{11}B-enriched boron-rod target. The ablated ions are then entrained in a carrier gas pulse of helium ($\sim$ 5.5 bar backing pressure), and boron clusters are subsequently formed through expansion in a confinement channel ending in a cone-shaped nozzle held at a temperature of 270 K. In order to obtain a stable cluster signal, the turning speed of the

rod is set to ~ 1 turn per minute corresponding to about two laser shots for each position of the rod. The laser pulse energy is attenuated to roughly 5 mJ. The beam of ions passes a 4 mm diameter skimmer, is then collimated in a radio frequency (RF) buffer-gas-filled decapole ion-guide, and the mass of interest is selected via a quadrupole mass-filter (Extrel CMS). The mass-selected beam of $^{11}B_{13}^+$ is focused into a cryogenically-cooled RF ring electrode ion-trap. The trap is continuously filled with D_2 at a trap temperature of 16 K, which allows for the accumulation and thermalization of the ions. Inside the ion trap, the bare $^{11}B_{13}^+$ ions undergo three-body collisions with the buffer gas, which promote the formation of weakly bound ion-D_2 complexes [112]. After an ion trap fill time of 200 ms all ions are extracted from the ion trap and focused in the center of the extraction region of a time-of-flight (TOF) mass spectrometer, where they are irradiated by an intense and wavelength-tunable IR laser pulse. When resonant with a vibrational transition, the parent ions can absorb a photon, eventually leading to loss of one or more messenger molecules via intramolecular vibrational predissociation.

The IR free electron laser at the FHI is used as a light source in the present measurements (see section 3.5.1 and references therein). Its wavelength is tuned from 5.5 to 23 μm with a bandwidth of between 0.3 and 0.5 % root mean square of the central wavelength. TOF mass spectra are measured as a function of the irradiation wavelength and converted into an IR spectrum. To this end, a time window Δt_i is defined for each mass channel i (corresponding to the parent or fragment ions) and the frequency dependent ion yields $I_i'(\nu)$ are determined by integration. The intensities are normalized to the total number of parent and fragment ions, to account for fluctuations in the ion signal. IRPD spectra are obtained by plotting the laser fluence corrected photodissociation cross section σ_{IRPD} as a function of the laser wavenumber (see section 3.4 and references therein). TOF mass spectra are averaged over 200 measurements.

Computational methods*

DFT calculations are performed within TurboMole V6.6 [274] using the PBE0 hybrid functional[275], def2-TZVP basis sets[201] and the third version of Grimme's dispersion correction [276]. For low energy isomers harmonic IR spectra are calculated. The harmonic vibrational frequencies are scaled by a previously determined scaling factor [277] of 0.9575 to account for anharmonic effects as well as systematic errors on the harmonic force constants. Anharmonic VPT2 frequencies and intensities of the lowest energy isomer are calculated at the corresponding level of theory using the Second-order Vibrational Perturbation theory (VPT2) method by Bloino and Barone [278] as implemented in the Gaussian 09 rev. D.01 software package [210]. To aid the comparison to the experimental spectrum the obtained IR

*Harmonic DFT calculations were performed by Dr. André Fielicke from the Institut für Optik und Atomare Physik of Technische Universität in Berlin. BOMD simulations were performed by Petko Petkov in the group of Prof. Thomas Heine from the Wilhelm-Ostwald-Institut für Physikalische und Theoretische Chemie of the Universität Leipzig. I have performed VPT2 anharmonic calculations.

stick spectra are folded with a Gaussian line shape of full width at half maximum of 1.5 % of the line frequency. Low energy isomers of $B_{13}D_2^+$ are identified by means of a basin hopping algorithm [279] allowing only random movement of the D_2 unit. Relative energies include zero point vibrational energies obtained from the harmonic vibrational analysis.

BOMD simulations were carried out employing the Gaussian Plane Wave (GPW) formalism as implemented in the QUICKSTEP [280] module within the CP2K program suite (Version 2.7) [281, 282]. Molecularly optimized basis sets of double-ζ quality plus polarization in their shorter-range variant (DZVP-MOLOPT-SR-GTH) [283] were used. The auxiliary plane wave basis set was truncated at a cut-off of 400 Ry. The cubic simulation box size was set to 1 nm, which ensures that the closest possible distance between two images will be always more than 5 Å. The computational level has been tested against the (computationally more expensive) harmonic calculations described above (see Fig. D.1). BOMD simulations were performed at 100, 300, and 600 K with time steps of 0.5 fs within the NVT ensemble employing the Nosé-Hoover thermostat. The power and IR spectra from the BOMD trajectories were obtained via the velocity autocorrelation function as implemented in TRAVIS, as described by Brehm and Kirchner [284]. For each temperature an initial equilibration run of 10 ps was performed followed by a productive run of 50 ps length. The power and IR spectra were calculated on the base of the trajectory obtained in the productive BOMD run. In order to check the convergence of the IR spectra with the length of the simulations, the productive runs were extended with additional 20 ps and the IR spectra were compared. Since there were no differences in the IR spectra from 50 ps and 70 ps productive runs we considered the length of the simulations as converged with respect to the quality of the IR spectra.

In order to check the dependency of the calculations on the exchange correlation functional, IR spectra have been calculated using the harmonic approximation with hybrid functional PBE0 and the generalized gradient approximation-type PBE functionals, the latter one with basis sets of both double and triple zeta quality. These calculations were performed with the ADF package [285–287]. As shown in Fig. D.1, these calculations give a nearly identical IR spectrum with maximum deviations of 10 cm^{-1}, which allows employing the computationally less expensive PBE/DZVP level during the BOMD calculations in order to achieve longer trajectories.

5.1.3 Results and Discussion

The gas-phase vibrational spectrum of B_{13}^+ measured by way of IRPD spectroscopy of the messenger-tagged $^{11}B_{13}^+(D_2)$ complex is shown in Fig. 5.1. It exhibits four bands at 1029 cm^{-1}(b), 878 cm^{-1}(c), 809 cm^{-1}(d) and 556 cm^{-1}(h). All bands appear substantially broader than the spectral bandwidth ($\lesssim$ 10 cm^{-1}). Band d, for example, extends from 750 to 830 cm^{-1}, and we therefore attribute the additional structure observed on its lower-energy side in the form of two peaks at 782 cm^{-1}(e) and 764 cm^{-1}(f) to additional, overlapping transitions. Weaker absorptions, close to the signal/noise ratio, are present at higher energies in-between

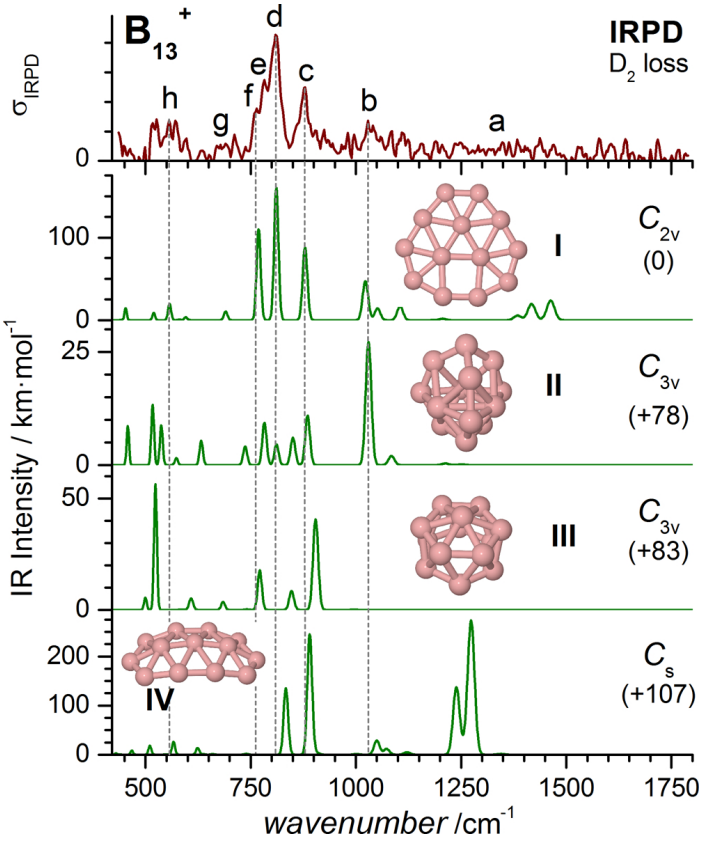

Figure 5.1: Comparison of the experimental IRPD spectrum of D_2-tagged $^{11}B_{13}^+$ obtained by monitoring the D_2-loss channel with four computed IR spectra of low-energy PBE0/TZVP minimum energy structures, derived from scaled (0.9575) harmonic frequencies and intensities, of bare $^{11}B_{13}^+$. TPSS/def2-TZVPP energies[4b] (in kJ mol^{-1}), relative to that of bare $^{11}B_{13}^+$ are given in parentheses. Broken lines are shown to aid the eye and coincide with experimental band maxima listed in Table 5.1.

1200 and 1500 cm^{-1}(a) and centered around 700 cm^{-1}(g).

Also shown in Fig. 5.1 are the computed harmonic IR spectra, derived from scaled harmonic frequencies and intensities (see Table 5.1), of four low-energy isomers, which were also considered in the previous ion mobility study [14]. These are the planar C_{2v} structure (**I**), now generally accepted as the global ground state, two 3D C_{3v} structures (**II** and **III**), computed 78 and 83 kJ mol^{-1} higher in energy, respectively, as well as a quasi-planar Cs structure (**IV**, +107 kJ mol^{-1}). Satisfactory agreement with the experimental spectrum is only found for the computed spectrum of the global ground state structure **I**, spectroscopically confirming its assignment. The IR spectra of isomers **II**-**IV** also show characteristic absorption bands in-between 750-900 cm^{-1}, but each of them exhibits its highest intensity transition (**II**: 1028 cm^{-1}, **III**: 523 cm^{-1}, **IV**: 1273 cm^{-1}) in a spectral region where there is no comparably intense

Table 5.1: Experimental IR band positions (in cm^{-1}), computed vibrational frequencies (in cm^{-1}) and intensities (in km mol^{-1}, in parenthesis) as well as tentative normal mode assignments. All computed normal modes above 700 cm^{-1}as well as those normal modes below 700 cm^{-1}involving the inner B_3 ring are listed.

Band	Expt.	Harmonic (PBE0/TZVP) [a]	Anharmonic (VPT2/PBE0/TZVP)	Assignment [b]
a	1200-1500	1463 (24), 1418 (20), 1384 (6), 1206 (2), 1185 (0)	1492 (20), 1450 (14), 1419 (4), 1235 (1), 1220 (0)	B–B stretches (B_{10}-ring)
		1105 (17)	1128 (13)	B_3 sym. stretch
b	1029	1051 (14), 1023 (47)	1086 (10), 1052 (31)	B–B stretches (B_{10}-ring)
c	878	881 (22), 879 (67)	898 (31), 897 (16)	B_3 asym. stretches
d	809	811 (160)	827 (129)	B_3 frust. translation (ip)
e	782	n/a	796 (22)	1st overtone of B3 frust. rotation (op) [c]
f	762	769 (110)	784 (63)	B_{10}-ring def. (ip)
g	711/690	690 (11)	713 (7)	B_3 frust. rotation (ip) / B_{10}-ring def. (ip)
h	556	557 (19)	577 (9)	B_3 frust. translation (ip)
		404 (0)	419 (0)	B_3 frust. rotation (op)
		390 (0)	397 (0)	B_3 frust. rotation (op)
		148 (14)	150 (12)	B_3 frust. translation (op)
		126 (10)	101 (8)	B_{10}-ring def. (ip) / B_3 frust. rotation (ip)

[a] Scaled by 0.9575 to account for anharmonic effects as well as systematic errors on the harmonic force constants.
[b] Sym. (symmetric), asym. (antisymmetric), frust. (frustrated), def. (deformation), ip (in-plane), op (out-of-plane).
[c] See Table D.1 for other weaker transitions predicted in this spectral region.

signal in the experimental spectrum.

The vibrational normal modes of isomer **I** can be roughly classified into those that predominantly involve displacement of the atoms comprising either the outer B_{10}-ring or the inner B_3-ring (see Table 5.1). The B–B stretching modes of the B_{10}-ring are found at highest energy (> 1000 cm^{-1}) and have low IR intensity (≤ 48 km mol^{-1}). The most intense B–B stretch transition is predicted at 1023 cm^{-1}(see Table 5.1) and is therefore assigned to band b. The higher energy modes (1206-1463 cm^{-1}) then contribute to the broad and weak absorptions associated with feature a. Band c is associated with the two antisymmetric stretching modes of the B_3-ring predicted at 888 and 886 cm^{-1}. The corresponding B_3 symmetric stretch is computed at 1114 $cm^{-1}$with lower IR activity. The most intense IR band d as well as band h correspond to the excitation of the two in-plane frustrated translational modes of the B_3-ring with harmonic intensities of 163 and 20 km mol^{-1}, respectively. The remaining (out-of-plane) frustrated translation mode is predicted much lower in energy at 148 cm^{-1}, outside of the accessible measurement window with the present experimental setup. Peak f is attributed to

the highest energy B_{10} ring deformation mode and is the second most intense IR transition (112 km mol^{-1}). The normal mode associated with band g shows similar contributions from inner and outer atoms. It is one of two b_1 modes (the other is predicted at 133 cm^{-1}) that correspond to a combination of outer ring deformations with the B_3 in plane librational mode. This leaves peak e unassigned, which cannot be attributed to a fundamental harmonic mode of isomer **I** (see below).

While the harmonic spectrum of **I** reproduces the main absorption bands observed in the IRPD spectrum, it does not account for several of the weaker features, including the small but significant IR activity below 750 cm^{-1}as well as peak e. These may either be due to the perturbation from the messenger molecule or anharmonic effects, including those related to the predicted exceptional fluxionality of B_{13}^+. To address the first point, we compare the harmonic spectra of bare B_{13}^+ to those of three $[B_{13}D_2]^+$ species in Fig. 5.2. D_2 can in principle either be physi- or chemisorbed. This leads to the weakly bound top-on and side-on isomers with binding energies of 4 and 5 kJ mol^{-1}, respectively, and a $B_{11}(BD)_2^+$ structure with a binding energy of 188 kJ mol^{-1}. From the two physisorbed D_2-complexes, the top-on species leads to a nearly identical spectrum as that of bare B_{13}^+ (see Fig. 5.2), while the spectrum of the side-on species does not agree as well with the experimental one. The computed spectrum of the species containing dissociatively adsorbed D_2 could indeed account for peak e. However, photodissociation of this species is not likely under the present experimental conditions (unfocussed IR laser beam), considering the comparably low absolute computed IR intensities ($\leq$ 163 km mol^{-1}), in combination with a high dissociation limit, which would require the absorption of more than ten IR photons. Moreover, its formation in the cold ion trap under thermalized conditions is probably kinetically inhibited.

To characterize static anharmonic effects we computed the anharmonic spectrum (see Fig. 5.3 and Table 5.1) of structure **I** using vibrational perturbation theory (see section 5.1.2). The main difference with respect to the corresponding harmonic spectrum is a slight broadening of most spectral features, particularly in the region of bands c, d and f, due to excitation of combination and overtone transitions. We then computed the harmonic spectrum associated with the first-order transition state (TS) for the in-plane rotation of the B_3 ring. Note, the TS lies only 0.4 kJ mol^{-1} above the minimum energy configuration (including zero-point energy correction) [47, 49], leading to a vibrational ground state wavefunction with non-zero probability near the TS region for internal rotation. Compared to the spectrum of the global minimum energy structure **I**, the harmonic spectrum of the TS (see Fig. 5.3) is characterized by a blue-shifted outer-ring in-plane deformation mode at 778 cm^{-1}(*vs.* 769 cm^{-1}), which can account for the additional signal in-between peaks d (809 cm^{-1}) and f (762 cm^{-1}). Hence, this provides a first evidence that peak e (782 cm^{-1}) can be associated with the internal quasi-rotation of the B_3 moiety in B_{13}^+.

That internal quasi-rotation is the origin of these rather subtle effects observed in the IRPD spectrum is further corroborated by the results of BOMD simulations (see section 5.1.2) performed at 100, 300 and 600 K. The corresponding BOMD vibrational spectra are

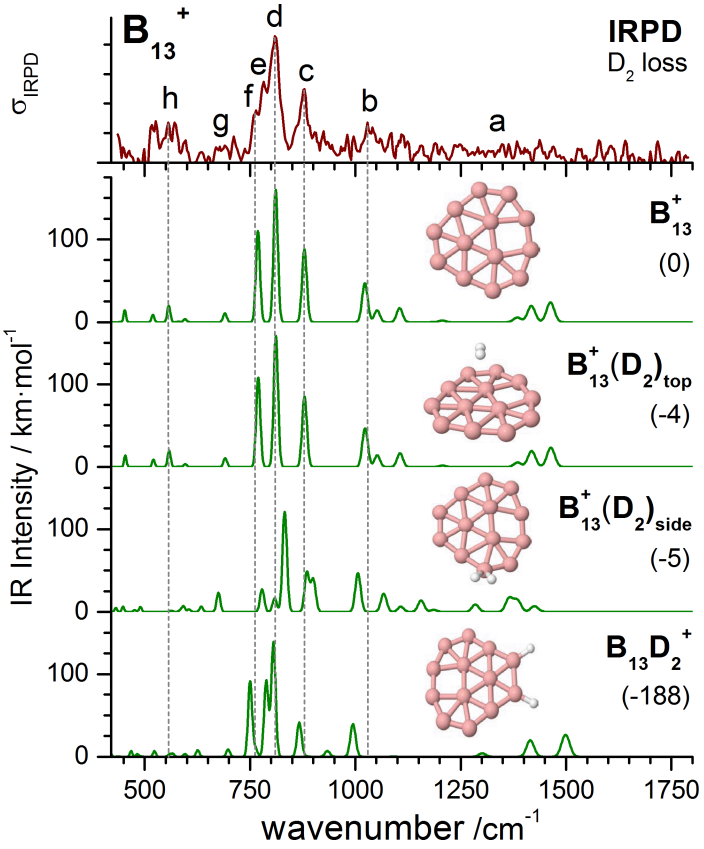

Figure 5.2: Comparison of the computed IR spectra, derived from PBE0/TZVP scaled (0.9575) harmonic frequencies and intensities of bare and D_2-tagged $^{11}B_{13}^+$. The top and side isomers of $^{11}B_{13}^+(D_2)$ as well as a covalently bound $^{11}B_{13}D_2^+$ isomer are shown. D_2 binding energies (in kJ mol^{-1}) are given in parentheses. Broken lines are shown to aid the eye and coincide with experimental band maxima listed in Table 5.1.

shown in the bottom panels of Fig. 5.3 and include both static and dynamic anharmonic effects. Indeed, we observe a motion of both rings with a rate of 20 GHz (100K), 80 GHz (300K) and 220 GHz (600K) (see Fig. D.2). Note, the BOMD simulation temperature is not a justified thermodynamic quantity for such a small molecule and should rather be considered as a measure of the internal kinetic energy. Inspecting the evolution of the BOMD vibrational signature with increasing temperature reveals a consistent picture of the fluxionality of B_{13}^+: we observe a broadening of all spectral features, in particular of bands a, b, g and h, which is comparable to that observed in the experimental IRPD spectrum. Moreover, the computed intensity of band g, which is attributed to the in-plane B_3 frustrated rotation (see Table 5.1), decreases with increasing temperature, that is, it decreases due to the thermal activation of the mutual quasi-rotation between inner and outer ring. Band e is also reproduced by the BOMD spectra and its intensity increases with temperature, eventually forming a wide

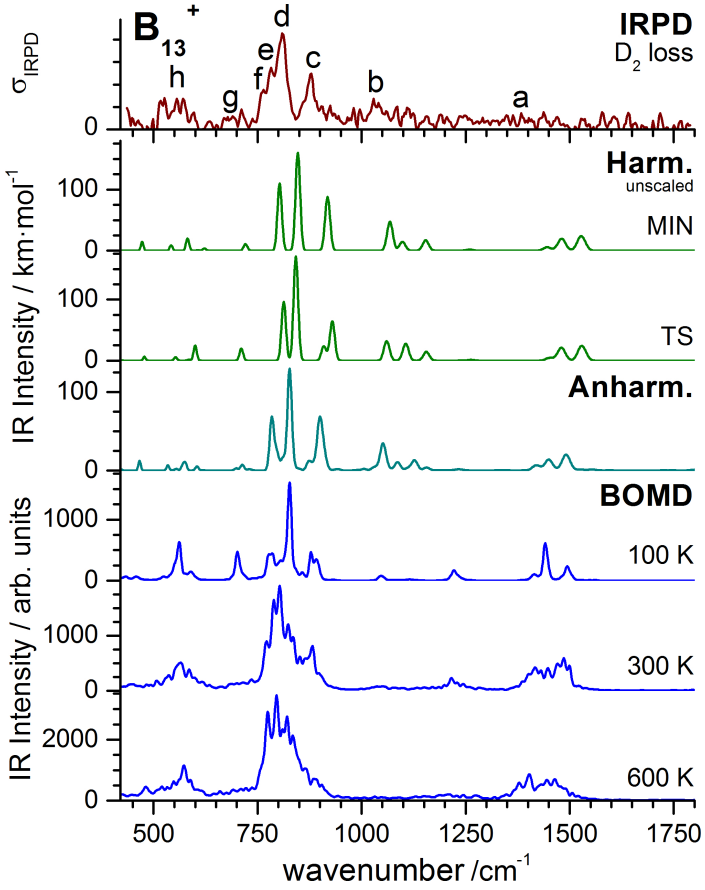

Figure 5.3: Comparison of computed IR spectra of bare $^{11}B_{13}^+$, derived either from PBE0/TZVP harmonic frequencies and intensities of the global minimum energy structure I (MIN) and the first order transition state (TS), VPT2/PBE0/TZVP anharmonic frequencies and intensities of I or from BOMD simulations (PBE/DZVP, for comparison of both levels see Fig. D.1) performed at 100, 300 and 600 K, respectively.

feature comprising bands c, d, e and f. Analysis of the BOMD trajectories finally reveals that bands e and g are directly related to the large amplitude motion involving the unhindered internal quasi-rotation of the B_3 moiety of a planar concentric double ring structure. Note, no fluxionality is found for the related neutral B_{12} cluster that has one boron atom less in the outer ring [288]. Consequently, static and BOMD calculations yield similar IR spectra and in particular no "disappearing" bands are observed in the BOMD spectra at elevated temperatures (see Fig. D.3).

5.1.4 Conclusions

The highly fluxional character of B_{13}^+ discussed here illustrates a peculiar dynamical behavior, which goes substantially beyond the typical conformational dynamics observed within weekly

bound van-der-Waals complexes and hydrogen-bonded clusters. It is also characteristically different from that previously described in strongly bound clusters like Au_7^+ or $Si_{16}V^+$ [289, 290]. Here, the inherent fluxionality of B_{13}^+ is directly linked to its aromaticity, *i.e.* its delocalized bonding, resulting in the absence of any localized bonds between the inner B_3- and outer B_{10}-ring. Consequently, internal rotation does not require the formal breaking and reformation of any covalent bonds in this case. The identification and characterization of such special bonding situations may ultimately prove quite helpful in the conception and design of new materials with tailored properties. Finally, our study also demonstrates that molecular stability does not demand structural rigidity.

5.2 Opening of an icosahedral boron framework: A combined infrared spectroscopic and computational study*

5.2.1 Introduction

In boron chemistry, deltahedra are the major structural motif of compounds with multiple B–B bonds. Closed icosahedral boron structures are not only found in the most common elemental modifications of boron (β- and α-rhombohedral boron), but also represent the skeletal structure of the *closo*-dodecaborates $B_{12}X_{12}^{2-}$ with X = H, halogen [291, 292]. These substances have raised the interest of the inorganic chemistry community for decades and are standard textbook material now [293–296]. Dodecaborates and related polyhedral boranes with their three-center-two-electron (3c-2e) bonds have peculiar electronic properties [297] like 3D σ-aromaticity and stable delocalized negative charges resulting in a low chemical reactivity. For these reasons they are of paramount interest, *e.g.*, in the field of "weakly coordinating anions" with its high variety of applications [35, 298–300].

Single units of pure boron atoms without further substituents, first studied mass spectrometrically by Anderson and coworkers [271], on the other hand, are essentially planar, as was initially predicted computationally [272, 301, 302] and then confirmed experimentally [37, 303–305]. This has recently been rationalized by aromaticity arguments and has stressed the importance of non-polyhedral boron frameworks [47, 306, 307]. Thus, when a fully substituted dodecaborate is stripped from its substituents step by step, it must pass a degree of substitution where the closed icosahedral structure opens. For the partially hydrogenated borates $B_{12}H_n^-$ and $B_6H_n^-$ a 3D to 2D transition is predicted in between $n = 4$ and $n = 3$ [308, 309]. Recently, the complete series of partly iodinated dodecaborates $B_{12}I_n^{x-}$(with n from 1 to 12) was studied mass spectrometrically in combination with electronic structure calculations [54, 55] by starting from $B_{12}I_{12}^{2-}$ and successively removing iodine atoms or iodide ions and ending with neutral B_{12}. Evidence was presented that the global minimum

*Section based on: Matias R. Fagiani, L. Liu Zeonjukl, Tim K. Esser, Detlef Gabel, Thomas Heine, Knut R. Asmis, and Jonas Warneke, editor's choice article in *Chem. Phys. Lett.* **2015**, *625*, 48–52 DOI: 10.1016/j.cplett.2015.02.030

energy structures for $n = 12$ to $n = 8$ represent icosahedral B_{12}-cages, while planar geometries are most stable for $n = 4$ to $n = 0$. Open framework motifs intermediate to planar and icosahedral structures were suggested for $n = 5$–7 depending on the internal temperature of the anions [55].

To this end $B_{12}I_{12}{}^{2-}$ dianions are produced in a room temperature nanospray ion-source, mass-selected and subsequently thermalized to low internal temperatures in a He buffer gas filled ion trap held at 15–19 K. In order to obtain vibrational action spectra by way of infrared photodissociation (IRPD) in the linear absorption regime, the trapped ions are messenger-tagged with D_2, extracted from the ion trap and irradiated with intense and tunable IR radiation in the spectral range from 750 to 1700 cm^{-1}. Partially deiodinated dodecaborates are formed via collision-induced dissociation (CID) in the source region and their IRPD spectra are measured in the same way. As a result of the significant natural abundance of two boron isotopes (80% ^{11}B, 20% ^{10}B) an isotopologue distribution is observed for each cluster size in the mass spectrum. The most favorable signal-to-noise ratio is obtained by mass-selecting the most abundant isotopologue $(^{10}B_2{}^{11}B_{10}{}^{127}I_n)^{-x}(x = 1 \text{ or } 2)$ and the IRPD measurements were performed on these corresponding anions.

5.2.2 Experimental and Computational Methods

Experimental methods

IRPD experiments are conducted on the 6 K ion-trap triple mass spectrometer described in Chapter 3. $B_{12}I_{12}{}^{2-}$ ions produced in a nanospray ion-source (see section 3.2.1) from a 0.48 mmol/L solution of $B_{12}I_{12}{}^{2-}[C_6H_5CH_2N(CH_3)_3{}^{+}]_2$ in 1:1 H_2O and CH_3CN. Partially deiodinated dodecaborates are formed via CID in the source region. All anions are collimated in a radio-frequency (RF) decapole ion-guide filled with argon as a buffer gas. Anions of interest are mass-selected using a quadrupole mass-filter, deflected into 90° and focused in a RF linear ring-electrode ion-trap held at cryogenic temperatures (15–19 K). Trapped ions are accumulated and thermalized by collisions with the D_2 buffer gas continuously supplied to the trap. Ion-messenger complexes are formed via three-body collisions [112, 310]. Every 200 ms all ions are extracted from the ion trap, focused in the center of the extraction region of a time-of-flight mass spectrometer and irradiated by a tunable wavelength IR laser pulse (pulse energies < 2 mJ) from an OPO/OPA/AgGaSe2 laser system (Laser Vision) [158] pumped by a seeded Nd:YAG laser (Continuum, Powerlite DLS-8000) (see section 3.5.3). IRPD spectra are obtained by plotting the normalized total parent ion signal as a function of the photon energy [12, 311]. The intensities are normalized to the total number of ions, to account for fluctuations in the source conditions. The individual measurement points are averaged over at least 250 sweeps.

Computational Details*

Following previously established computational methodology [55, 312], all of the low-lying isomers were optimized using the GGA BP86 functional [200, 260], in junction with a triple-zeta plus polarization (TZP) Slater-type basis set [313]. The scalar relativistic corrections were applied within the ZORA formalism [314–316]. Harmonic frequency analyses were performed to characterize the local minima through the absence of imaginary frequencies. A scaling factor of 1.045 was obtained by the least-squares procedure proposed by Scott and coworkers [317] for the calculated harmonic frequencies of the isotopomeric mixture of $B_{12}I_{12}{}^{2-}$ (see Appendix E). Simulated IR spectra were derived from scaled harmonic frequencies and harmonic intensities and the so obtained stick spectra were convoluted using a Gaussian line shape function with a full width at half maximum (FWHM) of 7 cm^{-1}, which accounts for the spectral resolution of the IR laser radiation ($\sim$ 5 cm^{-1}) as well as rotational band contours in a general way.

It was pointed out that the BP functional yields good molecular geometries, but not the electronic energies [318]. Therefore, for low lying isomers of $B_{12}I_7{}^-$, additional single point calculations upon the optimized geometries were performed at CCSD (for most isomers, see Table E.3) and CCSD(T) (selected isomers, Table E.2) level of theory [319], to get more accurate electronic energies. In the coupled clusters calculations, a basis set of 6-311+G* was assigned for B atoms [320], and LanL2DZ effective core potential (ECP) and corresponding basis functions for I atoms [321]. The enthalpy and Gibbs free energies were then calculated through the following procedure [322]: the zero point energies (ZPE), internal energies and the entropy contributions were adopted from lower BP86 level, while the electronic energies were adopted from higher CCSD(T) level. Throughout the calculations, the determined scaling factor of 1.045 was used for the ZPE as well as the vibrational contributions to the entropy. The density functional theory (DFT) calculations were performed by means of Amsterdam density functional (ADF) 2012 [285, 323, 324], and the CCSD(T) calculations by gaussian09 [210], respectively. Energies, structures and IR stick spectra are given in the Supplementary materials section.

5.2.3 Results and Discussion

In order to characterize the structure of the fully iodinated parent ion ($n = 12$), the IRPD spectrum of D_2-tagged $B_{12}I_{12}{}^{2-}$ is compared to simulated linear absorption spectra derived from density-functional theory (DFT) in Figure 5.4. The predicted IR spectrum of the icosahedral cage structure of $^{11}B_{12}{}^{127}I_{12}{}^{2-}$ is characteristically simple due to its very high symmetry (see Figure 5.4(c)), exhibiting three groups of IR-active bands centered at $\sim$ 934, 372 and 83 cm^{-1}, of which only the first lies within the measurement window of the IR laser. The highest energy band is assigned to breathing modes of the icosahedral boron framework.

*Calculations were performed by L. Liu Zeonjuk and Detlef Gabel in the group Prof. Thomas Heine of the Engineering and Science department of the Jacobs University in Bremen.

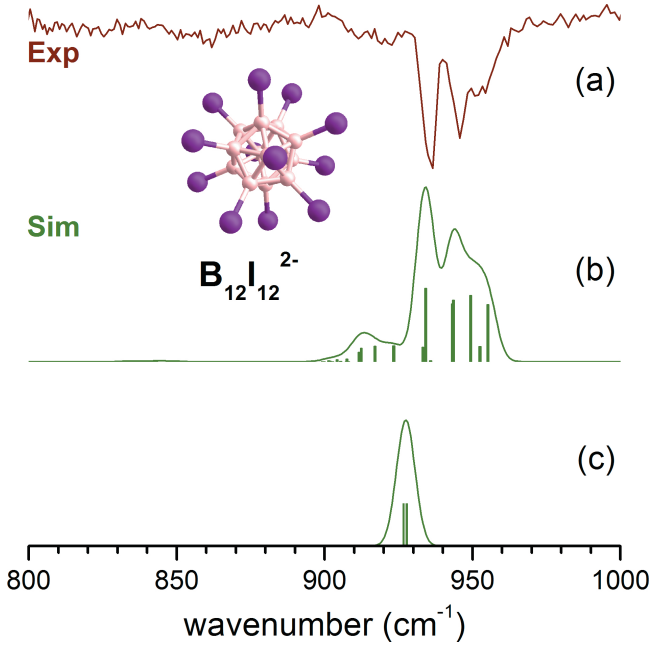

Figure 5.4: (a) Experimental IRPD spectrum of D_2-tagged $B_{12}I_{12}^{2-}$ dianions. The spectrum was obtained by mass-selecting the most abundant isotopologue $(^{10}B_2{}^{11}B_{10}{}^{127}I_{12})^{2-}$ at a mass/charge ratio (m/z) of 826.5 amu, messenger-tagging with D_2 in the ion trap held at 19 K and subsequent IR irradiation. (b,c) Simulated linear absorption spectra (solid lines) of the icosahedral cage structure. The center trace (b) corresponds to the weighted sum of simulated IR spectra derived for the three possible isotopomers of $(^{10}B_2{}^{11}B_{10}{}^{127}I_{12})^{2-}$ (see Figure E.2 for details). For comparison, the simulated IR spectrum of $(^{11}B_{12}{}^{127}I_{12})^{2-}$, is plotted in the bottom trace (c). The simulated spectra were determined from scaled harmonic frequencies and harmonic intensities (see text) and the so obtained stick spectra (solid bars) were convoluted using a gaussian line shape function with a FWHM of 7 cm^{-1}.

The high symmetry is broken by the inclusion of lighter ^{10}B isotopes and the simulated IR spectrum of the most abundant isotopologue $^{10}B_2{}^{11}B_{10}I_{12}{}^{2-}$, consisting of contributions from the three possible isotopomers (see Figure E.2), shows additional features within ± 30 cm^{-1} of the original peak. A net blue shift of the center of this absorption band is predicted as a result of the two lighter ^{10}B atoms and hence smaller reduced mass of the corresponding normal modes. Excellent agreement regarding the absorption band profile is observed between the experimental IRPD spectrum and the simulated one (Figure 5.4(a) and (b)), confirming the exclusive presence of the icosahedral cage structure as well as the neglible influence of the D_2 messenger atoms.

The influence of partial deiodination of the parent anion $B_{12}I_{12}{}^{2-}$ on the structure of these dodecaborates is probed by increasing the collision energy in the nanospray ion source. For lower energy collision conditions fragmentation is observed under the consecutive loss of either an iodide anion (I^-) or an atomic iodine radical ($I^\bullet$) in the mass spectrum (see Figure E.1).

The ionic fragments formed from CID are the doubly charged $B_{12}I_{11}^{2-}$ and $B_{12}I_{10}^{2-}$, and the singly charged $B_{12}I_{11}^{-}$, $B_{12}I_{10}^{-}$ and $B_{12}I_{9}^{-}$. As previously found, a higher probability for $I^{\bullet}$ loss in the first fragmentation step is observed even though I^{-} is energetically highly favored, due to spin crossing between triplet and singlet state during iodine abstraction[55]. Increasing the collision energy leads to more extensive fragmentation (see Figure E.1) and singly charged anions, $B_{12}I_{n}^{-}$, are detected down to $n = 5$.

The IRPD spectra of D_2-tagged $B_{12}I_{12}^{2-}$, $B_{12}I_{9}^{-}$, $B_{12}I_{8}^{-}$, and $B_{12}I_{7}^{-}$ are shown in Figure 5.5 in the spectral range from 750 to 1300 cm^{-1} (a–c) and 750 to 1700 cm^{-1}(d). The spectra for $n = 12$, $n = 9$ and $n = 8$ species are very similar, exhibiting a dominant absorption feature (labeled A in Figure 5.5) in-between 850 and 1000 cm^{-1} and no significant signal above 1000 cm^{-1}, suggesting that the B_{12}-dodecehedron remains intact upon removal of up to four I-units. On the other hand, the $n = 7$ spectrum looks considerably more complex and distinctly different. A series of absorption peaks is observed extending from 750 cm^{-1} up to 1300 cm^{-1} that can be grouped into two sets of bands labeled A (750–1050 cm^{-1}) and B (1050–1300 cm^{-1}) in Figure 5.5. The increase in the number of IR-active bands as well as the observation of substantial IR-activity above 1050 cm^{-1} implies a more significant structural change of the B_{12} core concomitant with a stiffening of the B–B bonds upon removal of the fifth I-atom ($n = 8 \rightarrow n = 7$).

The above observations can be rationalized by the comparison of the experimental IRPD spectra to the simulated IR spectra of the global minimum energy structures for $n = 12$, 9, 8 and 7, also shown in Figure 5.5. For reasons of simplicity, the simulated IR spectra of the all-^{11}B isotopomers are shown, as the number of (symmetry-inequivalent) $^{10}B_2{}^{11}B_{10}$-isotopomers, which are probed in the experiment, increases significantly upon partial deiodination. The differences between the predicted spectra of these two isotopologues are expected to be similar to those described above for the spectra of $B_{12}I_{12}^{2-}$ and hence deviations are expected to be roughly within ± 30 cm^{-1} of the predicted all-^{11}B spectra. For all deiodinated species down to $n = 7$ quasi-icosahedral B_{12}-cages are found to be lowest in energy. Indeed, the simulated IR spectra of the cage structures for $n = 12$ to $n = 7$ are very similar in that they are all dominated by a strong absorption around ~ 930 cm^{-1} with some weaker features at lower energies and negligible IR-activity above 1000 cm^{-1}. Satisfactory agreement between experimental and simulated spectra is only found for $n = 12$, $n = 9$ and $n = 8$ in Figure 5.5, while the simulated spectrum of the icosahedral minimum energy structure for $n = 7$ cannot account for the series of IR active bands (feature B) above 1050 cm^{-1} observed experimentally, indicating that a different structural isomer is responsible for this IRPD spectrum.

In order to characterize the IRPD spectrum for $n = 7$ in more detail we compare it to simulated spectra of several low energy $B_{12}I_{7}^{-}$ isomers in Figure 5.6. The energetics of these anions has been discussed in detail earlier [55]. All isomers have been taken into account that can be created either by a decorated icosahedron or by a ring-decorated B_{12} ring. Full geometry optimization reveals that for $n = 7$ closed and open cages as well as quasi-planar structures are close in energy and even more so in Gibbs free energy (ΔG). In

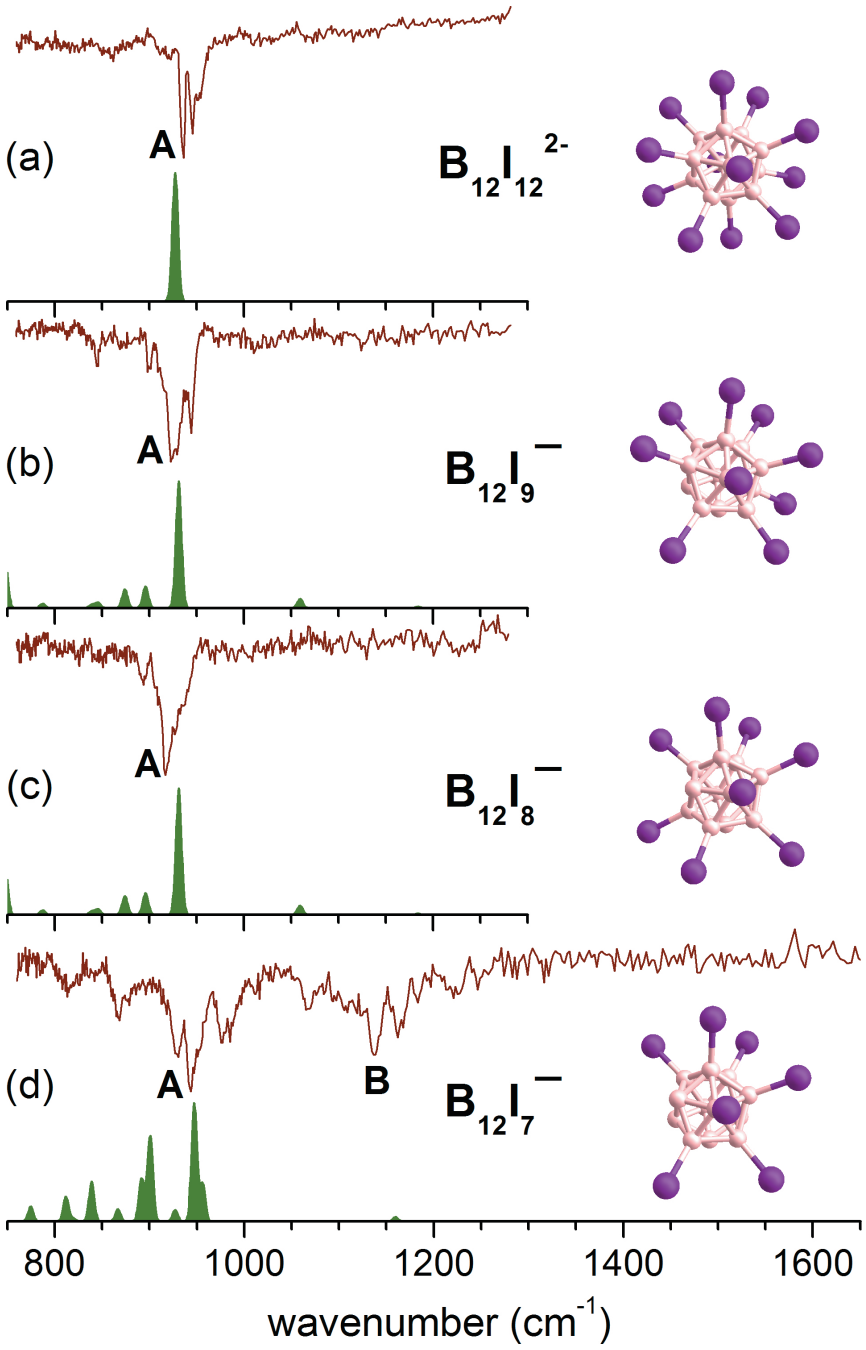

Figure 5.5: Comparison of the experimental IRPD spectra (upper traces) of D_2-tagged (a) $B_{12}I_{12}^{2-}$, (b) $B_{12}I_9^-$, (c) $B_{12}I_8^-$ and (d) $B_{12}I_7^-$ to the corresponding simulated linear absorption spectra (lower traces) of the lowest energy quasi-icosahedral cage structures (all-^{11}B isotopomers). The corresponding minimum energy structures are shown on the right. Bands are labeled with capital letters.

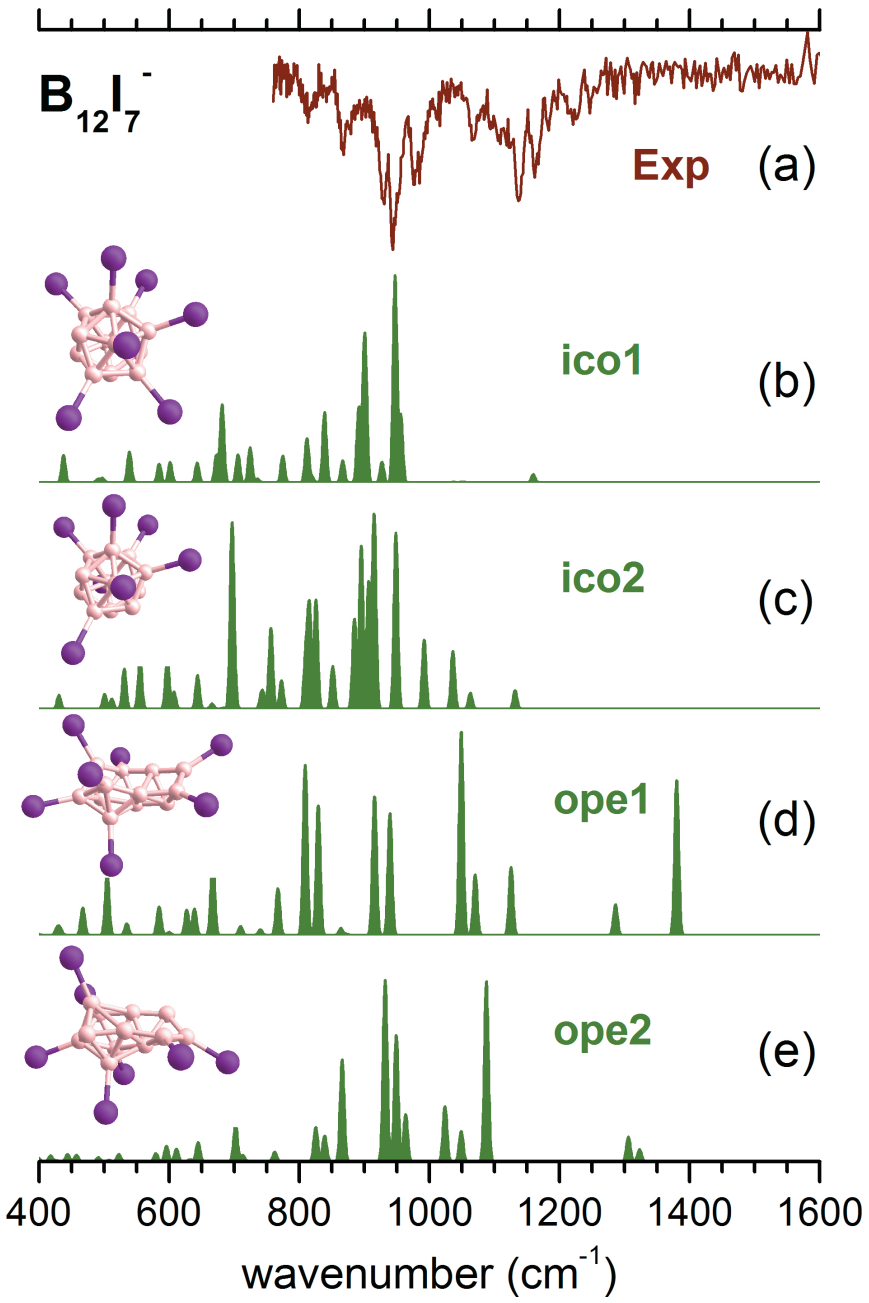

Figure 5.6: Comparison of the experimental IRPD spectrum of D_2-tagged $B_{12}I_7^-$(a) to the simulated linear absorption spectra of two low energy quasi-icosahedral cage (b, c) and two open structures (d, e), respectively. The DFT minimum energy structures corresponding to the simulated spectra are shown on the right (see Table 5.2 for relative energies).

fact, isomeric mixtures are feasible depending on the internal temperature. Tables 5.2, E.2 and E.3 summarize the relative energies including zero-point and thermal contributions. Note that the employed DFT level of theory (BP86) yields excellent structures and vibrational frequencies, but performs poorly in terms of total energy [325]. Therefore, we calculate the relative energies using coupled cluster theory on top of DFT-optimized structures, and add zero-point energy and thermal contributions as obtained from the DFT calculations.

Table 5.2: Relative energies (in kJ/mol) without (ΔE) and with zero-point-energy corrections (ΔE_{ZPE}), enthalpy (ΔH) and Gibbs free energy (ΔG) for various temperatures (indicated as subscript) for the low-energy isomers of icosahedral (labeled ico) as well as open (ope) structures of $B_{12}I_7^-$ at CCSD(T)/B/6-311+G*/I/LanL2DZ level of theory, with thermal contributions calculated at the BP86 level. The closed icosahedral structure of $B_{12}I_7^-$ is selected as the reference.

	ico1	ope1	ope2
ΔE	0.0	68.7	117.9
ΔE_{ZPE}	0.0	57.8	106.4
$\Delta H_{300\mathrm{K}}$	0.0	60.2	111.5
$\Delta G_{300\mathrm{K}}$	0.0	49.7	98.4
$\Delta H_{600\mathrm{K}}$	0.0	61.2	115.2
$\Delta G_{600\mathrm{K}}$	0.0	38.6	72.9
$\Delta H_{900\mathrm{K}}$	0.0	59.5	116.2
$\Delta G_{900\mathrm{K}}$	0.0	27.7	51.5
$\Delta H_{1200\mathrm{K}}$	0.0	57.2	116.6
$\Delta G_{1200\mathrm{K}}$	0.0	17.4	29.9
$\Delta H_{1500\mathrm{K}}$	0.0	54.9	116.9
$\Delta G_{1500\mathrm{K}}$	0.0	7.7	8.2
$\Delta H_{1800\mathrm{K}}$	0.0	52.4	117.1
$\Delta G_{1800\mathrm{K}}$	0.0	–1.5	–13.6

The comparison in Figure 5.6 allows for some additional insights. First, neither the lowest energy cage structure (ico1), *i.e.* the global minimum energy structure, nor energetically higher-lying states (ico2–4) in the quasi-icosahedral cage manifold (see also Table E.2) can account for the pronounced IR activity above 1050 cm^{-1}. On the other hand, the IR spectra of the open structures (ope1–4) do show relatively strong IR absorptions($>$ 100 km/mol) in the 1050–1400 cm^{-1}spectral range, suggesting that open structures do contribute significantly to the experimental IRPD spectrum for $n = 7$. This confirms previous predictions based on ΔG estimates, which suggested that at higher temperatures($\geq$ 1200 K) population of cage and open isomers is competitive, as the vibrational contributions to the internal energy U and to the entropy S favor the open over the cage structures [55]. Note, the conditions in the ion formation process (sCID) can indeed lead to internal energies, which correspond to thermal energies larger than 1000 K [326]. While agreement with the spectrum of the lowest energy open structure ope1 is equally poor as observed for the spectra of the cage structures, a

better agreement is observed for the higher energy isomer ope2 (Figure 5.6(e)). The difference in ΔG between ico1 and the open structures ope1 and ope2 is significant (> 50 kJ/mol) at low temperatures, but gets competitive above 1500 K (Table 5.2). Note that ions in our experiment are thermalized to cryogenic temperatures prior to IR irradiation, otherwise they would not form messenger complexes with D_2. Hence, the ions, initially formed by sCID under conditions corresponding to the high internal temperatures discussed above, are subsequently kinetically trapped, due to the presence of sufficiently high energy barriers separating the different structural families of these boron-containing clusters, preventing the isomerization back to the energetically most favored structures at lower temperatures.

5.2.4 Conclusions

Saturated boron-hydrogen and boron-halogen compounds are classified by the Wade's rules and the structure of pure boron clusters has also been studied extensively, but there is only scarce information regarding intermediate compounds that fall outside of the classical rules in boron chemistry. Here, we presented first results on the gas phase vibrational spectroscopy of $B_{12}I_{12}{}^{2-}$ and the partially deiodinated $B_{12}I_n{}^-$ ions with $n = 7 - 9$. The IRPD spectrum of the $n = 7$ anion exhibits characteristics IR bands above 1000 cm^{-1}, that are not observed in the spectra of the larger clusters. Aided by electronic structure calculations these high energy IR active modes are identified to originate from open B_{12}-framework structures and hence the $n = 7$ cluster is the largest partially deiodinated cluster to prefer such an open structure under the present experimental conditions. The formation of more open structures is not favored energetically, but the differences in the vibrational contributions to the Gibbs free energy make the isomerization competitive at higher temperatures, *i.e.*, under conditions characteristic for the sCID process. The properties of the underlying potential energy landscape then prevent reformation of the caged structures on the time scale of collisional cooling of the cluster ions.

5.3 Summary

A number of theoretical studies on the $B_{13}{}^+$ cluster have predicted a planar global minimum structure composed of two concentric rings, an inner B_3 ring surrounded by a B_{10} ring. A delocalized bonding between the two boron rings grants stability and give rise to a small barrier towards the internal rotation of the inner triangle. The examination of the experimental vibrational spectrum in comparison with BOMD and DFT computations (Section 5.1) confirms the predicted structure and reveals the spectroscopic signature of the internal rotation. In fact, the experimental spectrum matches the dynamic simulations predicting a broadening and an intensity decrease of the band associated with the in-plane B_3 frustrated rotation due to the thermal activation of the mutual quasi-rotation between the two rings.

The perhalogenated dodecaborate $B_{12}I_{12}{}^{2-}$ exhibits a B_{12} icosahedral cage structure with each boron atom decorated with an iodine atom. The neutral B_{12} cluster on the contrary

favors a planar arrangement. The results shown in Section 5.2 confirm the icosahedral cage structure of $B_{12}I_{12}^{2-}$ and identify $B_{12}I_7^-$ as the largest partially deiodinated cluster with an open B_{12} cage.

An intriguing boron structure that exhibits 3D aromaticity is the recently observed all-boron fullerene B_{40}^-. Fig. 5.7 presents Kr-tagged IRPD spectra of the cationic B_{39}^+, B_{40}^+ and B_{41}^+. The three spectra display a similar pattern, indicating that the clusters share a common structural motif, even though structural assignment has not yet been achieved and more computations are required. However, preliminary results suggest that the fullerene-like structure of B_{40}^- is not retained in the cation.

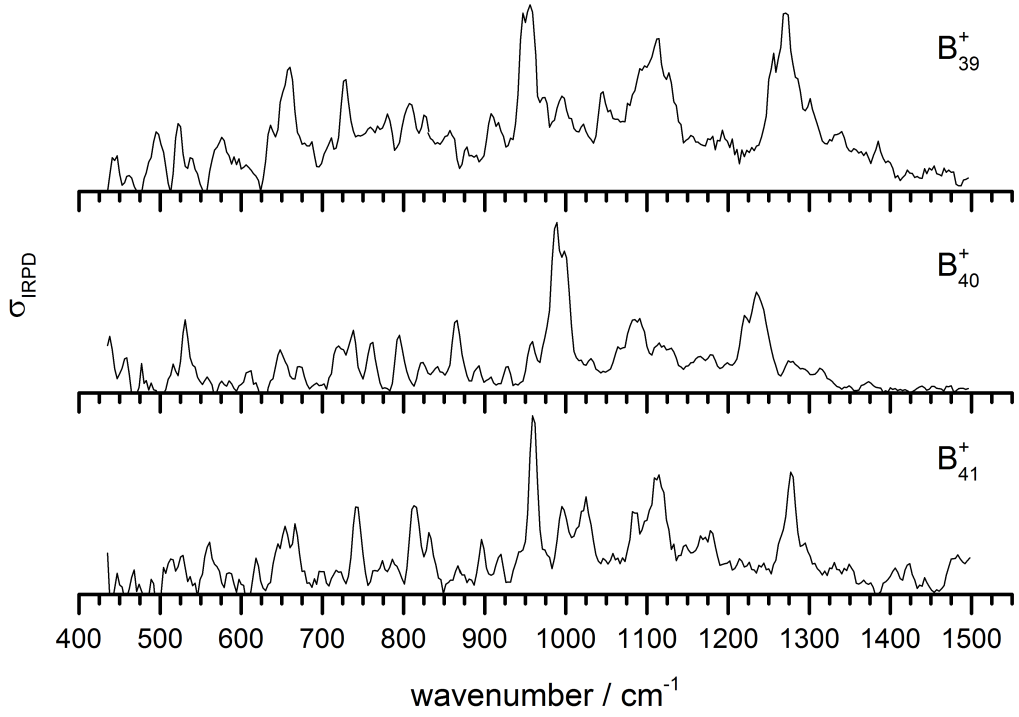

Figure 5.7: Comparison of the vibrational spectra of B_{39}^+, B_{40}^+ and B_{41}^+. The spectra are obtained by predissoctiation of the complexes formed by the ^{11}B isotopically enriched clusters with Kr atoms in the ion trap (69 K).

6 Gas Phase Vibrational Spectroscopy of the Protonated Water Pentamer: The Role of Isomers and Nuclear Quantum Effects*

Understanding the origin of all the features in the vibrational spectra of even the smallest protonated water clusters is challenging. Common theoretical approaches struggle at coping with either anharmonic or nuclear quantum effects. For example, reproducing the vibrational spectrum of the $H_5O_2^+$ cluster, required a 15 dimensional full quantum mechanical treatment of the nuclear motion combined with accurate potential energy and dipole surfaces [327]. The debated origin of absorption bands in the IR spectrum of the protonated water pentamer, $H^+(H_2O)_5$, which are not readily assignable to fundamental transitions, resulted in controversies over its structural assignment. This chapter presents IRPD experiments on the protonated water pentamer and its fully deuterated isotopologue, $D^+(D_2O)_5$, in combination with harmonic and anharmonic electronic structure calculations as well as RRKM modelling. The obtained results clear existing doubts over the structural assignment and over the vibrational fingerprints of the O–H stretches of the embedded distorted H_3O^+. Finally, the results are extrapolated in the context of a follow-up collaborative study that provided crucial information for understanding the proton transfer mechanism.

6.1 Introduction

How ions are hydrated has intrigued chemists since the birth of the field of Physical Chemistry [328]. Proton hydration, in particular, is of fundamental importance in chemical, biological and atmospheric processes, but the molecular level interpretation of the anomalously high mobility of protons in aqueous solutions remains hotly debated [329]. Size-selected protonated water clusters, $H^+(H_2O)_n$, isolated in the gas phase, play an important role in clarifying the spectroscopic markers that encode the collective mechanics involved in long range proton translocation. The advantage of the clusters is that they allow direct spectroscopic char-

*Chapter based on: Matias R. Fagiani, Harald Knorke, Tim K. Esser, Nadja Heine, Conrad T. Wolke, Sandy Gewinner, Wieland Schöllkopf, Marie-Pierre Gaigeot, Riccardo Spezia, Mark A. Johnson, and Knut R. Asmis, *Phys. Chem. Chem. Phys.* **2016**, *18*, 26743–26754 DOI: 10.1039/c6cp05217g

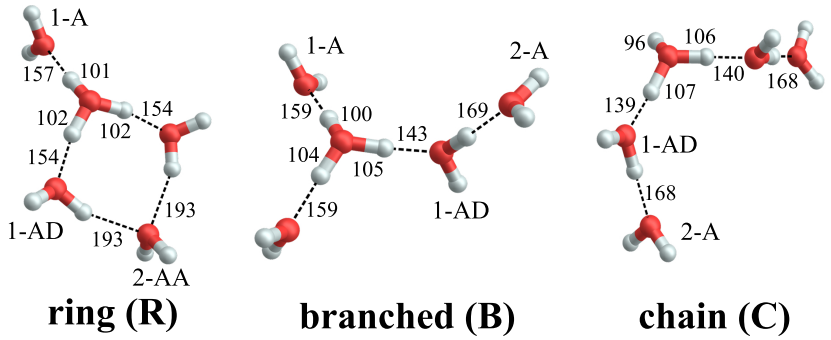

Figure 6.1: B3LYP-D3/aug-cc-pVTZ minimum-energy structures of the three constitutional isomers discussed in the text. Intramolecular hydronium ion O–H and intermolecular hydrogen bond lengths are reported in pm. Water molecules are classified according to their location in the first (1) or second (2) hydration shell of H_3O^+, and their function as hydrogen bond acceptor (A) or donor (D).

acterization of key local hydration motifs that are metastable in solution, but can occur naturally in the size- and temperature-dependent structures of the clusters. Since protonated water clusters can be characterized experimentally with high selectivity and sensitivity and are also amenable to higher level quantum chemical calculations, such measurements deliver stringent benchmarks for evaluating the validity of approximations necessary for treating ions in extended solvation environments. However, the widely accepted structural assignment of small protonated water clusters, in particular that of the protonated water tetramer and pentamer, has recently been drawn into question based on the implications of ab initio molecular dynamics (AIMD) simulations [85, 330].

In this study, we characterize the gas-phase vibrational spectroscopy of the protonated water pentamer over nearly the complete IR spectral range and show experimentally, using an isomer-specific, double resonance technique as well as temperature-dependent measurements (13–250 K), that the observed IR transitions are due to a single spectroscopically unique species. We then address the assignments of the strong bands in the cold spectrum to fundamentals expected for the branched structure originally proposed by Jiang *et al.* [84] by comparison to anharmonic spectra from electronic structure calculations. Finally, we use RRKM theory to explore the kinetic stability of the isomers at low temperatures, highlighting the importance of considering nuclear quantum effects.

The vibrational spectroscopy of the protonated water pentamer has been studied by several groups. Jiang *et al.* measured the infrared photodissociation (IRPD) spectrum of $H^+(H_2O)_5$ in the O–H stretching region (2700–3900 cm^{-1}) at an estimated temperature of 170 K [84]. Aided by harmonic vibrational frequencies and intensities from electronic structure calculations, they identified an acyclic, branched isomer (labelled **B** in Fig. 6.1) as the signal carrier in the IRPD spectrum. Temperature-dependent measurements confirmed that the IRPD spectrum

was free of contributions from other isomers. Subsequently, Headrick *et al.* probed colder clusters using argon-tagging [79]. They measured IRPD spectra down into the fingerprint region (1000–3900 cm^{-1}), identifying the evolution of the spectral signature of the hydrated proton with cluster size. These studies confirmed the assignment to the branched isomer **B** [79]. The effect of messenger-tagging on the IRPD spectra of protonated water clusters was systematically studied by Mizuse *et al.* also confirming the presence of a single isomer (**B**) [80]. Tagging with H_2, Ar and Ne leads to sharper vibrational features due to colder clusters but hardly perturbs the IRPD spectrum. Douberly *et al.* then studied the effect of deuteration on the band pattern in the IRPD spectrum in the O–D stretching region (2300–2900 cm^{-1}) [261]. They found that the spectra of $H^+(H_2O)_5$·Ar and $D^+(D_2O)_5$·Ar both agree best with the predicted harmonic spectrum of the branched isomer **B** and that the contribution from other isomers was insignificant. This is particularly remarkable, since their electronic structure calculations predict that **B** is not the global minimum energy structure [261].

Electronic structure calculations[84, 85, 261, 331–335] (Monte Carlo, DFT and MP2) of bare $H^+(H_2O)_5$ consistently predicted a cyclic fourmember ring with an Eigen core (labelled **R** in Fig. 6.1) as the global minimum-energy structure, closely followed by two non-cyclic Eigen isomers: one branched (**B**: +3.7 kJ/mol)[335] and the other non-branched (**C**: +17 kJ/mol) [335]. When zero-point energy (ZPE) is considered, the energetic ordering changes and **B** is found to be 0.3 kJ/mol more stable than **R** [261]. Such a change in ordering is not found for the perdeuterated analogue because its ZPE is smaller. In both cases, however, **B** is favoured by entropy and it represents the global minimum above 50 K in terms of free energy [261]. The comparison of the computed harmonic spectra with the experimental IR spectra, in particular in the O–H (O–D) stretching region, supports the assignment of the protonated water pentamer and of its fully deuterated isotopologue to the branched isomer **B** [79, 80, 84, 261]. The agreement is less satisfactory in the fingerprint region, namely for the Eigen core O–H stretching mode, which involves a displacement towards the single acceptor–single donor (1-AD) H_2O. It is predicted by MP2 calculations to occur about 460 cm^{-1}above the experimentally observed band at 1885 cm^{-1}[79]. However, Vibrational Self-Consistent Field calculations (VSCF) accurately recover the red shift of this band, thus supporting the assignment to isomer **B** [79]. The complexity of this assignment is apparent, however, by the fact that application of the VPT2 perturbative treatment supports the assignment of a previously unassigned, relatively strong feature at 1470 cm^{-1}(labelled a_9 in Fig. 6.3) to the key O–H stretching band of the embedded H_3O^+ moiety [82]. The appearance of such unassigned "extra features" (*i.e.* , those not readily assignable to fundamentals) [79, 82] has, in fact raised the idea that distinct isomers may be in play, and indeed the assignment of the vibrational spectrum to the branched isomer **B** has recently been challenged by Kulig and Agmon, based on insights derived from AIMD simulations [85]. These authors suggest that two other isomers contribute to the observed spectrum: the cyclic Eigen isomer **R** and the higher energy chain isomer **C**. A major motivation for the present study was, therefore, to address the heterogeneity in the spectrum of the light isotopologue and to follow how the

bands evolve with increasing temperature as well as upon isotopic substitution.

6.2 Experimental Methods

IRPD experiments are conducted using the 6 K ion-trap triple mass spectrometer described in Chapter 3. Clusters are produced in a nanospray ion-source using a 10 mM H_2SO_4 in CH_3OH/H_2O (1:1, v:v) solution and D_2SO_4 in a CD_3OD/D_2O (2:1, v:v) solution for the all-H and all-D isotopologues, respectively. The ions of interest are thermalized at room temperature in a gas-filled ion guide and then mass-selected using a quadrupole mass filter and focused in a radiofrequency (RF) ring-electrode ion-trap. The trap, filled with pure D_2 buffer gas, is cooled with a closed-cycle He cryostat and held at temperatures between 13 K and 250 K. Many collisions of the trapped ions with the buffer gas provide gentle cooling of the internal degrees of freedom close to the ambient temperature and typically avoid the production of kinetically trapped species. At sufficiently low ion-trap temperatures, ion-messenger complexes are formed *via* three-body collisions [112, 310]. All ions are extracted either every 100 ms or 200 ms, depending on the lasers used, and focused both temporally and spatially into the centre of the extraction region of an orthogonally mounted reflectron time-of-flight (TOF) tandem photofragmentation mass spectrometer. Here, the ions are irradiated with a counter-propagating IR laser pulse produced either by one of the two OPO/OPA/$AgGaSe_2$ IR laser systems (700–4500 cm^{-1}) or by the FHI FEL (210–3000 cm^{-1}). More details on the laser sources are provided in Section 3.5. All parent and photofragment ions are then accelerated towards an MCP detector. An IRPD spectrum is recorded by averaging over 50–200 TOF mass spectra per wavelength and scanning the wavelength of the laser pulse. The photodissociation cross section σ_{IRPD} is determined as described in Section 3.4.

The covered spectral range from 220–4000 cm^{-1}requires the use of three different laser configurations. The individual spectra covering these overlapping spectral regions (200–1000 cm^{-1}, 900–2300 $cm^{-1}$and 2000–4000 cm^{-1}) are then scaled in intensity such that the intensity of common peaks match, in order to correct for changes in laser beam/ion cloud overlap.

Alternatively, isomer-specific IR^2MS^2 double resonance measurements [83, 157, 336] can be performed using the analogous 10 K setup (see Chapter 3 and Section 3.4.1), employing two IR laser pulses [108, 109]. The first laser pulse generates a set of photofragment ions, which are separated from parent ions in the 180° reflectron stage of the tandem TOF mass-spectrometer, where they separate in time and space according to their mass-to-charge ratio. They are then refocused between the extraction plates, and the parent ion packet is irradiated with a second, properly timed laser pulse to generate a second set of photofragment ions. All ions located between the acceleration plates are then reaccelerated and mass analysed using the linear TOF stage[12, 311].

We used two ways to measure IR^2MS^2 spectra, which differ in the sequence of the probe and scan laser pulses. If the probe pulse (fixed wavelength) interacts with the ions after

the scan pulse (tuneable wavelength), the IR^2MS^2 spectrum manifests itself in the form of dips in the otherwise constant fragment ion signal from the probe pulse (ion-dip technique). If the scanned pulse is applied after the probe pulse, then two TOF spectra are acquired, one with and the other without the probe pulse using an additional mechanical chopper (a population-modulation or hole-burning technique). In this case, the IR^2MS^2 spectrum is obtained by subtracting these two TOF spectra. Probe laser pulses with wavenumbers larger than 2300 $cm^{-1}$are typically generated with one of the OPO/OPA systems while those at smaller wavenumbers (< 2300 cm^{-1}) are produced by the FHI FEL. The macropulse duration of the IR FEL pulses (~ 10 μs) requires that the FEL laser beam is aligned counter-propagating to the ion cloud extracted from the trap and prior to acceleration into the tandem TOF mass spectrometer to ensure a sufficient temporal overlap. Hence, the FHI FEL laser pulse always needs to be timed prior to the laser pulse from the OPO/OPA system, which is sufficiently short in duration (< 7 ns) that the fast (few keV) ions can be efficiently irradiated.

6.3 Computational Methods

Quantum Chemistry

Electronic structure calculations were performed using the Gaussian 09 rev. D.01 software package [210]. We optimized geometries of a number of energetically low-lying isomers using density functional theory (DFT), in particular, the B3LYP functional [202] in combination with the 6-311++G(3df,3pd) and the aug-cc-pVTZ basis sets [320, 337–339]. Additionally, we checked the influence of the dispersion interactions by using the D3 version of Grimme's dispersion correction [276]. Tight convergence criteria and the "superfine" grid option are employed. We identified transition states (TS) of the unimolecular isomerization reactions by locating first-order saddle points along the reaction coordinate. The reaction paths were followed using the intrinsic reaction coordinate (IRC) method (See Fig. F.4 and F.5) [340, 341]. Vibrational harmonic frequencies of minima and TS configurations were computed at the same level of theory. To account for anharmonic effects as well as systematic errors on the harmonic force constants, we determined scaling factors on the basis of a comparison of the IRPD spectra with harmonic spectra of isomer **B** for both the all-H and all-D isotopologues. Two scaling factors for each method (see Table F.4), one for the spectral region below 1500 cm^{-1}(1100 $cm^{-1}$for the perdeuterated complex) and one for the higher energy region, were calculated with a least squares procedure by minimizing the residuals as proposed by Scott and Radom [317]. Additionally, we performed anharmonic frequency calculations using the Second-order Vibrational Perturbation Theory (VPT2) method as implemented by Bloino and Barone [278]. To obtain more reliable electronic energies and further improve the energetic description of the isomers, we performed CCSD(T)/aug-cc-pVTZ single point calculations at the DFT geometries.

RRKM rate constants and kinetics

Microcanonical isomerization rate constants of the protonated water pentamer *k(E)*, where E refers to the internal energy of the system, were calculated using RRKM theory [342]. The sequential kinetic scheme consisting of three isomerization equilibria is depicted in Fig. 6.2. We used CCSD(T) energies of the B3LYP-D3 structures plus the B3LYP-D3 ZPEs, derived from scaled harmonic wavenumbers. To obtain the rate constants, we used the code written by Zhu and Hase [343], using the standard formula [342]:

$$k(E) = \frac{\sigma}{h}\frac{N^{\#}(E-E_0)}{\rho(E)}, \tag{6.1}$$

where σ is the reaction path degeneracy, E_0 is the unimolecular threshold, $N^{\#}(E-E_0)$ is the TS sum of states and $\rho(E)$ the reactant density of states. $N^{\#}(E-E_0)$ and $\rho(E)$ refer only to active degrees of freedom. The reaction path is doubly degenerate for all isomerizations considered. Note that the contribution from rotational excitation was neglected, since the minima and TS configurations have very similar moments of inertia and this thus cancelled out. Indeed, test calculations with different J values provided consistent results. Classical RRKM rate constants were calculated disregarding quantization of vibrational modes with classical state counting. In contrast, to obtain the quantum rate constants, ZPEs were taken into account and state counting was performed with the direct count method using the Beyer–Swinehart algorithm [344].

From microcanonical rate constants and densities of states, the canonical rate constants can be expressed as [345]

$$k(T) = \frac{1}{Q(T)}\mathcal{L}[k(E)\rho(E)], \tag{6.2}$$

where $\mathcal{L}$ is the Laplace transform operator and $Q(T)$ is the partition function, which can be expressed as the Laplace transform of density of states, $Q(T) = \mathcal{L}[\rho(E)]$.

We then solved the four kinetic differential equations associated with the system for different initial conditions to study the kinetic stability of the four isomers:

$$\frac{\mathrm{d}[\mathbf{R}]}{\mathrm{d}t} = -k_1[\mathbf{R}] + k_{-1}[\mathbf{B}]\,, \tag{6.3}$$

$$\frac{\mathrm{d}[\mathbf{B}]}{\mathrm{d}t} = k_1[\mathbf{R}] - (k_{-1}+k_2)[\mathbf{B}] + k_{-2}[\mathbf{B2}]\,, \tag{6.4}$$

$$\frac{\mathrm{d}[\mathbf{B2}]}{\mathrm{d}t} = k_2[\mathbf{B}] - (k_{-2}+k_3)[\mathbf{B2}] + k_{-3}[\mathbf{C}] \quad \text{and} \tag{6.5}$$

$$\frac{\mathrm{d}[\mathbf{C}]}{\mathrm{d}t} = k_3[\mathbf{B2}] - k_{-3}[\mathbf{C}]\,. \tag{6.6}$$

The kinetic constants k_1, k_{-1}, k_2, k_{-2}, k_3 and k_{-3} of the isomerization reactions considered are defined in Fig. 6.2. The system of differential equations was numerically solved using the ODE45 solver as implemented in Matlab [346, 347] and yields the time evolution of the

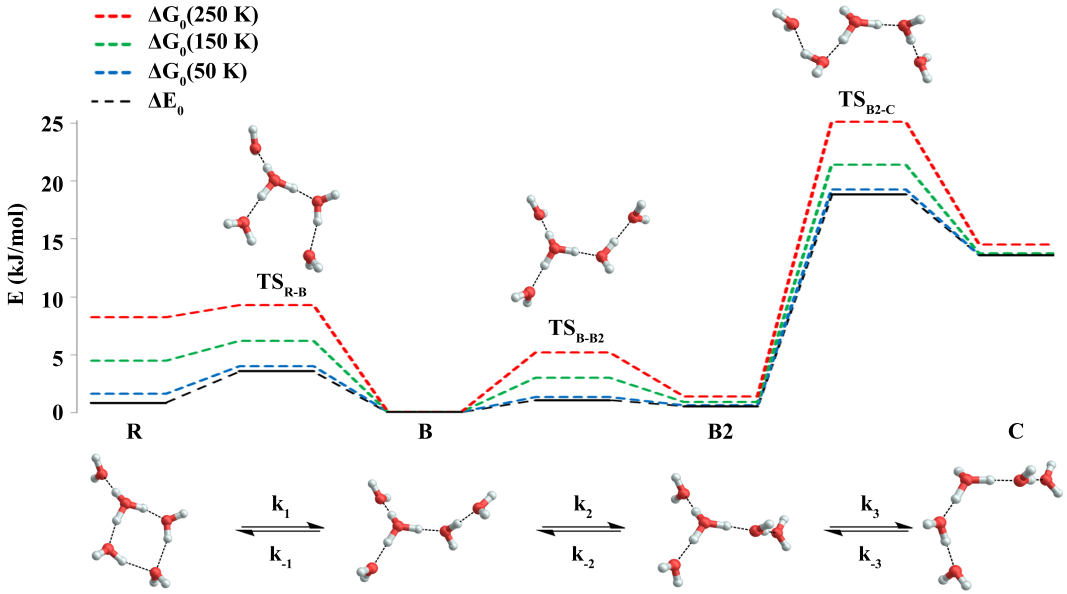

Figure 6.2: B3LYP-D3/aug-cc-pVTZ minimum-energy and TS structures of the protonated water pentamer discussed in the text. The energy diagram reports relative energies (ΔE_0), determined from CCSD(T) energies plus DFT ZPEs, and relative Gibbs free energies (ΔG_0), determined from CCSD(T) energies plus thermal corrections to Gibbs free energies at 50, 150 and 250 K. All energies are given in kJ/mol (see Table 6.2). The bottom panel illustrates the sequence of the equilibrium reactions assumed for the RRKM calculations.

relative isomer populations.

6.4 Results and discussion

Fig. 6.3 shows a comparison of the IRPD spectra of the D_2-tagged protonated water pentamer and its fully perdeuterated isotopologue from 210 $cm^{-1}$to 4000 cm^{-1}. Band positions are listed in Table 6.1. For better comparability, a scaling factor (1/1.36) is used for the alignment of the two wavenumber scales, which brings the sharp water bending fundamentals of the two isotopologues (a_8 and b_8) into alignment. The scaling factor is close to the theoretical value of 1/1.37 that is expected for isolated O–H vs. O–D oscillators. The spectra are in good agreement with previous measurements (1000–4000 $cm^{-1}$for $H^+(H_2O)_5$ and 2300–2900 for $D^+(D_2O)_5$) considering the different experimental setups [79, 80, 84, 261]. Additionally, the D_2-tagged IRPD spectrum of $D^+(D_2O)_5$ (1000–3000 cm^{-1}) measured at the Yale photofragmentation mass spectrometer [348] confirms the reproducibility of the experimental results presented here (see Fig. F.3). The striking resemblance of the two spectra shown in Fig. 6.3 provides unambiguous evidence that both spectra probe signal carriers with similar structures and, in particular, identical connectivity. Note that the absorption near the key a_9 feature is

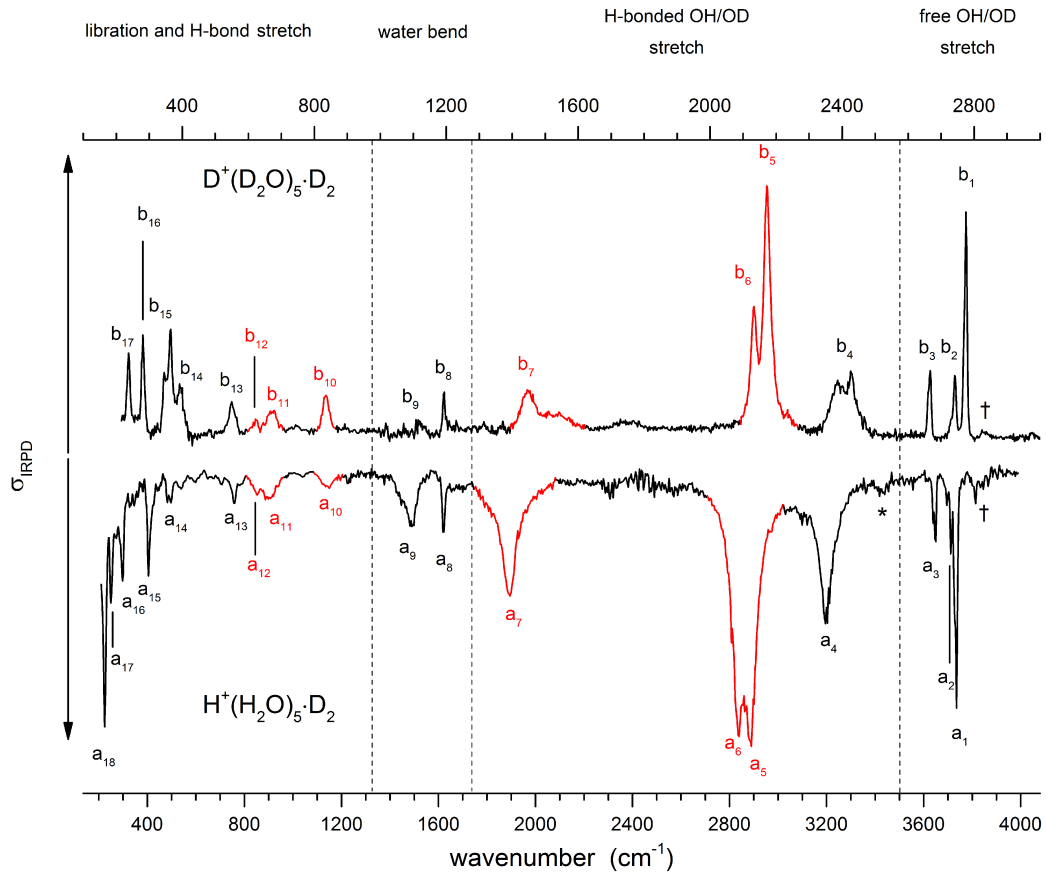

Figure 6.3: IRPD spectra of D_2-tagged isotopologues of the protonated water pentamer: $D^+(D_2O)_5$ (top) and $H^+(H_2O)_5$ (bottom). For better comparability the spectra are plotted against opposing ordinates and the abscissa of the top spectrum has been scaled by 1.36 (see text). Bands coloured red indicate modes assigned to the hydronium ion. See Table 6.1 for band assignments.

substantially less intense in the spectrum of the perdeuterated species, as are the weaker features that appear higher in energy, labelled by * and †. Such selectivity in the affected bands could arise from the appearance of a second isomer in the all-H isotopologue, or from the suppression of anharmonic bands in the heavy isotopologue. As mentioned above, Kulig and Agmon [85] have recently invoked an assignment scheme for the $H^+(H_2O)_5$ based on two isomers (**R** and **C** in Fig. 6.2) and not involving isomer **B**. We address these key issues of isomeric composition and temperature dependence in the next two sections.

Table 6.1: Experimental band positions, scaled harmonic vibrational wavenumbers (both in cm^{-1}) and assignments of the features observed in the IRPD of D_2-tagged $H^+(H_2O)_5$ and $D^+(D_2O)_5$ shown in Fig. 6.3

Label		**Exp.**		**Theory**				**Assignment**
all-H	all-D	all-H[a]	all-D[a]	harm. all-H[b]	VPT2 all-H[c]	ham. all-D[b]	VPT2 all-D[c]	
†	†	3814	2824		3823, 3825, 3850		2808, 2808, 2810	Combination bands[d] (see text)
a_1	b_1	3732	2775	3737, 3727, 3727	3694, 3722, 3723	2772, 2765, 2764	2764, 2759, 2759	Free O–H antisym. H_2O stretch (2-A-H_2O) Free O–H antisym. H_2O stretch (1-A-H_2O)
a_2	b_2	3710	2741	3703	348	2729	2720	Free O–H antisym. H_2O stretch (1-AD-H_2O)
a_3	b_3	3647	2667	3648 3640, 3639	3629 3640, 3639	2658 2653, 2652	2657 2654, 2653	Free O–H sym. H_2O stretch (2-A-H_2O) Free O–H sym. H_2O stretch (1-A-H_2O)
*		3420			3457, 3406			Combination bands[d] (see text)
a_4	b_4	3200	2407	3220	3263	2367	2350	H-bonded O–H stretch (1-AD-H_2O)
a_5	b_5	2883	2175	2973	2862	2180	2115	H-bonded O–H stretch ($H_3O^+\cdots$1-A-H_2O)
a_6	b_6	2837	2133	2908	2826	2161	2097	H-bonded O–H stretch ($H_3O^+\cdots$1-A-H_2O)
a_7	b_7	1889	1446	2238	1548	1681	1328	H-bonded O–H stretch ($H_3O^+\cdots$1-AD-H_2O)[e]
a_8	b_8	1618	1194	1649, 1627 1586, 1576 1568, 1560	1598, 1537 1574, 1583 1581, 1564	1205, 1187 1175, 1169 1159, 1152	1173, 1160 1165, 1171 1158, 1131	A-H_2O bend
a_9	b_9	1470	1115	1560	1564	1152	1131	Combination bands and 1-AD-H_2O bend[e]
a_{10}	b_{10}	1150	836	1134	1126	844	821	H_3O^+ umbrella
a_{11}	b_{11}	895	672	913	910	672	686	H_3O^+ libration
a_{12}	b_{12}	850	621	834	856	611	627	H_3O^+ libration
a_{13}	b_{13}	760	550	768	743	566	567	1-AD-H_2O libration
a_{14}	b_{14}	490	392	494	457	377	406	1-AD-H_2O libration
a_{15}	b_{15}	405	365	377	397	348	365	HB stretch (1-AD-$H_2O\cdots H_3O^+$)
a_{16}	b_{16}	298	281	345, 319	326, 307	287, 268	258, 257	HB stretch (1-A-$H_2O\cdots H_3O^+$) 1-A-H_2O libration[e]
a_{17}	b_{17}	248	237	297, 274	261, 304	244, 232	230, 223	HB stretch (1-A-$H_2O\cdots H_3O^+$) 1-A-H_2O libration[e]
a_{18}		226		254, 238	183, –83			HB stretch (1-A-$H_2O\cdots$2-H_2O) 1-AD-H_2O libration[e]

[a] Band positions are given with an error of ±5 cm^{-1}. [b] B3LYP-D3/aug-cc-pVTZ harmonic wavenumbers of the all-H (all-D) isotopologue, scaled by 0.962 (0.973) above and 0.908 (0.927) below 1500 cm^{-1}(1100 cm^{-1}). [c] Anharmonic VPT2/B3LYP/6-311++G(3df,3pd). [d] Only combination bands with intensities higher than 2 km/mol are considered. [e] Tentative assignment.

Double resonance IR^2MS^2 measurements: identifying the number of spectroscopically unique species

In order to assess how many different isomers contribute to the IRPD spectra of the D_2-tagged protonated water pentamer, we performed isomer-specific IR^2MS^2 measurements [83, 157, 336]. More precisely, the method is sensitive to laser-induced population changes that are maintained longer than the delay between the two IR laser pulses ($\sim 10^{-5}$ s). Hence, the IR spectra of more quickly interconverting isomers cannot be isolated using this double resonance technique, but their presence may be indicated by broadening of spectral features (see below). The results of the IR^2MS^2 experiments are shown in Fig. 6.4, along with the IRPD spectrum of $H^+(H_2O)_5{\cdot}D_2$ (top trace). The IR^2MS^2 traces are colour-coded to easily identify the probe wavenumber (green: a_4, 3205 cm^{-1}; red: a_5, 2890 cm^{-1}; blue: a_7, 1879 cm^{-1}), which is also indicated by coloured arrows. The choices of the probe wavenumbers were motivated by a previous assignment of these bands to isomers C (a_4 and a_7) and R (a_5) based on AIMD simulations [85]. Depending on the laser used for the probe pulse (either OPO/OPA or FEL) we applied different experimental schemes to obtain the isomer specific spectra (see Section 6.2 and 3.4.1), explaining the differences in the signal-to-noise ratios of the traces in Fig. 6.4. The measured spectra show no distinct differences, thus providing strong evidence for the presence of a single, spectroscopically unique species and hence a single constitutional isomer under the present experimental conditions.

Empirical band assignments based on isomer B

The persistent bands across both isotopologues are readily assigned in the context of those expected for isomer **B**. Three sharp peaks with characteristic spacing and relative intensities (a_1–a_3/b_1–b_3) are found at highest energy in the free O–H/O–D stretch region. Further to the red, the next four features (a_4–a_7/b_4–b_7) are attributed to hydrogen-bonded (H-bonded) O–H/O–D stretches and appear broader, as is typical for modes that contain embedded OH groups. The sharp transitions (a_8/b_8) are associated with the water bending modes. Characteristic triplets (a_{10}, a_{11}, a_{13}/b_{10}, b_{11}, b_{13}) emerge in the high energy part of the libration region, of which band a_{10}/b_{10} corresponds to the umbrella mode of the Eigen core (see Table 1). Interestingly, the peaks at lowest energy, *i.e.* a_{15}–a_{18}/b_{15}–b_{17}, are among the sharpest in the IR spectrum, similar to the corresponding bands observed in the IRPD spectrum of $H^+(H_2O)_6$ [83]. The weak features just above the highest energy free O–H (O–D) stretches (see † band in Fig. 6.5) are often observed in cationic water clusters. They originate from excitation of the frustrated rotations of the single acceptor water molecules in combination with the antisymmetric O–H stretch [349].

The strongly isotope-dependent feature, the a_9/b_9 pair near 1400 cm^{-1}, is much more intense in the all-H isotopologue. This is important because, as mentioned above, the assignment of a_7 and a_9 has been controversial, with VSCF theory supporting the assignment of a_7 to the OH stretch of the embedded Eigen motif [79] in **B**, while a VPT2 treatment [82] suggested

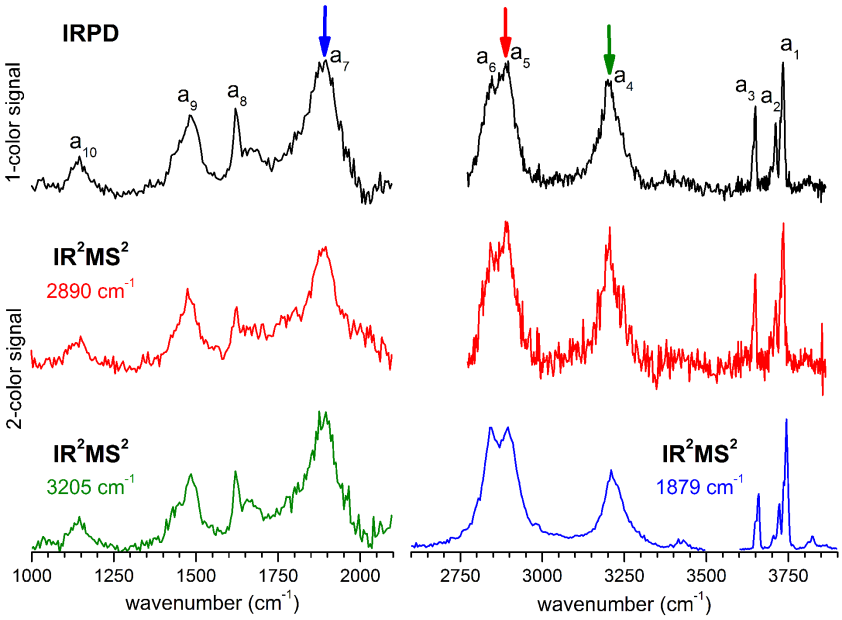

Figure 6.4: IRPD (top row) and IR^2MS^2 (middle and bottom row) spectra of D_2- tagged $H^+(H_2O)_5$ from 1000 to 2100 $cm^{-1}$and from 2600 to 3900 cm^{-1}. Probe energies are indicated by vertical coloured arrows and IR^2MS^2 traces are coloured accordingly.

that a_9 was a more likely candidate. In either case, one of these features remains unassigned. The persistence of the a_7/b_7 pair, however, strongly argues for that feature as the bonded OH stretch, because it appears with the shift and intensity expected for an anharmonic fundamental, while b_9 is much weaker in the spectrum of the heavy isotope. This suggests that the transitions contributing to band a_9 predominantly arise from anharmonicities that are suppressed as the range of the vibrational zero-point wavefunction is reduced upon deuteration. The reduction of anharmonicities is also reflected by the difference in the scaling factors obtained for the two isotopologues (see Table 6.1 and F.4). When comparing the calculated values at the same level of theory for the two species, the method-related contributions to the scaling factor cancel out. The result is an evaluation of the change in anharmonicity upon deuteration, which amounts to $\sim$ 20–30% smaller anharmonicities in the heavier isotopologue.

Temperature-dependent IRMPD spectra: the role of entropy

In order to probe how the anharmonicity-induced bands respond to temperature, we measured vibrational spectra at five ion trap temperatures in-between 50 and 250 K. Fig. 6.5 shows the temperature-dependent IRMPD spectra of $H^+(H_2O)_5$ in the O–H stretching region (2650–4000 cm^{-1}). The IRMPD spectrum measured at 50 K is similar to the IRPD spectrum of D_2-tagged $H^+(H_2O)_5$ obtained at 13 K, confirming that the D_2-tag has a minor influence on the vibrational spectrum as well as the energetic ordering of the lowest-lying isomers. At higher

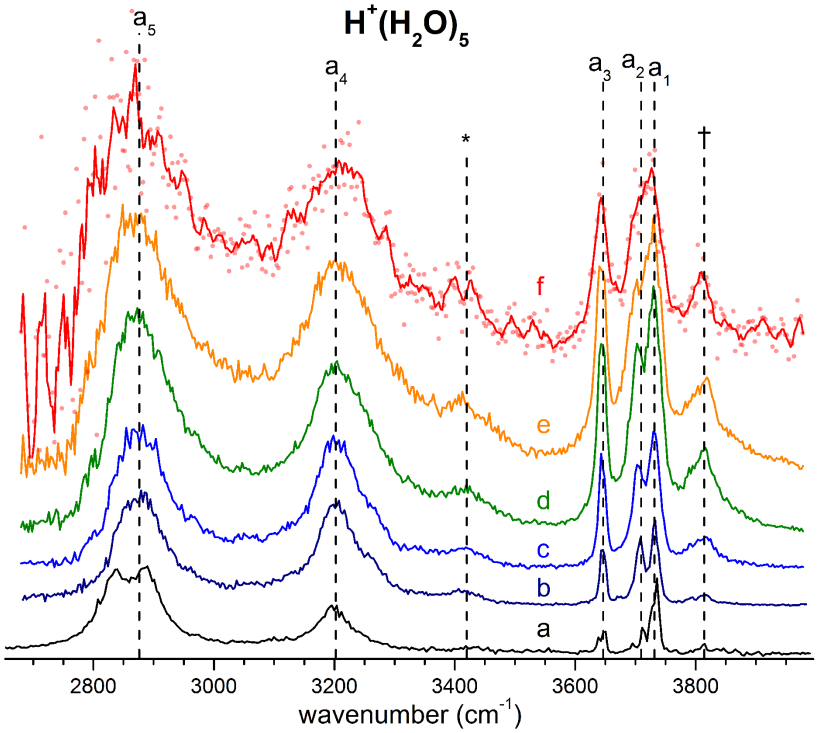

Figure 6.5: (b–f) Temperature-dependent IRMPD spectra of $H^+(H_2O)_5$ in the O–H stretching region recorded by varying the trap temperature in 50 K steps from 50 to 250 K. (a) The D_2-predissociation spectrum at 13 K is reported for comparison. See Table 6.1 for band labels and assignments.

temperatures, band broadening due to thermal rotational and low-energy vibrational excitation is observed leading, for example, to a coalescence of bands a_1 and a_2 above 150 K. Interestingly, the combination bands, labelled with an asterisk and a dagger in Fig. 6.5, gain substantially in relative intensity with increasing temperature, which is consistent with their oscillator strengths being derived from large amplitude displacements. Here, increasing temperature plays a role analogous to that attributed to isotopic modulation of the displacements available in the vibrational ground state. Besides these minor temperature effects, the overall appearance of the IRMPD spectra remain quite similar up to 250 K, providing no clear experimental indication for a significant change in relative isomer populations up to 250 K. Hence, we find no experimental evidence for the presence of multiple isomers, in agreement with all previous spectroscopic studies [79, 80, 84, 261].

Assignment of the vibrational spectrum of $D^+(D_2O)_5 \cdot D_2$

Much of the confusion regarding the assignment of the vibrational spectra of protonated water clusters arises from the fact that standard quantum computational approaches, due to their

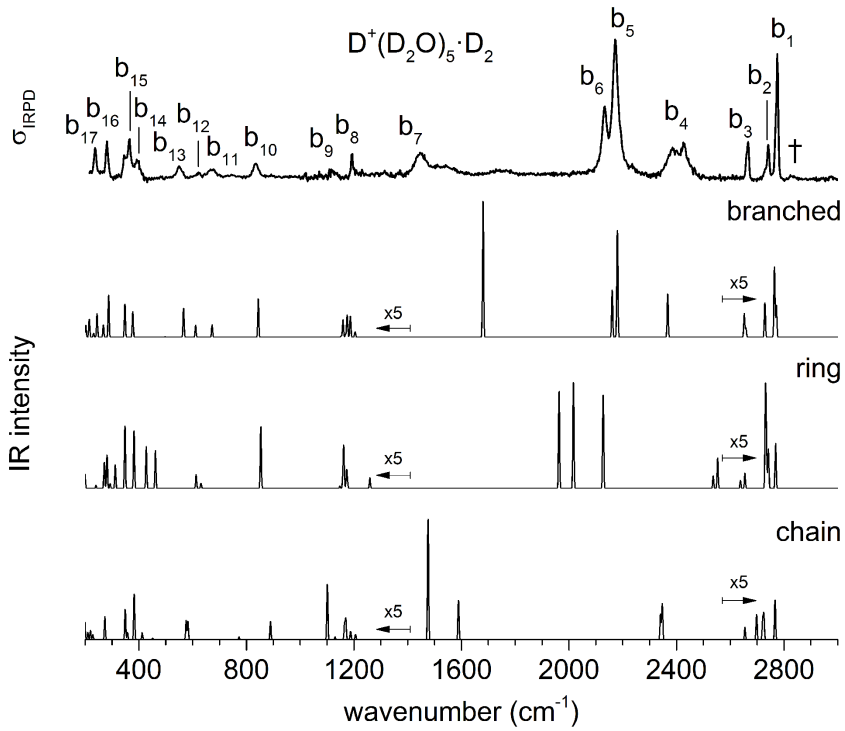

Figure 6.6: IRPD spectra of D_2-tagged $D^+(D_2O)_5$ in the region from 215 to 3000 cm^{-1}compared to the scaled (0.922 below 1100 $cm^{-1}$and 0.974 above) B3LYP-D3/aug-cc-pVTZ harmonic spectra for the three isomers **B** (branched), **R** (ring) and **C** (chain) discussed in the text. Traces below 1400 $cm^{-1}$and above 2580 $cm^{-1}$are shown with a vertical magnification of $\times 5$ for better visibility.

approximate nature, do not fully recover the pronounced anharmonic effects in these systems [327]. With this in mind, we first evaluate which single isomer yields the best fit vibrational spectrum before discussing the remaining discrepancies, and then assess if this is a reasonable choice regarding its thermodynamic and kinetic stability.

The vibrational spectrum of the protonated water pentamer has been extensively discussed in the literature [79, 80, 84, 261]. Therefore, we focus on the description of the IRPD spectrum of the fully deuterated isotopologue here. Fig. 6.6 shows a comparison of the IRPD spectrum of the D_2-tagged perdeuterated water pentamer (top trace) with the B3LYP-D3/aug-cc-pVTZ harmonic vibrational spectra of the **B**, **R** and **C** isomers (see Fig. 6.1) in the range from 215 to 3000 cm^{-1}(see Fig. F.1 for the analogous comparison figure of the light isotopologue spectrum). The experimental spectrum shows seventeen distinct absorption features labelled with b_1 to b_{17}. Band positions and assignments are summarized in Table 6.1. The calculated harmonic spectrum of **B** provides the best fit, reproducing nearly all the main features observed in the experiment, in particular the new experimental data in the far IR region (see also Fig. 6.8). Three sharp peaks, b_1, b_2 and b_3, are found at the high energy end of the spectrum, in the

free O–D stretching region. The band positions and relative intensities of these modes are very sensitive to the environment of a particular water molecule. With this in mind, it is worth noting that the calculated harmonic spectrum of **B** is the only one that reproduces the characteristic spectral pattern of these bands. Features b_4, b_5, b_6 and b_7 correspond to the hydrogen-bonded O–D stretches. b_4 arises from the O–D stretch of the 1-AD water. The symmetric and antisymmetric combination of the two O–D stretches of the D_3O^+ core towards the 1-A waters are responsible for peaks b_5 and b_6. b_7 corresponds to the third O–D stretch of the D_3O^+ core (towards 1-AD-D_2O) and shows the largest deviation (+235 cm^{-1}) from the experiment. Once again, this discrepancy highlights the fact that the structure associated with these motions is not well described within either the harmonic approximation or the VPT2 approach (*vide infra*). The sharp feature b_8 is assigned to D_2O and D_3O^+ bending modes, although the calculated spectrum does not reproduce the relative intensities very well. b_9 is most strongly affected by isotopic substitution and only a weak feature remains in the all-D spectrum, which we tentatively attribute to the AD-D_2O bend. Band b_{10}, which spans the range from 810 to 855 cm^{-1}, arises from the umbrella motion of the hydronium core. In the libration region, features b_{11}/b_{12} and b_{13}/b_{14} correspond to frustrated rotations of D_3O^+ and AD-D_2O, respectively. The sharp features b_{15} and b_{17} are assigned to hydrogen bond stretches involving D_3O^+ coupled to terminal water librations.

Fig. 6.7 shows a comparison of the IRPD spectrum (top trace) with the VPT2/B3LYP/6-311++G(3df,3pd) vibrational spectrum (anharmonic) of $D^+(D_2O)_5$ (middle trace) and the scaled harmonic one obtained at the corresponding level of theory (bottom trace). Anharmonic combination bands and overtones are colour coded in red and blue, respectively. The feature recorded at 2824 $cm^{-1}$and labelled with a dagger arises from combination bands of the O–D antisymmetric stretching modes of the 1-A-D_2O molecules with two terminal D_2O librations (50 and 54 cm^{-1}). The additional structure observed for band b_4 is rather well reproduced by the VPT2 calculation, revealing substantial contribution from combination bands. Note, the four hydrogen-bonded O–D stretching modes are consistently computed too low in energy. In particular the strong red shift of the hydrogen-bonded O–D stretch of the D_3O^+ towards the 1-AD-D_2O (b_7) is overestimated by about 120 cm^{-1}. Several combination bands account for the broad and weak structure to the blue of band b_7. The position of the two water bend peaks, b_8 and b_9, is also improved by including anharmonic effects. The combination of a libration mode of the 1-AD water molecule with the hydrogen bond stretch involving the same water molecule and D_3O^+ gives rise to a calculated peak at 867 cm^{-1}(labelled ♦ in Fig. 6.7) which is not observed in the experimental spectrum. Finally, the positions and relative intensities of bands b_{14}, b_{15}, b_{16} and b_{17} are better reproduced by the anharmonic calculations. Summarizing, the anharmonic calculations support our spectral assignments based on the presence of a single constitutional isomer and provide further insight into some of the details of the vibrational spectrum of $D^+(D_2O)_5$. However, besides overestimating the exceptional red shift of band b_7, two low energy fundamental modes, as well as their overtones and combination bands, are predicted to have negative energies. Furthermore, the

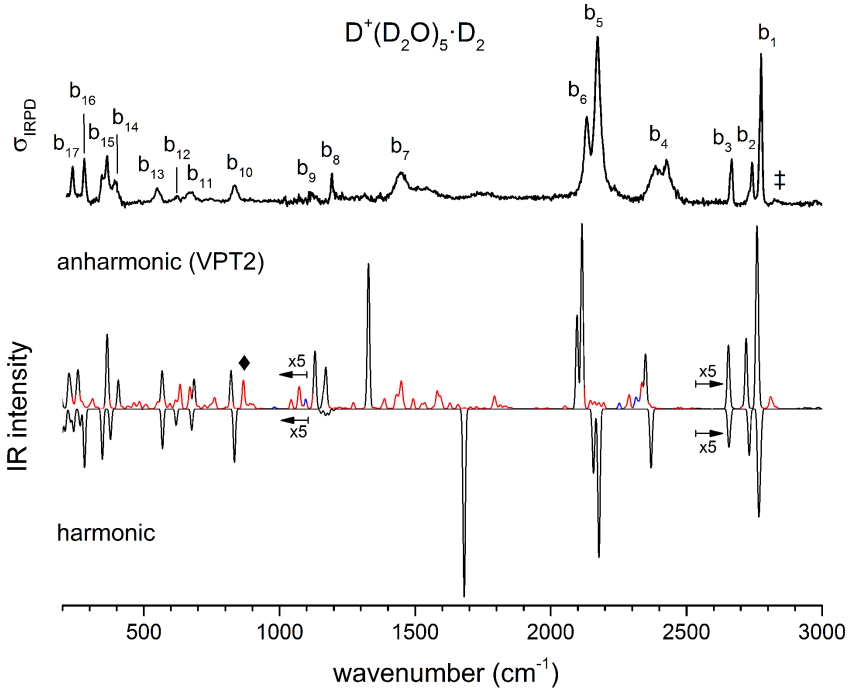

Figure 6.7: IRPD spectrum of D_2-tagged $D^+(D_2O)_5$ in the region 215 to 3000 cm^{-1}(top trace) compared to the anharmonic (middle trace) and the scaled (0.92/0.97) harmonic spectrum (bottom trace) of the branched isomer **B** calculated at the B3LYP/6-311++G(3df,3pd) level of theory. Combination bands and overtones in the VPT2 spectrum are coloured in red and blue, respectively. Traces below 1085 $cm^{-1}$and above 2600 $cm^{-1}$are shown with a vertical magnification of $\times 5$ for better visibility.

obtained intensities of two other low energy modes are unreasonably high (on the order of 200 000 km/mol). The VPT2 calculation showed poorer performance when applied to the light isotopologue or employing the aug-cc-pVTZ basis set, resulting in additional negative energies and high intensities. The a_7 mode is most unstable with respect to correction at the VPT2 level, raising the possibility that the levels involving this motion require inclusion of higher order terms in the potential to converge on the experimentally observed band location.

A conformational isomer of **B**, referred to as **B2**, with an almost identical vibrational spectrum (see Fig. 6.8 and Fig. F.2 for the spectra of the light isotopologue), is obtained by rotating the 1-AD/2-A waters by roughly 180 degrees around an axis parallel to the hydrogen bond between the D_3O^+ and the 1-AD water (see Fig. 6.2). The two branched rotamers are approximately isoenergetic and the low barrier between them can easily be overcome, even at the low temperatures of the experiment, as is supported by the kinetic model (see below). The system is thus expected to be so fluxional that it can explore all the configurations connecting the two structures. This fluxionality is likely the cause of the broadening of bands b_{10} and b_{11}. The corresponding vibrational modes show a shift in wavenumber of 39 and 37 cm^{-1},

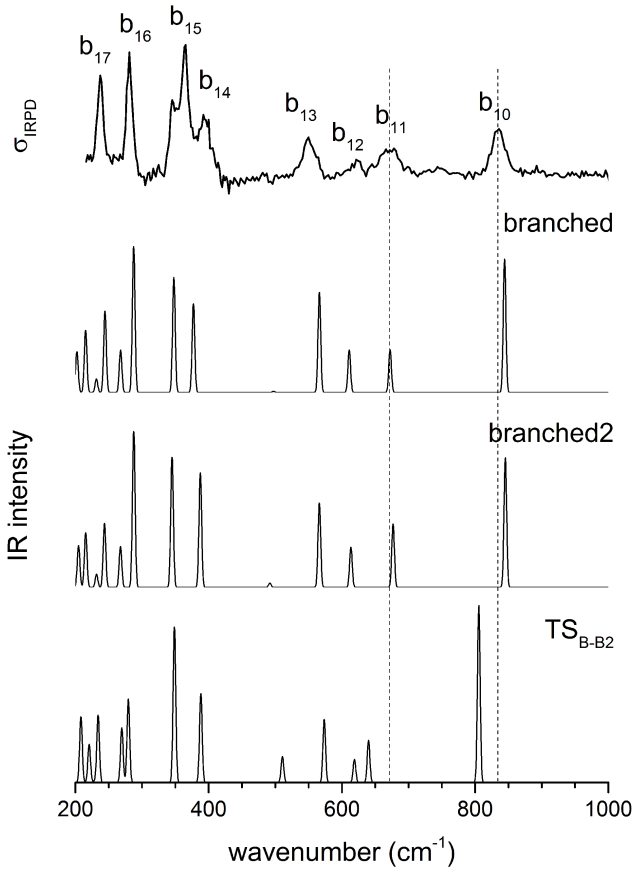

Figure 6.8: IRPD spectrum of D_2-tagged $D^+(D_2O)_5$ in the region 215 to 1000 cm^{-1}compared to the scaled B3LYP-D3/aug-cc-pVTZ harmonic spectra for the two versions of the branched isomer and the TS between them.

respectively, upon isomerization via $\mathbf{TS_{B\text{-}B2}}$ (see Fig. 6.8). We thus refine our assignment of the structure of $D^+(D_2O)_5$ and note the fluxional character of the branched structure.

The assignments of the fundamentals in the all-D isotopologue spectrum are useful in unravelling the origin of the more complex band patterns in the all-H system. Because all of the bands in the latter are demonstrated by IR^2MS^2 to arise from the same carrier, the "extra" bands in the light isotopologue must be due to overtone and combination bands induced by anharmonic coupling. For example, the feature labelled with an asterisk denotes a combination band and, as mentioned above, is present only in the IRPD spectrum of $H^+(H_2O)_5{\cdot}D_2$. Anharmonic VPT2 calculations on the all-H isotopologue predict several active combination bands in this region. The main contribution stems from the combination of the hydrogen bonded O–H stretch 1-AD-H_2O (a_4) with two low energy modes. One of these is the frustrated rotation of a 1-A-H_2O combined with the hydrogen bond stretch between the 1-AD and the 2-A water molecules and the second is the frustrated rotation of the 2-A

Table 6.2: Relative B3LYP and CCSD(T) electronic energies (in kJ/mol) without ZPE (ΔE), CCSD(T) electronic energies with ZPE ($DeltaE_0$), and Gibbs free energies (ΔG_0) of the B3LYP-D3/aug-cc-pVTZ minimum energy and first order transition state structures considered in this work

Species	ΔE (B3LYP)	ΔE (CCSD(T))	ΔE_0 (H, harm.)[a]	ΔG_0 (H, 150 K)[b]	ΔE_0 (D, harm.)[a]	ΔG_0 (D, 150 K)[b]
R	**0.0**	**0.0**	+0.8	+4.5	**0.0**	+3.5
B	+4.6	+4.5	**0.0**	**0.0**	+0.5	**0.0**
B2	+4.5	+4.4	+0.5	+0.9	+0.9	+0.8
C	+18.0	+19.9	+13.6	+13.7	+14.7	+14.6
$\mathbf{TS_{R\text{-}B}}$	+7.0	+6.5	+3.5	+6.2	+3.6	+5.9
$\mathbf{TS_{B\text{-}B2}}$	+5.9	+5.9	+1.0	+3.0	+1.6	+3.1
$\mathbf{TS_{B2\text{-}C}}$	+22.4	+23.3	+18.8	+21.4	+18.9	+21.9

[a] ZPE is calculated using scaled harmonic B3LYP-D3/aug-cc-pVTZ wavenumbers.
[b] The thermal energy contributions are calculated at 0.001 atm and with a vibrational scaling factor of 0.962 (0.973) for the all-H (all-D) isotopologue. Note the different scaling below 1500 in Table 6.1.

water. In the spectrum of the perdeuterated species only the latter combination band has some IR intensity but falls under the broad feature b_4.

RRKM calculations and kinetic modelling

The relative B3LYP and CCSD(T) energies of the three lowest energy isomers of the protonated water pentamer **B**, **R** and **C** and the first-order transition states $\mathbf{TS_{R\text{-}B}}$ and $\mathbf{TS_{B\text{-}C}}$, connecting the corresponding potential minima, are listed in Table 6.2 (see also Table F.1). For the branched isomer, two nearly isoenergetic structures, labelled **B** and **B2** in Fig. 6.2 and Table 6.1, exist, separated by a shallow barrier ($\mathbf{TS_{B\text{-}B2}}$: 1.0 kJ/mol). As we show later, only these conformational isomers **B** and **B2** are predicted to be kinetically stable at low temperature, while the constitutional isomers **R** and **C** are not.

R represents the global minimum energy structure on both the B3LYP and presumably the CCSD(T) potential energy hypersurfaces (see Table 6.2). However, **B** is stabilized relative to **R**, when (harmonic) ZPE is taken into account reducing the energy difference to less than 1 kJ/mol, making them nearly isoenergetic. While the level of theory used here is not sufficiently accurate to predict the energetic ordering of **B** and **R** at 0 K, it is apparent that **B** is entropically favoured over **R** at higher temperatures (see Gibbs free energies ΔG_0, equilibrium constants K_0 and Boltzmann weighted populations P_0 in Table 6.2, F.2 and F.3). Moreover, the free energy difference between **B** and **C** remains nearly constant and larger than 10 kJ/mol, indicating that **C** can only be spectroscopically probed at low temperature if it is kinetically trapped behind the ~ 5 kJ/mol barrier.

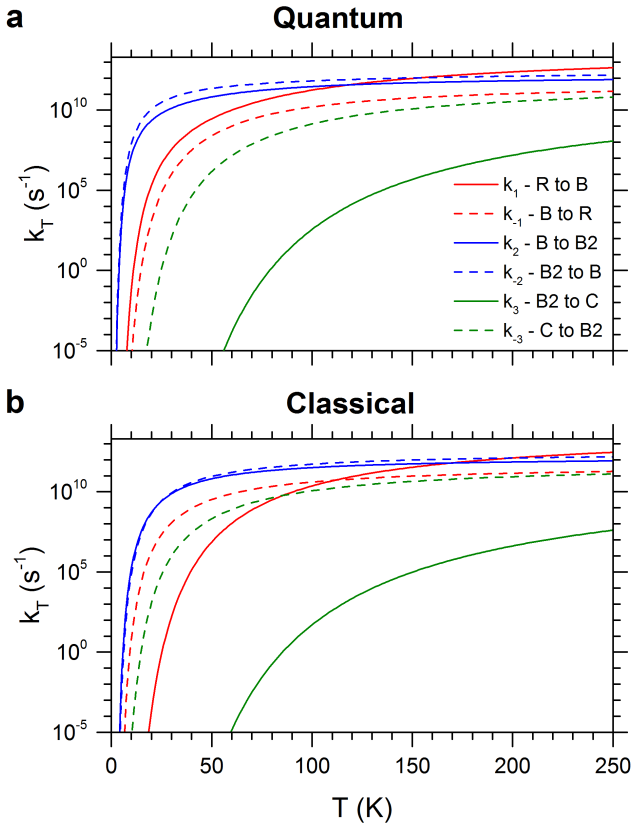

Figure 6.9: Quantum (a) classical (b) canonical rate constants obtained with RRKM calculations for the forward and backward elementary reactions of the three isomerization pathways considered.

The RRKM canonical rate constants are shown in Fig. 6.9: panel (a) depicts the results obtained from the quantum treatment (*i.e.* quantum density and sum of rovibrational states and inclusion of ZPE) while panel (b) the ones from the classical approach (*i.e.* classical density and sum of rovibrational states and no inclusion of ZPE). In particular, rate constants are reported as a function of the temperature for the forward and backward elementary reactions of the three isomerization pathways considered (see Fig. 6.2). Microcanonical rate constants are reported in Fig. F.6. First, we analyse the quantum case. It is helpful to compare the two rate constants for opposite directions of the same isomerization process at the same temperature. For example, the fact that k_1 exceeds k_{-1} by one to three orders of magnitude indicates a preference for the branched isomer **B** over the ring isomer **R** across the entire energy range considered. On the other hand, similar values for k_2 and k_{-2} suggest that the conformational isomers **B** and **B2** will interconvert very fast. k_3 and k_{-3} show the largest difference, in particular at low energies (or temperature), revealing that the chain isomer **C** will convert nearly completely to the branched conformers **B** and **B2**. The main

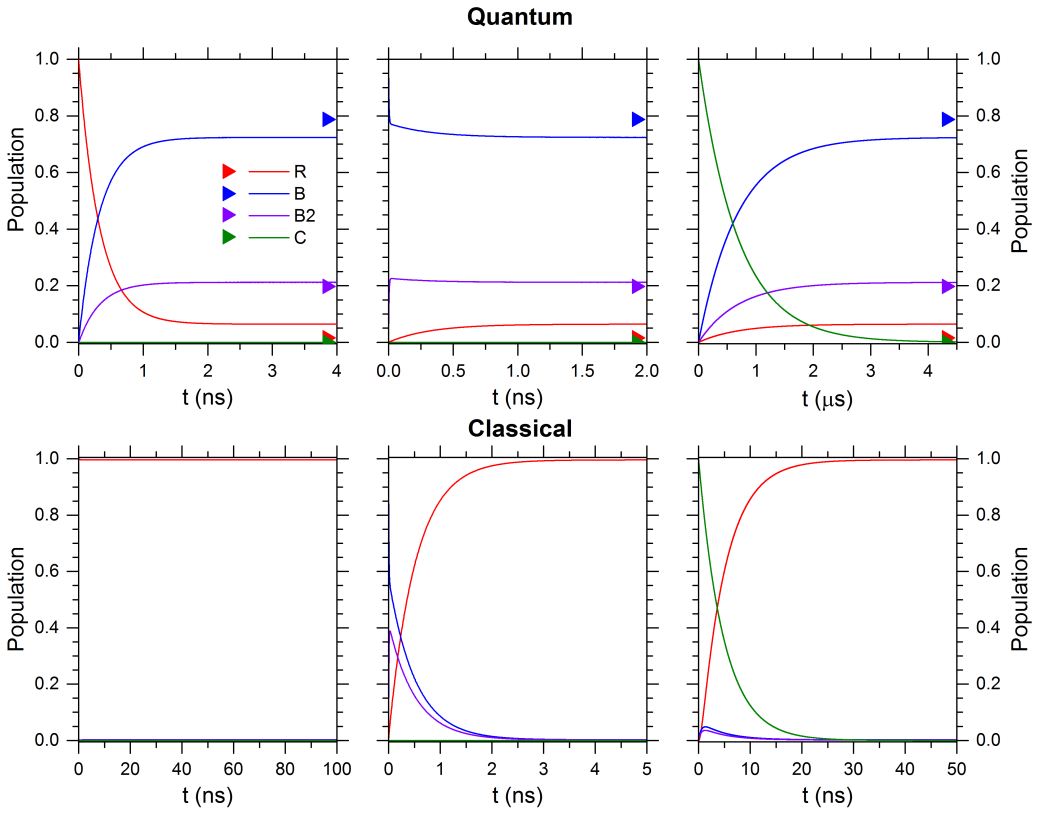

Figure 6.10: The kinetic stability of the isomers **R**, **B**, **B2** and **C** is tested with a kinetic model that uses either quantum (top row) or classical (bottom row) rate constants obtained from RRKM calculations at 50 K. Boltzmann weighted populations at 50 K obtained from relative Gibbs free energies (see Table F.2) are indicated by colour-coded triangles.

difference between the classical and the quantum treatment is found in the low temperature region, where the classical rate constants are smaller. As expected, the values of the classical and quantum rate constants approach each other with increasing temperature.

The most striking difference between the classical and quantum RRKM calculations manifests itself in the rate constants for the **R**/**B** isomerization reaction, which leads to a qualitatively different kinetic stability at low energies (temperatures). In the absence of ZPE **R**, the global minimum energy structure, is also the kinetically preferred isomer, which is reflected in a larger isomerization rate constant for the back reaction ($k_{-1} > k_1$) forming **R** at low energies (temperatures). The rate constants are equal at 40 kJ/mol (111 K) and above this energy (temperature) the forward reaction leading to **B** is preferred ($k_1 > k_{-1}$).

The kinetic stability of each isomer at 50 K is evaluated in Fig. 6.10 for the quantum (upper row) and the classical case (lower row). Independent of the initially prepared constitutional isomer, **R** (left column), **B**/**B2** (center column) or **C** (right column) the thermodynamic

limit is reached within a few tens of nanoseconds with the exception of the quantum case for isomer **C**, where it is reached in several microseconds. **B**/**B2** are predominantly formed for the quantum case, while interconversion to **R** is dominant in the classical case.

We also tested the effect of the quality of the potential energy surface on the RRKM calculation by using the energies obtained without dispersion correction or with different basis sets (*e.g.* 6-311++G(3df,3pd)). This leads to small changes in the relative energies and thus the respective equilibrium constants, which in return can lead to slightly larger numbers for the population of **R** in the quantum case. The equilibration times are also affected, but overall the results remain in qualitative agreement. A more thorough description of the details and the results of the RRKM calculations, also involving higher energy isomerization reactions, lies outside the scope of the present study and will be part of a separate publication.

Summarizing, the results of the RRKM calculations lead to two important insights. First, the kinetic stability of the considered isomers below 100 K changes dramatically, when nuclear quantum effects in the form of ZPE are considered. Second, isomer **C** is not kinetically stable (on a microsecond timescale) at 50 K.

6.5 Summary and conclusions

We have shown that the IRPD spectra of the D_2-tagged protonated water pentamer and its fully deuterated isotopologue probe the same spectroscopic species that is most consistent with a branched structure, consisting of two conformational isomers that interconvert readily on the time scale of the experiment.

Harmonic DFT calculations of the branched isomer B reproduce the IRPD spectra of the D_2-tagged $H^+(H_2O)_5$ and $D^+(D_2O)_5$ with reasonable agreement, with the exception of bands a_7/b_7 and a_9/b_9. The strong feature a_9 just below the intramolecular HOH bending mode in $H^+(H_2O)_5$, previously attributed to an H-bonded OH fundamental of the Eigen core, is dramatically suppressed in the perdeutero isotopologue, indicating that it contains significant contributions arising from anharmonic coupling, while the higher energy feature (a_7/b_7) is the fundamental associated with this oscillator. Anharmonic VPT2 calculations accurately account for most of the features across the $D^+(D_2O)_5$ spectrum. However, this approach overestimates the pronounced red shift of mode b_7. It also performs considerably worse in reproducing the $H^+(H_2O)_5$ spectrum, since anharmonic effects are more pronounced here as a result of the higher ZPE. In summary, higher level anharmonic calculations are necessary to achieve satisfactory convergence between experiment and theory for the IR spectra of the protonated water pentamer, similar to the archetypal case of $H_5O_2^+$ [327].

A simple kinetic treatment shows that for a reliable understanding of the equilibrium dynamics between the various isomers of the protonated water pentamer nuclear quantum effects must be taken into account at low temperature. Hence, conclusions derived from standard AIMD simulations, which make use of quantum mechanics (at the DFT level) for the electronic structure but treat nuclear motion in a pure Newtonian way, can be unreliable when

dealing with (i) effects that result from the quantum nature of protons and/or (ii) kinetically instable isomers. Improved convergence between experiment and theory could certainly be achieved by the application of path integral molecular dynamics simulations to the present system (as well as related methods) [350–354], thus including the quantum dynamics of the nuclei.

6.6 Spectroscopic snapshots of the proton-transfer mechanism in water

The results from this study and of the work of the group of Prof. Mark A. Johnson on the perdeutereted water tetramer[82] lead to a collaborative study [87] that gives fundamental insights into the proton transfer mechanism in water. The structure of the water tetramer is built on an H_3O^+ core symmetrically hydrated by three water molecules. When an H-bond acceptor binds to an OH group of one of the solvent water molecules (see Fig. 6.11), its basicity increases and therefore also the strength with which it pulls the proton of the hydronium the water is bounded to. As a result, by complexing molecules with increasingly larger proton affinities (H_2, N_2, CO and H_2O) to the protonated water tetramer, it is possible to generate stable clusters with one hydronium proton incrementally pulled towards the solvated water. IRPD experiments of these systems hence deliver spectroscopic snapshots of the proton transfer process. However, the small splittings in the vibrational spectrum expected by the onset of the proton transfer event become apparent only in the perdeutereted isotopologues which features sharper bands as a result of the reduced anharmonicity. Theoretical support for this study was provided by the groups of Prof. Anne B. McCoy and of Prof. Kenneth D. Jordan who used MP2/VPT2 and VSCF calculations to deal with the anharmonic potential energy surfaces of these floppy clusters. The compelling structural assignments (see Fig. 6.12) give the opportunity of quantifying the relationship between a hydron's stretching frequency and the distortion of the Eigen core along the reaction coordinate of the proton transfer process. The extent of the proton transfer is expressed in terms of the distance between the two oxygen atoms involved in the process, R_{OO} (see Fig. 6.11). A parametric dependence is determined between R_{OO} and the stretching frequencies of the OD groups highlighted in red, blue and green in Fig. 6.11 and 6.12. These relations encode the collective response of the surrounding H-bonding network throughout the course of the hydron transfer. The extremely large effect on the vibrational spectrum induced by the H-bond acceptors is in agreement with the broad absorption continuum of strong acids (see Fig. 6.12). The effect can be understood in terms of the Zundel's model for the breadth of the hydrated proton spectrum [355]. The electric field generated by the solvent surrounding the Zundel ion perturbs the potential that governs the "proton-transfer vibration" such that the resulting potential is in close agreement with the potential of the assigned Eigen-type structures.

The IR spectrum of the bulk-water solvated proton will therefore reflect the population of

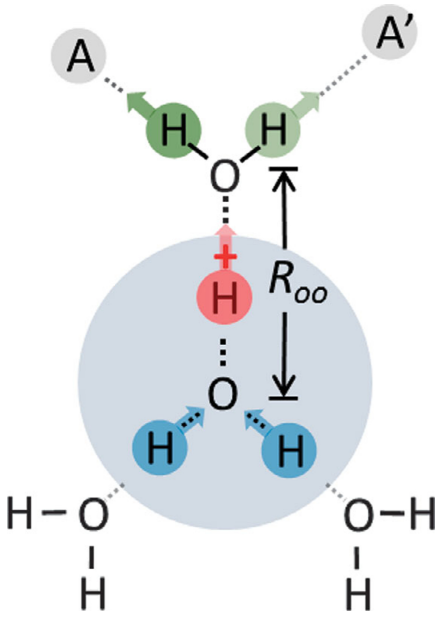

Figure 6.11: The symmetric $H_9O_4^+$ Eigen ion is distorted upon the addition of proton acceptors A and A' (A = H_2, N_2, CO, H_2O; A' = H_2O) to one of the water molecules. Formation of these complexes induces the attraction of a proton in the H_3O^+ core toward the solvated H_2O molecule and reduces the corresponding O–O distance, R_{OO}. Figure taken from [87].

R_{OO} values weighted for the strengths of the associated oscillators. This information can be particularly helpful for the interpretation and planning of 2D IR experiments. The selective excitation of the Zundel isomer in solution might not be easily achieved, especially with broad band lasers, given that absorption of different Eigen-type structures are found at frequencies close to those of the Zundel-type ones, *i.e.* H_3O^+ umbrella mode and AD-D_2O O-D stretch mode (see Fig. 6.12). It is important to note, however, that the R_{OO} values obtained for these small clusters can be significantly different from those in solution, calling for further studies on larger systems.

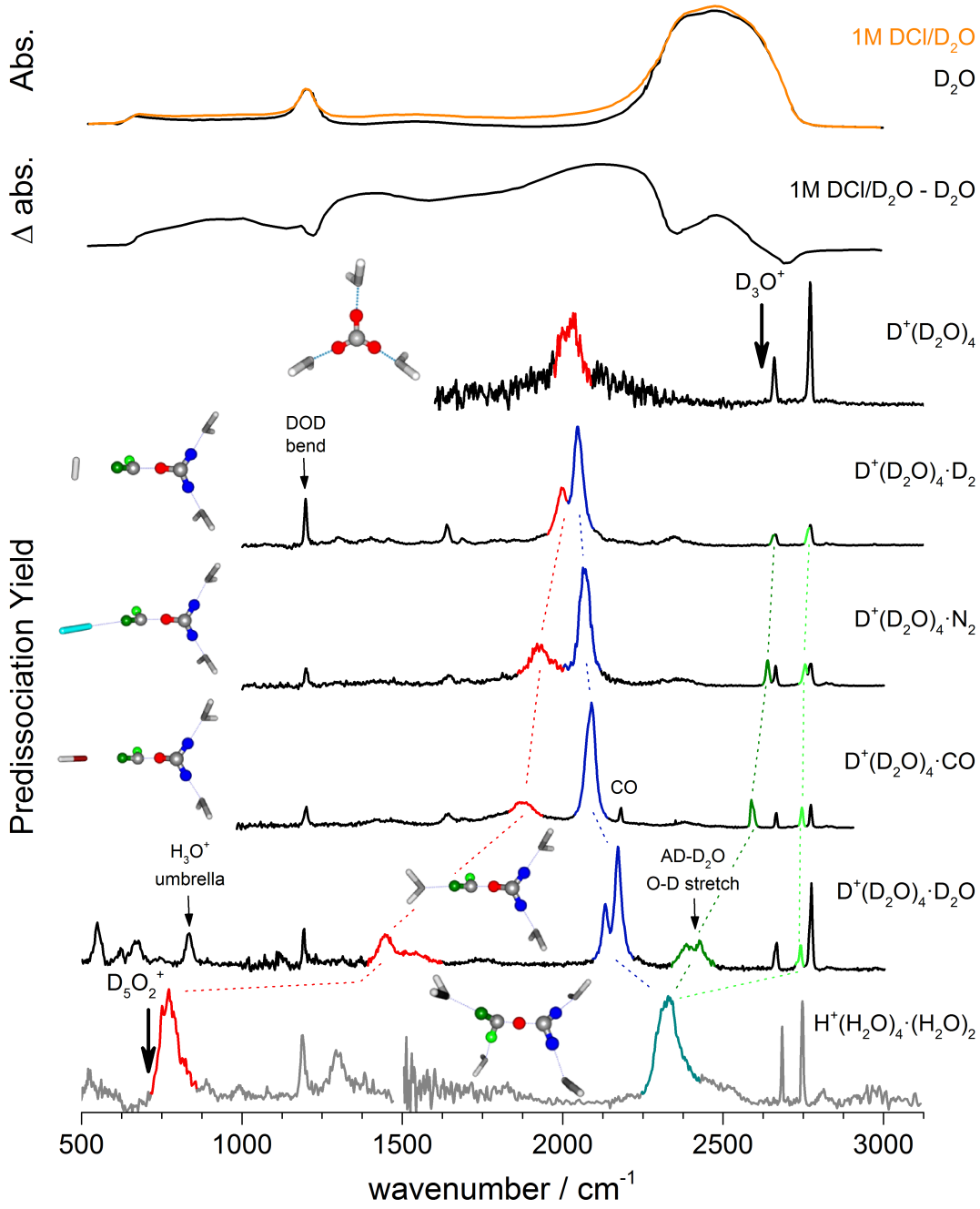

Figure 6.12: Comparison of the absorption spectra of 1M DCl in D_2O and pure D_2O, as well as their difference, with the IRMPD spectrum of the perdetureted water tetramer and with the IRPD spectra of the adducts, $D^+(D_2O)_4{\cdot}A$ with A = D_2, N_2, CO and D_2O. The latter is the D_2-tagged spectrum of the perdeuterated water pentamer. The bottom spectrum is the H_2-tagged spectrum of the Zundel isomer of the $H^+(H_2O)_6$ cluster [83] scaled by 1/1.36 to estimate the locations of key bands in the heavy isotopologue with this geometry. The assigned structure are also reported. Figure adapted from [87].

7 Outlook

In the present work, vibrational action spectroscopy was used in combination with quantum chemistry computations to study the structure, stability and reactivity of cryogenically-cooled mass-selected cluster ions. These experiments, performed under precisely controlled conditions on well-defined signal carriers allowed for a molecular level insight into the unusual properties of this unique form of matter. In particular, how these evolve with cluster size as well as the importance of considering quantum effects in reliably describing these properties. Not all questions were fully answered and therefore some of the remaining open questions as well as new ones that evolved on the basis of the present results are summarized in this final chapter.

How can the present experiments be improved? Enhancements to the design of the 10 K experimental setup, implemented in the newer 6 K setup, have been discussed in Chapter 3. Among those, the doubling of the number of variable DC voltage stages in the ion trap and the lower final trap temperature, represent the major improvements. In fact, they (i) result in an increased messenger-tagging efficiency and consequently better signal-to-noise ratio of the IRPD experiments and, (ii) allow the use of lower pressures ($\sim 10^{-6}$ mbar) in the trap chamber leading to a reduced ion temperature and therefore vibrational spectra that are easier to interpret. An even lower ion temperature can be achieved by evacuating the buffer gas from the trap prior to their extraction. To this end, the gas is injected in a single short pulse at the beginning of the trapping cycle. For efficient ion trapping, the molecular beam is pre-bunched, for example in a modified ion-guide such that all ions experience a similar thermalization time [156].

Increasing the degree of control and flexibility in the generation and preparation of ions is another desirable improvement of the experimental setup. The setups used in this work would greatly benefit from the addition of a second temperature-controllable ion trap, separated from the first by another mass-selection stage. This configuration allows to separately tune the temperature at which complexes are formed or reactions are performed and the temperature used for the detection of the final product. This could be used, for example, to obtain cold spectra of bigger Al-oxide/water complexes (see below).

A planned modification of the laser vaporization source consists in replacing the solenoid gas valve (*Parker*, Series 99) with a copper Even-Lavie valve. The latter produces shorter ($\sim 10^{-5}$ s) and denser gas pulses that should result in cluster growth and cooling with a lower gas load on the pumping system. The valve can also be operated continuously from 10 to 400 K without adjustments. Coupling the valve to a cryogenic motor for the movement of the metal rod, allows cooling the entire source block to cryogenic temperatures, resulting in

improved clustering compared to the present setup that is limited to ~ 200 K.

The studies presented in Chapter 4 allowed characterizing the structure of smaller Al-oxide clusters (with up to 13 Al atoms) and their reactivity towards water. Al-oxide clusters can also be seen as model systems for Fe-oxide clusters. In fact, Al-oxide favors the same oxidation state (+III) and coordination numbers (4 or 6). On the other hand, the redox activity and the complex electronic structure typical of transition metals make experiments and particularly calculations on Fe-oxide clusters more demanding. Preliminary studies on Fe-oxide clusters and their interaction with water were also performed and reported in Section 4.4 and Appendix C. Possible next steps are to investigate the interaction of water with metal-oxide clusters as a function of the oxidation state as well as with larger clusters containing metal atoms with coordination numbers more like those found at metal oxide surfaces. Another intriguing question is, how the evolution of the hydration shell proceeds with the number of water molecules. In order to produce clusters with many water molecules the use of isotopically-enriched metal targets is favorable to avoid multiple isobaric species. Alternatively, water can be adsorbed after the oxide of interest is mass-selected. This could be achieved with the present setup by forming the hydrated complexes in the ion trap held at room temperature and irradiating the ions after mass selection in the first stage of the reflectron time-of-flight mass spectrometer. Structure and reactivity studies of doped metal oxide clusters are also of great interest. These studies can provide useful information to gauge the effect of the dopant on the properties of the particles.

The exceptional fluxionality of B_{13}^+ described in Section 5.1, manifests itself already at cryogenic temperatures. B_{13}^+ represents a potential candidate for the field of nanomachinery. In fact, this cluster could be used as a molecular motor. Nanomachinery is a very exciting and promising scientific field, as demonstrated by the fact that the Nobel Prize in Chemistry for 2016 was awarded to Sauvage, Stoddart and Feringa for the design and synthesis of molecular machines. Other molecular engines require electronic excitation, for example, the rotation of a chiral helical alkene is activated by two UV light induced cis-trans isomerizations [356]. In contrast, rotation of the inner ring in B_{13}^+ is already feasible in the electronic ground state, reducing heat dissipation. The rotation of B_{13}^+ molecules aligned in space can, in principle, be directionally driven by the use of circularly polarized IR radiation near 3 THz (at room temperature) [48]. B_{19}^- is another interesting candidate in this sense, with a similar structure and with the rotation predicted to proceed barrierless [357]. Gas-phase studies of metal doped boron clusters can also provide useful insight into the properties of boron deposited on metal surfaces, *e.g.* a 2D boron layer on Ag [42]. Structure characterization of such systems allows assessing the cluster-support material interaction. What effect does it have on the structure of the cluster? How does it affect the tendency of boron to share electrons? The level of detail of such studies allows for stringent tests of theoretical models that may lead to new ways for producing 2D boron sheets.

The study presented in Chapter 6 highlights the importance of considering nuclear quantum effects when calculating the kinetic stability of protonated water clusters. Isotopic substitution

has been used in the study of the protonated water pentamer to quench anharmonic effects. However, the reduction of ZPE can have a dramatic effect on the energetic order of isomers in other systems. The protonated water hexamer is a prototypical example for this. Fig. 7.1 reports the vibrational spectra of the all-H and all-D isotopologues of the protonated water hexamer with the wavenumber axis scaled by 1.36 to account for the different masses of the O-H and O-D oscillators. The marked change in the spectrum upon deuteration is a clear indication for different structures in the two isotopomers. Application of the IR^2MS^2 technique revealed the presence of multiple isomers in the light isotopologue [83] while preliminary results suggest otherwise in the all-D case.

The results presented in this thesis show that cryogenic ion vibrational spectroscopy is a powerful tool for retrieving structural information of gas-phase clusters. The potential of this technique is greatly enhanced when paired with an intense and widely tunable IR source like an FEL. The level of detail of the vibrational spectra is sufficient to identify anharmonic and fluxional effects. Consequently, it is possible to resolve controversial assignments as well as to identify exotic properties. In the field of nanotechnology, information on the size effects of material properties is needed. The evolution of size-dependent properties can be studied atom-by-atom in gas-phase clusters and such studies are therefore likely to contribute to this flourishing field. Future improvements in the construction of ion sources and in material synthesis will open the door to study increasingly complex systems in the gas phase.

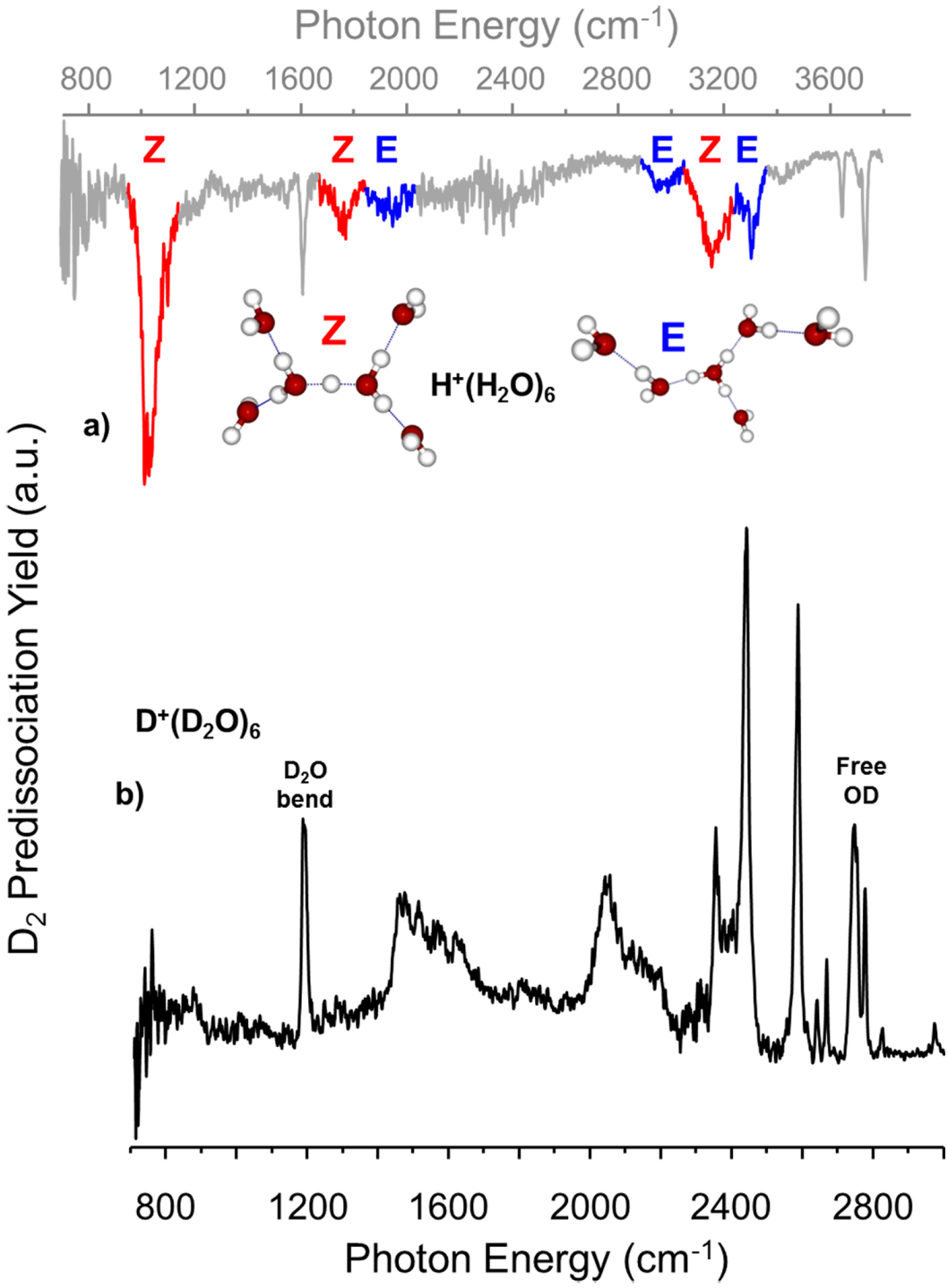

Figure 7.1: Comparison of the light $H^+(H_2O)_6$ cluster, displaying features corresponding to both Zundel (Z) and Eigen (E) cores shown in the two smaller insets, to the fully perdeuterated isotopologue, which has been scaled by 1.36. The very different patterns in the spectra of the two isotopologues indicates that, unlike the situation in $n = 4$ and 5, different structures are adopted by $n = 6$ upon deuteration. Picture from [87].

Appendix A
$(Al_2O_3)_{1-6}AlO_2^-$

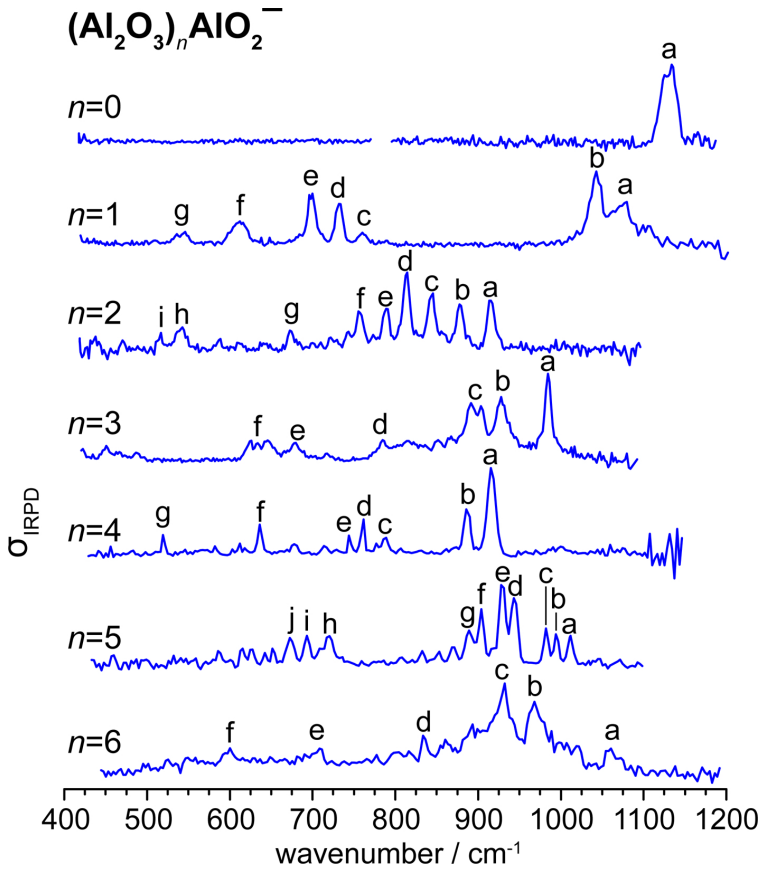

Figure A.1: Experimental IRPD spectra of $(Al_2O_3)_nAlO_2^-{\cdot}D_2$ ($n = 0 - 6$). See Table A.1 for band positions and assignments.

Table A.1: Band positions (in cm^{-1}) of the features observed in the IRPD spectra of D_2-tagged $(Al_2O_3)_nAlO_2^-$ clusters shown in Fig. A.1.

n	Band position
0	1143 (**a**)
1	1074 (**a**), 1042 (**b**), 760 (**c**), 732 (**d**), 699 (**e**), 611 (**f**), 542 (**g**)
2	916 (**a**), 879 (**b**), 843 (**c**), 814 (**d**), 789 (**e**), 757 (**f**), 673 (**g**), 541 (**h**), 515 (**i**)
3	985 (**a**), 928 (**b**), 905/892 (**c**), 784 (**d**), 678 (**e**), 646/634/624 (**f**)
4	916 (**a**), 887 (**b**), 788/777 (**c**), 761 (**d**), 745 (**e**), 639 (**f**), 520 (**g**)
5	1011 (**a**), 995 (**b**), 982 (**c**), 944 (**d**), 928 (**e**), 904 (**f**), 890 (**g**), 718 (**h**), 693 (**i**), 673 (**e**)
6	1065 (**a**), 968 (**b**), 931 (**c**), 835 (**d**), 704 (**e**), 599 (**f**)

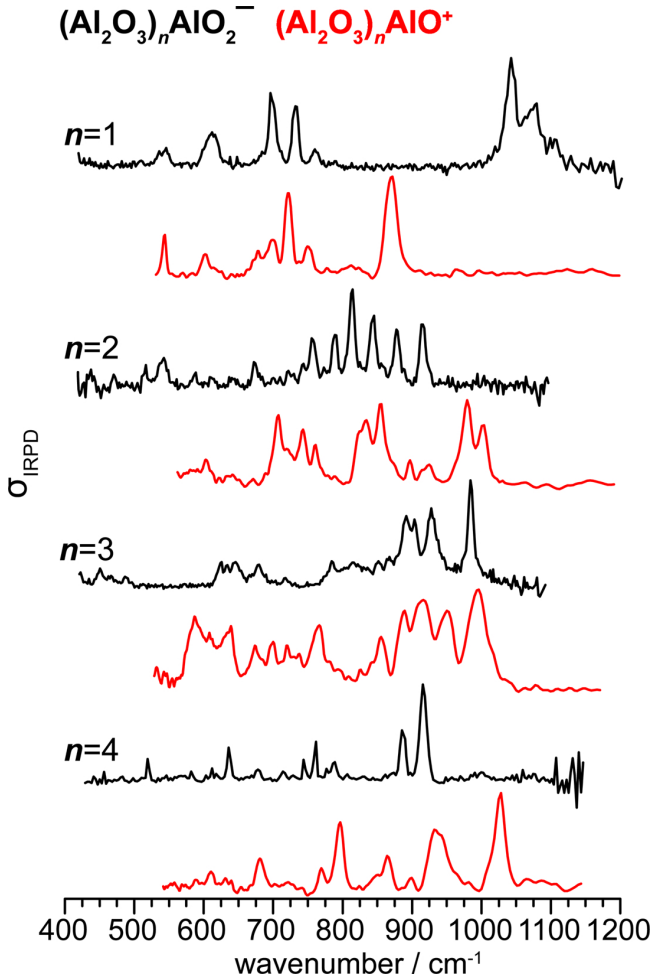

Figure A.2: IRPD spectra of D_2-tagged $(Al_2O_3)_nAlO_2^-$ anions compared to the IRPD spectra of He-tagged $(Al_2O_3)_nAlO^+$ cations (red trace) for $n = 1$–4 from G. Santambrogio *et al.* ., *J. Am. Chem. Soc.*, **2008**, *130*, 15143.

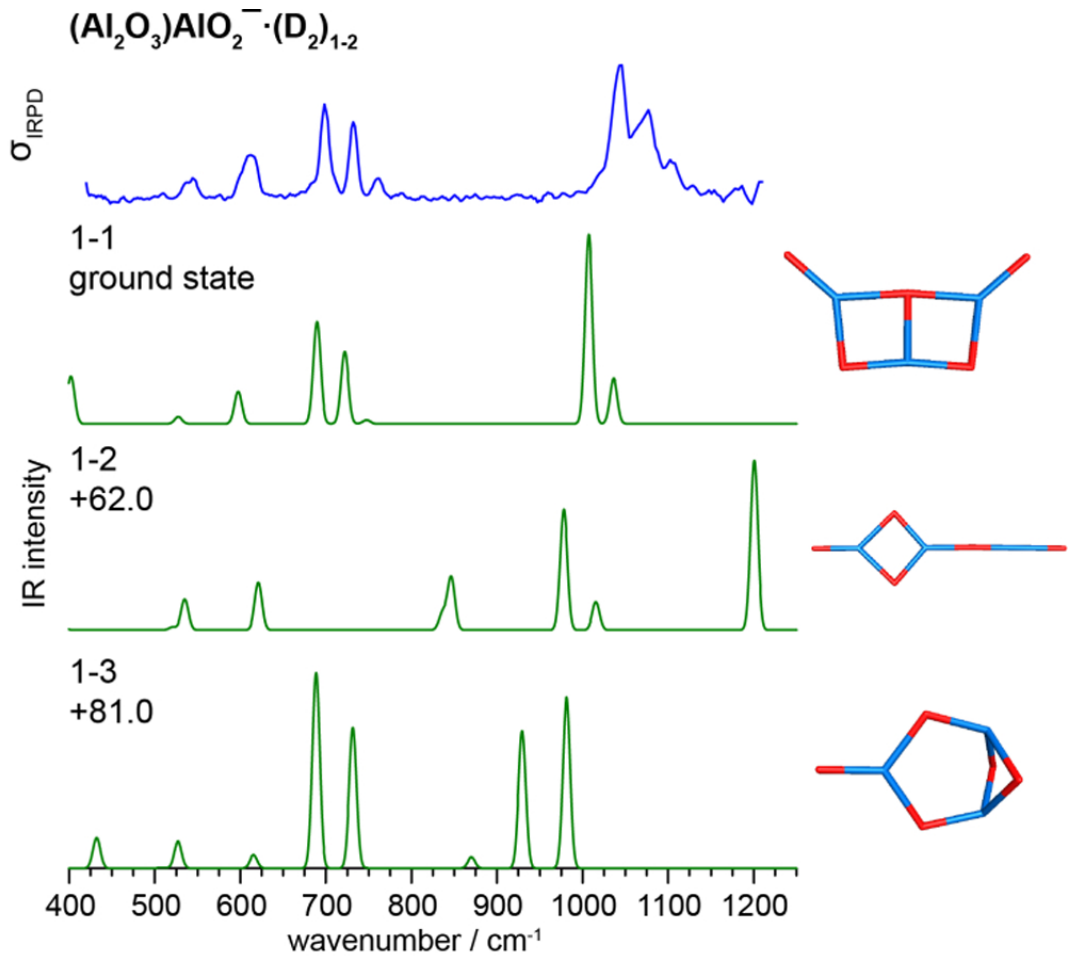

Figure A.3: Experimental IRPD spectra (blue) of $(Al_2O_3)AlO_2^- \cdot D_2$ is compared to simulated harmonic IR spectra (green) of low lying structures (Al=blue, O=red). Relative energy including vibrational zero point energy of each isomer is given in kJ/mol.

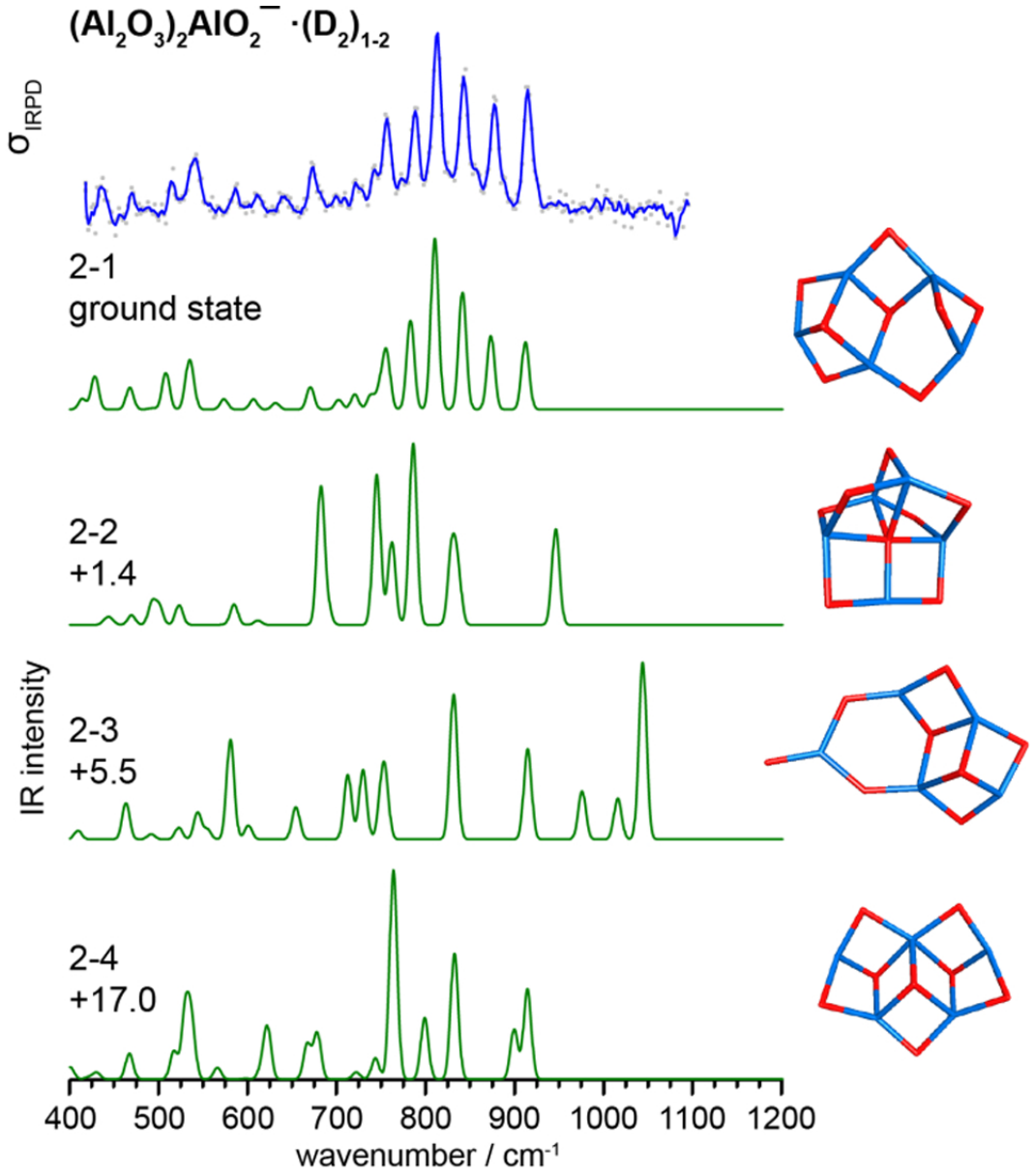

Figure A.4: Experimental IRPD spectra (blue) of $(Al_2O_3)_2AlO_2^- \cdot D_2$ is compared to simulated harmonic IR spectra (green) of low lying structures (Al=blue, O=red). Relative energy including vibrational zero point energy of each isomer is given in kJ/mol.

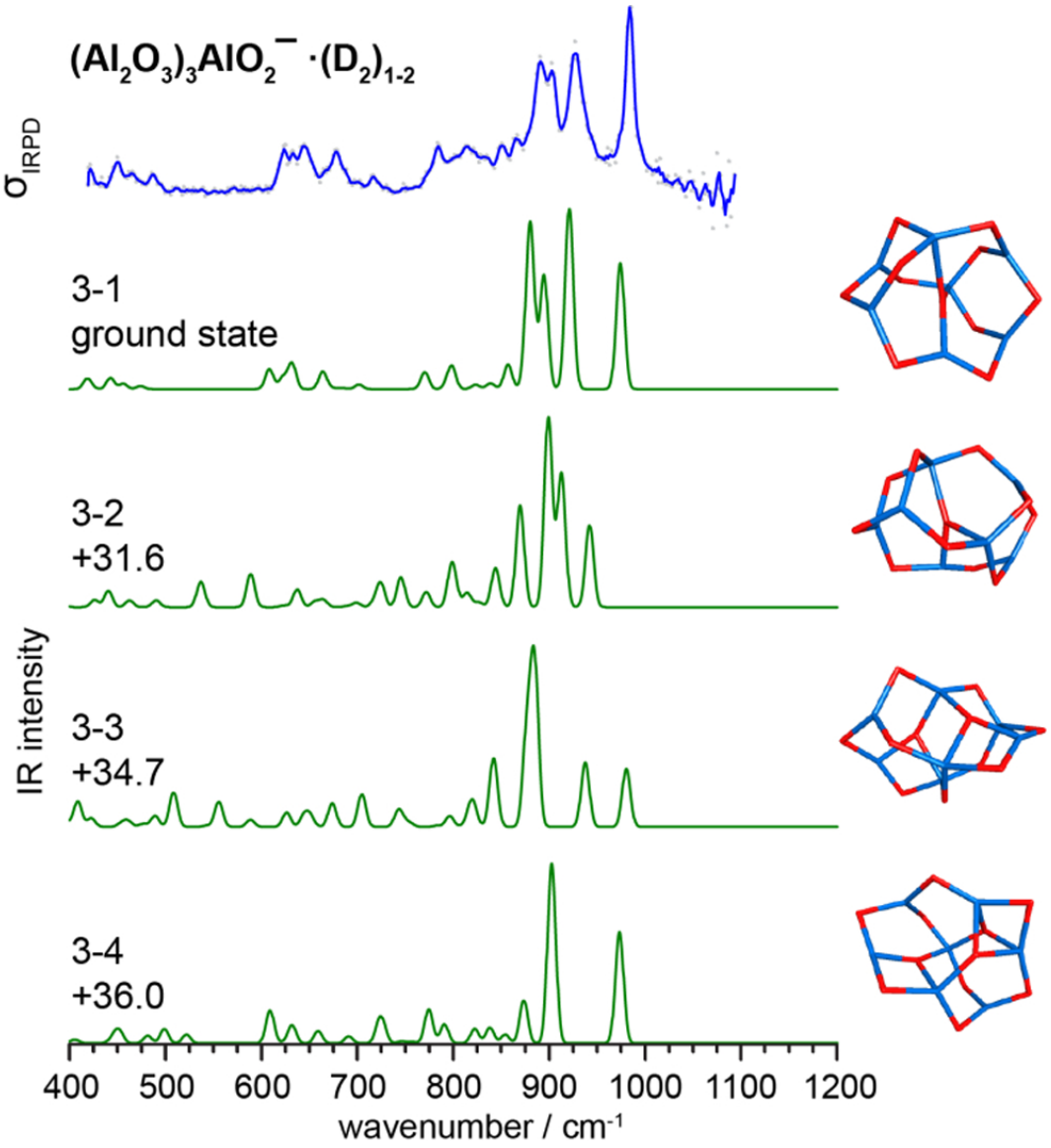

Figure A.5: Experimental IRPD spectra (blue) of $(Al_2O_3)_3AlO_2^-\cdot D_2$ is compared to simulated harmonic IR spectra (green) of low lying structures (Al=blue, O=red). Relative energy including vibrational zero point energy of each isomer is given in kJ/mol.

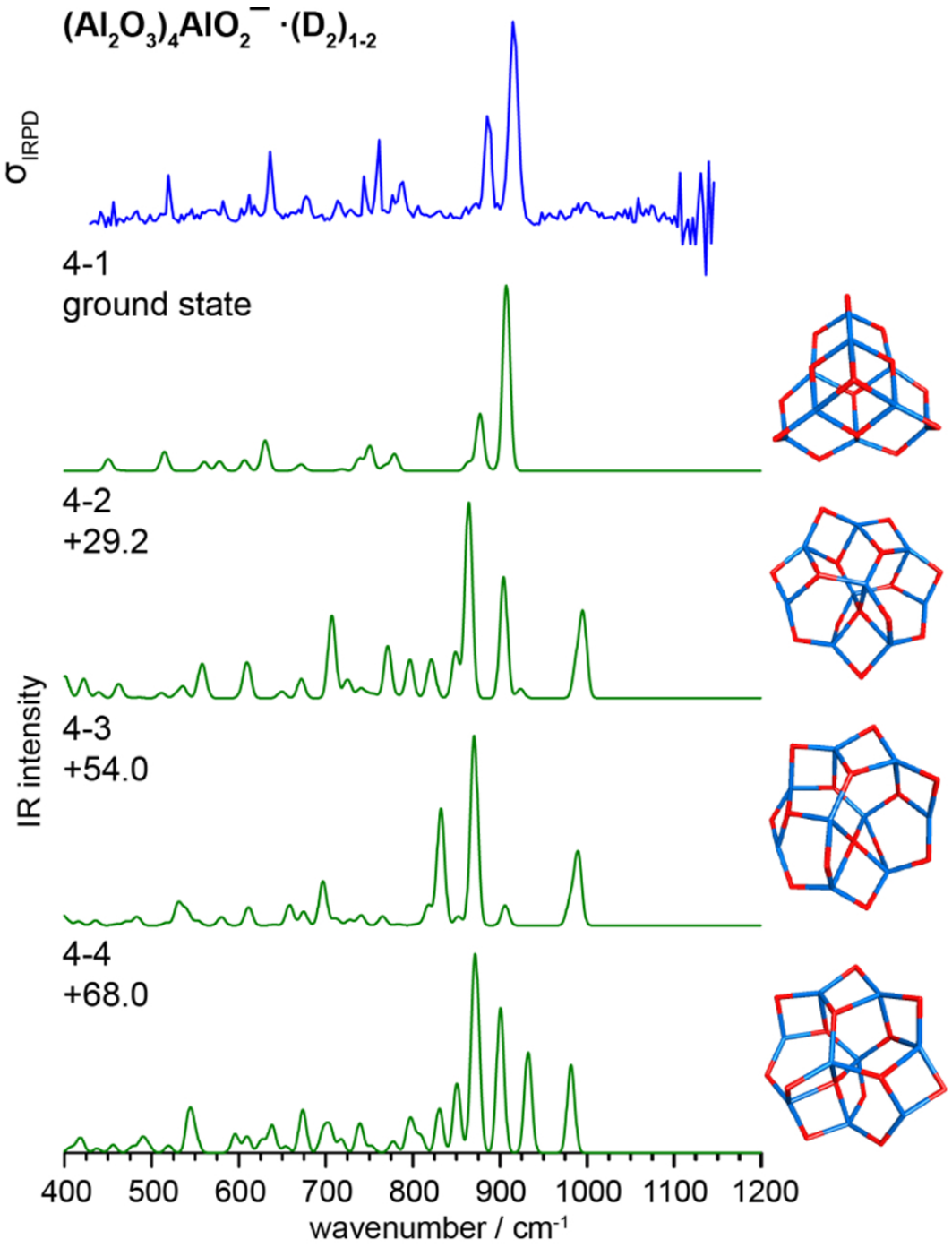

Figure A.6: Experimental IRPD spectra (blue) of $(Al_2O_3)_4AlO_2^-\cdot D_2$ is compared to simulated harmonic IR spectra (green) of low lying structures (Al=blue, O=red). Relative energy including vibrational zero point energy of each isomer is given in kJ/mol.

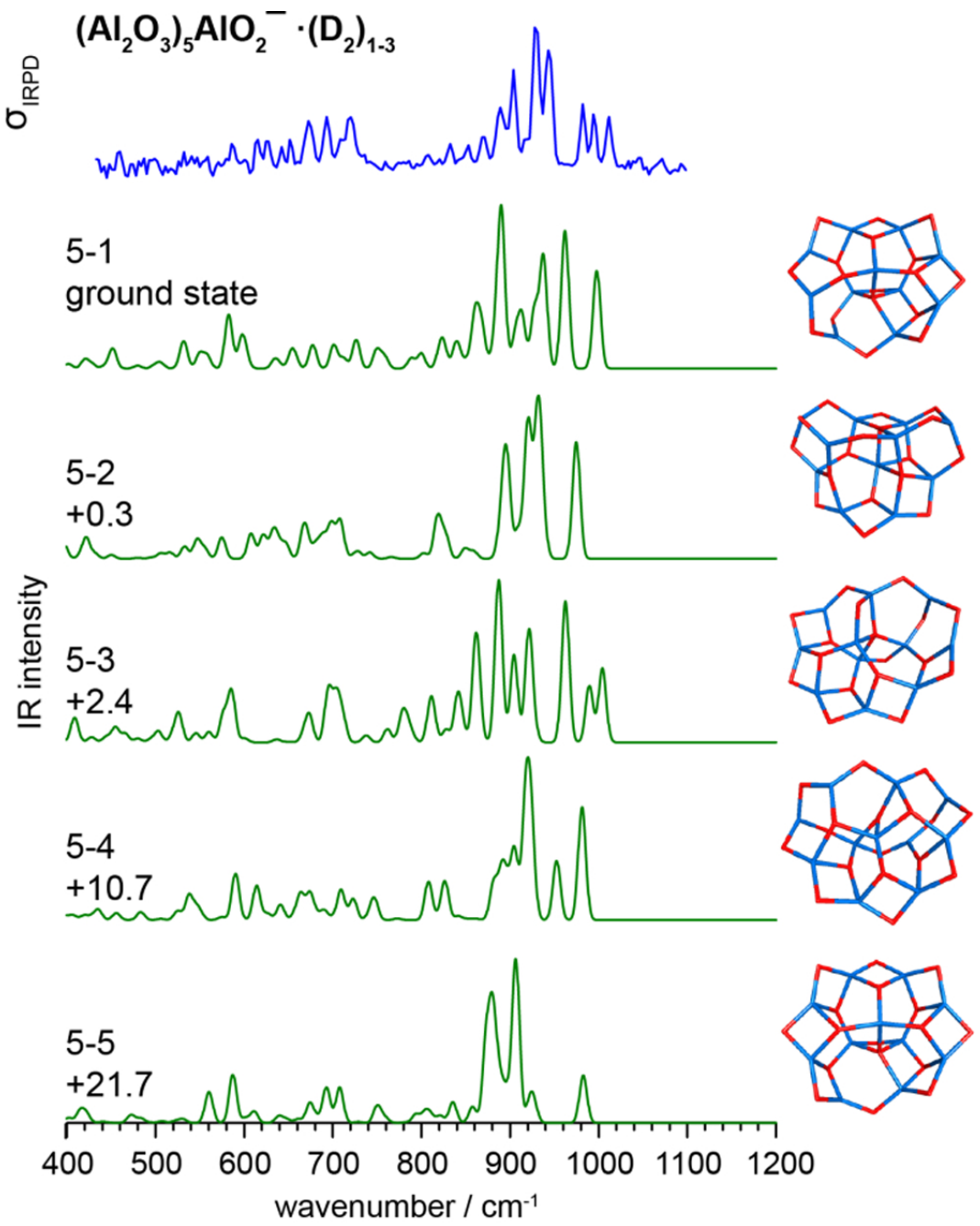

Figure A.7: Experimental IRPD spectra (blue) of $(Al_2O_3)_5AlO_2^-\cdot D_2$ is compared to simulated harmonic IR spectra (green) of low lying structures (Al=blue, O=red). Relative energy including vibrational zero point energy of each isomer is given in kJ/mol.

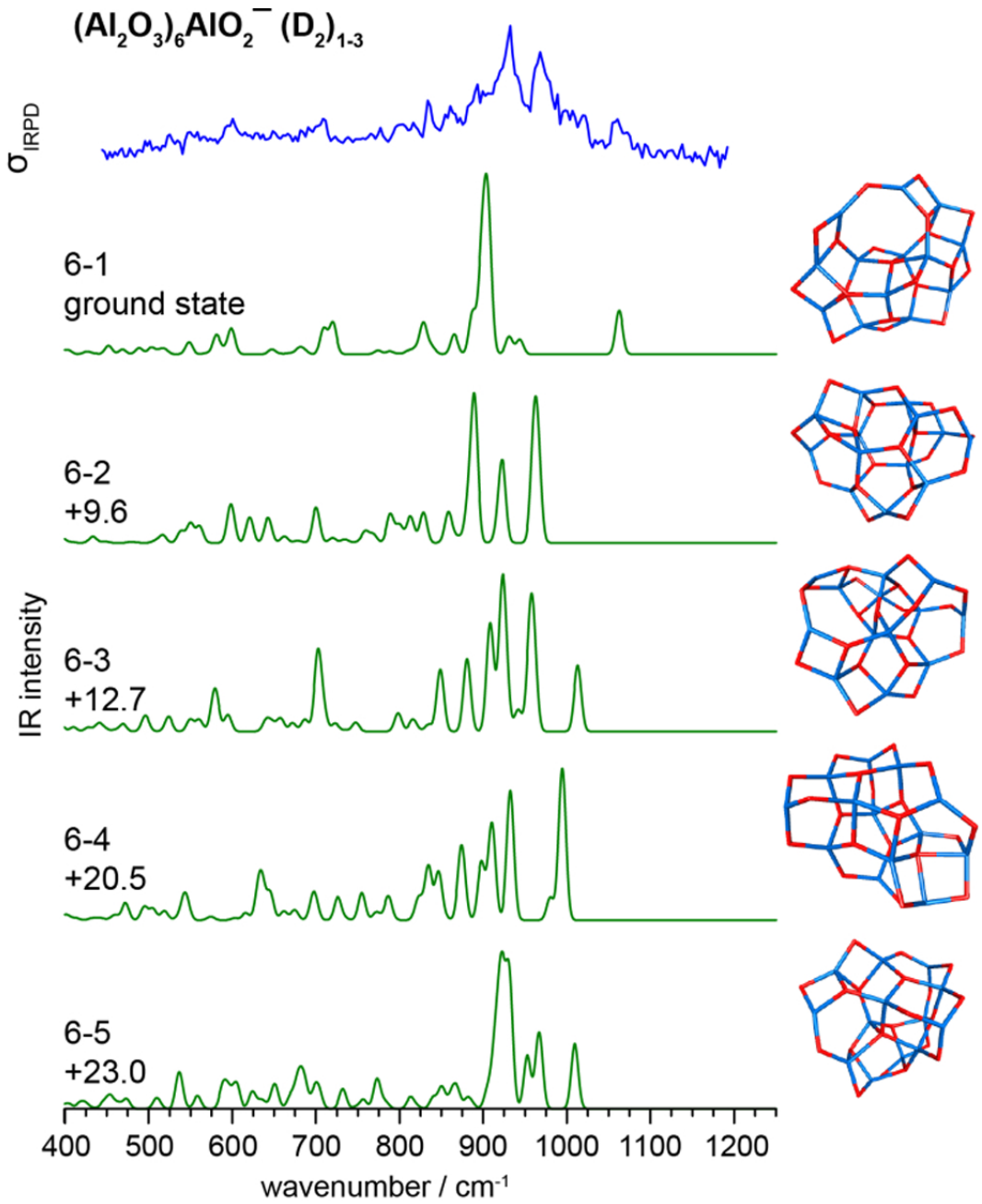

Figure A.8: Experimental IRPD spectra (blue) of $(Al_2O_3)_6AlO_2^-\cdot D_2$ is compared to simulated harmonic IR spectra (green) of low lying structures (Al=blue, O=red). Relative energy including vibrational zero point energy of each isomer is given in kJ/mol.

Table A.2: Bond length analysis of $(Al_2O_3)_nAlO_2^-$ (n = 1–6) of assigned structure.

cluster	coordination number Al–O (No pf bonds)	bond length range (pm)	average bond length (pm)
1-1	3-1 (2)	161.6	161.6
	3-2 (4)	168.0–181.8	174.9
	3-3 (3)	179.6–185.6	183.5
2-1	3-2 (5)	170.7–174.8	172.4
	3-3 (1)	176.1	176.1
	4-2 (7)	173.9–182.0	178.6
	4-3 (5)	180.1–193.9	188.1
3-1	3-2 (14)	169.3–173.9	171.6
	3-3 (1)	177.6	177.6
	4-2 (6)	172.9–175.2	173.7
	4-3 (2)	215.3	215.3
4-1	3-2 (9)	170.5–173.9	172.4
	4-2 (9)	172.9–173.6	178.6
	4-3 (15)	178.7–189.9	184.4
5-1	3-2 (8)	168.3–173.0	170.4
	3-3 (1)	177.4	177.4
	4-2 (14)	170.8–176.3	173.2
	4-3 (14)	173.9–196.2	183.8
	4-4 (4)	186.7–210.0	199.3
5-2	3-2 (8)	168.1–171.6	170.3
	3-3 (1)	173.7	173.7
	4-2 (14)	171.5–175.4	173.0
	4-3 (9)	182.2–201.9	188.3
	4-4 (5)	183.4–194.5	190.9
	5-3 (3)	174.3–183.5	180.2
	5-4 (2)	195.5–207.9	201.6
6-1	3-2 (4)	168.6–169.7	169.1
	3-3 (2)	174.3	174.3
	4-2 (18)	171.4–174.9	172.9
	4-3 (22)	174.7–198.8	184.7
	4-4 (4)	191.3–196.8	194.1
6-2	3-2 (6)	170.3–172.0	170.9
	4-2 (18)	169.8–177.0	172.9
	4-3 (18)	173.4–199.1	183.5
	4-4 (8)	183.7–208.9	192.4

Appendix B
$(Al_3O_4)(D_2O)_{0\text{-}4}^+$

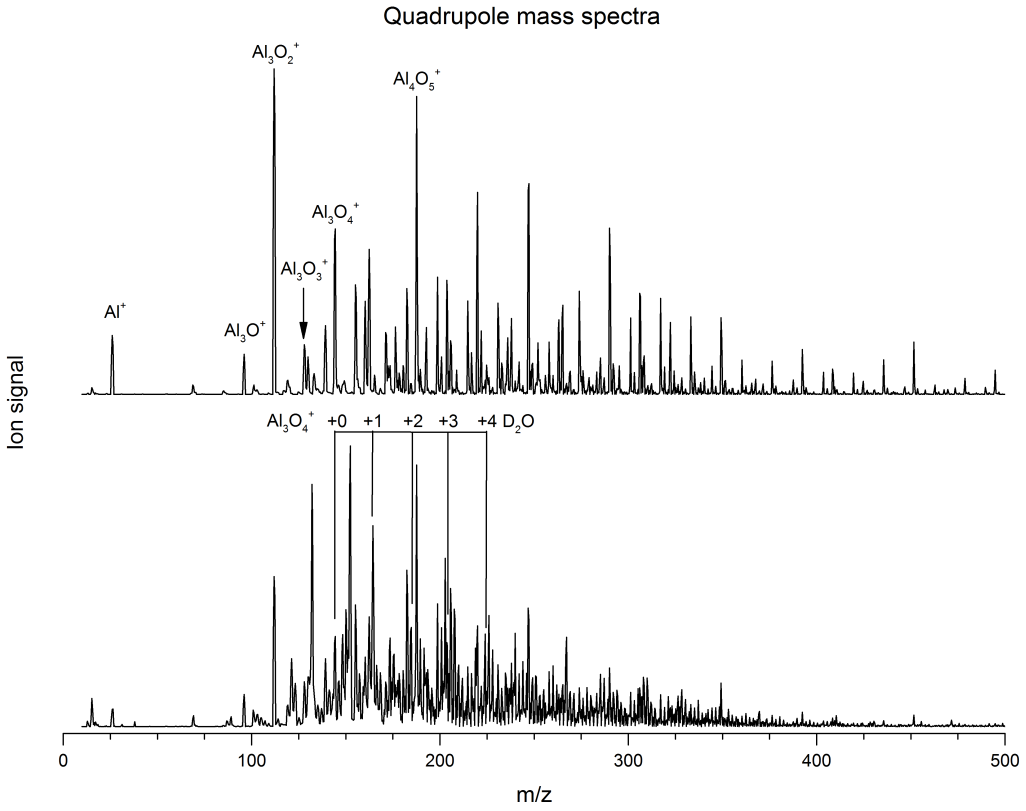

Figure B.1: Typical quadrupole mass spectra mass distribution of aluminum oxide cationic clusters (**top**) and of the complexes formed with D_2O (**bottom**) produced by laser vaporization source. See Section 4.3.2 for source conditions.

Table B.1: Experimental IRPD/IRMPD band positions (in cm^{-1}), B3LYP/def2-TZVPP harmonic frequencies (in cm^{-1}) of the lowest energy isomer and normal mode assignments for $[Al_3O_4(D_2O)_n]^+$ with $n = 0$–4.

System	Exp.	DFT	Assignment
$n = 0^a$	871 (E), 750 (F), 722 (G), 700 (H)	866, 865, 752, 749, 713, 713	Al_2-(μ_2-O) stretch
	678 (I), 543 (K)	693, 537, 536	Al_3-(μ_3-O) stretch
	602 (J)	600	frame deformation (μ_3-O)
$n = 1^b$	2806 (A)	2876, 2874	terminal Al-(O–D) stretch
	1023 (E)	1022, 1014	Al–OD stretch
	971 (F), 873 (G), 772 (H), 722 (I)	994, 871[c] ,758 ,727, 700	Al_2-(μ_2-O) and Al_3-(μ_3-O) stretch
	593 (J), 539 (K), 497 (L)	515	frame deformation (μ3-O)
$n = 2$	2800 (A)	2878, 2870, 2868	terminal Al-(O–D) stretch
	2651 (B)	2732	terminal Al_2-(μ_2-O-D) stretch
	1104 (E), 1077 (F)	1109, 1079	Al_2-(μ_2-O) stretch
	981 (G)	976, 891, 857	Al–OD stretch
	694 (I), 625 (J)	689, 620	Al_2-(μ_2-O) stretch
	819 (H)	826	Al_2-(μ_2-OD) in-plane bend
	436 (K)	442	Al_2-(μ_2-OD) out-of-plane bend
$n = 3$	2797 (A)	2897, 2895, 2895	terminal Al-(O–D) stretch
	2714 (B)	2822, 2818, 2818	terminal Al_2-(μ_2-O-D) stretch
	943 (E)	979, 949, 949	Al–OD stretch
	712 (F), 647 (G)	727, 727, 667, 666, 648, 648	Al_2-(μ_2-OD) in-plane bend
	647 (G)	658, 649	Al_3-(μ_3-O) stretch
$n = 4$	2807 (A)	2896, 2895, 2894, 2865[d]	terminal Al-(O–D) stretch
	2750 (C), 2688 (B), 2352 (D)	2835, 2792, 2790, 2424[d]	terminal Al_2-(μ_2-O-D) stretch
	946 (E)	965, 942, 929, 739[d]	Al–OD stretch
	790 (F), 740 (G), 695 (H)	852[d], 794, 768, 709, 702	Al_2-(μ_2-OD) in-plane bend
	650 (I), 610 (J), 570 (K), 526 (L)	670, 648, 608, 570, 523	Al_3-(μ_3-O) stretch

[a] $[Al_3O_4]He_3$. [b] $[Al_3O_4(D_2O)]^+D_2$. [c] Al_3-(μ_3-O) in sheet structure. [d] hydrogen-bonded.

Table B.2: B3LYP/def2-TZVPP bond lengths (in pm) and harmonic frequencies (in cm^{-1}) of the lowest energy isomer and normal mode assignments for $[Al_3O_4(D_2O)_n]^+$ with $n = 0$–4.

n	**Bond**	**Calc. freq.**	**Bond length**	**Note**
1	Al-(O–D)	2876 and 2874	95.6	sym and antisym
	Al–OD	1022 and 1014	164.5	sym and antisym
2	Al-(O–D)	2878	95.5	
		2870, 2868	95.6, 95.7	sym and antisym of the two Al-(O–D) separated by bridging OD
	Al_2-(μ_2-O)	1108, 1079	165.2, 165.2	sym and antisym of the two Al_2-(μ_2-O) separated by bridging OD
	Al–OD	976, 891, 857	165.8	
	Al_2-(μ_2-O-D)	2732	96.9	
	Al_2-(μ_2-O)	689, 620	182.3, 182.4	sym and antisym
3	Al-(O–D)	2897, 2895, 2895	95.4, 95.4, 95.4	
	Al–OD	979, 949, 949	165.5, 165.5, 165.5	
	Al_2-(μ_2-O-D)	2822, 2818, 2818	96.0, 96.0, 96.0	
	Al_2-(μ_2-OD)	667,666, 648	(183.5, 183.6), (183.4, 183.6), (183.5, 183.6)	
4	Al-(O–D)	2896, 2895, 2894	95.4, 95.4, 95.4	
	Al–OD	965, 942	165.6, 165.7	sym and antisym of the ones with Al part of the 4 ring
		929	167.3	
		739	172.5	H-bond acceptor
	Al_2-(μ_2-O-D)	2792, 2790	96.3, 96.3	sym and antisym
		2835	95.9	in the 4 ring (NOT H-bonded)
		2424	99.0	H-bonded
	Al_2-(μ_2-OD)	670, 648	(182.6, 182.6), (183.2, 183.2)	sym and antisym in the 4 ring. The first pair is with the H-bonded
		608, 570, 523	(180.8,186.4), (180.7,186.4)	

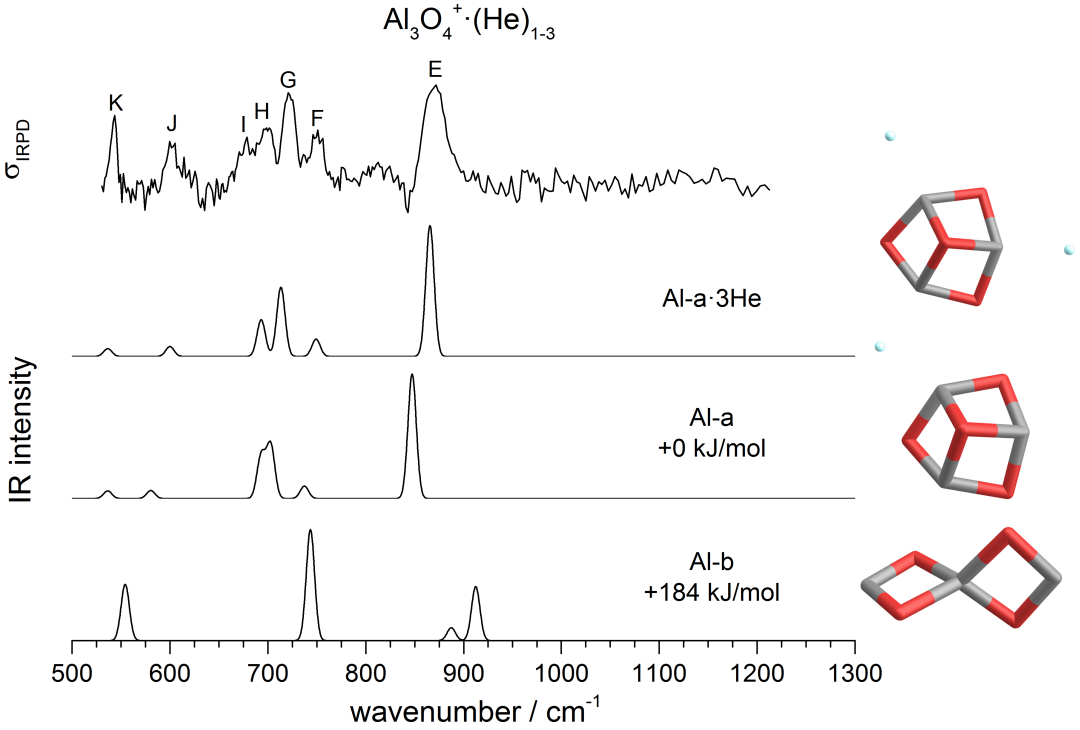

Figure B.2: IRPD vibrational spectrum (**top**) of $Al_3O_4{}^+\cdot(He)_{1-3}$ compared with B3LYP/def2-TZVPP harmonic frequencies and intensities of low lying structures (also reported) with and without He-tag and convoluted with a Gaussian line shape function (fwhm width: 10 cm^{-1}) to account for the spectral width of the laser radiation as well as rotational broadening. Relative energy including vibrational zero point energy of each isomer is given in kJ/mol.

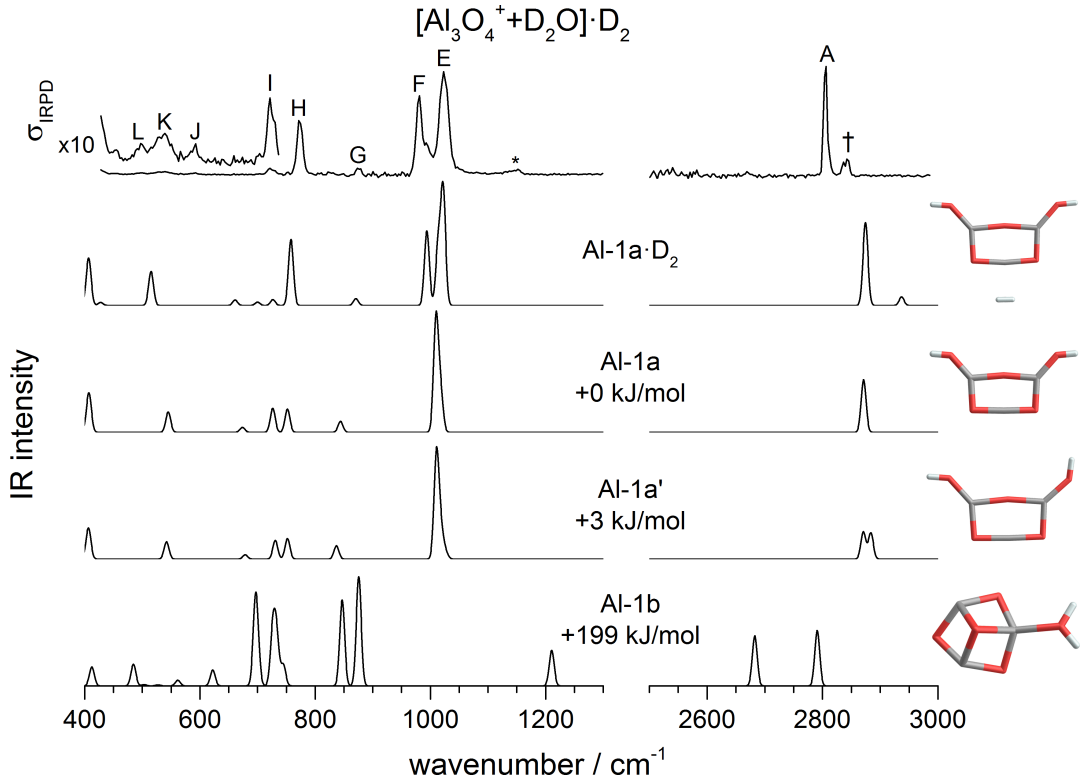

Figure B.3: IRPD vibrational spectrum (**top**) of $[Al_3O_4^+ + D_2O]\cdot D_2$ compared with B3LYP/def2-TZVPP harmonic frequencies and intensities of low lying structures (also reported) with and without D_2-tag and convoluted with a Gaussian line shape function (fwhm width: 10 cm^{-1}) to account for the spectral width of the laser radiation as well as rotational broadening. Relative energy including vibrational zero point energy of each isomer is given in kJ/mol.

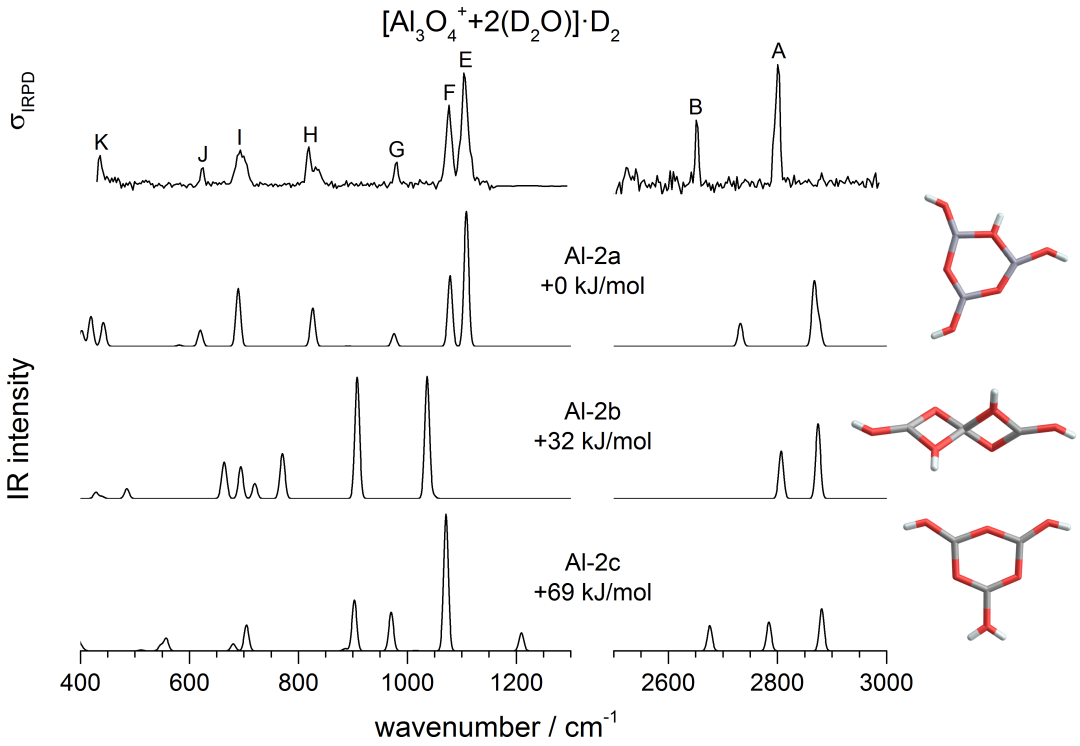

Figure B.4: IRPD vibrational spectrum (**top**) of $[Al_3O_4^+ + 2\ D_2O]{\cdot}D_2$ compared with B3LYP/def2-TZVPP harmonic frequencies and intensities of low lying structures (also reported) convoluted with a Gaussian line shape function (fwhm width: 10 cm^{-1}) to account for the spectral width of the laser radiation as well as rotational broadening. Relative energy including vibrational zero point energy of each isomer is given in kJ/mol.

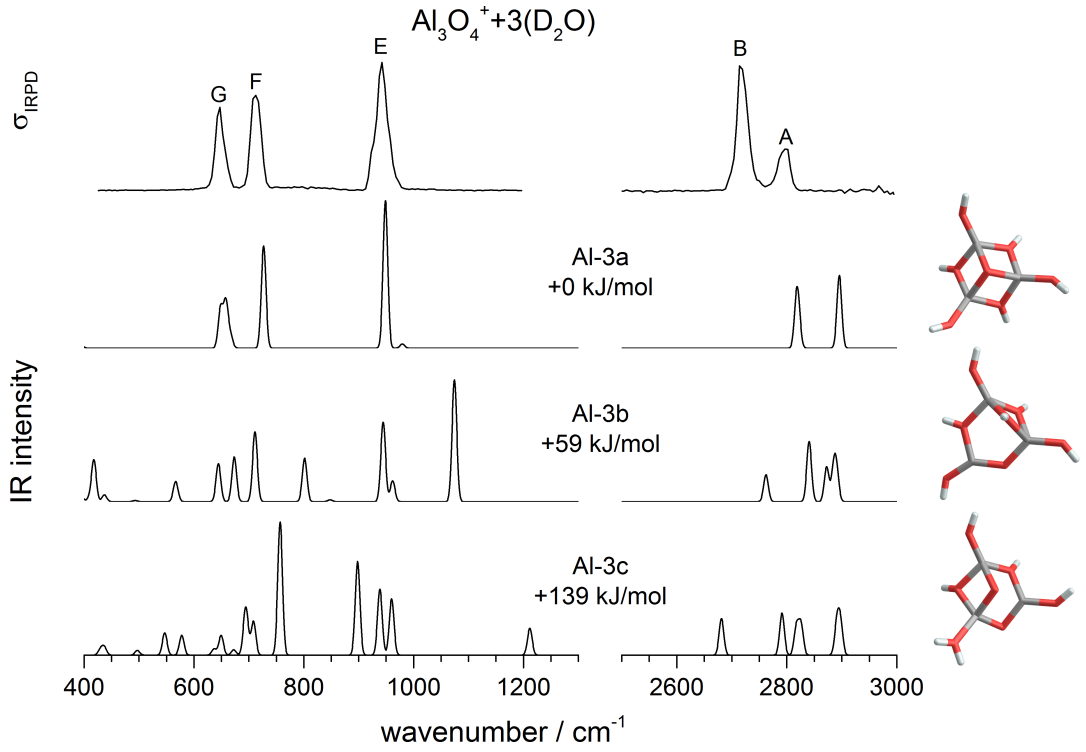

Figure B.5: IRMPD vibrational spectrum (**top**) of $Al_3O_4^+$ + 3 D_2O compared with B3LYP/def2-TZVPP harmonic frequencies and intensities of low lying structures (also reported) convoluted with a Gaussian line shape function (fwhm width: 10 cm^{-1}) to account for the spectral width of the laser radiation as well as rotational broadening. Relative energy including vibrational zero point energy of each isomer is given in kJ/mol.

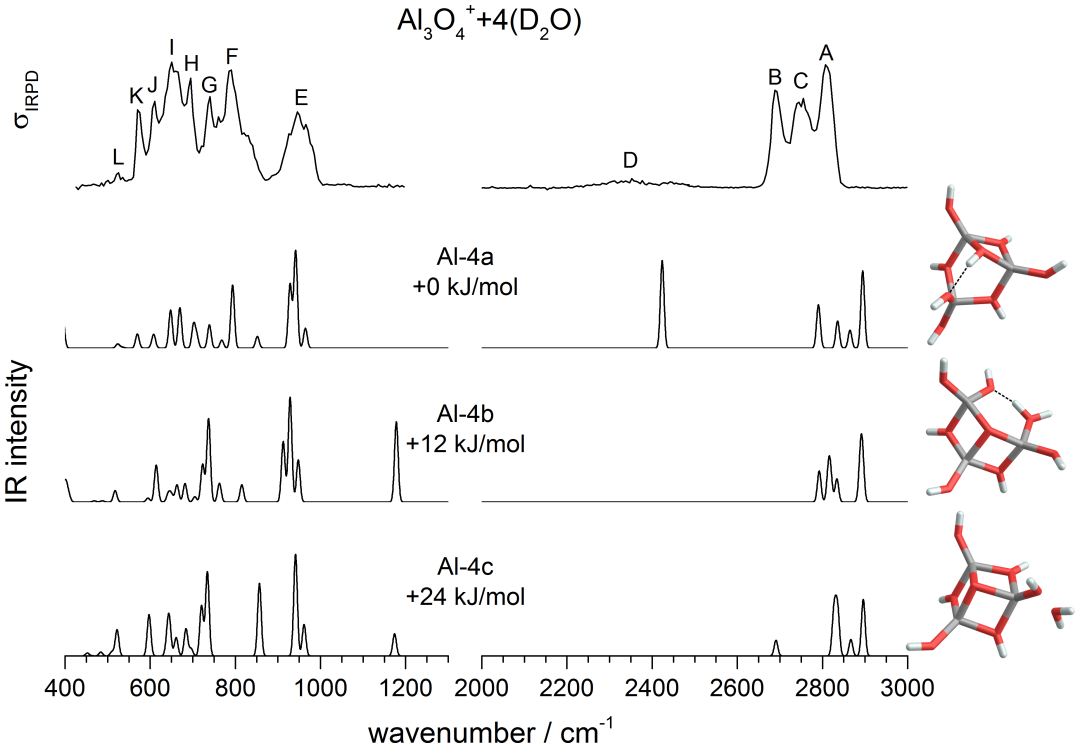

Figure B.6: IRMPD vibrational spectrum (**top**) of $Al_3O_4^+$ + 4 D_2O compared with B3LYP/def2-TZVPP harmonic frequencies and intensities of low lying structures (also reported) convoluted with a Gaussian line shape function (fwhm width: 10 cm^{-1}) to account for the spectral width of the laser radiation as well as rotational broadening. Relative energy including vibrational zero point energy of each isomer is given in kJ/mol.

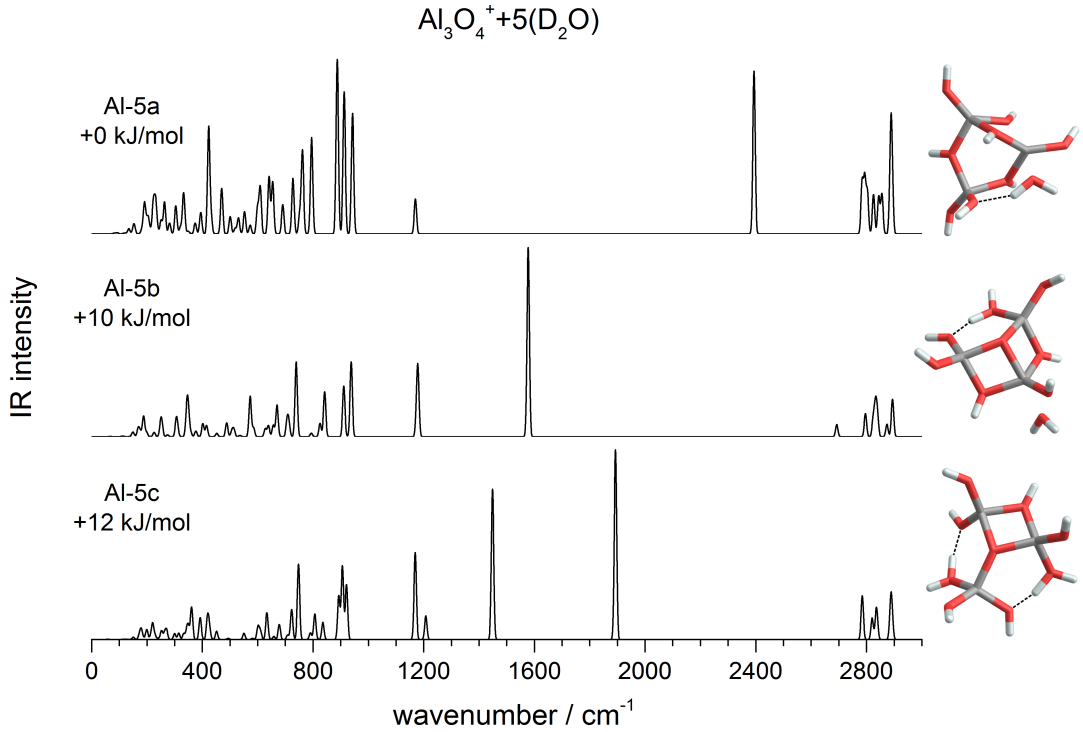

Figure B.7: B3LYP/def2-TZVPP harmonic frequencies and intensities of low lying structures (also reported) of $Al_3O_4^+$ + 4 D_2O convoluted with a Gaussian line shape function (fwhm width: 10 cm^{-1}) to account for the spectral width of the laser radiation as well as rotational broadening. Relative energy including vibrational zero point energy of each isomer is given in kJ/mol.

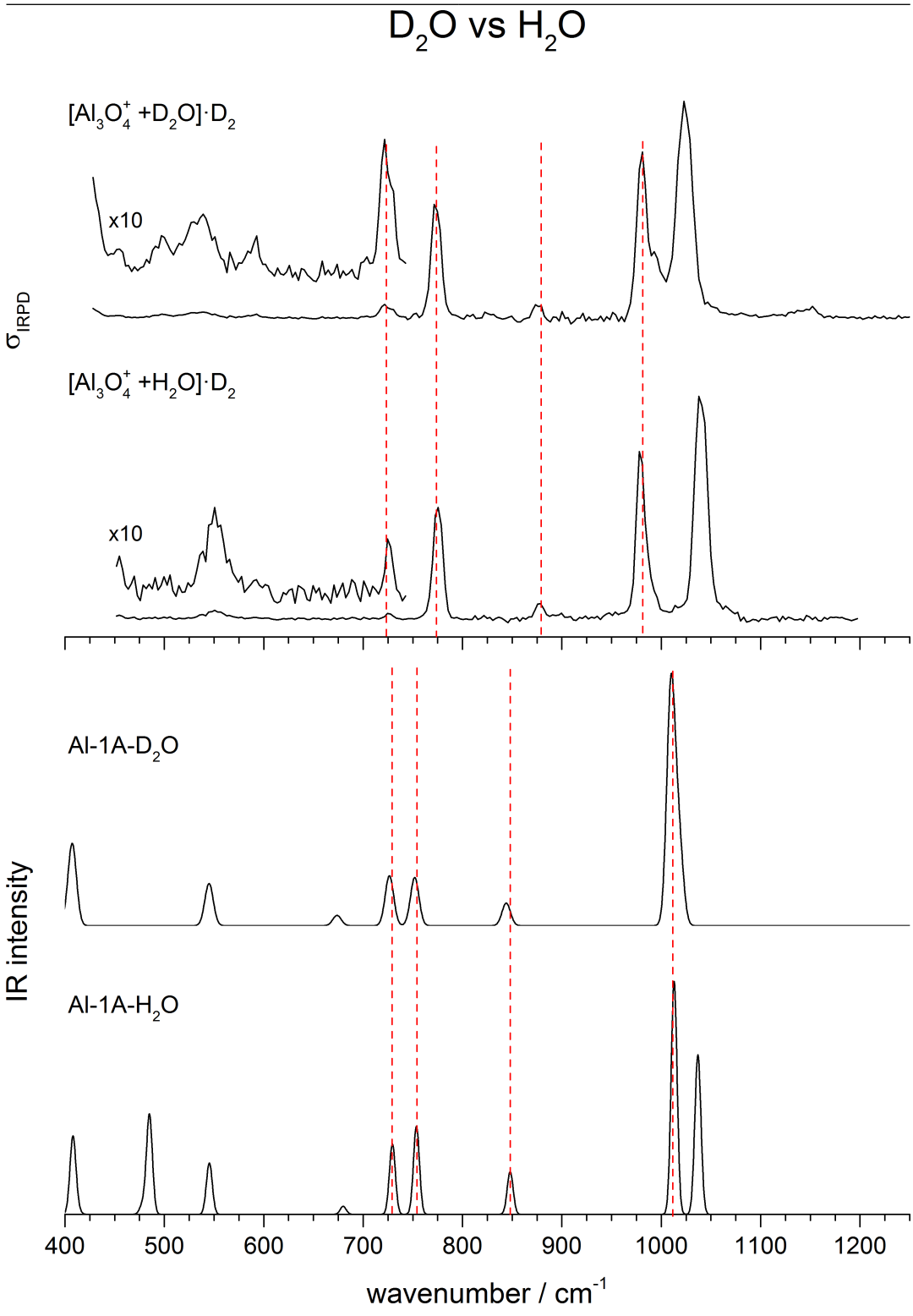

Figure B.8: (**top**) IRPD vibrational spectrum of $[Al_3O_4^+ + D_2O]\cdot D_2$ compared with that of $[Al_3O_4^+ + H_2O]\cdot D_2$. (**bottom**) Analogous comparison of B3LYP/def2-TZVPP harmonic frequencies and intensities of lowest energy structures convoluted with a Gaussian line shape function (fwhm width: 10 cm^{-1}) to account for the spectral width of the laser radiation as well as rotational broadening.

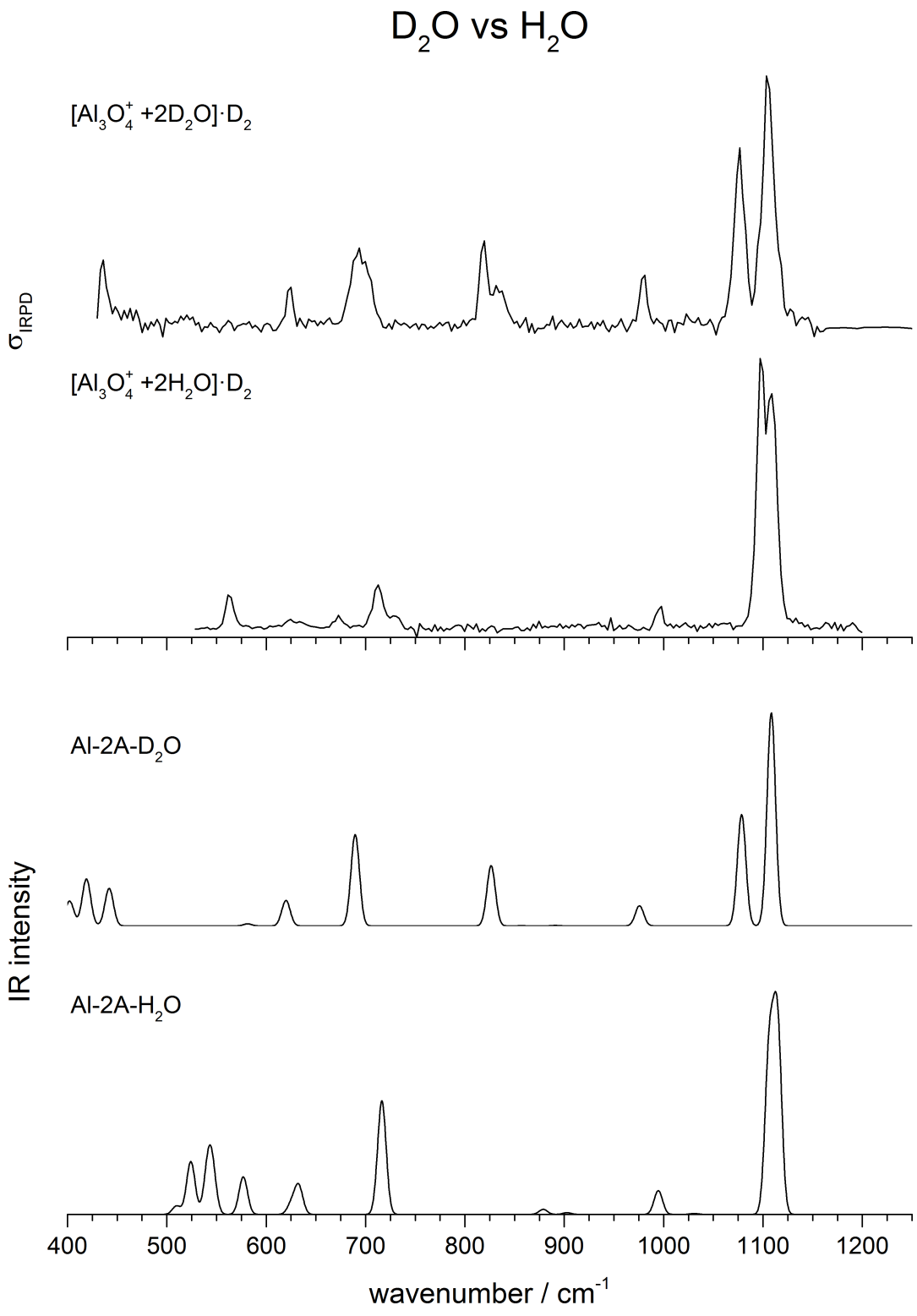

Figure B.9: (**top**) IRPD vibrational spectrum of $[Al_3O_4^+ + 2\ D_2O]{\cdot}D_2$ compared with that of $[Al_3O_4^+ + 2\ H_2O]{\cdot}D_2$. (**bottom**) Analogous comparison of B3LYP/def2-TZVPP harmonic frequencies and intensities of lowest energy structures convoluted with a Gaussian line shape function (fwhm width: 10 cm^{-1}) to account for the spectral width of the laser radiation as well as rotational broadening.

Table B.3: Spectral regions for characteristic vibrational normal modes from gas-phase IRPD/IRMPD spectroscopy (gas phase, present study), VSF spectroscopy and DFT calculations (surface, Ref. [9, 10]).

Bond	**Gas Phase Exp.**	**DFT**[d]	**Surface Exp.**	**DFT**
terminal Al-(O–D) stretch	2797–2807	2860–2900	(2910, 2900)[a], 2737[b]	2696[a], 2697[a], 2713[a], 2737[b], 2779[b,c]
terminal Al_2-(μ_2-O-D) stretch	2651–2750	2732–2835	(2790, 2764, 2729)[a], 2772[b]	2523[a], 2541[a], 2583
H-bonded O–D stretch	2150–2550	2420–2430		
Al–OD stretch	929–1022	850–1030		
Al_2-(μ_2-O) stretch	700–1104	620-1110		
Al_3-(μ_3-O) stretch	526–694	510–700		
Al_2-(μ_2-OD) in-plane bend	695–819	470–860		

[a] αAl_2O_3 (0001) from Ref [9]. [b] αAl_2O_3 ($1\bar{1}02$) from Ref [10].
[c] O–D stretch of a molecularly absorbed water. [d] Rounded.

Appendix C
Fe-oxide

C.1 Experimental methods

IRPD experiments are conducted on the 10 K Setup described in Chapter 3. A pulsed beam of cationic iron-oxide clusters is formed by laser vaporization with the suorce described in Section 3.2.2. Vaporization is induced by focusing (30 cm focal length) the second harmonic output (532 nm) of a pulsed 50 Hz Nd:YAG laser (*Soliton*, Nano LG 100-50) onto the surface of a moving metal-rod target. The ablated ions are then entrained in a carrier gas pulse of 0.75 % O_2 seeded in helium, and aluminum-oxide clusters $Al_mO_o{}^+$ are subsequently formed through expansion in a clustering channel ending with a cone shape nozzle held at a temperature of 270 K. In order to obtain a stable cluster signal, the turning speed of the rod is set to ~ 3 turns per minute and laser pulse energies of up to 5 mJ are applied. Using a backing pressure of ~ 5.5 bar, $Fe_mO_o{}^+$ clusters are efficiently produced in the mass range from 100 to 600 amu. (see Fig. 3.8 top panel). The time delay between firing of the laser and opening of the pulsed valve is optimized to enhance the formation of the clusters of interest. In order to form Fe-oxide/water complexes, a flow of helium at 1.5 bar passes through a bubbler containing H_2O at room temperature (294 K). Water vapor pressure mixes with He and the gas mixture is injected with the second pulsed valve in the source block expanding through the separated gas channel. $Fe_mO_o{}^+(H_2O)_n$ complexes with $n \leq 6$–8 are efficiently formed. The beam of ions passes a 4 mm diameter skimmer, is then collimated in a RF buffer-gas-filled decapole ion-guide, and ions of interest are selected according to their mass/charge ratio using a quadrupole mass-filter. The mass-selected beam is focused into a cryogenically-cooled RF ring electrode ion-trap. The trap is continuously filled with He buffer gas at a trap temperature of 13–15 K, which allows for the accumulation and thermalization of the trapped ions. Inside the ion trap, ions undergo three-body collisions with the buffer gas, which promote the formation of weakly bound ion–He complexes. After an ion trap fill time of 199 ms all ions are extracted from the ion trap and focused in the center of the extraction region of TOF mass spectrometer, where they are irradiated by an intense and wavelength-tunable IR laser pulse. When resonant with a vibrational transition, the parent ions can absorb a photon, eventually leading to loss of one or more messenger molecules via intramolecular vibrational predissociation. For the larger water complexes ($n > 2$) ion-messenger complex formation is not efficient and the vibrational spectra are measured via IRMPD.

The IR free electron laser FHI FEL (see Section 3.5.2) is used as a light source for the wavelength from 8.3 to 50 μm with a bandwidth between 0.3 and 0.6 % root mean square of the central wavelength. Laser light for IRPD experiments in the O–H stretch region, from 2.5 to 2.85 μm, is produced by an OPO/OPA laser system (double OPO, see Section 3.5.3). The infrared photodissociation cross sections σ_{IRPD} is obtained as described in Section 3.4. The IRMPD vibrational spectrum is obtained monitoring the fragment originated by the loss of one D_2O molecule. Each spectrum is averaged over at least 60 measurements.

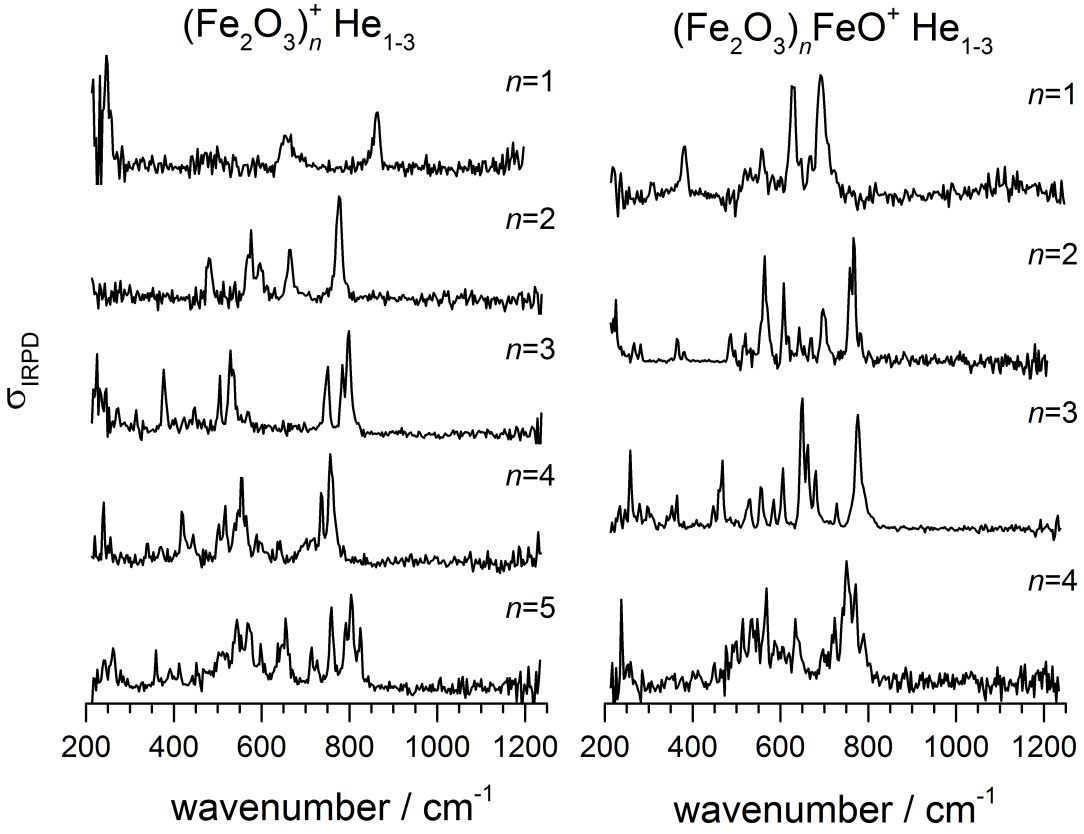

Figure C.1: Experimental vibrational spectra of $(Fe_2O_3)_m{}^+He_{1–3}$ with $m = 1$–5 (**left**) and $(Fe_2O_3)_nFeO^+He_{1–3}$ with $n = 1$–4 (**right**).

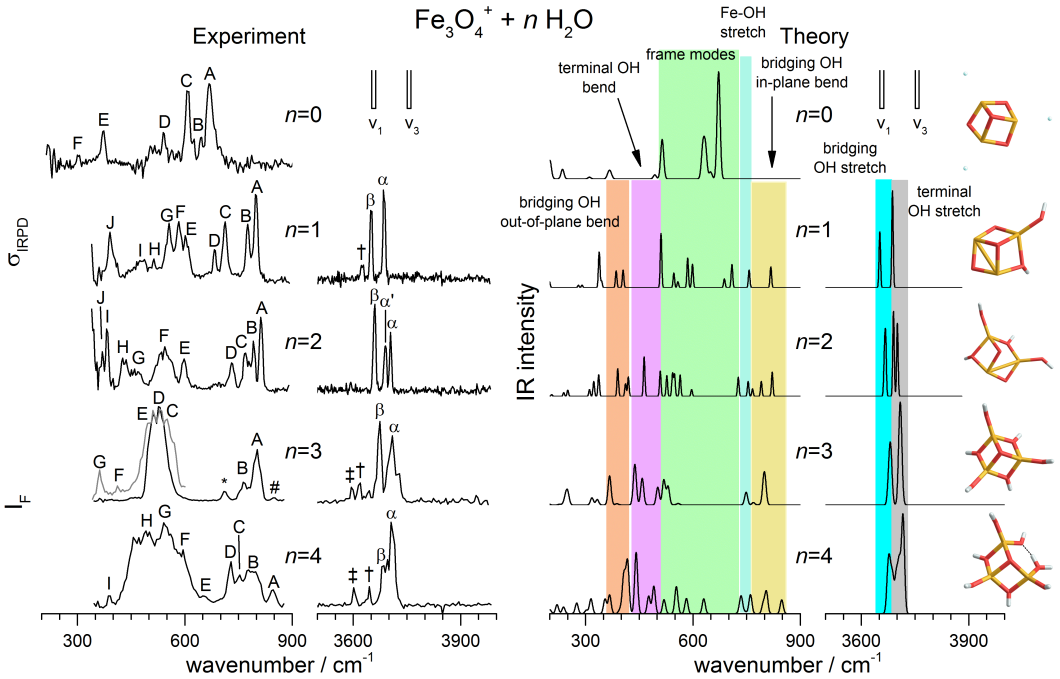

Figure C.2: Experimental (**left**) and computed (**right**) vibrational spectra of $[Fe_3O_4(H_2O)_n]^+$ clusters containing n adsorbed water molecules. (**left**) IRPD (n = 0–2) and IRMPD (n = 3,4) spectra are obtained by monitoring the He loss for n = 0–2) and H_2O loss (n = 3, 4) channel, respectively. (**right**) Computed vibrational spectra derived from B3LYP/def2-TZVPP harmonic frequencies and intensities of the global minimum energy structures (also reported) and convoluted with a Gaussian line shape function (fwhm width: 10 cm^{-1}) to account for the spectral width of the laser radiation as well as rotational broadening. Characteristic IR absorption region of various O–H and Fe–O stretching as well as Fe–O–H bending modes are indicatated. The experimental band positions of the antisymmetric streching (ν_3), symmetric streching (ν_1) of free H_2O are indicated by the bars.

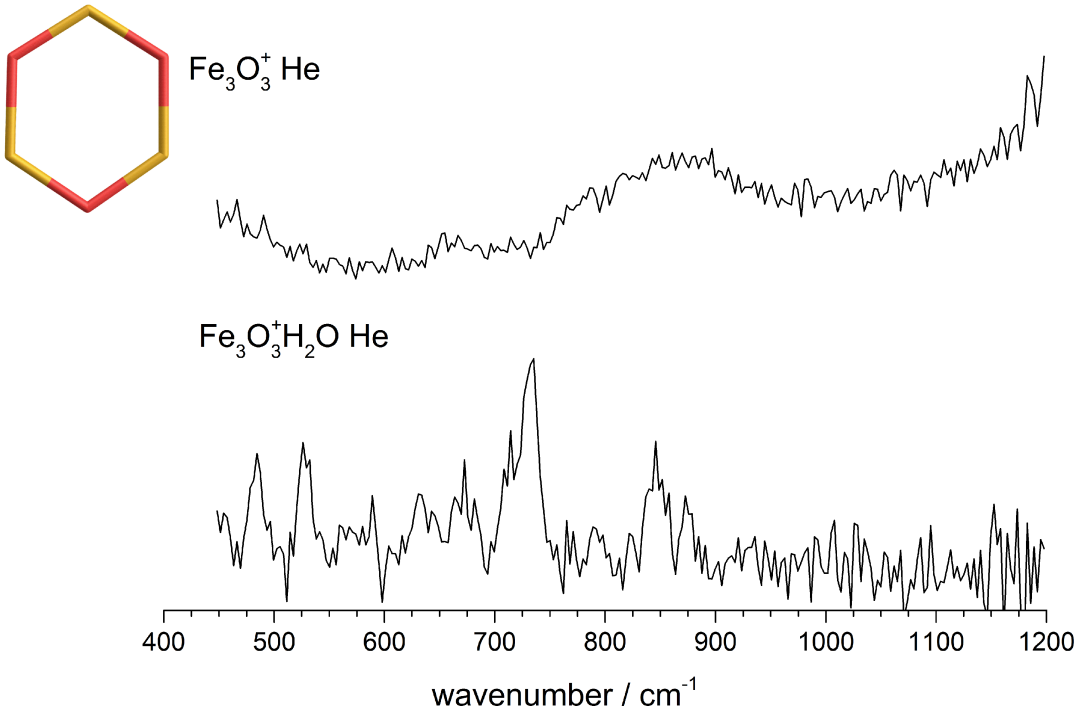

Figure C.3: Experimental vibrational spectra of $Fe_3O_3^+$He (**top**) and the complex formed with one H_2O (**bottom**). The structure of $Fe_3O_3^+$ assigned by Ohshimo *et al.* [358] by means of ion mobility experiments is also reported.

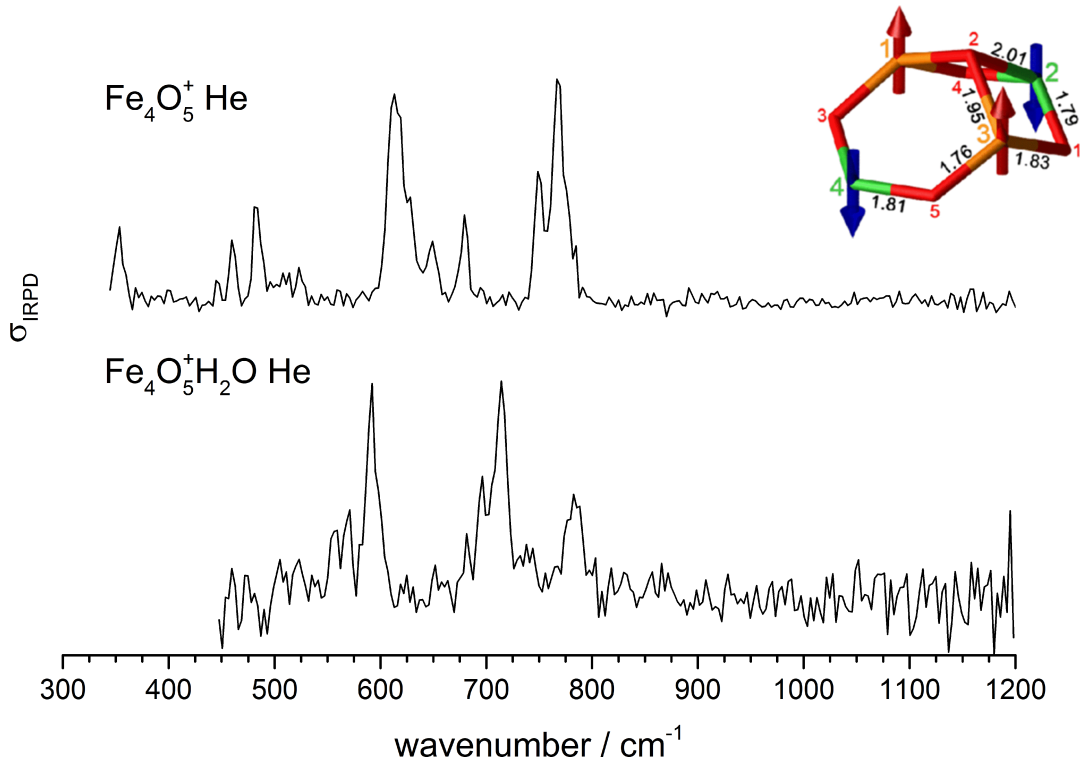

Figure C.4: Experimental vibrational spectra of $Fe_4O_5{}^+He$ (**top**) and the complex formed with one H_2O (**bottom**). The spectrum of $Fe_4O_5{}^+He$ is in agreement with the IRMPD spectrum measures previously by Kirilyuk *et al.* [359]. The structure (also reported) and vibrational spectrum was calculated and assigned by Logemann *et al.* [360].

Appendix D
B_{13}^+

Table D.1: List of IR-active anharmonic VPT2/PBE0/TZVP vibrational frequencies (in cm^{-1}) and intensities (in km mol^{-1}, in parenthesis) calculated between 795 and 815 cm^{-1}. Harmonic frequencies of the contributing normal modes are also listed.

Anharmonic	Harmonic	Assignmentband maximum
815 (4)	422 + 408	combination band of the two out-of-plane B_3 frustrated rotations
810 (13)	721 + 136	combination band of the in-plane B_3 frustrated rotation and B_{10}-ring deformation
796 (22)	408 + 408	1^{st} overtone of lower energy out-of-plane B_3 frustrated rotation

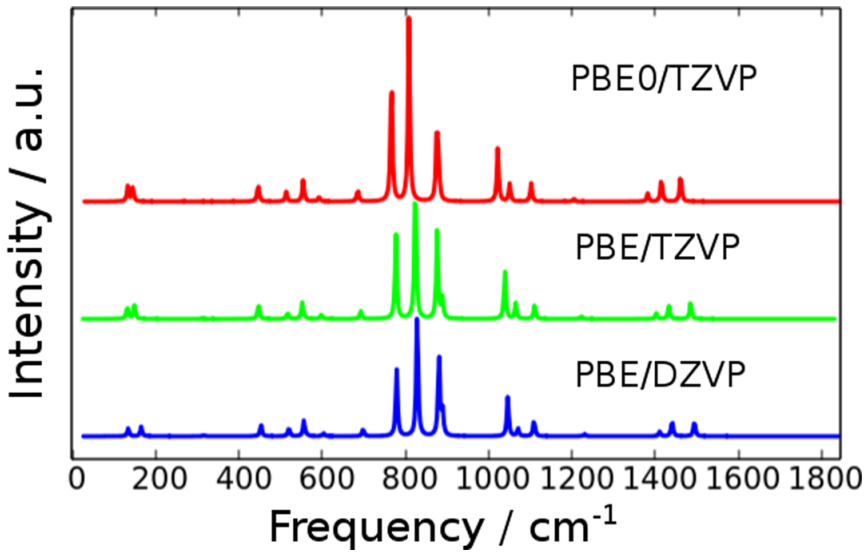

Figure D.1: Calculated harmonic IR spectra of B_{13}^+ with PBE0/TZVP (scaled by factor 0.9575), PBE/TZVP and PBE/DZVP (both not scaled).

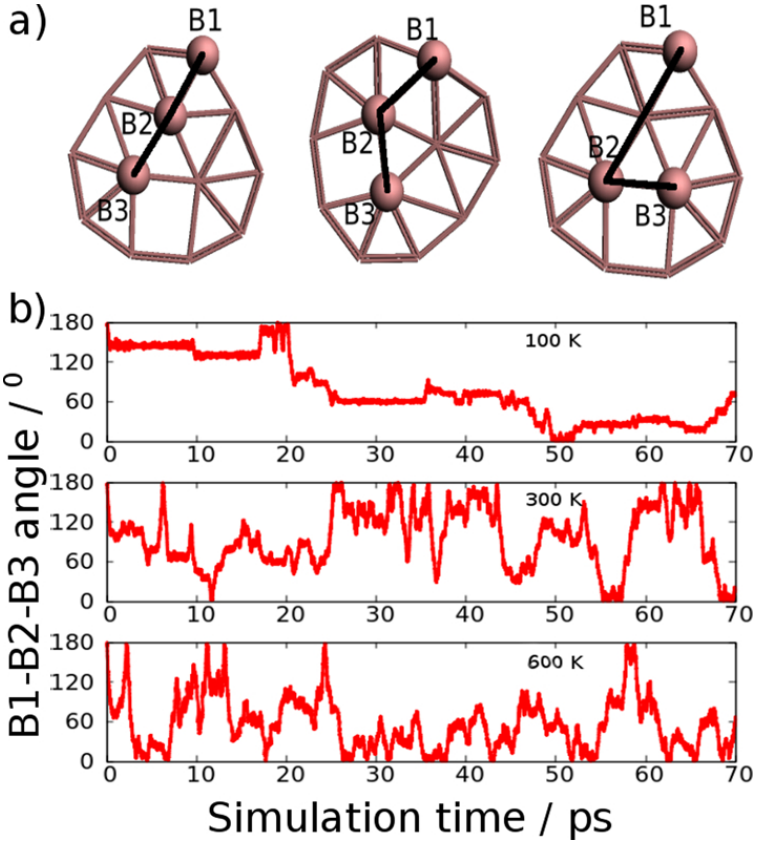

Figure D.2: Rotation of the inner B3 ring with respect to the outer B_{10} ring during the BOMD simulation, represented with angle B1-B2-B3 (shown on panel **a**) at 100, 300, and 600 K (panel **b**).

B_3 ring rotation

Increasing the temperature in the simulation lead to higher mobility of the inner B_3 ring. At 100K the B1-B2-B3 angle (Fig. D.2) changes from 0° to 180° in $\sim$ 50 ps, while at 300 and 600 K it reaches 180° rotation in much shorter simulation time, that is, at $\sim$ 12 and $\sim$ 4.5 ps, respectively. From these values we estimate how many rotations per time unit are possible at the different temperatures. To compare the impact of fluxionality on the IR spectrum, we have studied closely related $^{11}B_{12}$. B_{12} is a nearly planar molecule and lacks the 4-membered ring that offers the space for an unhindered rotation. Fig. D.3 compares calculated IR spectra from anharmonic static calculation and BOMD. Evidently, none of the signals disappears when increasing simulation temperature, indicating a stable bond framework of the cluster.

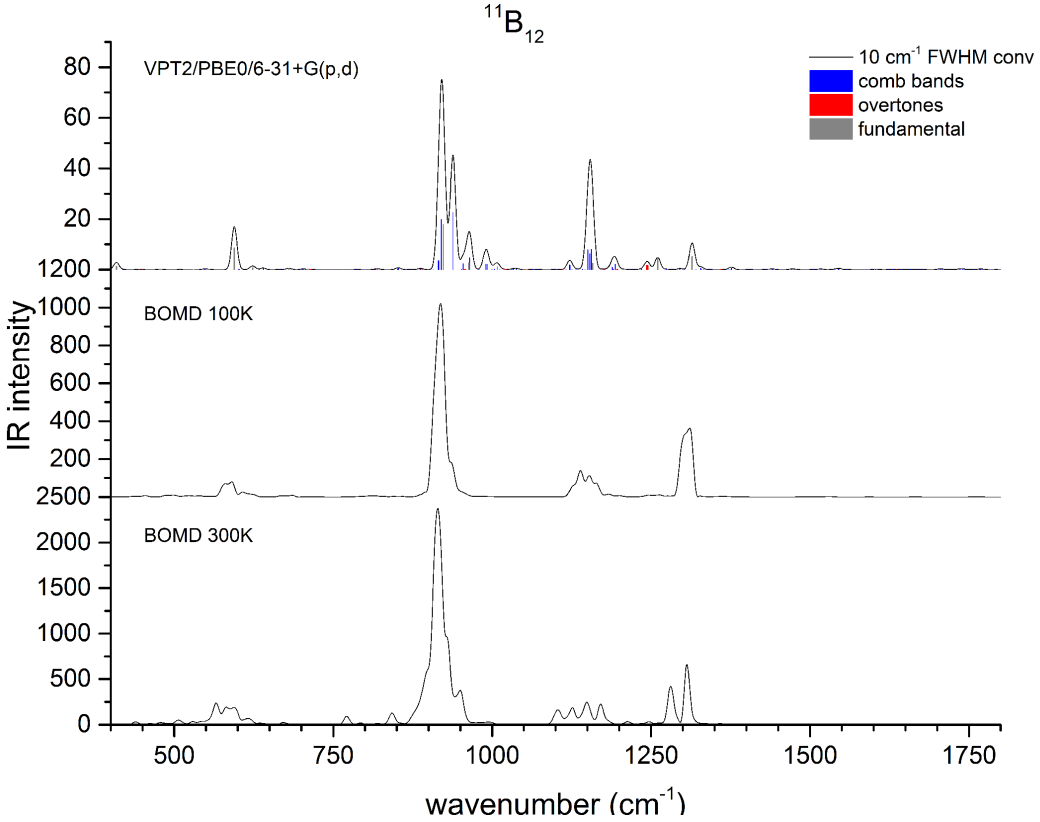

Figure D.3: Calculated IR spectra for $^{11}B_{12}$. Intensities of the VPT2 anharmonic frequencies are given in km mol^{-1}, those of the MOBD in arbitrary units. Computational details are identical to those in the corresponding $^{11}B_{13}{}^{+}$ calculations.

Appendix E
Perhalogenated dodecaborate clusters

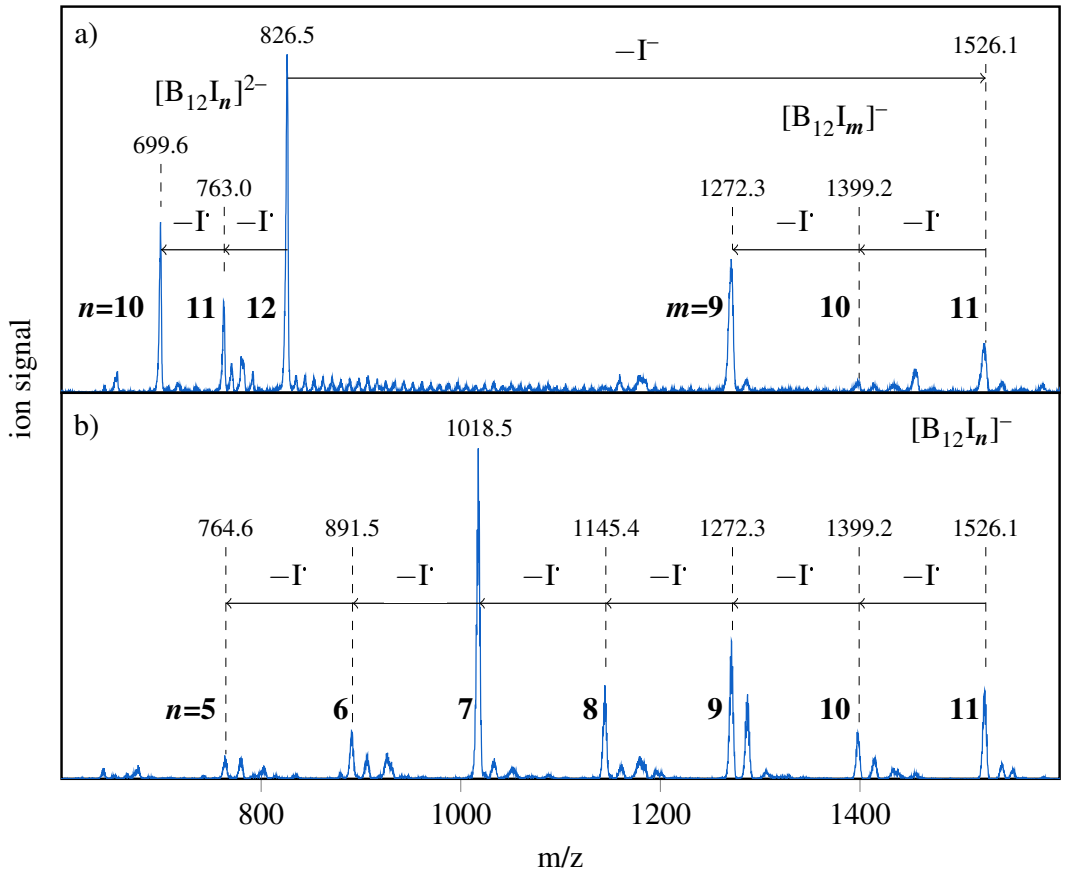

Figure E.1: Quadrupole mass spectrum of the cluster distribution produced by the nanospray ion source. The labels represent the mass of the most abundant isotopologue and the number of iodine atoms in the corresponding cluster. The settings were (a) optimized for a mass-to-charge ratio of 826.5 amu ($B_{12}I_{12}^{2-}$) and (b) of 1018.5 amu ($B_{12}I_7^-$). The sample also contained $B_{12}I_{11}OH^{2-}$ as an impurity which explains the peaks at +17 amu of $B_{12}I_8^-$, $B_{12}I_{10}^-$, and $B_{12}I_{11}^-$. Some of the smaller peaks are due to attachment of H_2O and Ar.

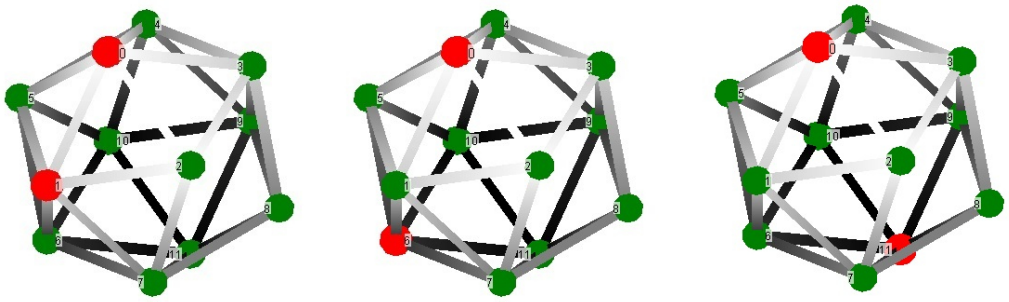

Figure E.2: The 66 isotopomers of the $^{10}B_2{}^{11}B_{10}{}^{127}I_{12}{}^{2-}$ isotopologue can be classified into three isotopomer families with statistical weights of 5:5:1.

Procedure for determining scaling factor

A scaling factor of 1.04467 was obtained by the least-squares procedure proposed by Scott and coworkers [317] for the band maxima (in cm^{-1}) of the convoluted spectrum of the isotopomeric mixture of $B_{12}I_{12}{}^{2-}$ and the experimental IRPD spectrum of D_2-tagged $B_{12}I_{12}{}^{2-}$.

Table E.1: Experimental and theoretical band maxima used to calculate the scaling factor.

band maximum theory	band maximum experiment
874.08	911.4
883.07	921.4
894.07	935
903.56	945.7

Table E.2: Relative energies (in kJ/mol) without (ΔE) zero-point-energy corrections (ΔE_{ZPE}), for the low-lying isomers of icosahedral (ico) and open (ope) structures of $B_{12}I_7^-$ at BP/ZORA-Scalar/TZP, B3LYP/ZORA-Scalar/TZP, and CCSD(T)/B/6-311+G*/I/LanL2DZ level of theory. The most stable icosahedral structure of $B_{12}I_7^-$ is selected as reference.

	BP	**B3LYP[a]**	**CCSD(T)**
	ΔE	ΔE	ΔE
ico1	0.0	0.0	0.0
ico2	9.0	8.8	14.0
ico3	8.9	7.4	18.2
ico4	17.4	19.4	26.0
ope1	62.6	23.1	68.7
ope2	59.3	46.4	117.9
ope3	113.0	95.9	123.8
ope4	28.7	105.4	211.5

[a]The energies obtained at B3LYP/ZORA-Scalar/TZP are taken from ref. [55].

Table E.3: ZPE corrected relative energies (in kJ/mol) at the BP and CCSD levels of theory. The most stable icosahedral $B_{12}I_7^-$ is selected as reference

	BP	**CCSD**
	ΔE	ΔE
ico1	0.0	0.0
ico2	9.4	14.5
ico3	9.5	14.5
ico4	9.8	19.1
ico5	17.5	26.1
ico6	24.6	34.0
ico7	24.6	34.0
ico8	51.2	47.9
ico9	35.4	50.4
ico10	55.5	52.2
ico11	31.8	71.4
ico12	85.1	89.3
ico13	51.6	112.7
ico14	111.0	124.4
ope1	51.6	57.8
ope2	47.8	106.4
ope3	101.4	112.3
ope4	40.8	128.8
ope5	21.1	203.8
ope6	108.4	208.3
ope7	159.8	228.1

Appendix F
Protonated water pentamer

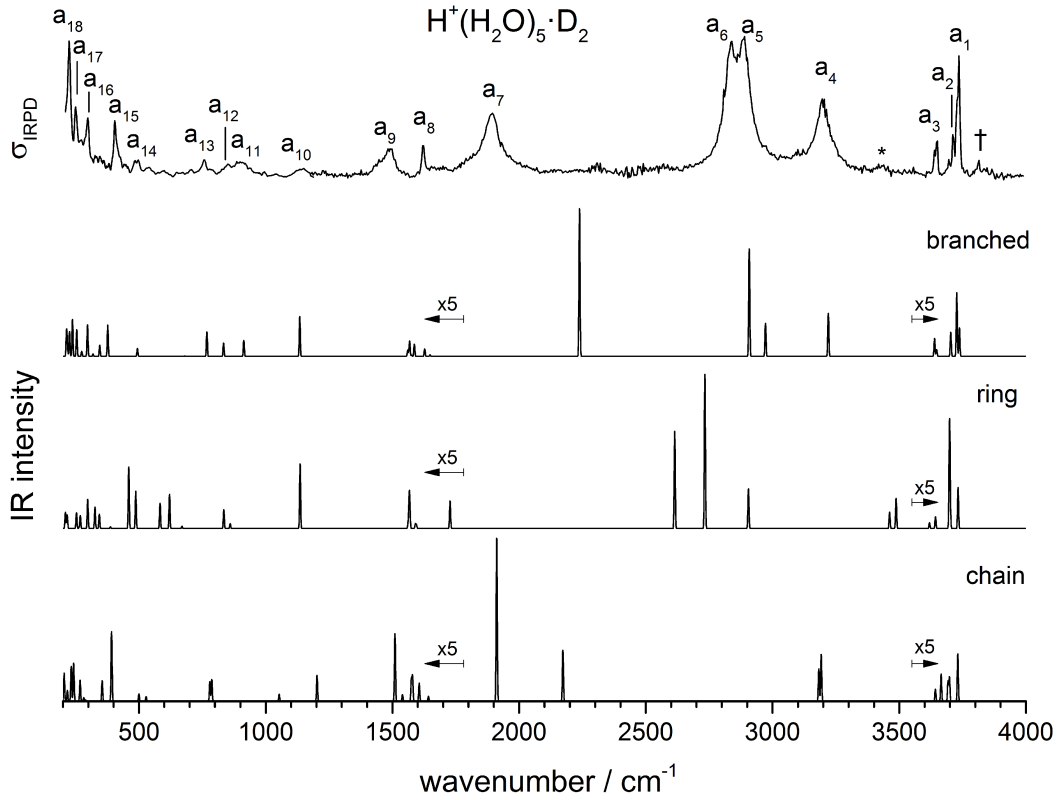

Figure F.1: D_2-predissociation spectra of $H^+(H_2O)_5$ in the region 210 to 4000 cm^{-1}compared to scaled (0.908 below 1500 $cm^{-1}$and 0.962 above) B3LYP-D3/aug-cc-pVTZ harmonic spectra for the three isomers discussed in this work. Traces below 1800 $cm^{-1}$and above 3550 $cm^{-1}$are shown with a vertical magnification of $\times 5$ for better visibility.

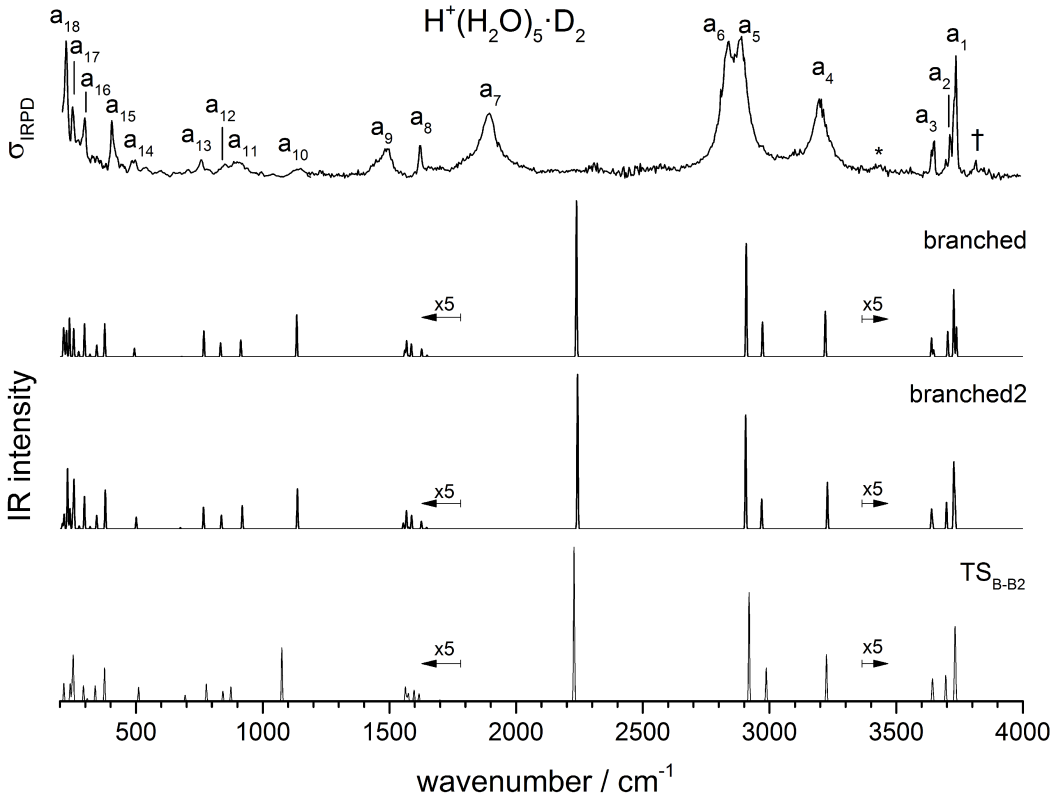

Figure F.2: D_2-predissociation spectra of $H^+(H_2O)_5$ in the region 200 to 4000 cm^{-1}compared to scaled (0.908/0.962) B3LYP-D3/aug-cc-pVTZ harmonic spectra for the two conformers of the branched isomer, **B** and **B2**, and the **TS** between them $\mathbf{TS_{B\text{-}B2}}$. Traces below 1800 $cm^{-1}$and above 3400 $cm^{-1}$are shown with a vertical magnification of $\times 5$ for better visibility.

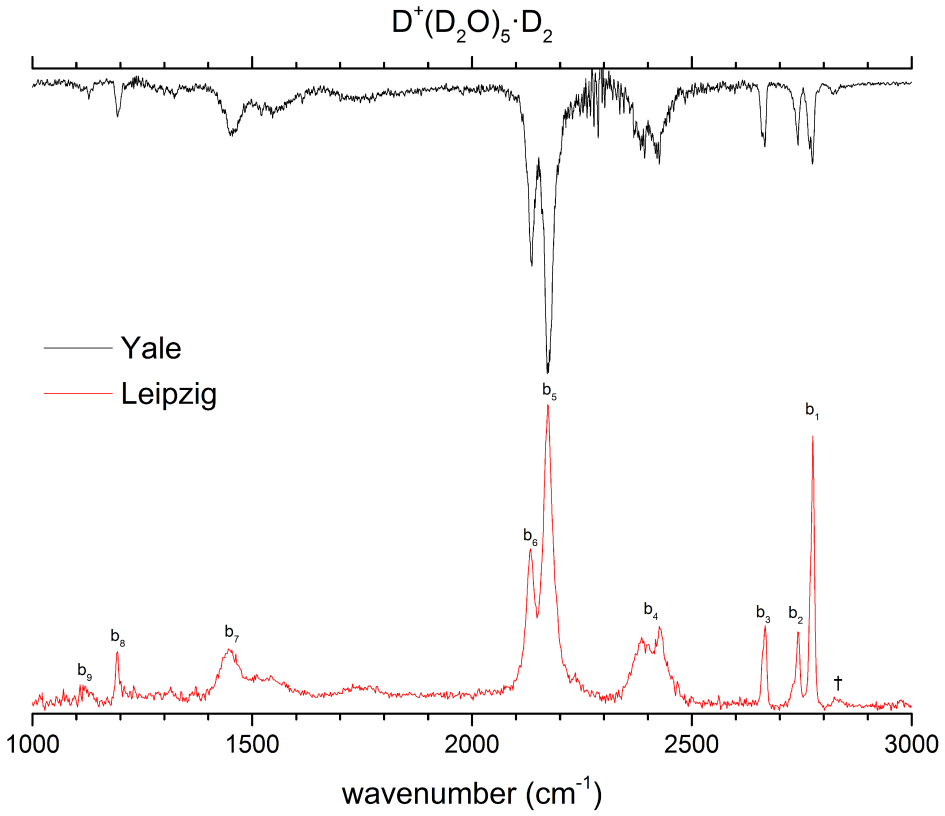

Figure F.3: Comparison of the D_2-tagged IRPD spectra of $D^+(D_2O)_5$ obtained from the experiment performed in Yale (top) and in Leipzig (bottom). The experiments show excellent agreement with the exception of the intensity of band b_1.

Table F.1: Relative electronic energies (in kJ/mol), without (ΔE) and with ZPE (ΔE_0), of the minimum energy structures (isomers **R**, **B**, **B2** and **C**) and transition states (TS) for $H^+(H_2O)_5$. The energies obtained from CCSD(T) single point calculations at the corresponding geomerties are reported in parenthesis.

	B3LYP 6-311++G(3df,3pd)		**B3LYP aug-cc-pVTZ**		**B3LYP-D3 aug-cc-pVTZ**	
	ΔE	ΔE_0	ΔE	ΔE_0	ΔE	ΔE_0
B	0.4 (4.1)	**0.0 (0.0)**	**0.0** (4.5)	**0.0 (0.0)**	4.6 (4.5)	**0.0 (0.0)**
B2	0.4 (4.0)	0.6 (0.6)	0.0 (4.5)	0.6 (0.5)	4.5 (4.4)	0.6 (0.5)
R	**0.0 (0.0)**	5.0 (1.4)	0.4 **(0.0)**	5.7 (0.8)	**0.0 (0.0)**	0.7 (0.8)
C	13.2 (19.5)	11.1 (13.7)	12.9 (19.9)	11.2 (13.7)	18.0 (19.9)	11.6 (13.6)
$\mathbf{TS_{R\text{-}B}}$	4.3 (6.1)	6.3 (4.4)	4.2 (6.1)	6.7 (4.0)	7.0 (6.5)	4.0 (3.5)
$\mathbf{TS_{B\text{-}B2}}$	2.0 (5.6)	1.4 (1.4)	1.5 (5.9)	1.2 (1.0)	6.0 (5.9)	1.0 (1.0)
$\mathbf{TS_{B2\text{-}C}}$	20.1 (23.1)	20.1 (19.5)	20.0 (22.8)	20.5 (18.8)	22.4 (23.3)	17.9 (18.8)

Table F.2: Relative Gibbs free energies (ΔG_0, in kJ/mol) of the minimum energy structures (isomers **R**, **B**, **B2** and **C**) and transition states (TS) for $H^+(H_2O)_5$ computed at 50, 150 and 250 K from CCSD(T) electronic energies and B3LYP-D3/aug-cc-pVTZ thermal correction to Gibbs Free Energies. Boltzmann weighted populations (P_0, in percent) are obtained from the reported relative Gibbs free energies. The equilibrium populations obtained from the classical (P_{RRKM}) and quantum ($P_{0,RRKM}$) RRKM kinetic model at 50 K are also reported.

	ΔG_0 **50 K**	P_0 **50 K**	$P_{\mathbf{RRKM}}$ **50 K**	$P_{\mathbf{0,RRKM}}$ **50 K**	ΔG_0 **150 K**	P_0 **150 K**	ΔG_0 **250 K**	P_0 **250 K**
B	**0.0**	**78.7**	0.2	**72.4**	**0.0**	**65.6**	**0.0**	**64.7**
B2	0.6	19.7	0.2	21.2	0.9	32.5	1.3	34.0
R	1.6	1.6	**99.6**	6.4	4.5	1.9	8.2	1.2
C	13.6	0.0	0.0	0.0	13.7	0.0	14.5	0.1
$\mathbf{TS_{R\text{-}B}}$	4.0				6.2		9.2	
$\mathbf{TS_{B\text{-}B2}}$	1.3				3.0		5.2	
$\mathbf{TS_{B2\text{-}C}}$	19.2				21.4		25.1	

Table F.3: The equilibrium constants (K_0) of the three reactions considered in the kinetic model (see Fig. 6.2) are calculated from the relative Gibbs free energies at 50, 150 and 250 K.

	K_0 **50 K**	K_0 **150 K**	K_0 **250 K**
$\mathbf{R \rightleftharpoons B}$	47.8	35.4	51.8
$\mathbf{B \rightleftharpoons B2}$	0.250	0.495	0.526
$\mathbf{B2 \rightleftharpoons C}$	2.5E-14	3.4E-5	0.002

Table F.4: Scaling factors for $H^+(H_2O)_5$ and $D^+(D_2O)_5$ calculated with the least-squares procedure on the basis of the comparison of the IRPD spectra with the simulated spectra of the **B** isomer. Two scaling factors for each method have been computed, one for the spectral region below 1500 (1100) $cm^{-1}$and one for the higher energy region.

B3LYP 6-311++G(3df,3pd)		**B3LYP aug-cc-pVTZ**		**B3LYP-D3 aug-cc-pVTZ**	
$H^+(H_2O)_5$	$D^+(D_2O)_5$	$H^+(H_2O)_5$	$D^+(D_2O)_5$	$H^+(H_2O)_5$	$D^+(D_2O)_5$
0.894/0.958	0.920/0.970	0.905/0.962	0.928/0.973	0.908/0.962	0.927/0.973

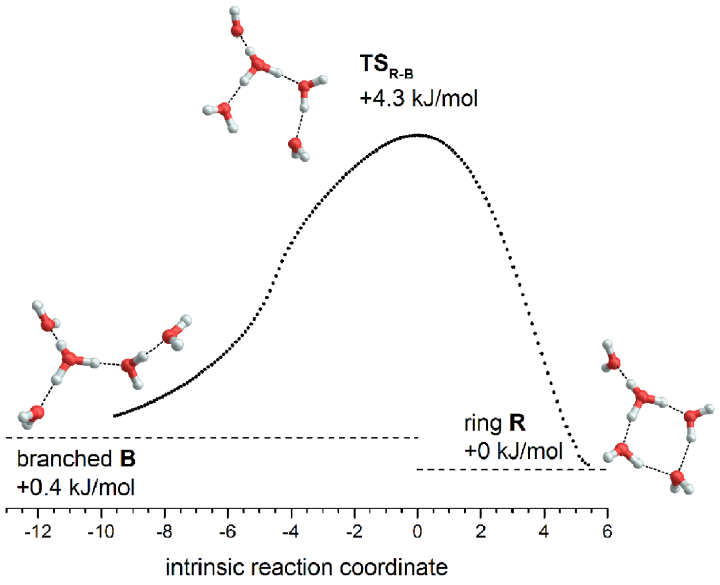

Figure F.4: B3LYP/6-311++G(3df,3pd) IRC path from the branched isomer **B** through the $\mathbf{TS_{R\text{-}B}}$ to the ring isomer **R**.

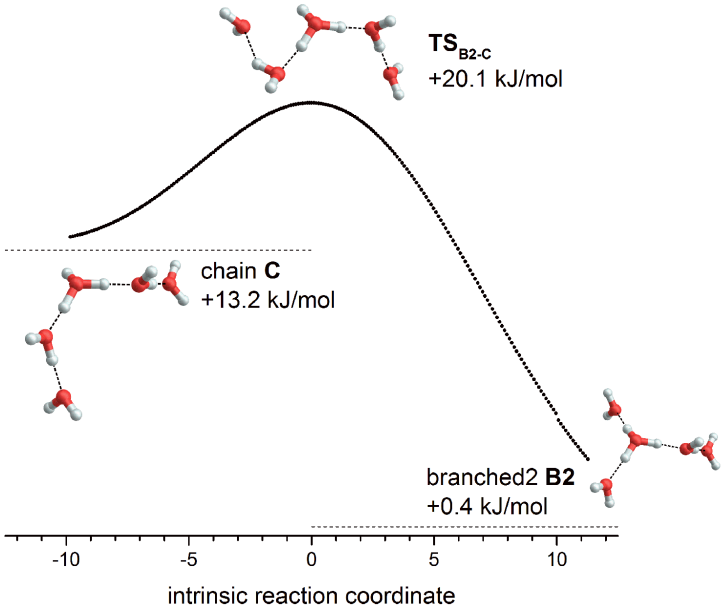

Figure F.5: B3LYP/6-311++G(3df,3pd) IRC path from the isomer **C** through the $\mathbf{TS_{B2\text{-}C}}$ to the isomer **B2**.

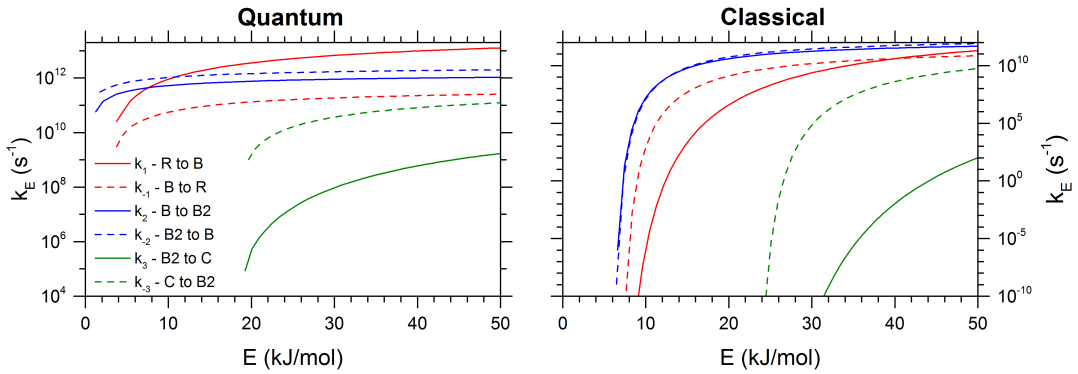

Figure F.6: Quantum and classical microcanonical rate constants obtained from RRKM calculations for the forward and backward elementary reactions of the three isomerization pathways considered.

Bibliography

[1] Laurent, S.; Forge, D.; Port, M.; Roch, A.; Robic, C.; Vander Elst, L.; Muller, R. N. *Chemical Reviews* **2008**, *108*, 2064–2110.

[2] Tartaj, P.; Morales, M. P.; Gonzalez-Carreño, T.; Veintemillas-Verdaguer, S.; Serna, C. J. *Advanced Materials* **2011**, *23*, 5243–5249.

[3] Bargar, J. R.; Towle, S. N.; Brown Jr, G. E.; Parks, G. A. *Geochimica et Cosmochimica Acta* **1996**, *60*, 3541–3547.

[4] Towle, S. N.; Bargar, J. R.; Brown Jr, G. E.; Parks, G. A. *Journal of Colloid and Interface Science* **1999**, *217*, 312–321.

[5] Franks, G. V.; Gan, Y. *Journal of the American Ceramic Society* **2007**, *90*, 3373–3388.

[6] Brown, G. E.; Henrich, V. E.; Casey, W. H.; Clark, D. L.; Eggleston, C.; Felmy, A.; Goodman, D. W.; Grätzel, M.; Maciel, G.; McCarthy, M. I.; Nealson, K. H.; Sverjensky, D. A.; Toney, M. F.; Zachara, J. M. *Chemical Reviews* **1999**, *99*, 77–174.

[7] Vázquez, B. A.; Pena, P.; de Aza, A. H.; Sainz, M. A.; Caballero, A. *Journal of the European Ceramic Society* **2009**, *29*, 1347–1360.

[8] Kelber, J. A. *Surface Science Reports* **2007**, *62*, 271–303.

[9] Kirsch, H.; Wirth, J.; Tong, Y.; Wolf, M.; Saalfrank, P.; Campen, R. K. *The Journal of Physical Chemistry C* **2014**, *118*, 13623–13630.

[10] Wirth, J.; Kirsch, H.; Wlosczyk, S.; Tong, Y.; Saalfrank, P.; Campen, R. K. *Physical Chemistry Chemical Physics* **2016**, *18*, 14822–14832.

[11] Asmis, K. R. *Physical Chemistry Chemical Physics* **2012**, *14*, 9270–9281.

[12] Heine, N.; Asmis, K. R. *International Reviews in Physical Chemistry* **2015**, *34*, 1–34.

[13] de Heer, W. A. *Reviews of Modern Physics* **1993**, *65*, 611–676; RMP.

[14] Oger, E.; Crawford, N. R. M.; Kelting, R.; Weis, P.; Kappes, M. M.; Ahlrichs, R. *Angewandte Chemie International Edition* **2007**, *46*, 8503–8506.

[15] Li, S.; Zhang, Z.; Long, Z.; Sun, G.; Qin, S. *Scientific Reports* **2016**, *6*, 25020.

[16] Chen, Q.; Li, W.-L.; Zhao, Y.-F.; Zhang, S.-Y.; Hu, H.-S.; Bai, H.; Li, H.-R.; Tian, W.-J.; Lu, H.-G.; Zhai, H.-J.; Li, S.-D.; Li, J.; Wang, L.-S. *ACS Nano* **2015**, *9*, 754–760.

[17] Okumura, M.; Yeh, L. I.; Myers, J. D.; Lee, Y. T. *The Journal of Chemical Physics* **1986**, *85*, 2328–2329.

[18] Okumura, M.; Yeh, L. I.; Myers, J. D.; Lee, Y. T. *The Journal of Physical Chemistry* **1990**, *94*, 3416–3427.

[19] Asmis, K. R.; Brummer, M.; Kaposta, C.; Santambrogio, G.; von Helden, G.; Meijer, G.; Rademann, K.; Woste, L. *Physical Chemistry Chemical Physics* **2002**, *4*, 1101–1104.

[20] Wang, Y. S.; Tsai, C. H.; Lee, Y. T.; Chang, H. C.; Jiang, J. C.; Asvany, O.; Schlemmer, S.; Gerlich, D. *The Journal of Physical Chemistry A* **2003**, *107*, 4217–4225.

[21] Patzke, G. R.; Zhou, Y.; Kontic, R.; Conrad, F. *Angewandte Chemie International Edition* **2011**, *50*, 826–859.

[22] Bogue, R. *Sensor Review* **2009**, *29*, 310–315.

[23] Weidenkaff, A.; Robert, R.; Aguirre, M. H.; Bocher, L.; Schlapbach, L. *physica status solidi (RRL) - Rapid Research Letters* **2007**, *1*, 247–249.

[24] Zäch, M.; Hägglund, C.; Chakarov, D.; Kasemo, B. *Current Opinion in Solid State and Materials Science* **2006**, *10*, 132–143.

[25] Garcia-Barriocanal, J.; Rivera-Calzada, A.; Varela, M.; Sefrioui, Z.; Díaz-Guillén, M. R.; Moreno, K. J.; Díaz-Guillén, J. A.; Iborra, E.; Fuentes, A. F.; Pennycook, S. J.; Leon, C.; Santamaria, J. *ChemPhysChem* **2009**, *10*, 1003–1011.

[26] Bell, A. T. *Science* **2003**, *299*, 1688–1691.

[27] Song, X.; Fagiani, M.; Gewinner, S.; Schöllkopf, W.; Asmis, K.; Bischoff, F.; Berger, F.; Sauer, J. *Journal of Chemical Physics* **2016**, *144*, 244305.

[28] Santambrogio, G.; Janssens, E.; Li, S.; Siebert, T.; Meijer, G.; Asmis, K.; Döbler, J.; Sierka, M.; Sauer, J. *Journal of the American Chemical Society* **2008**, *130*, 15143–9.

[29] Clauß, B.; Fitzer, E. *Fibers, 11. Inorganic Fibers, Survey*; Wiley-VCH Verlag GmbH & Co. KGaA, 2000.

[30] Zhang, F. X.; Xu, F. F.; Mori, T.; Liu, Q. L.; Sato, A.; Tanaka, T. *Journal of Alloys and Compounds* **2001**, *329*, 168–172.

[31] Solozhenko, V. L.; Kurakevych, O. O.; Andrault, D.; Le Godec, Y.; Mezouar, M. *Physical Review Letters* **2009**, *102*, 015506; PRL.

[32] Isberg, J.; Hammersberg, J.; Johansson, E.; Wikström, T.; Twitchen, D. J.; Whitehead, A. J.; Coe, S. E.; Scarsbrook, G. A. *Science* **2002**, *297*, 1670–1672.

[33] Ekimov, E. A.; Sidorov, V. A.; Bauer, E. D.; Mel'nik, N. N.; Curro, N. J.; Thompson, J. D.; Stishov, S. M. *Nature* **2004**, *428*, 542–545; 10.1038/nature02449.

[34] Ringstrand, B. *Liquid Crystals Today* **2013**, *22*, 22–35.

[35] Nieuwenhuyzen, M.; Seddon, K. R.; Teixidor, F.; Puga, A. V.; Viñas, C. *Inorganic Chemistry* **2009**, *48*, 889–901.

[36] Lipscomb, W. N. *Science* **1977**, *196*, 1047–1055.

[37] Sergeeva, A. P.; Popov, I. A.; Piazza, Z. A.; Li, W.-L.; Romanescu, C.; Wang, L.-S.; Boldyrev, A. I. *Accounts of Chemical Research* **2014**, *47*, 1349–1358; PMID: 24661097.

[38] Albert, B.; Hillebrecht, H. *Angewandte Chemie-International Edition* **2009**, *48*, 8640–8668.

[39] Boustani, I.; Quandt, A.; Hernandez, E.; Rubio, A. *Journal of Chemical Physics* **1999**, *110*, 3176–3185.

[40] Ciuparu, D.; Klie, R. F.; Zhu, Y. M.; Pfefferle, L. *Journal of Physical Chemistry B* **2004**, *108*, 3967–3969.

[41] Liu, F.; Shen, C. M.; Su, Z. J.; Ding, X. L.; Deng, S. Z.; Chen, J.; Xu, N. S.; Gao, H. J. *Journal of Materials Chemistry* **2010**, *20*, 2197–2205.

[42] Feng, B.; Zhang, J.; Zhong, Q.; Li, W.; Li, S.; Li, H.; Cheng, P.; Meng, S.; Chen, L.; Wu, K. *Nature Chemistry* **2016**, *8*, 563–568.

[43] Zhai, H.-J.; Zhao, Y.-F.; Li, W.-L.; Chen, Q.; Bai, H.; Hu, H.-S.; Piazza, Z. A.; Tian, W.-J.; Lu, H.-G.; Wu, Y.-B.; Mu, Y.-W.; Wei, G.-F.; Liu, Z.-P.; Li, J.; Li, S.-D.; Wang, L.-S. *Nature Chemistry* **2014**, *6*, 727–731.

[44] Piazza, Z. A.; Hu, H.-S.; Li, W.-L.; Zhao, Y.-F.; Li, J.; Wang, L.-S. *Nature Communications* **2014**, *5*, 3113.

[45] Alexandrova, A. N.; Boldyrev, A. I.; Zhai, H.-J.; Wang, L.-S. *Coordination Chemistry Reviews* **2006**, *250*, 2811–2866.

[46] Fowler, J. E.; Ugalde, J. M. *Journal of Physical Chemistry A* **2000**, *104*, 397–403.

[47] Martinez-Guajardo, G.; Sergeeva, A. P.; Boldyrev, A. I.; Heine, T.; Ugalde, J. M.; Merino, G. *Chemical Communications* **2011**, *47*, 6242–6244.

[48] Zhang, J.; Sergeeva, A. P.; Sparta, M.; Alexandrova, A. N. *Angewandte Chemie International Edition* **2012**, *51*, 8512–8515.

[49] Merino, G.; Heine, T. *Angewandte Chemie-International Edition* **2012**, *51*, 10226–10227.

[50] Fagiani, M. R.; Song, X.; Petkov, P.; Debnath, S.; Gewinner, W., Sandy Schöllkopf; Heine, T.; Fielicke, A.; Asmis, K. R. *Angewandte Chemie International Edition* **2016**; DOI: 10.1002/anie.201609766.

[51] Fagiani, M. R.; Song, X.; Petkov, P.; Debnath, S.; Gewinner, W., Sandy Schöllkopf; Heine, T.; Fielicke, A.; Asmis, K. R. *Angewandte Chemie* **2016**; DOI: 10.1002/ange.201609766.

[52] Knoth, W. H.; Miller, H. C.; Sauer, J. C.; Balthis, J. H.; Chia, Y. T.; Muetterties, E. L. *Inorganic Chemistry* **1964**, *3*, 159–167.

[53] Sivaev, I. B.; Bregadze, V. I.; Sjoeberg, S. *Collect.Czech. Chem. Commun.* **2002**, *67*, 679–727.

[54] Warneke, J.; Dulcks, T.; Knapp, C.; Gabel, D. *Physical Chemistry Chemical Physics* **2011**, *13*, 5712–5721.

[55] Farrás, P.; Vankova, N.; Zeonjuk, L. L.; Warneke, J.; Dülcks, T.; Heine, T.; Viñas, C.; Teixidor, F.; Gabel, D. *Chemistry – A European Journal* **2012**, *18*, 13208–13212.

[56] Fagiani, M. R.; Liu Zeonjuk, L.; Esser, T. K.; Gabel, D.; Heine, T.; Asmis, K. R.; Warneke, J. *Chemical Physics Letters* **2015**, *625*, 48–52.

[57] Angell, C. A.; Shuppert, J.; Tucker, J. C. *The Journal of Physical Chemistry* **1973**, *77*, 3092–3099.

[58] Gallo, P.; Amann-Winkel, K.; Angell, C. A.; Anisimov, M. A.; Caupin, F.; Chakravarty, C.; Lascaris, E.; Loerting, T.; Panagiotopoulos, A. Z.; Russo, J.; Sellberg, J. A.; Stanley, H. E.; Tanaka, H.; Vega, C.; Xu, L.; Pettersson, L. G. M. *Chemical Reviews* **2016**, *116*, 7463–7500.

[59] Debenedetti, P. G. *Journal of Physics: Condensed Matter* **2003**, *15*, R1669.

[60] Arunan, E.; Desiraju, G. R.; Klein, R. A.; Sadlej, J.; Scheiner, S.; Alkorta, I.; Clary, D. C.; Crabtree, R. H.; Dannenberg, J. J.; Hobza, P.; Kjaergaard, H. G.; Legon, A. C.; Mennucci, B.; Nesbitt, D. J. *Pure and Applied Chemistry* **2011**, *83*, 1637–1641.

[61] Tokmakoff, A. *Science* **2007**, *317*, 54–55.

[62] Buszek, R. J.; Francisco, J. S.; Anglada, J. M. *International Reviews in Physical Chemistry* **2011**, *30*, 335–369.

[63] Tang, M.; Cziczo, D. J.; Grassian, V. H. *Chemical Reviews* **2016**, *116*, 4205–4259.

[64] Bellissent-Funel, M.-C.; Hassanali, A.; Havenith, M.; Henchman, R.; Pohl, P.; Sterpone, F.; van der Spoel, D.; Xu, Y.; Garcia, A. E. *Chemical Reviews* **2016**, *116*, 7673–7697.

[65] Björneholm, O.; Hansen, M. H.; Hodgson, A.; Liu, L.-M.; Limmer, D. T.; Michaelides, A.; Pedevilla, P.; Rossmeisl, J.; Shen, H.; Tocci, G.; Tyrode, E.; Walz, M.-M.; Werner, J.; Bluhm, H. *Chemical Reviews* **2016**, *116*, 7698–7726.

[66] Butler, R. N.; Coyne, A. G. *Chemical Reviews* **2010**, *110*, 6302–6337.

[67] van Dishoeck, E. F.; Herbst, E.; Neufeld, D. A. *Chemical Reviews* **2013**, *113*, 9043–9085.

[68] Cukierman, S. *Biochimica et Biophysica Acta (BBA) - Bioenergetics* **2006**, *1757*, 876–885.

[69] von Grotthus, T. C. J. D. *Annales de Chimie* **1806**, *LVIII*, 54–74.

[70] Agmon, N. *Chemical Physics Letters* **1995**, *244*, 456–462.

[71] Marx, D. *ChemPhysChem* **2006**, *7*, 1848–1870.

[72] Berkelbach, T. C.; Lee, H.-S.; Tuckerman, M. E. *Physical Review Letters* **2009**, *103*, 238302; PRL.

[73] Marx, D.; Tuckerman, M. E.; Hutter, J.; Parrinello, M. *Nature* **1999**, *397*, 601–604; 10.1038/17579.

[74] Eigen, M. *Angewandte Chemie International Edition in English* **1964**, *3*, 1–19.

[75] Schuster, P.; Zundel, G.; Sandorfy, C. *The Hydrogen bond : recent developments in theory and experiments.*; North-Holland Pub. Co.: Amsterdam, 1976.

[76] Kim, J.; Schmitt, U. W.; Gruetzmacher, J. A.; Voth, G. A.; Scherer, N. E. *The Journal of Chemical Physics* **2002**, *116*, 737–746.

[77] Xu, J.; Zhang, Y.; Voth, G. A. *The Journal of Physical Chemistry Letters* **2011**, *2*, 81–86.

[78] Asmis, K. R.; Pivonka, N. L.; Santambrogio, G.; Brümmer, M.; Kaposta, C.; Neumark, D. M.; Wöste, L. *Science* **2003**, *299*, 1375–1377.

[79] Headrick, J. M.; Diken, E. G.; Walters, R. S.; Hammer, N. I.; Christie, R. A.; Cui, J.; Myshakin, E. M.; Duncan, M. A.; Johnson, M. A.; Jordan, K. D. *Science* **2005**, *308*, 1765–1769.

[80] Mizuse, K.; Fujii, A. *The Journal of Physical Chemistry A* **2012**, *116*, 4868–4877.

[81] Fournier, J. A.; Johnson, C. J.; Wolke, C. T.; Weddle, G. H.; Wolk, A. B.; Johnson, M. A. *Science* **2014**, *344*, 1009–1012.

[82] Fournier, J. A.; Wolke, C. T.; Johnson, M. A.; Odbadrakh, T. T.; Jordan, K. D.; Kathmann, S. M.; Xantheas, S. S. *The Journal of Physical Chemistry A* **2015**, *119*, 9425–9440.

[83] Heine, N.; Fagiani, M. R.; Rossi, M.; Wende, T.; Berden, G.; Blum, V.; Asmis, K. R. *Journal of the American Chemical Society* **2013**, *135*, 8266–8273.

[84] Jiang, J.-C.; Wang, Y.-S.; Chang, H.-C.; Lin, S. H.; Lee, Y. T.; Niedner-Schatteburg, G.; Chang, H.-C. *Journal of the American Chemical Society* **2000**, *122*, 1398–1410.

[85] Kulig, W.; Agmon, N. *Physical Chemistry Chemical Physics* **2014**, *16*, 4933–4941.

[86] Fagiani, M. R.; Knorke, H.; Esser, T. K.; Heine, N.; Wolke, C. T.; Gewinner, S.; Schollkopf, W.; Gaigeot, M.-P.; Spezia, R.; Johnson, M. A.; Asmis, K. R. *Physical Chemistry Chemical Physics* **2016**, *18*, 26743–26754.

[87] Wolke, C. T.; Fournier, J. A.; Dzugan, L. C.; Fagiani, M. R.; Odbadrakh, T. T.; Knorke, H.; Jordan, K. D.; McCoy, A. B.; Asmis, K. R.; Johnson, M. A. *Science* **2016**, *354*, 1131–1135.

[88] Morse, P. M. *Physical Review* **1929**, *34*, 57–64.

[89] Lehmann, K. K.; Scoles, G.; Pate, B. H. *Annual Review of Physical Chemistry* **1994**, *45*, 241–274.

[90] Grüne, P.; Lyon, J.; Fielicke, A. *Chapter 9: Vibrational Spectroscopy of Strongly Bound Clusters*; Handbook of Nanophysics. Clusters and Fullerenes.; CRC Press, 2010.

[91] Drake, G. W. F. *Springer Handbook of Atomic, Molecular, and Optical Physics*; Springer New York, 2006.

[92] Wheeler, M. D.; Newman, S. M.; Orr-Ewing, A. J.; Ashfold, M. N. R. *Journal of the Chemical Society, Faraday Transactions* **1998**, *94*, 337–351.

[93] Gerlich, D. *Inhomogeneous RF Fields: A Versatile Tool for the Study of Processes with Slow Ions*; John Wiley & Sons, Inc., 2007; pp 1–176.

[94] Black, J. G.; Yablonovitch, E.; Bloembergen, N.; Mukamel, S. *Physical Review Letters* **1977**, *38*, 1131–1134.

[95] Makarov, A. A.; Petrova, I. Y.; Ryabov, E. A.; Letokhov, V. S. *The Journal of Physical Chemistry A* **1998**, *102*, 1438–1449.

[96] Asmis, K. R.; Sauer, J. *Mass Spectrometry Reviews* **2007**, *26*, 542–562.

[97] Bagratashvili, V. N.; Letokhov, V. S.; Makarov, A. A.; Ryabov, E. A. *Multiple-Photon Infrared Laser Photophysics and Photochemistry*; Harwood Academic Publishers: Great Britan, 1983; Vol. 1.

[98] Yacovitch, T. I.; Heine, N.; Brieger, C.; Wende, T.; Hock, C.; Neumark, D. M.; Asmis, K. R. *The Journal of Physical Chemistry A* **2013**, *117*, 7081–7090.

[99] Roscioli, J. R.; McCunn, L. R.; Johnson, M. A. *Science* **2007**, *316*, 249–254.

[100] Pankewitz, T.; Lagutschenkov, A.; Niedner-Schatteburg, G.; Xantheas, S. S.; Lee, Y.-T. *The Journal of Chemical Physics* **2007**, *126*, 074307.

[101] Beck, J. P.; Lisy, J. M. *The Journal of Chemical Physics* **2011**, *135*, 044302.

[102] Johnson, M. A. *Vibrational Predissociation Ion Spectroscopy*; The Encyclopedia of Mass Spectrometry: Theory and Ion Chemistry, Vol. 1; Elsevier: Oxford, 2003.

[103] Asmis, K. R.; Fielicke, A.; von Helden, G.; Meijer, G. *Chapter 8 Vibrational spectroscopy of gas-phase clusters and complexes*; Woodruff, D. P., Ed.; Elsevier, 2007; Vol. Volume 12, pp 327–375.

[104] Asmis, K. R.; Wende, T.; Brummer, M.; Gause, O.; Santambrogio, G.; Stanca-Kaposta, E. C.; Dobler, J.; Niedziela, A.; Sauer, J. *Physical Chemistry Chemical Physics* **2012**, *14*, 9377–9388.

[105] Gehrke, R.; Gruene, P.; Fielicke, A.; Meijer, G.; Reuter, K. *The Journal of Chemical Physics* **2009**, *130*, 034306.

[106] Mizuse, K.; Fujii, A. *Physical Chemistry Chemical Physics* **2011**, *13*, 7129–7135.

[107] Oomens, J.; Sartakov, B. G.; Meijer, G.; Von Helden, G. *Int. J. Mass. Spectrom.* **2006**, *254*, 1.

[108] Goebbert, D. J.; Meijer, G.; Asmis, K. R. *AIP Conference Proceedings* **2009**, *1104*, 22–29.

[109] Goebbert, D. J.; Garand, E.; Wende, T.; Bergmann, R.; Meijer, G.; Asmis, K. R.; Neumark, D. M. *Journal of Physical Chemistry A* **2009**, *113*, 7584–7592.

[110] Wende, T.; Ph.D. thesis; 2012; Freie Universität Berlin.

[111] Heine, N.; Ph.D. thesis; 2014; Freie Universität Berlin.

[112] Brümmer, M.; Kaposta, C.; Santambrogio, G.; Asmis, K. R. *The Journal of Chemical Physics* **2003**, *119*, 12700–12703.

[113] Dole, M.; Mack, L. L.; Hines, R. L.; Mobley, R. C.; Ferguson, L. D.; Alice, M. B. *The Journal of Chemical Physics* **1968**, *49*, 2240–2249.

[114] Fenn, J. B.; Mann, M.; Meng, C. K.; Wong, S. F.; Whitehouse, C. M. *Science* **1989**, *246*, 64–71.

[115] Fenn, J. B. *Angewandte Chemie International Edition* **2003**, *42*, 3871–3894.

[116] Kebarle, P.; Verkerk, U. H. *Mass Spectrometry Reviews* **2009**, *28*, 898–917.

[117] Marchese, R.; Grandori, R.; Carloni, P.; Raugei, S. *Journal of The American Society for Mass Spectrometry* **2012**, *23*, 1903–1910.

[118] Konermann, L.; Ahadi, E.; Rodriguez, A. D.; Vahidi, S. *Analytical Chemistry* **2013**, *85*, 2–9.

[119] Konermann, L.; McAllister, R. G.; Metwally, H. *The Journal of Physical Chemistry B* **2014**, *118*, 12025–12033.

[120] McAllister, R. G.; Metwally, H.; Sun, Y.; Konermann, L. *Journal of the American Chemical Society* **2015**, *137*, 12667–12676.

[121] Kebarle, P. *Journal of Mass Spectrometry* **2000**, *35*, 804–817.

[122] Smith, D. P. H. *IEEE Transactions on Industry Applications* **1986**, *IA-22*, 527–535.

[123] Taylor, G. I.; McEwan, A. D. *Journal of Fluid Mechanics* **1965**, *22*, 1–15.

[124] Esser, T.; Master thesis; 2013; Freie Universität Berlin.

[125] Duncan, M. A. *Review of Scientific Instruments* **2012**, *83*, 041101.

[126] Dietz, T. G.; Duncan, M. A.; Powers, D. E.; Smalley, R. E. *The Journal of Chemical Physics* **1981**, *74*, 6511–6512.

[127] Powers, D. E.; Hansen, S. G.; Geusic, M. E.; Puiu, A. C.; Hopkins, J. B.; Dietz, T. G.; Duncan, M. A.; Langridge-Smith, P. R. R.; Smalley, R. E. *The Journal of Physical Chemistry* **1982**, *86*, 2556–2560.

[128] Bondybey, V. E.; English, J. H. *The Journal of Chemical Physics* **1981**, *74*, 6978–6979.

[129] Maruyama, S.; Anderson, L. R.; Smalley, R. E. *Review of Scientific Instruments* **1990**, *61*, 3686–3693.

[130] Milani, P.; deHeer, W. A. *Review of Scientific Instruments* **1990**, *61*, 1835–1838.

[131] Gangopadhyay, P.; Lisy, J. M. *Review of Scientific Instruments* **1991**, *62*, 502–506.

[132] Weidele, H.; Frenzel, U.; Leisner, T.; Kreisle, D. *Zeitschrift für Physik D Atoms, Molecules and Clusters* **1991**, *20*, 411–412.

[133] Neal, C. M.; Breaux, G. A.; Cao, B.; Starace, A. K.; Jarrold, M. F. *Review of Scientific Instruments* **2007**, *78*, 075108.

[134] Maier, T. M.; Boese, A. D.; Sauer, J.; Wende, T.; Fagiani, M.; Asmis, K. R. *The Journal of Chemical Physics* **2014**, *140*, 204315.

[135] Zheng, L.-S.; Brucat, P. J.; Pettiette, C. L.; Yang, S.; Smalley, R. E. *The Journal of Chemical Physics* **1985**, *83*, 4273–4274.

[136] Brucat, P. J.; Zheng, L.-S.; Pettiette, C. L.; Yang, S.; Smalley, R. E. *The Journal of Chemical Physics* **1986**, *84*, 3078–3088.

[137] Cox, D. M.; Reichmann, K. C.; Trevor, D. J.; Kaldor, A. *The Journal of Chemical Physics* **1988**, *88*, 111–119.

[138] Goldby, I. M.; vonIssendorff, B.; Kuipers, L.; Palmer, R. E. *Review of Scientific Instruments* **1997**, *68*, 3327–3334.

[139] Rossnagel, S. M. *Sputter Deposition*; Sproul, W. D.; Legg, K. O., Eds.; Technomic Publishing Co.: Switzerland, 1995.

[140] Kelly, P. J.; Arnell, R. D. *Vacuum* **2000**, *56*, 159–172.

[141] Rossnagel, S. M. *Plasma Sputter Deposition Systems: Plasma Generation, Basic Physics and Characterization*; Auciello, O.; Engemann, J., Eds.; Springer Netherlands: Dordrecht, 1993; pp 1–20.

[142] Hagemann, F. P.; Ph.D. thesis; 2015; Freie Universität Berlin.

[143] Haberland, H.; Mall, M.; Moseler, M.; Qiang, Y.; Reiners, T.; Thurner, Y. *Journal of Vacuum Science & Technology A* **1994**, *12*, 2925–2930.

[144] Friedburg, H.; Paul, W. *Naturwissenschaften* **1951**, *38*, 159–160.

[145] Bennewitz, H. G.; Paul, W.; Schlier, C. *Zeitschrift fÃ¼r Physik* **1955**, *141*, 6–15.

[146] Paul, W. *Angewandte Chemie International Edition in English* **1990**, *29*, 739–748.

[147] Friedman, M. H.; Yergey, A. L.; Campana, J. E. *Journal of Physics E: Scientific Instruments* **1982**, *15*, 53.

[148] Earnshaw, S. *Transactions of the Cambridge Philosophical Society* **1848**, *7*, 97–112.

[149] Paul, W. *Reviews of Modern Physics* **1990**, *62*, 531–540; RMP.

[150] Warnke, S.; Ph.D. thesis; 2015; Freie Universität Berlin.

[151] Luca, A.; Schlemmer, S.; Čermák, I.; Gerlich, D. *Review of Scientific Instruments* **2001**, *72*, 2900–2908.

[152] Wiley, W. C.; McLaren, I. H. *Review of Scientific Instruments* **1955**, *26*, 1150–1157.

[153] Oomens, J.; Tielens, A. G. G. M.; Sartakov, B.; von Helden, G.; Meijer, G. *Astrophys. J.* **2003**, *591*, 968.

[154] Dian, B. C.; Longarte, A.; Zwier, T. S. *Science* **2002**, *296*, 2369–2373.

[155] Chin, W.; Dognon, J.-P.; Canuel, C.; Piuzzi, F.; Dimicoli, I.; Mons, M.; Compagnon, I.; von Helden, G.; Meijer, G. *The Journal of Chemical Physics* **2005**, *122*, 054317.

[156] Rizzo, T. R.; Stearns, J. A.; Boyarkin, O. V. *International Reviews in Physical Chemistry* **2009**, *28*, 481–515.

[157] Elliott, B. M.; Relph, R. A.; Roscioli, J. R.; Bopp, J. C.; Gardenier, G. H.; Guasco, T. L.; Johnson, M. A. *The Journal of Chemical Physics* **2008**, *129*, 094303.

[158] Bosenberg, W. R.; Guyer, D. R. *Journal of the Optical Society of America B* **1993**, *10*, 1716–1722.

[159] Gerhards, M. *Optics Communications* **2004**, *241*, 493–497.

[160] Onuki, H.; Elleaume, P. *Undulators, Wigglers and Their Applications*; Taylor & Francis, 2003.

[161] Schöllkopf, W.; Gewinner, S.; Junkes, H.; Paarmann, A.; von Helden, G.; Bluem, H.; Todd, A. M. M. *Proceedings of SPIE* **2015**, *9512*, 95121L1–95121L13.

[162] Trueba, M.; Trasatti, S. P. *European Journal of Inorganic Chemistry* **2005**, 3393–3403.

[163] Sauer, J.; Freund, H.-J. *Catalysis Letters* **2015**, *145*, 109–125.

[164] Böhme, D.; Schwarz, H. *Angewandte Chemie, International Edition in English* **2005**, *44*, 2336–2354.

[165] Feyel, S.; Döbler, J.; Hökendorf, R.; Beyer, M. K.; Sauer, J.; Schwarz, H. *Angewandte Chemie, International Edition in English* **2008**, *47*, 1946–1950.

[166] Wang, Z.-C.; Weiske, T.; Kretschmer, R.; Schlangen, M.; Kaupp, M.; Schwarz, H. *Journal of the American Chemical Society* **2011**, *133*, 16930–16937.

[167] Tian, L.-H.; Ma, T.-M.; Li, X.-N.; He, S.-G. *Dalton Transactions* **2013**, *42*, 11205–11211.

[168] Cherchneff, I.; Dwek, E. *Astronomical Journal* **2010**, *713*, 1–24.

[169] Scott, J. R.; Groenewold, G. S.; Gianotto, A. K.; Benson, M. T.; Wright, J. B. *Journal of Physical Chemistry A* **2000**, *104*, 7079–7090.

[170] Johnson, G. E.; Tyo, E. C.; Castleman, J., A. W. *Journal of Physical Chemistry A* **2008**, *112*, 4732–4735.

[171] Kretschmer, R.; Wang, Z.-C.; Schlangen, M.; Schwarz, H. *Angewandte Chemie, International Edition in English* **2013**, *52*, 9513–9517.

[172] Bach, S. B. H.; McElvany, S. W. *Journal of Physical Chemistry* **1991**, *95*, 9091–9094.

[173] Serebrennikov, L. V.; Osin, S. B.; Maltsev, A. A. *Journal of Molecular Structure* **1982**, *81*, 25–33.

[174] Sonchik, S. M.; Andrews, L.; Carlson, K. D. *Journal of Physical Chemistry* **1983**, *87*, 2004–2011.

[175] Bares, S. J.; Haak, M.; Nibler, J. W. *Journal of Chemical Physics* **1985**, *82*, 670–675.

[176] Stößer, G.; Schnöckel, H. *Angewandte Chemie, International Edition in English* **2005**, *44*, 4261–4264.

[177] Desai, S. R.; Wu, H.; Wang, L.-S. *International Journal of Mass Spectrometry and Ion Processes* **1996**, *159*, 75–80.

[178] Desai, S. R.; Wu, H.; Rohlfing, C. M.; Wang, L.-S. *Journal of Chemical Physics* **1997**, *106*, 1309–1317.

[179] Meloni, G.; Ferguson, M. J.; Neumark, D. M. *Physical Chemistry Chemical Physics* **2003**, *5*, 4073–4079.

[180] Akin, F. A.; Jarrold, C. C. *Journal of Chemical Physics* **2003**, *118*, 5841–5851.

[181] Sierka, M.; Döbler, J.; Sauer, J.; Zhai, H. J.; Wang, L. S. *ChemPhysChem* **2009**, *10*, 2410–2413.

[182] Mascaritolo, K. J.; Gardner, A. M.; Heaven, M. C. *Journal of Chemical Physics* **2015**, *143*.

[183] Archibong, E. F.; ; St-Amant, A. *The Journal of Physical Chemistry A* **1998**, *102*, 6877–6882.

[184] Archibong, E. F.; ; St-Amant, A. *The Journal of Physical Chemistry A* **1999**, *103*, 1109–1114.

[185] Gutsev, G. L.; Jena, P.; Bartlett, R. J. *Journal of Chemical Physics* **1999**, *110*, 2928–2935.

[186] Martínez, A.; Tenorio, F. J.; Ortiz, J. V. *Journal of Physical Chemistry A* **2001**, *105*, 11291–11294.

[187] Patzer, A. B.C.; Chang, Ch.; Sedlmayr, E.; Sülzle, D. *Eur. Phys. J. D* **2005**, *32*, 329–337.

[188] Nemukhin, A.; Almlöf, J. *Journal of Molecular Structure: THEOCHEM* **1992**, *253*, 101 – 107.

[189] Nemukhin, A. V.; Weinhold, F. *The Journal of Chemical Physics* **1992**, *97*, 3420–3430.

[190] Patzer, A. B.C.; Chang, Ch.; Sedlmayr, E.; Sülzle, D. *Eur. Phys. J. D* **1999**, *6*, 57–62.

[191] Neukermans, S.; Veldeman, N.; Janssens, E.; Lievens, P.; Chen, Z.; Schleyer, P.v.R. *Eur. Phys. J. D* **2007**, *45*, 301–308.

[192] Woodley, S. M. *Proceedings of the Royal Society of London A: Mathematical, Physical and Engineering Sciences* **2011**, *467*, 2020–2042.

[193] Rahane, A. B.; Deshpande, M. D.; Kumar, V. *The Journal of Physical Chemistry C* **2011**, *115*, 18111–18121.

[194] Sarker, M. I. M.; Kim, C. S.; Choi, C. H. *Chemical Physics Letters* **2005**, *411*, 297–301.

[195] Archibong, E. F.; Seeburrun, N.; Ramasami, P. *Chemical Physics Letters* **2009**, *481*, 169–172.

[196] Gutsev, G. L.; Weatherford, C. A.; Pradhan, K.; Jena, P. *Journal of Computational Chemistry* **2011**, *32*, 2974–82.

[197] Sierka, M. *Progress in Surface Science* **2010**, *85*, 398–434.

[198] Sierka, M.; Döbler, J.; Sauer, J.; Santambrogio, G.; Brümmer, M.; Wöste, L.; Janssens, E.; Meijer, G.; Asmis, K. *Angewandte Chemie, International Edition in English* **2007**, *46*, 3372–5.

[199] Perdew, J. P. *Phys. Rev. B* **1986**, *33*, 8822–8824.

[200] Becke, A. *Physical Review A* **1988**, *38*, 3098–3100.

[201] Weigend, F.; Ahlrichs, R. *Phys. Chem. Chem. Phys.* **2005**, *7*, 3297–3305.

[202] Becke, A. D. *Journal of Chemical Physics* **1993**, *98*, 5648.

[203] TURBOMOLE V6.5 2013; a development of University of Karlsruhe and Forschungszentrum Karlsruhe GmbH, 1989-2007, TURBOMOLE GmbH, since 2007; available from http://www.turbomole.com.

[204] Becke, A. D. *Journal of Chemical Physics* **1993**, *98*, 1372.

[205] Raghavachari, K.; Trucks, G. W.; Pople, J. A.; Head-Gordon, M. *Chemical Physics Letters* **1989**, *157*, 479–483.

[206] Peterson, K. A.; Dunning, T. H. *Journal of Chemical Physics* **2002**, *117*, 10548.

[207] Sierka, M.; Helmich, B.; Wlodarczyk, R. *Program DoDo*; Humboldt University Berlin, Friedrich-Schiller University Jena (since 2012), 2013.

[208] Barone, V. *The Journal of Chemical Physics* **2005**, *122*, 14108.

[209] Werner, H.-J.; Knowles, P. J.; Knizia, G.; Manby, F. R.; Schütz, M. *Wiley Interdisciplinary Reviews: Computational Molecular Science* **2012**, *2*, 242–253.

[210] M. J. Frisch and G. W. Trucks and H. B. Schlegel and G. E. Scuseria and M. A. Robb and J. R. Cheeseman and G. Scalmani and V. Barone and B. Mennucci and G. A. Petersson and H. Nakatsuji and M. Caricato and X. Li and H. P. Hratchian and A. F. Izmaylov and J. Bloino and G. Zheng and J. L. Sonnenberg and M. Hada and M. Ehara and K. Toyota and R. Fukuda and J. Hasegawa and M. Ishida and T. Nakajima and Y. Honda and O. Kitao and H. Nakai and T. Vreven and Montgomery, Jr., J. A. and J. E. Peralta and F. Ogliaro and M. Bearpark and J. J. Heyd and E. Brothers and K. N. Kudin and V. N. Staroverov and R. Kobayashi and J. Normand and K. Raghavachari and A. Rendell and J. C. Burant and S. S. Iyengar and J. Tomasi and M. Cossi and N. Rega and J. M. Millam and M. Klene and J. E. Knox and J. B. Cross and V. Bakken and C. Adamo and J. Jaramillo and R. Gomperts and R. E. Stratmann and O. Yazyev and A. J. Austin and R. Cammi and C. Pomelli and J. W. Ochterski and R. L. Martin and K. Morokuma and V. G. Zakrzewski and G. A. Voth and P. Salvador and J. J. Dannenberg and S. Dapprich and A. D. Daniels and Ö. Farkas and J. B. Foresman and J. V. Ortiz and J. Cioslowski and D. J. Fox; *Gaussian 09*; Gaussian Inc. Wallingford CT USA 2009.

[211] Andrews, L.; McCluskey, M. *Journal of Molecular Spectroscopy* **1992**, *154*, 223–225.

[212] Gowtham, S.; Costales, A.; Pandey, R. *Journal of Physical Chemistry B* **2004**, *108*, 17295–17300.

[213] Zhai, H.-J.; Wang, L.-M.; Li, S.-D.; Wang, L.-S. *Journal of Physical Chemistry A* **2007**, *111*, 1030–1035.

[214] Tremblay, B.; Roy, P.; Manceron, L.; Alikhani, M. E.; Roy, D. *Journal of Chemical Physics* **1996**, *104*, 2773.

[215] Beste, A.; Bartlett, R. J. *Chemical Physics Letters* **2002**, *366*, 100–108.

[216] Gowtham, S.; Deshpande, M.; Costales, A.; Pandey, R. *Journal of Physical Chemistry B* **2005**, *109*, 14836–14844.

[217] Archibong, E. F.; Ramasami, P. *Computational and Theoretical Chemistry* **2011**, *964*, 324–328.

[218] Merrick, J. P.; Moran, D.; Radom, L. *Journal of Physical Chemistry A* **2007**, *111*, 11683–700.

[219] Avramov, P. V.; Adamovic, I.; Ho, K.-M.; Wang, C. Z.; Lu, W. C.; Gordon, M. S. *Journal of Physical Chemistry A* **2005**, *109*, 6294–6302.

[220] Rahane, A.; Deshpande, M. *Journal of Physical Chemistry C* **2012**, *116*, 26912701.

[221] Kandalam, A. K.; Kiran, B.; Jena, P.; Pietsch, S.; Gantefor, G. *Physical Chemistry Chemical Physics* **2015**, *17*, 26589–26593.

[222] Archibong, E. F.; Mvula, E. N. *Chemical Physics Letters* **2005**, *408*, 371–376.

[223] Asmis, K.; Meijer, G.; BrÃ¼mmer, M.; Kaposta, C.; Santambrogio, G.; WÃ¶ste, L.; Sauer, J. *Journal of Chemical Physics* **2004**, *120*, 6461–70.

[224] Sodupe, M.; Bertran, J.; Rodriguez-Santiago, L.; Baerends, E. J. *Journal of Physical Chemistry A* **1999**, *103*, 166–170.

[225] Asmis, K. R.; Santambrogio, G.; BrÃ¼mmer, M.; Sauer, J. *Angewandte Chemie, International Edition in English* **2005**, *44*, 3122–3125.

[226] Pacchioni, G.; Frigoli, F.; Ricci, D.; Weil, J. A. *Physical Review B* **2001**, *63*.

[227] Solans-Monfort, X.; Branchadell, V.; Sodupe, M.; Sierka, M.; Sauer, J. *Journal of Chemical Physics* **2004**, *121*, 6034–6041.

[228] Sumio, I. *Japanese Journal of Applied Physics* **1984**, *23*, L347.

[229] Levin, I.; Brandon, D. *Journal of the American Ceramic Society* **1998**, *81*, 1995–2012; 110fb Times Cited:535 Cited References Count:80.

[230] Boch, P.; Niepce, J.-C. *Ceramic Materials: Processes, Properties, and Applications*; John Wiley and Sons, 2010; Vol. 98.

[231] Warneck, P. *Chemistry of the Natural Atmosphere*; Elsevier Science, 1999.

[232] Gomes, L.; Gillette, D. A. *Atmospheric Environment. Part A. General Topics* **1993**, *27*, 2539–2544.

[233] van Heijnsbergen, D.; Demyk, K.; Duncan, M. A.; Meijer, G.; von Helden, G. *Physical Chemistry Chemical Physics* **2003**, *5*, 2515.

[234] Frank, M.; Wolter, K.; Magg, N.; Heemeier, M.; Kühnemuth, R.; Bäumer, M.; Freund, H.-J. *Surface Science* **2001**, *492*, 270–284.

[235] Demyk, K.; van Heijnsbergen, D.; von Helden, G.; Meijer, G. *Astronomy and Astrophysics* **2004**, *420*, 547–552; Times Cited: 40.

[236] Bohren, C. F.; Huffman, D. R. *Absorption and Scattering of Light by Small Particles*; Wiley-VCH Verlag GmbH, 2007.

[237] Lee, S. K.; Lee, S. B.; Park, S. Y.; Yi, Y. S.; Ahn, C. W. *Physical Review Letters* **2009**, *103*, 095501; PRL.

[238] Lamparter, P.; Kniep, R. *Physica B: Condensed Matter* **1997**, *234*, 405–406.

[239] Kresse, G.; Schmid, M.; Napetschnig, E.; Shishkin, M.; Kohler, L.; Varga, P. *Science* **2005**, *308*, 1440–2; Kresse, Georg Schmid, Michael Napetschnig, Evelyn Shishkin, Maxim Kohler, Lukas Varga, Peter eng 2005/06/04 09:00 Science. 2005 Jun 3;308(5727):1440-2.

[240] Husson, E.; Repelin, Y. *European Journal of Solid State and Inorganic Chemistry* **1996**, *33*, 1223–1231.

[241] Smrcok, L.; Langer, V.; Krestan, J. *Acta Crystallogr C* **2006**, *62*, i83–4.

[242] Digne, M. *Journal of Catalysis* **2004**, *226*, 54–68.

[243] Krokidis, X.; Raybaud, P.; Gobichon, A.-E.; Rebours, B.; Euzen, P.; Toulhoat, H. *The Journal of Physical Chemistry B* **2001**, *105*, 5121–5130.

[244] Ollivier, B.; Retoux, R.; Lacorre, P.; Massiot, D.; Ferey, G. *Journal of Materials Chemistry* **1997**, *7*, 1049–1056.

[245] Lutterotti, L.; Scardi, P. *Journal of Applied Crystallography* **1990**, *23*, 246–252.

[246] Zhou, R.-S.; Snyder, R. L. *Acta Crystallographica Section B* **1991**, *47*, 617–630.

[247] Gutiérrez, G.; Belonoshko, A. B.; Ahuja, R.; Johansson, B. *Physical Review E* **2000**, *61*, 2723–2729; PRE.

[248] Godin, T. J.; LaFemina, J. P. *Phys. Rev. B* **1994**, *49*, 7691–7696.

[249] Momida, H.; Hamada, T.; Takagi, Y.; Yamamoto, T.; Uda, T.; Ohno, T. *Physical Review B* **2006**, *73*, 054108–054108.

[250] Álvarez, J.; Serrano, C.; Hill, D.; MartÃnez-Pastor, J. *Optics Letters* **2013**, *38*, 1058–1060.

[251] Brown, G. E. *Science* **2001**, *294*, 67–69.

[252] Lemire, C.; Meyer, R.; Henrich, V. E.; Shaikhutdinov, S.; Freund, H. J. *Surface Science* **2004**, *572*, 103–114.

[253] Tong, Y. J.; Wirth, J.; Kirsch, H.; Wolf, M.; Saalfrank, P.; Campen, R. K. *Journal of Chemical Physics* **2015**, *142*; Tong, Yujin Wirth, Jonas Kirsch, Harald Wolf, Martin Saalfrank, Peter Campen, R. Kramer.

[254] Akin, F. A.; Jarrold, C. C. *The Journal of Chemical Physics* **2004**, *120*, 8698–8706.

[255] Das, U.; Raghavachari, K.; Jarrold, C. C. *The Journal of Chemical Physics* **2005**, *122*, 014313.

[256] Das, U.; Raghavachari, K. *The Journal of Chemical Physics* **2007**, *127*, 154310.

[257] Tenorio, F. J.; Murray, I.; Martínez, A.; Klabunde, K. J.; Ortiz, J. V. *The Journal of Chemical Physics* **2004**, *120*, 7955–7962.

[258] Guevara-García, A.; Martínez, A.; Ortiz, J. V. *The Journal of Chemical Physics* **2005**, *122*, 214309.

[259] Guevara-GarcÃa, A.; MartÃnez, A.; Ortiz, J. V. *The Journal of Chemical Physics* **2007**, *126*, 024309.

[260] Perdew, J.; Yue, W. *Physical Review B* **1986**, *33*, 8800–8802.

[261] Douberly, G. E.; Walters, R. S.; Cui, J.; Jordan, K. D.; Duncan, M. A. *The Journal of Physical Chemistry A* **2010**, *114*, 4570–4579.

[262] Fournier, J. A.; Wolke, C. T.; Johnson, C. J.; Johnson, M. A.; Heine, N.; Gewinner, S.; Schöllkopf, W.; Esser, T. K.; Fagiani, M. R.; Knorke, H.; Asmis, K. R. *Proceedings of the National Academy of Sciences* **2014**, *111*, 18132–18137.

[263] Douberly, G. E.; Ricks, A. M.; Duncan, M. A. *The Journal of Physical Chemistry A* **2009**, *113*, 8449–8453.

[264] Tennyson, J.; Bernath, P. F.; Brown, L. R.; Campargue, A.; Császár, A. G.; Daumont, L.; Gamache, R. R.; Hodges, J. T.; Naumenko, O. V.; Polyansky, O. L.; Rothman, L. S.; Vandaele, A. C.; Zobov, N. F.; Dénes, N.; Fazliev, A.; Furtenbacher, T.; Gordon, I. E.; Hu, S. M.; Szidarovszky, T.; Vasilenko, I. A. *Journal of Quantitative Spectroscopy and Radiative Transfer* **2014**, *142*, 93–108.

[265] Wolke, C. T.; DeBlase, A. F.; Leavitt, C. M.; McCoy, A. B.; Johnson, M. A. *The Journal of Physical Chemistry A* **2015**, *119*, 13018–13024.

[266] Dickenson, G. D.; Niu, M. L.; Salumbides, E. J.; Komasa, J.; Eikema, K. S. E.; Pachucki, K.; Ubachs, W. *Physical Review Letters* **2013**, *110*, 193601; PRL.

[267] Knözinger, H.; Ratnasamy, P. *Catalysis Reviews* **1978**, *17*, 31–70.

[268] Knözinger, H. *Hydrogen Bonds in Systems of Adsorbed Molecules.*; In *The Hydrogen Bond*, Schuster, P.; Zundel, G.; Sandorfy, C., Eds. North Holland: Amsterdam, 1976; Vol. III, p 1263.

[269] Morterra, C.; Magnacca, G. *Catalysis Today* **1996**, *27*, 497 – 532.

[270] Coustet, V.; Jupille, J. *Surface Science* **1994**, *307 - 309, Part B*, 1161 – 1165.

[271] Hanley, L.; Whitten, J. L.; Anderson, S. L. *The Journal of Physical Chemistry* **1988**, *92*, 5803–5812.

[272] Ricca, A.; Bauschlicher Jr, C. W. *Chemical Physics* **1996**, *208*, 233–242.

[273] Romanescu, C.; Harding, D. J.; Fielicke, A.; Wang, L.-S. *Journal of Chemical Physics* **2012**, *137*, 014317.

[274] TURBOMOLE V6.6 2014; a development of University of Karlsruhe and Forschungszentrum Karlsruhe GmbH, 1989-2007, TURBOMOLE GmbH, since 2007; available from http://www.turbomole.com.

[275] Adamo, C.; Barone, V. *Journal of Chemical Physics* **1999**, *110*, 6158–6170.

[276] Grimme, S.; Antony, J.; Ehrlich, S.; Krieg, H. *The Journal of Chemical Physics* **2010**, *132*, 154104.

[277] Kesharwani, M. K.; Brauer, B.; Martin, J. M. L. *Journal of Physical Chemistry A* **2015**, *119*, 1701–1714.

[278] Bloino, J.; Barone, V. *The Journal of Chemical Physics* **2012**, *136*, 124108.

[279] Harding, D. J.; Kerpal, C.; Meijer, G.; Fielicke, A. *Journal of Physical Chemistry Letters* **2013**, *4*, 892–896.

[280] VandeVondele, J.; Krack, M.; Mohamed, F.; Parrinello, M.; Chassaing, T.; Hutter, J. *Computer Physics Communications* **2005**, *167*, 103–128; VandeVondele, J Krack, M Mohamed, F Parrinello, M Chassaing, T Hutter, J.

[281] *CP2K version 2.7*; the CP2K developers group (2013). CP2K is freely available from http://www.cp2k.org/.

[282] Hutter, J.; Iannuzzi, M.; Schiffmann, F.; VandeVondele, J. *Wiley Interdisciplinary Reviews-Computational Molecular Science* **2014**, *4*, 15–25; Hutter, Juerg Iannuzzi, Marcella Schiffmann, Florian VandeVondele, Joost.

[283] VandeVondele, J.; Hutter, J. *Journal of Chemical Physics* **2007**, *127*, 114105; VandeVondele, Joost Hutter, Juerg.

[284] Brehm, M.; Kirchner, B. *Journal of Chemical Information and Modeling* **2011**, *51*, 2007–2023; Brehm, Martin Kirchner, Barbara.

[285] te Velde, G.; Bickelhaupt, F. M.; Baerends, E. J.; Fonseca Guerra, C.; van Gisbergen, S. J. A.; Snijders, J. G.; Ziegler, T. *Journal of Computational Chemistry* **2001**, *22*, 931–967.

[286] Guerra, C. F.; Snijders, J. G.; te Velde, G.; Baerends, E. J. *Theoretical Chemistry Accounts* **1998**, *99*, 391–403; Guerra, CF Snijders, JG te Velde, G Baerends, EJ.

[287] *ADF2016*; SCM, Theoretical Chemistry, Vrije Universiteit, Amsterdam, The Netherlands, http://www.scm.com.

[288] Liu, L.; Moreno, D.; Osorio, E.; Castro, A. C.; Pan, S.; Chattaraj, P. K.; Heine, T.; Merino, G. *RSC Advances* **2016**, *6*, 27177–27182.

[289] Ghiringhelli, L. M.; Gruene, P.; Lyon, J. T.; Rayner, D. M.; Meijer, G.; Fielicke, A.; Scheffler, M. *New Journal of Physics* **2013**, *15*, 083003.

[290] Claes, P.; Janssens, E.; Ngan, V. T.; Gruene, P.; Lyon, J. T.; Harding, D. J.; Fielicke, A.; Nguyen, M. T.; Lievens, P. *Physical Review Letters* **2011**, *107*, 173401; Claes, P. Janssens, E. Ngan, V. T. Gruene, P. Lyon, J. T. Harding, D. J. Fielicke, A. Nguyen, M. T. Lievens, P.

[291] Kiran, B.; Bulusu, S.; Zhai, H.-J.; Yoo, S.; Zeng, X. C.; Wang, L.-S. *Proceedings of the National Academy of Sciences of the United States of America* **2005**, *102*, 961–964.

[292] Oganov, A. R.; Chen, J.; Gatti, C.; Ma, Y.; Ma, Y.; Glass, C. W.; Liu, Z.; Yu, T.; Kurakevych, O. O.; Solozhenko, V. L. *Nature* **2009**, *457*, 863–867; 10.1038/nature07736.

[293] Greenwood, N. N.; Earnshaw, A. *Chemistry of the Elements*, 2^{nd} ed.; Butterworth-Heinemann, 1997; ISBN 0080379419.

[294] Cotton, F. A.; Wilkinson, G.; Murillo, C. A.; Bochmann, M. *Advanced Inorganic Chemistry*, 6^{th} ed.; Wiley-Interscience, 1999; ISBN 0471199575.

[295] Fox, M. A.; Wade, K. *Pure and Applied Chemistry* **2003**, *75*, 1315–1323.

[296] Driess, M.; Nöth, H. *Molecular Clusters of the Main Group Elements*; Wiley-VCH, 2004; ISBN: 9783527602445.

[297] McKee, M. L. *Inorganic Chemistry* **2002**, *41*, 1299–1305.

[298] Geis, V.; Guttsche, K.; Knapp, C.; Scherer, H.; Uzun, R. *Dalton Transactions* **2009**, 2687–2694.

[299] Avelar, A.; Tham, F.; Reed, C. *Angewandte Chemie International Edition* **2009**, *48*, 3491–3493.

[300] Bolli, C.; Derendorf, J.; Keßler, M.; Knapp, C.; Scherer, H.; Schulz, C.; Warneke, J. *Angewandte Chemie International Edition* **2010**, *49*, 3536–3538.

[301] Boustani, I. *Chemical Physics Letters* **1995**, *240*, 135–140.

[302] Boustani, I. *Physical Review B* **1997**, *55*, 16426–16438; PRB.

[303] Zhai, H.-J.; Alexandrova, A. N.; Birch, K. A.; Boldyrev, A. I.; Wang, L.-S. *Angewandte Chemie International Edition* **2003**, *42*, 6004–6008.

[304] Zhai, H.-J.; Kiran, B.; Li, J.; Wang, L.-S. *Nat Mater* **2003**, *2*, 827–833; 10.1038/nmat1012.

[305] Sergeeva, A. P.; Zubarev, D. Y.; Zhai, H.-J.; Boldyrev, A. I.; Wang, L.-S. *Journal of the American Chemical Society* **2008**, *130*, 7244–7246; PMID: 18479137.

[306] Jiménez-Halla, J. O. C.; Islas, R.; Heine, T.; Merino, G. *Angewandte Chemie International Edition* **2010**, *49*, 5668–5671.

[307] Moreno, D.; Pan, S.; Zeonjuk, L. L.; Islas, R.; Osorio, E.; Martinez-Guajardo, G.; Chattaraj, P. K.; Heine, T.; Merino, G. *Chemical Communications* **2014**, *50*, 8140–8143.

[308] Bai, H.; Li, S.-D. *Journal of Cluster Science* **2011**, *22*, 525–535.

[309] Olson, J. K.; Boldyrev, A. I. *The Journal of Physical Chemistry A* **2013**, *117*, 1614–1620; PMID: 23331020.

[310] Goebbert, D. J.; Wende, T.; Bergmann, R.; Meijer, G.; Asmis, K. R. *The Journal of Physical Chemistry A* **2009**, *113*, 5874–5880.

[311] Heine, N.; Asmis, K. R. *International Reviews in Physical Chemistry* **2016**, *35*, 507.

[312] Zeonjuk, L. L.; Vankova, N.; Knapp, C.; Gabel, D.; Heine, T. *Physical Chemistry Chemical Physics* **2013**, *15*, 10358–10366.

[313] Barbieri, P. L.; Fantin, P. A.; Jorge, F. E. *Molecular Physics* **2006**, *104*, 2945–2954.

[314] van Lenthe, E.; Baerends, E. J.; Snijders, J. G. *The Journal of Chemical Physics* **1993**, *99*, 4597–4610.

[315] van Lenthe, E.; Baerends, E. J.; Snijders, J. G. *The Journal of Chemical Physics* **1994**, *101*, 9783–9792.

[316] van Lenthe, E.; Ehlers, A.; Baerends, E.-J. *The Journal of Chemical Physics* **1999**, *110*, 8943–8953.

[317] Scott, A. P.; Radom, L. *The Journal of Physical Chemistry* **1996**, *100*, 16502–16513.

[318] Sousa, S. F.; Fernandes, P. A.; Ramos, M. J. *The Journal of Physical Chemistry A* **2007**, *111*, 10439–10452.

[319] Pople, J. A.; Head-Gordon, M.; Raghavachari, K. *The Journal of Chemical Physics* **1987**, *87*, 5968–5975.

[320] Krishnan, R.; Binkley, J. S.; Seeger, R.; Pople, J. A. *The Journal of Chemical Physics* **1980**, *72*, 650–654.

[321] Hay, P. J.; Wadt, W. R. *The Journal of Chemical Physics* **1985**, *82*, 270–283.

[322] Zeonjuk, L. L.; Vankova, N.; Mavrandonakis, A.; Heine, T.; Röschenthaler, G.-V.; Eicher, J. *Chemistry – A European Journal* **2013**, *19*, 17413–17424.

[323] Fonseca Guerra, C.; Snijders, J. G.; te Velde, G.; Baerends, E. J. *Theoretical Chemistry Accounts* **1998**, *99*, 391–403.

[324] *ADF2012*; SCM, Theoretical Chemistry, Vrije Universiteit, Amsterdam, The Netherlands 2012.

[325] Koch, W.; Holthausen, M. C. *A Chemist's Guide to Density Functional Theory*, 2^{nd} ed.; Wiley-VCH, 2002; ISBN 9783527303724.

[326] Drahos, L.; Heeren, R. M. A.; Collette, C.; Pauw, E. D.; Vékey, K. *Journal of Mass Spectrometry* **1999**, *34*, 1373–1379.

[327] Vendrell, O.; Gatti, F.; Meyer, H.-D. *Angewandte Chemie International Edition* **2007**, *46*, 6918–6921.

[328] Arrhenius, S. *Z. Phys. Chem.* **1887**, *1*, 631–649.

[329] Thämer, M.; De Marco, L.; Ramasesha, K.; Mandal, A.; Tokmakoff, A. *Science* **2015**, *350*, 78–82.

[330] Kulig, W.; Agmon, N. *The Journal of Physical Chemistry B* **2014**, *118*, 278–286.

[331] Corongiu, G.; Kelterbaum, R.; Kochanski, E. *The Journal of Physical Chemistry* **1995**, *99*, 8038–8044.

[332] Hodges, M. P.; Wales, D. J. *Chemical Physics Letters* **2000**, *324*, 279–288.

[333] Kuo, J.-L.; Klein, M. L. *The Journal of Chemical Physics* **2005**, *122*, 024516.

[334] Bankura, A.; Chandra, A. *Chemical Physics* **2011**, *387*, 92–102.

[335] Christie, R. A.; Jordan, K. D. *The Journal of Physical Chemistry A* **2001**, *105*, 7551–7558.

[336] Heine, N.; Fagiani, M. R.; Asmis, K. R. *The Journal of Physical Chemistry Letters* **2015**, *6*, 2298–2304.

[337] McLean, A. D.; Chandler, G. S. *The Journal of Chemical Physics* **1980**, *72*, 5639–5648.

[338] Dunning, T. H. *The Journal of Chemical Physics* **1989**, *90*, 1007–1023.

[339] Kendall, R. A.; Dunning, T. H.; Harrison, R. J. *The Journal of Chemical Physics* **1992**, *96*, 6796–6806.

[340] Gonzalez, C.; Schlegel, H. B. *The Journal of Chemical Physics* **1989**, *90*, 2154–2161.

[341] Gonzalez, C.; Schlegel, H. B. *The Journal of Physical Chemistry* **1990**, *94*, 5523–5527.

[342] Baer, T.; Hase, W. L. *Unimolecular Reaction Dynamics. Theory and Experiments*; The International Series of Monographs on Chemistry; Oxford University Press: New York, 1996.

[343] Zhu, L.; Hase, W. L. *Quantum Chemistry Program Exchange Bulletin* **1994**, *644*.

[344] Beyer, T.; Swinehart, D. F. *Commun. ACM* **1973**, *16*, 379.

[345] Forst, W. *The Journal of Physical Chemistry* **1982**, *86*, 1771–1775.

[346] Shampine, L.; Reichelt, M. *SIAM Journal on Scientific Computing* **1997**, *18*, 1–22.

[347] *MATLAB version 8.4 (R2014b)*; The MathWorks, Inc.: Natick, Massachusetts, 2014.

[348] Wolk, A. B.; Leavitt, C. M.; Garand, E.; Johnson, M. A. *Accounts of Chemical Research* **2014**, *47*, 202–210.

[349] Carnegie, P. D.; McCoy, A. B.; Duncan, M. A. *The Journal of Physical Chemistry A* **2009**, *113*, 4849–4854.

[350] Ivanov, S. D.; Grant, I. M.; Marx, D. *The Journal of Chemical Physics* **2015**, *143*, 124304.

[351] Ivanov, S. D.; Witt, A.; Marx, D. *Physical Chemistry Chemical Physics* **2013**, *15*, 10270–10299.

[352] Bowman, J. M.; Braams, B. J.; Carter, S.; Chen, C.; Czakó, G.; Fu, B.; Huang, X.; Kamarchik, E.; Sharma, A. R.; Shepler, B. C.; Wang, Y.; Xie, Z. *The Journal of Physical Chemistry Letters* **2010**, *1*, 1866–1874.

[353] Marx, D.; Parrinello, M. *The Journal of Chemical Physics* **1996**, *104*, 4077–4082.

[354] Vendrell, O.; Brill, M.; Gatti, F.; Lauvergnat, D.; Meyer, H.-D. *The Journal of Chemical Physics* **2009**, *130*, 234305.

[355] Janoschek, R.; Weidemann, E. G.; Pfeiffer, H.; Zundel, G. *Journal of the American Chemical Society* **1972**, *94*, 2387–2396.

[356] Koumura, N.; Zijlstra, R. W. J.; van Delden, R. A.; Harada, N.; Feringa, B. L. *Nature* **1999**, *401*, 152–155; 10.1038/43646.

[357] Huang, W.; Sergeeva, A. P.; Zhai, H.-J.; Averkiev, B. B.; Wang, L.-S.; Boldyrev, A. I. *Nat Chem* **2010**, *2*, 202–206; 10.1038/nchem.534.

[358] Ohshimo, K.; Komukai, T.; Moriyama, R.; Misaizu, F. *The Journal of Physical Chemistry A* **2014**, *118*, 3899–3905; PMID: 24828389.

[359] Kirilyuk, A.; Fielicke, A.; Demyk, K.; von Helden, G.; Meijer, G.; Rasing, T. *Phys. Rev. B* **2010**, *82*, 020405.

[360] Logemann, R.; de Wijs, G. A.; Katsnelson, M. I.; Kirilyuk, A. *Phys. Rev. B* **2015**, *92*, 144427.

Acknowledgements

While working on my master thesis at the University of Bristol, I asked Andreas Wenge, the postdoc who was supervising the project, to suggest me good institutes to apply for a doctorate. He told me and I quote: "The group of Gerard Meijer at the Fritz-Haber Institute is most likely the best place to go if you want to stay in the field". You can imagine my excitement when I was invited for an interview. After almost five years at the Molecular Physics department I can certainly say he was right. The outstanding quality of the science and of the scientists, the friendly and collaborative atmosphere, the high-quality support from the workshops and the many great scientists visiting every year make of the MP department a unique and excellent place to do science. I would like to express my gratefulness to Gerard for creating such a great environment and for giving me the opportunity to be part of it.

My biggest thanks go to my first supervisor Knut Asmis. He always found the time for discussions, patiently providing directions when I felt lost, or motivations when a problem seemed unsolvable to me. At the same time he valued my opinions and made me feel a peer colleague. Even since he became professor at the University of Leipzig with all the related duties, he found the time every week to come to Berlin so that we could discuss in person and I wouldn't feel left behind. I also want to thank Knut for believing in me from the very beginning. Just a week after I joined the group, for example, he made me responsible of the laser systems. It was scary at first but it also gave me great confidence.

I would like to thank the other members of the group with whom I worked and shared the many joyful as well as stressful moments during these years. Thanks to Nadja and Torsten for taking the time to teach me all the tricks of the lab. Thanks to Tim and Harald, in particular for the very helpful codes you guys wrote. Big thanks go to Xiaowei. We worked together on many projects and shared an insane amount of hours in the lab. No matter the very stressful times we went through, we always managed to be positive and productive balancing each others mood. Thanks also to Sreekanta, I wish you the best of luck with your thesis!

Most of the experiments presented in this thesis were performed using the in-house Free-Electron-Laser. Having an FEL on the backyard of your institute is a real luxury and I want to express my gratitude to all the people who worked hard to make of it the stable and reliable machine it is today: Wieland, Sandy, Wolfgang, Andreas, Heinz and Gert. In particular, thanks to Sandy for the excellent tuning of the laser even under the pressure of my watch loudly ticking next to his hear. Thanks to Wieland for the uncountable late night shifts, for hearing my complaints when I felt stressed and for the help translating the abstract in German.

I want to extend my gratitude to the colleagues of the mechanic and electronic workshops. Their help was fundamental for keeping the experiment running. The sympathetic attitude in understanding the urgency of a repair or of a new part was a great bonus. Sincere thanks to Andrea, Inga and the rest of the non-scientific staff for the support in the administrative work. A special thanks to Andrea and Inga, you are the only people I felt comfortable when pretending to speak German. Believe me, that is the very opposite of what I feel usually. A big part of what makes working at the Molecular Physics department so enjoyable is the human component. Thanks to all the MPers for the good times and many events that always turned out to be great evenings. In particular, I would like to express my gratitude to those who invested their time organizing such events like Johanna, Alex and Christian. Special thanks go to Kevin, the best office mate I could have asked for, thanks for the many good advices and the relaxing breaks. A nice MP tradition I often embraced is the after-lunch kicker session. Thanks to the many that took part over the years for the great competitive and fun atmosphere.

The collaborative and international spirit of the department is not just political propaganda, but the very true approach to Science that is pursued. During the last five years I had the pleasure to collaborate with many theoretical and experimental groups, the group of Joachim Sauer (Humboldt Universität), the group of Mark Johnson (Yale University), the group of Thomas Heine (University of Leipzig), the group of André Fielicke (FHI), the group of Dan Neumark (University of California), the group of Ling Jiang (Dalian University), the group of Ludger Wöste (Freie Universität), the group of Anne McCoy (University of Washington) and the group of Kenneth Jordan (Pittsburgh). My thanks to all people involved for the high quality work. In particular, I would like to thank Marie-Pierre Gaigeot for having me as a guest in her group (Université d'Evry) and Riccardo Spezia for introducing me to RRKM calculations.

Partendo da Perugia attraverso Bristol per finire a Berlino, tanti sono stati i compagni di questo meraviglioso percorso. Un sentito grazie a tutti gli amici che mi sono stati vicini nei tanti anni di studi che culminano nel raggiungimento di questa meta. É vostro merito se ho preservato un minimo di sanitá mentale affrontando una sfida spesso alienante.

Starting from Perugia through Bristol to finish in Berlin, many have been the companions of this wonderful journey. Many thanks to all the friends who were close to me in so many years of studies that culminated in the achievement of this goal. It is thanks to you if I have preserved a minimum of mental health facing this often alienating challenge.

Nunca hubiese podido lograr este largo curso de formación sin el apoyo de mi familia. Gracias a Juan y a mis abuelos por el orgullo que siempre me demostraron. Quiero agradecer especialmente a mi mamá y a mi papá por los sacrificios y los esfuerzos que siempre hicieron, los cuales me abrieron la posibilidad de estar hoy acá. Son una constante fuente de inspiración. Mi logro es también el vuestro y se los quiero dedicar. Gracias por creer en mí y por haberme sostenido todos estos años.

Finalmente, le quiero agradecer a Laura, mi hermosa novia. Gracias por tus mil viajes a

Berlín y por la paciencia y el amor que me demostraste cada día al esperarme. La conclusión de este viaje también marca el principio de otro que vamos a vivir juntos.

List of Publications

Papers relating to this thesis:

Opening of an Icosahedral Boron Framework: A Combined Infrared Spectroscopic and Computational Study
M.R. Fagiani, L.L. Zeonjuk, T.K. Esser, D. Gabel, T. Heine, K.R. Asmis, and J. Warneke
Article highlighted as Editor's choice in Chem. Phys. Lett. **2015**, *625*, 48–52.

Gas Phase and Charge Localization in Small Aluminum Oxide Anions: Infrared Spectroscopy and Electronic Structure Calculations
X.Song, M.R. Fagiani, S.Gewinner, W. Schöllkopf, K.R. Asmis, F.A. Bischoff, F. Berger and J. Sauer
J. Chem. Phys. **2016**, *144*, 244305.

Nuclear Quantum Effects in the Gas Phase Vibrational Spectroscopy of the Pronotated Water Pentamer
M.R. Fagiani, H. Knorke, T. Esser, N. Heine, C.T. Wolke, S. Gewinner, W. Schöllkopf, M.-P. Gaigeot, R. Spezia, M.A. Johnson, and K.R. Asmis
Phys. Chem. Chem. Phys. **2016**, *18*, 26743.

Structure and Fluxionality of B_{13}^+ Probed by Infrared Photodissociation Spectroscopy
M.R. Fagiani, X. Song, P. Petkov, S. Debnath, S. Gewinner, W. Schöllkopf, T. Heine, A. Fielicke and K.R. Asmis
Very important paper in Angew. Chem. Int. Ed. **2016**, DOI: 10.1002/anie.201609766, in print.

Untersuchung der Struktur und Dynamik von B_{13}^+ mit Infrarot-Photodissoziations-spektroskopie
M.R. Fagiani, X. Song, P. Petkov, S. Debnath, S. Gewinner, W. Schöllkopf, T. Heine, A. Fielicke and K.R. Asmis
Very important paper in Angew. Chem. **2016**, DOI: 10.1002/ange.201609766, in print.

Gas Phase Vibrational Spectroscopy of $(Al_2O_3)_{1-6}AlO_2^-$
X. Song, M.R. Fagiani, S. Gewinner, W. Schöllkopf, K.R. Asmis, F.A. Bischoff, F. Berger and J. Sauer
manuscript in preparation.

Dissociative Water Adsorption by $Al_3O_4^+$ in the Gas Phase: A Combined Cryogenic Ion Vibrational Spectroscopy and Density Functional Theory Study
M.R. Fagiani, X. Song, S. Debnath, S. Gewinner, W. Schöllkopf, K.R. Asmis, F.A. Bischoff, F. Müller and J. Sauer
manuscript in preparation.

Additional papers not directly related to this thesis

Isomer-Selective Detection of Hydrogen-Bond Vibrations in the Protonated Water Hexamer
N. Heine, M.R. Fagiani, M. Rossi, T. Wende, G. Berden, V. Blum, K.R. Asmis
J. Am. Chem. Soc. **2013**, *135*, 8266–8273.

The vibrational spectrum of FeO_2^+ isomers-Theoretical benchmark and experiment
T.M. Maier, A.D. Boese, J. Sauer, T. Wende, M.R. Fagiani, K.R. Asmis
J. Chem. Phys. **2014**, *140*, 204315.

Site-specific spectral signatures of water molecules in the "magic" $H_3O^+(H_2O)_{20}$ and $Cs^+(H_2O)_{20}$ clusters in the regions of the OH(D) stretches and low frequency librations (215–1000 cm^{-1})
J.A. Fournier, C.T. Wolke, C.J. Johnson, M.A. Johnson, N. Heine, S. Gewinner, W. Schöllkopf, T.K. Esser, M.R. Fagiani, H. Knorke, K.R. Asmis
Proc. Natl. Acad. Sci. USA **2014**, *111*, 18132–18137.

Infrared Photodissociation Spectroscopy of $C_{2n+1}N^-$ Anions with $n = 1$–5
E.C. Stanca-Kaposta, F. Schwaneberg, M.R. Fagiani, T. Wende, F. Hagemann, A. Wünschmann, L. Wöste, and K.R. Asmis
Z. Phys. Chem. **2014**, *228*, 351–368.

Disentangeling the Contribution of Multiple Isomers to the Infrared Spectrum of the Protonated Water Heptamer
N. Heine, M.R. Fagiani, K.R. Asmis
J. Phys. Chem. Lett. **2015**, *6*, 2298–2304.

Gas Phase Vibrational Spectroscopy of cold $(TiO_2)_n^-$ ($n = 3$–8) clusters
M.L. Weichman, X. Song, M.R. Fagiani, S. Debnath, S. Gewinner, W. Schöllkopf, D.M. Neumark, and K.R. Asmis
J. Chem. Phys. **2016**, *144*, 124308.

Infrared Photodissociation Spectroscopy of C_4N^-, C_6N^- and C_8N^-
E.C. Stanca-Kaposta, F. Schwaneberg, M.R. Fagiani, M. Lalanne, L. Wöste, and K.R. Asmis
ChemPhysChem. **2016**, *17*, 3783–3789.

Spectroscopic snapshots of the Grotthuss proton relay mechanism in water
C.T. Wolke, J.A. Fournier, L.C. Dzugan, M.R. Fagiani, T.T. Odbadrakh, H. Knorke, K.D. Jordan, A.B. McCoy, K.R. Asmis, and M.A. Johnson
Science **2016**, *35*, 1131–1135.

The Mechanism of Dissociative Hydrogen Adsorption to $Ti_2O_4^-$ in the Gas Phase
X. Song, M.R. Fagiani, S. Debnath, A. Lyalin, M. Gao, S. Maeda, T. Taketsugu, S. Gewinner, W. Schöllkopf, K.R. Asmis
manuscript in preparation.